Titre: Title:	Numerical Investigation of the Bond Behaviour of Reinforcing Bars in UHPFRC
Auteur: Author:	Mohammadreza Zahedi
Date:	2021
Type:	Mémoire ou thèse / Dissertation or Thesis
Référence: Citation:	Zahedi, M. (2021). Numerical Investigation of the Bond Behaviour of Reinforcing Bars in UHPFRC [Master's thesis, Polytechnique Montréal]. PolyPublie. https://publications.polymtl.ca/6325/

URL de PolyPublie: PolyPublie URL:	https://publications.polymtl.ca/6325/
Directeurs de recherche: Advisors:	Bruno Massicotte
Programme: Program:	Génie civil

POLYTECHNIQUE MONTRÉAL

affiliée à l'Université de Montréal

Numerical investigation of the bond behaviour of reinforcing bars in UHPFRC

MOHAMMADREZA ZAHEDI

Département des génies civil, géologique et des mines

Mémoire présenté en vue de l'obtention du diplôme de *Maîtrise ès sciences appliquées*

Génie civil

Mai 2021

POLYTECHNIQUE MONTRÉAL

affiliée à l'Université de Montréal

Ce mémoire intitulé :

Numerical investigation of the bond behaviour of reinforcing bars in UHPFRC

Présenté par

Mohammadreza ZAHEDI

en vue de l'obtention du diplôme de *Maîtrise ès sciences appliquées*

a été dûment accepté par le jury d'examen constitué de :

Mahdi BEN FTIMA, Président

Bruno MASSICOTTE, Membre et directeur de recherche

Benoît MARLEAU, Membre

DEDICATION

To my wife and my family

ACKNOWLEDGEMENTS

I would like to take this opportunity to sincerely thank my research supervisor, Mr. Bruno Massicotte, for providing me with the opportunity to work alongside him in a field that interests me so much. His expertise, advice, listening skills and moral and financial support have not only contributed to the excellent progress of my Master's Degree but also have been of great professional and personal enrichment to me.

I am grateful to my co-supervisor and friend, Fabien Lagier, for the thoroughness and patience he has shown towards me. The exchanges of ideas we had during the meetings were highly informative, thanks to the extent of his knowledge and his references. His encouragement was decisive in the accomplishment of this project.

My appreciation also goes to the Ministry of Transport of Quebec and CRIB, which funded this research project.

I am further indebted to my friends Mehran Mehri, Mohammad Katirae and Siamak Ohadi, who helped me throughout undertaking the whole process.

Last but certainly not least, I am fully indebted to my wife, Anita, my dear parents and my lovely sister, without whose help, support, and patience throughout, nothing would have been possible.

RÉSUMÉ

La construction accélérée des ponts (ABC) gagne en popularité en Amérique du Nord. Avec cette approche des éléments préfabriqués sont assemblés sur chantier pour obtenir une structure au comportement monolithique. Les avantages de cette technique comprennent la réduction des coûts et du temps de construction tout en offrant une meilleure durabilité. Le succès de cette nouvelle méthode de construction repose sur la performance des joints entre les éléments préfabriqués. La disponibilité du béton armé fibré ultra-performant (BFUP) dans les connexions a été la clé de voûte pour accroître la popularité de cette approche de construction. La présente recherche s'inscrit dans le cadre d'un projet de recherche en cours à Polytechnique Montréal, parrainé par le ministère des Transports du Québec, qui vise à intégrer des critères de conception de joints performants pour les éléments préfabriqués.

Cette recherche numérique vise à quantifier la contribution des propriétés en traction directe du BFUP sur le comportement de l'ancrage des barres d'armature dans les joints de chevauchement sans contact. Pour atteindre cet objectif, le mémoire se concentre sur le comportement de spécimens d'essai d'ancrage en traction directe (ATD) à l'aide du logiciel d'éléments finis d'ABAQUS par le biais d'une résolution Explicit. Le modèle constitutif de béton EPM3D est adopté pour tenir compte des propriétés en traction du BFUP. La stratégie adoptée repose sur la modélisation des propriétés d'ancrage à l'échelle des nervures.

Pour atteindre l'objectif visé dans le cas d'une orientation aléatoire des fibres, les paramètres définissant le comportement en traction direct des phases écrouissage et d'adoucissement BFUP ont été regroupés en six ensembles. Ces ensembles comprennent la phase d'écrouissage en déformation, la résistance maximale à la traction et la déformation correspondant à cette résistance maximale à la traction, la pente de la branche adoucissante après localisation, l'énergie dissipée pendant la phase post-pic et la variation de contrainte de traction dans la première étape de l'adoucissement. L'étude a évalué la réponse des spécimens en ce qui a trait à la contrainte dans la barre ancrée, au glissement de la barre et à l'ouverture des fissures. Pour ces analyses, des propriétés matérielles isotropes ont été utilisées. Les résultats indiquent que les paramètres de la phase d'adoucissement jouent un rôle plus important dans le comportement des liaisons par rapport à la phase d'écrouissage. Le développement des contraintes de confinement dans les deux directions orthogonales autour de la barre ancrée a également été étudié pour comprendre le mécanisme

d'ancrage dans l'essai ATD. Les résultats indiquent que la résistance maximale à la traction affecte l'amplitude des contraintes de confinement, et la pente post-fissuration affecte la distribution des contraintes de confinement.

Les propriétés de traction orthotropes n'ont pas encore été implémentées dans EPM3D. Afin d'étudier l'effet des propriétés de traction du BFUP sur le comportement de l'ancrage pour les spécimens d'essai ATD, l'effet de l'orientation des fibres a été pris en considération en introduisant des bandes faibles dans les zones ou des propriétés réduites en traction sont attendues dans le modelé numérique ATD. Cette stratégie a d'abord été calibrée à l'aide d'un spécimen ATD d'une série d'essais. L'amélioration de la stratégie de modélisation a suivi une approche de type analyse inverse dans le cadre d'un processus d'essais et d'erreurs. Le modelé final a ensuite été valide à l'aide des résultats des 11 spécimens du programme d'essai. Les résultats indiquent que la stratégie adoptée est valide et mené a une exactitude adéquate. Cet exercice a également confirmé les conclusions obtenues dans l'analyse précédente avec une orientation aléatoire des fibres (propriétés isotropes) a l'effet que les paramètres de la phase d'adoucissement jouent un rôle significatif dans le comportement de l'ancrage. Dans le cas d'un essai ATD avec les fibres orientées perpendiculairement à l'axe des barres, un facteur d'efficacité de 0.9 a été obtenu dans le modèle calibre lors de l'utilisation de propriétés de traction directe obtenus de l'essais sur os.

ABSTRACT

Accelerated bridge construction (ABC) is gaining popularity in North America. With this approach, prefabricated elements are assembled on site to obtain a structure with monolithic behaviour. The benefits of this technique include reducing costs and construction time while providing better durability. The success of this new construction method depends on the performance of the joints between the prefabricated elements. The availability of high-performance fibre-reinforced concrete (UHPFRC) in connections has been the keystone to increasing the popularity of this construction approach. This research is part of an ongoing research project at Polytechnique Montréal, sponsored by the Quebec Ministry of Transportation, which aims to incorporate criteria for designing high-performance joints for prefabricated elements.

This numerical research aims to quantify the contribution of UHPFRC direct tensile properties on the behaviour of the bond of reinforcing bars in contactless lap-splice joints. To achieve this goal, the thesis focuses on the behaviour of direct tension bond (DTB) test specimens using ABAQUS finite element software through an Explicit solution strategy. The EPM3D concrete model is adopted to consider the traction properties of UHPFRC. The strategy adopted is based on modelling the bond properties at the rib scale.

To achieve the objective in the case of random fibre orientation, the parameters defining the direct tensile behaviour of the hardening and softening phases of UHPFRC were grouped into six sets. These sets include the hardening phase, maximum tensile strength and strain corresponding to this maximum tensile resistance, the slope of the softening branch after localization, the energy dissipated during the post-peak phase, and the change in traction stress in the first stage of the softening. The study assessed the specimen response to stress in the anchored bar, bar slip, and crack opening. For these analyses, isotropic material properties were used. The results indicate that the parameters of the softening phase play a more important role in the behaviour of the bond compared to the hardening phase. The development of confining stresses in both orthogonal directions around the anchored bar has also been studied to understand the bond mechanism in the DTB test specimens. The results indicate that the maximum tensile strength influences the magnitude of confining stresses, and the post-crack slope affects the confinement stress distribution.

Orthotropic traction properties have not yet been implemented in EPM3D. To study the effect of UHPFRC tensile properties on the bond behaviour for DTB test specimens, the effect of fibre orientation was considered by introducing weak bands in areas where reduced tensile properties are expected in the DTB numerical model. This strategy was first calibrated using a DTB specimen from a series of tests. The improvement in the modelling strategy followed an inverse analysis approach as part of a trial-and-error process. The final model was then validated using the results of the 11 specimens in the testing program. The results indicate that the strategy adopted is valid and leads to an adequate accuracy. This exercise also confirmed the conclusions obtained in the previous analysis with a random orientation of the fibers (isotropic properties), indicating that the parameters of the softening phase play a significant role in the behaviour of bond. In the case of a DTB test with fibers oriented perpendicular to the bar axis, an efficiency factor of 0.9 was obtained in the calibrated model when using direct traction properties obtained from dog-bone test.

TABLE OF CONTENTS

LIST OF TABLES

LIST OF FIGURES

LIST OF SYMBOLS AND ABBREVIATIONS

UHPFRC	Ultra-High-Performance Fibre Reinforced Concrete
UHPC	Ultra-High-Performance Concrete
DTB	Direct Tension Bond test

Variables:

b	Width of specimens
c_r	Clear lateral cover of a bar of a lap joint or anchorage with the outer surface parallel to the plane of the bars
c_{si}	Net space between two rebars
c_{so}	Net cover with the outer surface of a bar of a lap joint or anchorage, perpendicular to the plane of the bars
d_b	Diameter of a bar
e	Thickness of specimen
E_c	Elastic modulus of UHPFRC
E_{pc}	Unloading modulus of UHPFRC
E_s	Elastic modulus of steel
$E_{t,c}$	Tensile elastic modulus of UHPFRC
F_{ii}	Confining tensile force in UHPFRC around the tested bar for principal direction i
f'_c	Uniaxial compressive strength of UHPFRC
f_s	Stress in reinforcing steel
$f_{s,cr}$	Stress in reinforcing steel at initiating the main macro-crack
$f_{s,max}$	Stress in reinforcing steel at maximum force
$f_{t,el}$	Tensile strength at the end of elastic behaviour of UHPFRC
$f_{t,ts}$	Tensile strength at the beginning of hardening behaviour of UHPFRC
$f_{t,tu}$	Tensile strength at the end of hardening behaviour of UHPFRC
f_u	Ultimate strength in reinforcing steel
f_y	Yield strength stress in reinforcing steel
f_w	Tensile strength of UHPFRC at the crack opening of w
$G_{f,CO}$	Dissipated energy per crack surface area of UHPFRC during the softening phase
$g_{f,SH}$	Dissipated energy per unit volume of UHPFRC during the hardening phase

h	Height of specimens
S_{ii}	Confining tensile stress in UHPFRC around the tested bar for principal direction
l_{dt}	Embedded length of the tested bar of the anchored bar
l_{dw}	Embedded length of the support bar
ℓ_d	Embedded length of steel of the anchored bar
ℓ_s	Lap splice length
E_{so}	Slope at initiating of softening phase of UHPFRC
RA	The ratio of stress in steel in each mode to stress in steel at failure mode
s_{LE_fsmax}	Slip at maximum force in the anchorage bar
$s_{LE\_fs,cr}$	Slip at initiating the main macro-crack

Greek variables:

ε	Strain of steel
$\varepsilon_{t,el}$	Strain at the end of elastic behaviour of UHPFRC
$\varepsilon_{t,ts}$	Strain at the beginning of hardening behaviour of UHPFRC
$\varepsilon_{t,u}$	Ultimate tensile strain corresponding to the end of hardening behaviour of UHPFRC
ε_u	Ultimate strain of steel
ε_y	Yielding strain of steel
v	Poisson's coefficient
τ	Bond stress at the contact surface of steel and UHPFRC
τ_{max}	Maximum bond stress at the contact surface of steel and UHPFRC
w	Crack opening
w_u	Maximum crack opening
w_{so}	Crack opening at the end of the first stage of softening
w_{i_fsmax}	Inner crack width at failure mode
w_{o_fsmax}	Outer crack width at failure mode
Δ_{fso}	Tensile stress variations in the first stage of softening of UHPFRC

LIST OF APPENDICES

CHAPTER 1 INTRODUCTION

1.1 General context and background

As reported by Massicotte et al. (2010) for decades, precast elements have been used in bridge construction, such as bridges of San Mateo-Hayward, Confederation and Lac Hawk. However, connections between precast elements have always been the major drawback for the larger development of this construction approach, especially in areas where durability is of prime concern. The advances made for developing efficient connections and the owners' interest to build or replace more efficiently their bridge infrastructure have triggered a large interest in a construction approach recently identified as Accelerated Bridge Construction (ABC). With this method, prefabricated elements are assembled on sites to obtain a structure with monolithic behaviour. The advantages of this technique include reducing costs and construction time while providing better structural durability for connections between each element. The availability of Ultra-High Performance Fibre Reinforced Concrete (UHPFRC) in connections has been the keystone for enhancing the popularity of this construction approach (Benjamin Graybeal, 2013). Given that, this method can be used for the construction of new bridges (Bruno Massicotte, 2019) or for the upgrading of existing bridges (Dagenais et al., 2018).

1.2 Problem

The foundation elements of most bridges are made of concrete, such as footings, piers and abutments. Applying the traditional method for constructing these elements is the most time-consuming step due to the required time to install the formwork and reinforcement. The use of precast elements for foundation elements has a high potential for significantly reducing the construction time by eliminating these two steps. Although this approach is utilized for building giant bridges such as the Confederation Bridge in the 1990s or the new Samuel-de-Champlain bridge (Bruno Massicotte, 2019; Bruno Massicotte et al., 2010), or is extensively used in the United States and Ontario (Benjamin Graybeal, 2013, 2019), it has not yet been implemented for the construction of ordinary bridges in Quebec due to certain limitations. Some of these limitations include the lack of specific standards or design guidelines to allow applying the UHPFRC technology for the lap-splice connections between prefabricated columns or retaining wall elements to the footing. This is particularly true in locations where a plastic hinge must form in the

elements that ensure the desired seismic performance of bridges. This applies to most populated regions of Quebec, where the seismic hazard ranges from moderate to high, with the highest peak-ground accelerations in the Charlevoix-Kamouraska regions (Canada, 2015).

Given that, it is essential to develop earthquake-resistant design criteria to obtain practical and economic lap splice joints. Several recent studies, funded by the Ministry of Transport of Quebec (MTQ), have shown that the UHPFRC joints have remarkable performance in meeting the design requirements of current standards in seismic rehabilitation situations (Bruno Massicotte, 2019; Dagenais et al., 2018). The studies also have demonstrated that these technologies can be extended into designing the new bridges.

The present research is part of an ongoing research project at Polytechnique, sponsored by the Ministère des Transports du Québec, which aims to integrate high-performance joints design criteria into the current standard for prefabricated elements.

1.3 Purpose

This thesis is part of a research project that intends to develop UHPFRC lap splice joint design criteria used to connect prefabricated bridge elements that must meet seismic ductility requirements. Given that, it is necessary to improve the lap splice joint efficiency. The main criteria that affect the lap splice joints are categorized into four groups: loading regime, system parameters, reinforcement properties and concrete properties (Holschemacher et al., 2005). The present thesis, which is part of this research, has been focused on concrete properties. Indeed, it plans to investigate the performance of UHPFRC tensile properties on the bond behaviour in non-contact lap splice joints. The specific objectives of this thesis are as follows:

1. determining the influence of UHPFRC tensile properties on the bond performance for random fibre orientation.
2. understanding the mechanisms of confinement stress distribution in the bond zone and interpreting the influences of the first objective according to the confinement stress.
3. developing the numerical models for the certain fibre orientation and calibrating the model with the experimental results of Bastide (2020)

1.4 Variables and methodology

The main focus applied throughout this numerical research is on the influence of parameters defining the tensile properties of UHPFRC on the bond behaviour. All the models will be done using the finite element software of ABAQUS (2016) to achieve its purposes. Furthermore, this research utilizes the constitutive model of EPM3D (B. Massicotte et al., 2015) to consider UHPFRC properties. The present study will also apply the rib scale modelling based on Lagier 's (2015) approach. It is worth mentioning that all the procedures in the preprocess and post-process will be done by PYTHON. This programming language enables us to model the many configurations of lap splice joints effectively in ABAQUS.

1.5 Thesis structure

In the second chapter, we review the definitions of general and principal concepts in UHPFRC tensile properties and the bond phenomenon. Then, we explore the main parameters that affect the UHPFRC tensile properties curve's shape. Finally, we review the studies that express the impacts of the parameters on the bond behaviour.

The third chapter explains the used strategy in this research for modelling and the main challenges. The strategy includes considering the UHPFRC mechanical properties, modelling the bond behaviour, and the solution method in the finite element software.

In chapter four, the first objective of this research is addressed. Indeed, it investigates the impacts of the parameters on the UHPFRC tensile properties on the bond behaviour. The chapter primary assumption is that fibres are uniformly orientated.

The fifth chapter examines the second objective of this project. It aims to review the distribution mechanism of confinement stress in the bond zone. Moreover, the results of the fourth chapter are examined through the confinement stress distribution.

Chapter six examines the third objective of this study in three steps. In the first step, the numerical model used in the previous chapters is developed to consider fibres orientation. In the second step, the main results of chapter four are confirmed for this new position of fibres. In the last step, Bastide’s (2020) test results are used to calibrate and validate the numerical model.

Chapter seven presents the results of this research in a way through which some suggestions are made to pave the way for further studies.

CHAPTER 2 LITERATURE REVIEW

2.1 Ultra-high-performance fibre reinforced concrete

Ultra-high performance fibre reinforced concretes (UHPFRC) have high tensile ductility because of fibre metal in the cement matrix and present an outstanding durability because of their cement matrix compactness (AFGC, 2013). The interest in using this type of concrete in construction is highly demanded because of its excellent mechanical properties. Canadian concrete material standard, CSA-23.1-19 (CSA, 2019a), defines three categories of Ultra-High-Performance Concrete (UHPC). For strain hardening materials as used in this thesis, the standard requires a tensile strength and compressive strength of 5 MPa and 120 MPa, respectively.

The principal constituents of ordinary concrete are seen in the structure of UHPC; but their dosage differs. UHPC is distinguished by its high cement content (700 to 1000 kg/m 3) combined with silica fumes. The aggregates' size is minimal; the maximum diameter varies between 0.5 and 7 mm depending on the UHPC. These characteristics improve the reduction of the material's capillary porosity. The water/cement ratio (*W/C*) is reduced to 0.2, thanks to additives in large quantities. Finally, the main difference originates from metal fibres addition, whose size varies according to the largest aggregate diameter, the matrix strength, and the desired properties. Table 2.1 presents the different types of concrete formulation.

Table 2.1 The classic composition of ordinary concrete, HPC and UHPFRC (Guénet, 2016)

Constituent	Ordinary concrete	HPC	UHPFRC
Water / binder ratio	0.4-0.6	0.3-0.35	0.16-0.2
Binders (kg/m ^{3})	300-375	350-500	700-1500
Water (kg/m ^{3})	150-200	140-160	160-230
Superplasticizer (kg/m ^{3})	-	3.5-10	10-45
Silica Fume (kg/m ^{3})	-	0-50	170-375
Steel fibres (kg/m ^{3})	-	-	160-260
Density (kg/m ^{3})	2300	2300	2400-2700

UHPFRC exposes very high compressive strength from 120 to 150 MPa or more at 28 days. Polytechnique Montreal produced UHPC with compressive strength in 120 to 130 MPa at 28 days

(Braike, 2006), which is accepted by the Canadian standard CSA A23.1. Besides, UHPFRC exhibits the ductile behaviour characterized by a slight decrease in the post-cracking phase of hardening and softening thanks to fibres used in the material's structure.

Table 2.2 summarized the main parameters that have been used in the literature based on different references in this chapter.

Table 2.2 Nomenclature of main parameters

Nomenclature			
A_{Lig}	Fracture area, or ligament area (mm2)	$G_{f,B}$	Energy per unit ligament area dissipated during softening (kJ/m2)
E_{pc}	Unloading modulus (MPa)	$G_{f,matrix}$	The energy dissipated through the concrete matrix (kJ/m2)
E_{CC}	Elastic modulus (MPa)	$Gf_{,fibre}$	The energy dissipated during fibre pullout (kJ/m2)
E_{hc}	Hardening modulus (MPa)	G_{fd}	Fracture energy under dynamic condition (kJ/m2)
F	Load applied in tension (N)	L_g	Gauge length (mm)
g	Energy absorption capacity (kJ/m3)	n_{cr}	Number of cracks within gauge length
G_f	Fracture energy (kJ/m2)	s_{cr}	Average crack spacing (mm)
W	Dissipated work (N mm)	ε_{res}	Residual strain (mm/mm)
δ	Crack opening (mm)	ε_{cc}	Matrix cracking strain (mm/mm)
δ_{pc}	Crack opening at the beginning of softening (mm)	ε_{pc}	Peak strain
δ_u	Ultimate crack opening (mm)	σ_{pc}	Peak stress (MPa)
Gf,A,n	Equivalent energy per unit area dissipated during strain hardening (kJ/m2)	σ_{cc}	Matrix cracking strength (MPa)
$g_{f,A}$	Relative fracture energy per unit volume dissipated during strain hardening (kJ/m3)	χf	Fibre factor (mm/mm)

2.2 Uniaxial materials properties of UHPFRC

2.2.1 Tensile behaviour

Tensile strength of UHPFRC is the main advantage of this material. The range of this strength typically varies from 7 to 15 MPa. The fibres considerably reduce the brittleness of concrete by resisting the cracks opening and maintaining some post-cracking resistance. Figure 2.1 describes this phenomenon and presents three different behaviours according to the level of deformations.

Phase I is the linear elastic phase in which the material stiffness describes the elastic modulus. In the conventional FRC (Figure 2.1-top), the crack matrix is not strong enough to open up another crack, so the mentioned concrete moves directly from phase I to phase III. In UHPFRC (Figure 2.1 - bottom), we observe phase II. In this phase, multiple cracking happens after cracking and before softening (Benjamin Graybeal et al., 2013; Habel, 2004; Antoine Naaman, 2003). As shown in Figure 2.2, Graybeal and Baby (2013; 2012) proposed that the strain hardening segment split into two multi-cracking and crack straining phases.

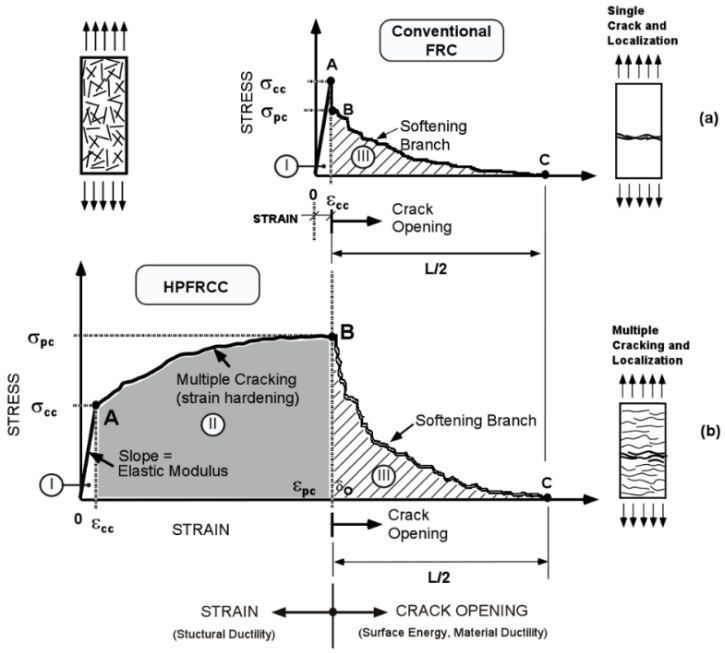

Figure 2.1 Typical stress elongation response of fibre-reinforced cement composites illustrating the cracking and maximum post-cracking stress (Antoine Naaman, 2003)

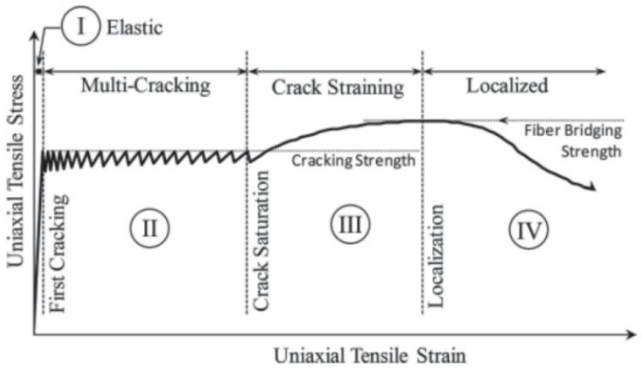

Figure 2.2 Idealized uniaxial tensile mechanical response of UHPFRC according to Graybeal and Baby (2013)

2.2.2 Classification

Compressive strength is the principal characteristic of UHPC that helps to categorize it. Unlike the compressive strength, the classification of UHPFRC based on tensile strength is more complicated. Naaman and Reinhardt (2006) recommended that UHPFRC is categorized based on its behaviour in tension and bending. Namely, the UHPFRC response in tension is strain-softening or strain-hardening; and its behaviour in bending is deflection-softening or deflection-hardening. Fracture energy, minimum ductility, and toughness are other additional parameters that UHPFRC can be classified based on (A. E. Naaman et al., 2012).

Naaman et al. (2003; 2014) classified the UHPFRC into five levels based on its uniaxial tension and flexural performances. As shown in Figure 2.3, the levels are as follows:

- Level 0: Brittle tensile failure
- Level 1: Strain softening, deflection softening
- Level 2: strain softening, deflection hardening
- Level 3: Strain hardening, deflection hardening with high energy absorption
- Level 4: Strain hardening with high energy absorption, deflection hardening with high energy absorption

The parameters on the curves are cracking stress σ_{cc}, associated strain ε_{cc}, elastic modulus E_{cc} composite tensile strength or post cracking strength σ_{pc}, modulus of rupture σ_{f1}, equivalent bending strength σ_{f2}.

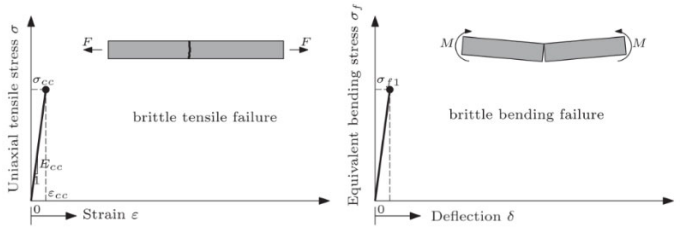

Level 0

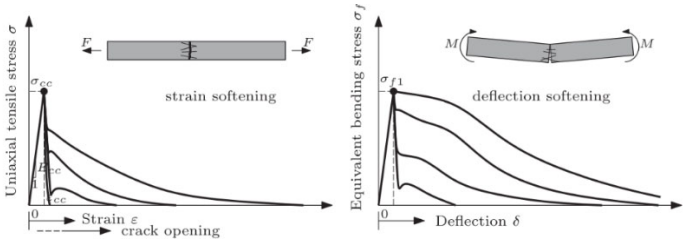

Level 1

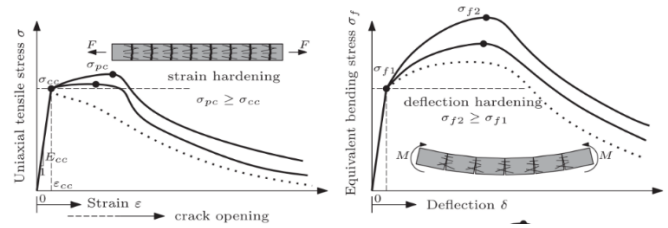

Level 2

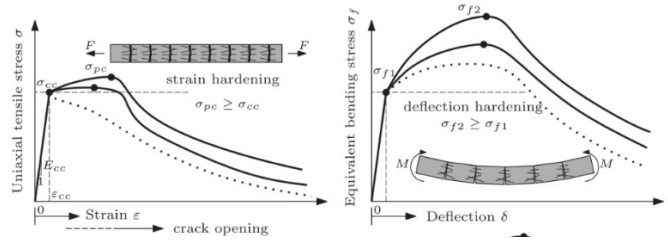

Level 3

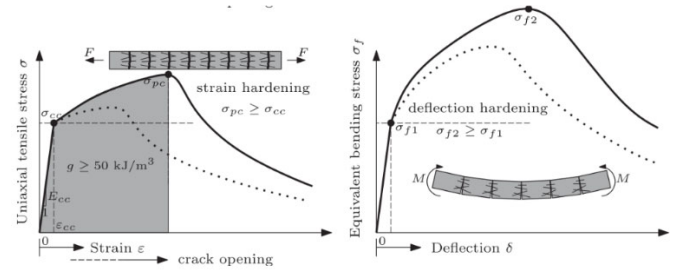

Level 4

Figure 2.3 Illustration and definition of the performance levels of fibre reinforced concrete (K Wille et al., 2014)

2.2.3 Idealized modelling approach of UHPFRC tensile behaviour

Wille et al. (2014) proposed the idealized approach for the typical tensile properties of UHPFRC (Figure 2.4). This approach distinguished the tensile behaviour into three parts as follows:

- Part I: "strain-based elastic part, determined by the initial tensile behavior up to σ_{cc}, which is defined as a fictitious point of transition from ideal linear elastic to best fitted linear strain-hardening behavior, and determined by the associated strain ε_{cc} and the elastic modulus $E_{cc.}$"
- Part II: "strain-based strain hardening part, determined by the dissipated energy per unit volume $g_{f,A,}$ 99% of the tensile strength of the composite σ_{pc}, its associated strain ε_{pc} and ε_{soft}, hardening modulus E_{hc} and the residual strain $\varepsilon_{res.}$"
- Part III: "crack opening based softening part, which is characterized by the dissipated energy per crack surface area $G_{f,B}$."

Figure 2.5 presents the idealized modelling approach to some test specimens by Wille et al. (2014).

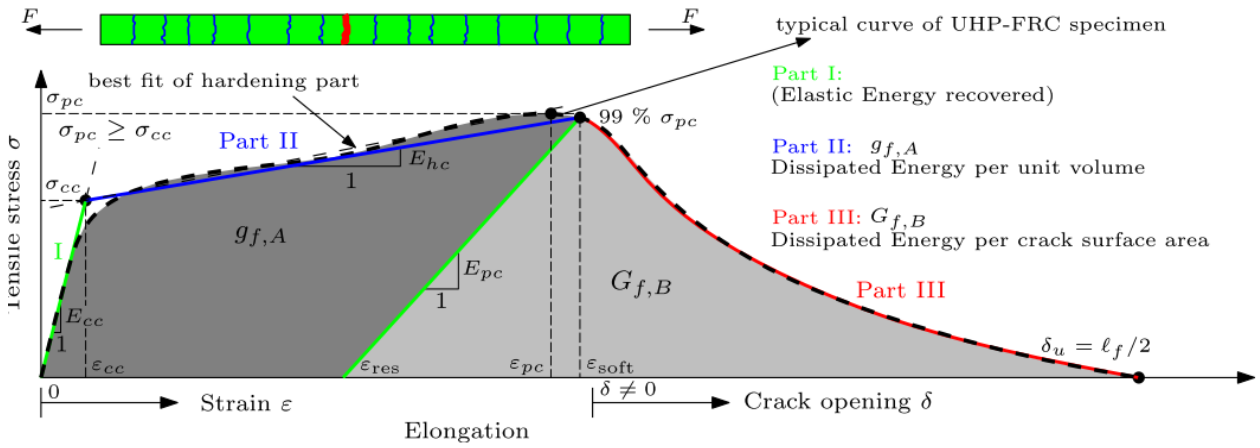

Figure 2.4 Strain hardening tensile behavior of UHPFRC and idealized modelling approach (K Wille et al., 2014).

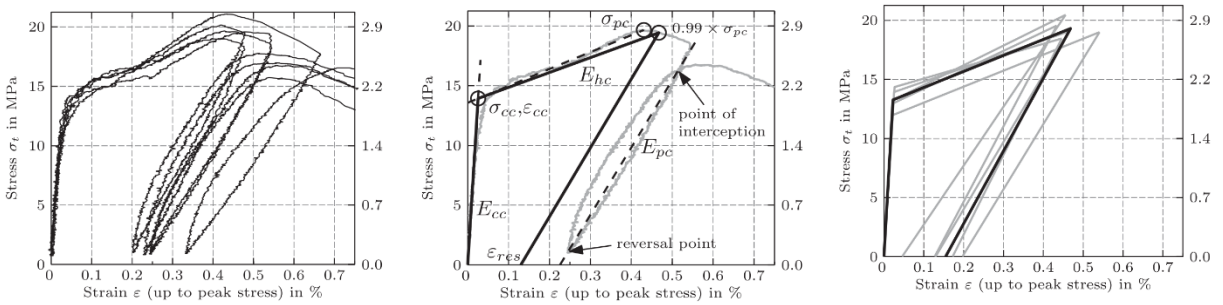

(a) Specimen 1- 5 experimental data

(b) Specimen 1 and idealized tensile behaviour

(c) Idealized tensile behaviour of specimen 1-5 and average curve

Figure 2.5 Analytical procedure for the example of series U-T-3(K Wille et al., 2014)

2.2.3.1 **Fracture energy**

Fracture energy is another primary criterion that can be considered for the classification of UHPFRC. Fibre and matrix mechanical properties, bond behavior, fibre volume fraction, and fibre orientation are the parameters that influence fracture energy. This parameter is defined as the amount of dissipated work needed to generate a unit crack with two wholly separated crack surfaces(K Wille et al., 2010).

$$Gf = \frac{W}{A_{Lig}} = \frac{\int_0^{\delta u} F(\delta) d\delta}{A_{Lig}} \tag{2-1}$$

where, F is the load applied in tension, δ is crack opening, and δu is crack opening to complete separation.

As shown in Figure 2.6, Xu and Wille (2015) presented the mechanisms contributing to fibre reinforced concrete fracture energy under tension obtained based on Li and Maalej (1996) and Wille (2008) finding.

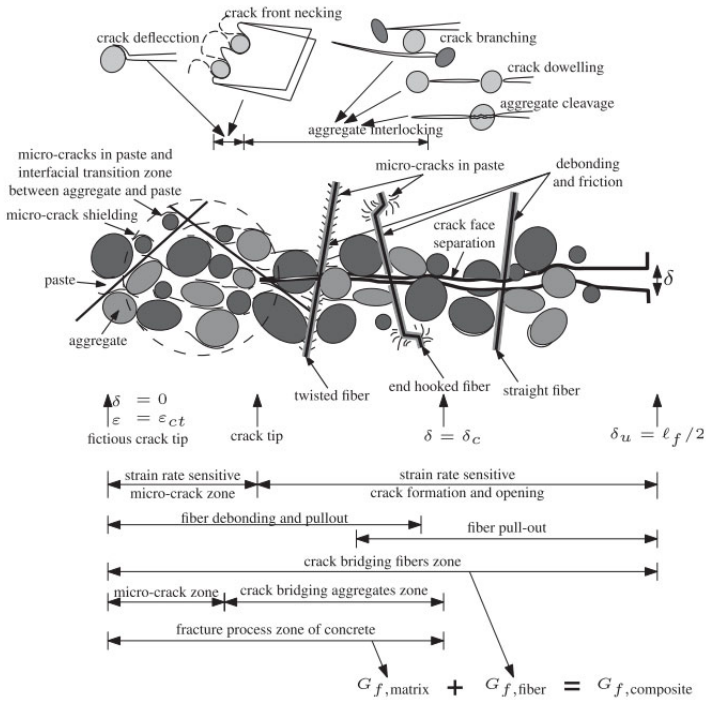

Figure 2.6 Mechanisms contributing to fracture energy of fibre reinforced concrete under tension (Based on (Li et al., 1996; Kay Wille, 2008))

Wille et al. (2010) separated the energy dissipated during strain hardening $G_{f,A,n}$ and the energy dissipated during softening $G_{f,B}$ per unit ligament area to evaluate strain hardening fibres fracture energy reinforced concrete un-notched specimens under direct tension (Figure 2.7).

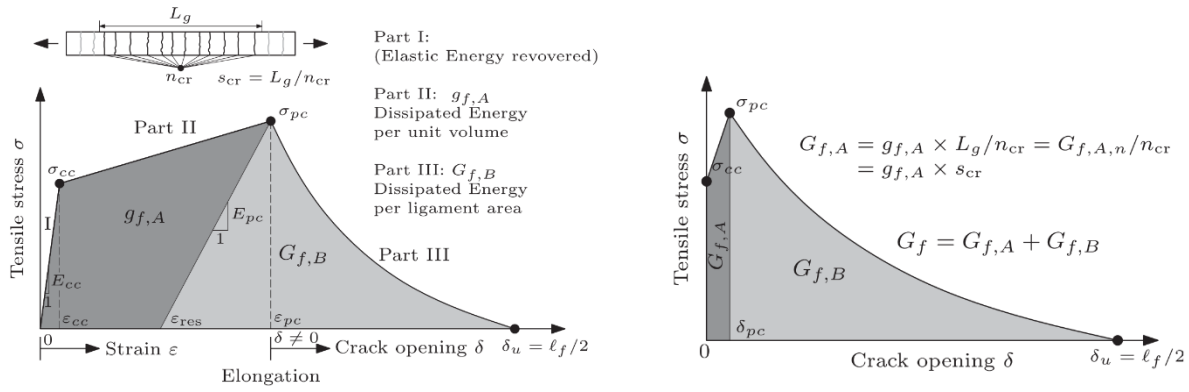

(a) Definition of energy per unit volume g_f and per unit area G_f

(b) Definition of G_f related to the failure causing crack

Figure 2.7 Strain hardening material under tension and the definition of fracture energy related parameters (K Wille et al., 2010).

Moreover, they determined the following equations to obtain the energy parameters indicated in Figure 2.7.

$$g_{f,A} = \int_0^{\varepsilon_{pc}} \sigma(\varepsilon)d\varepsilon - \frac{1}{2}\frac{\sigma_{pc}^2}{E_{pc}} \tag{2-2}$$

$$G_{f,A} = g_{f,A}.{}^{L_g}/_{n_{cr}} = g_{f,A}.S_{cr} = {}^{G_{f,A,n}}/_{n_{cr}} \tag{2-3}$$

$$G_{f,B} = L_g.\int_{\varepsilon_{pc}}^{\varepsilon_u} \sigma(\varepsilon)d\varepsilon + \frac{1}{2}\frac{\sigma_{pc}^2}{E_{PC}} \tag{2-4}$$

$$\delta_{pc} = {}^{2G_{f,A}}\Big/_{(\sigma_{cc}+\sigma_{pc})} \tag{2-5}$$

$$G_f = G_{f,A} + G_{f,B} \tag{2-6}$$

Where, $g_{f,A}$ is relative fracture energy per unit volume dissipated during strain hardening, $G_{f,A,n}$ is equivalent energy per unit area dissipated during strain hardening, $G_{f,B}$ is energy per unit area

dissipated during softening, δ_{pc} is crack opening at the beginning of softening, and G_f is fracture energy.

2.2.4 The variables which influence Tensile Behaviour of UHPFRC lows

2.2.4.1 Wille and Naaman

Wille and Naaman (2010) studied the effect of several parameters on fracture energy dissipation, including fibre content (1%,1.5%,2%,2.5%), types of fibres (straight, hooked, twisted), and finally fibre factor ($\chi_f = V_f\, l_f / d_f$). Their research for the 2% volume friction by high strength twisted steel fibres through the optimization of matrix and fibre parameters observed the following values for some parameters: G_f=32 kJ/m^2, σ_{pc}=16 MPa, ε_{pc}=0.61%, s_{cr}=3 mm, and an averaged residual crack width of 7-8 mm. The results showed that the fracture energy through the efficiency per unit volume of fibres is about one and a half times the amounts reported by the others, namely, G_f= 31 kJ/m^2 with a 1.5% volume fraction (Figure 2.8).

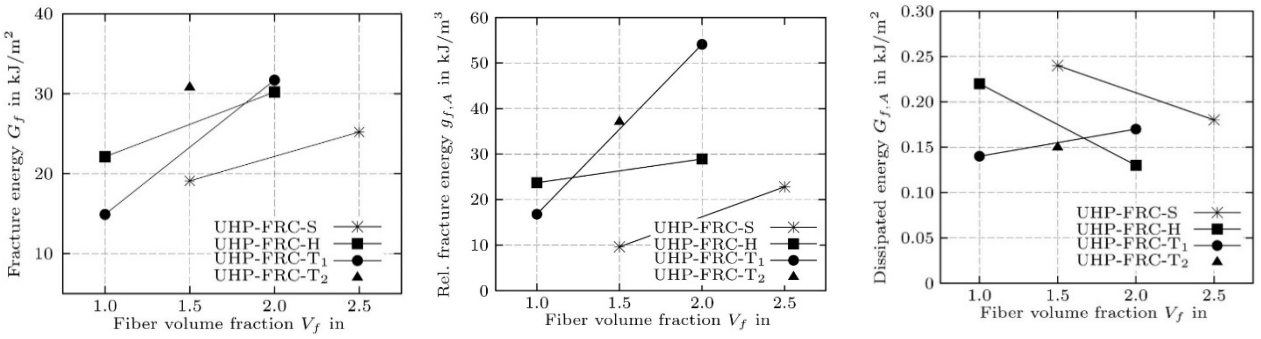

(a) Fracture energy G_f

(b) Dissipated energy $g_{f,A}$ per unit volume

(c) Dissipated energy $G_{f,A}$ per unit area of one crack during strain hardening

Figure 2.8 Energy dissipation of UHPFRC (K Wille et al., 2010)

2.2.4.2 **Delsol**

The behaviour of UHPC is very dependent on the orientation of the fibres in the matrix. Desol (2012) determined that a poor orientation of the fibres can lead to a loss of 60% of the tensile strength and 95% of the ductility for the strain hardening phase (Figure 2.9).

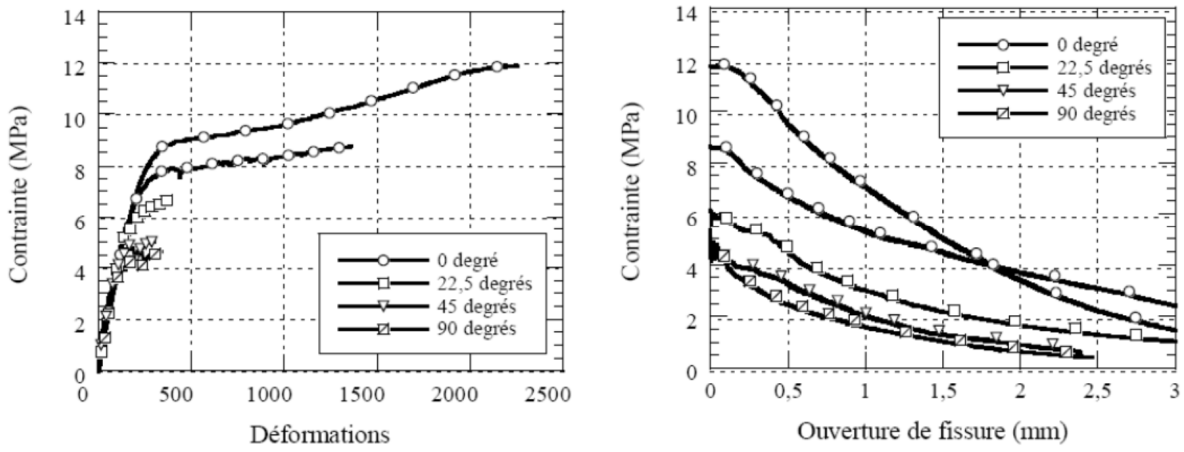

Figure 2.9 UHPC behaviour in the direct tensile pullout test for different fibre orientations(Delsol, 2012)

2.2.4.3 **Wille, El-Tawil and Naaman**

In their study Wille, El-Tawil and Naaman (2014) investigated three types of fibres, including Straight, Hooked and Twisted and each one with different volume fractions (i.e. .1.5%, 2%, 2.5%, 3%). The research showed that σ_{pc}, E_{hc}, g, s_{cr}, and E_{pc} depend strongly on the fibre volume fraction V_f (Figure 2.9), while ε_{pc} and ε_{soft} are almost independent of V_f. The study additionally found that the type of fibre has a low effect on peak stress σ_{pc}, peak strain ε_{pc} and fracture energy G_f while affecting E_{pc} (Figure 2.10).

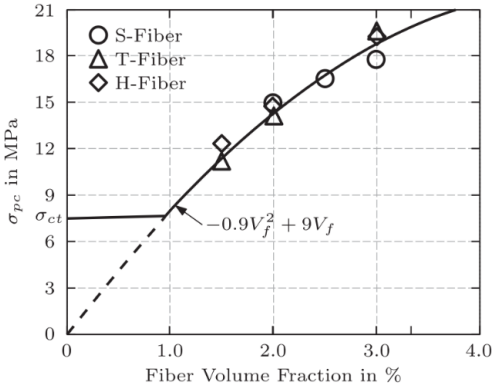

(a) Composite tensile strength -fibre volume fraction

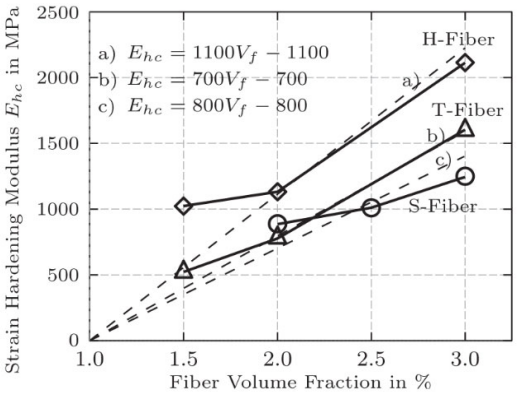

(b) Strain hardening modulus -fibre volume fraction

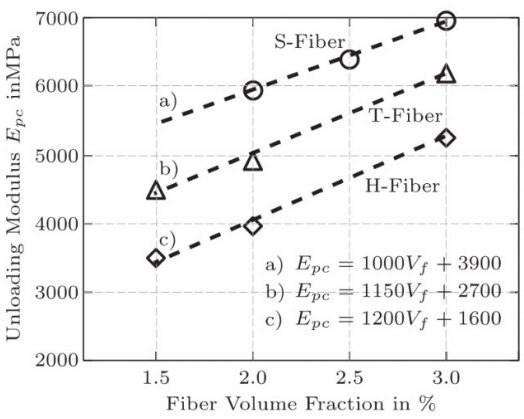

(c) Unloading modulus-fibre volume fraction

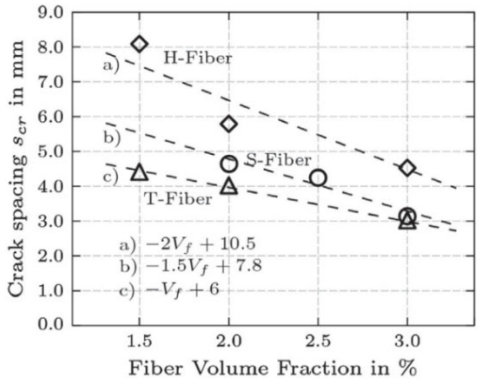

(d) Crack spacing -fibre volume fraction

Figure 2.10: Test results of composite tensile strength, strain hardening modulus, unloading modulus and crack spacing (K Wille et al., 2014)

2.2.4.4 **Xu and Wille**

The study of Xu and Wille (2015) examined the specimens with several variable parameters, including fibre types(i.e. straight, Hooked, Twisted), fibre volume fraction (i.e. 1.5%, 2%, 2.5%, 3%) and strain rates (i.e. 0.0001, 0.001, 0.01, 0.1), to investigate fracture energy at low strain, especially on post-peak behavior.

The results noted that the fracture energy G_f strongly depends on several parameters, such as the fibre factor χ_f (Figure2.10b), the fibre volume fraction V_f, fibre slenderness and matrix properties.

Moreover, the study showed the fibre type had not played a significant role with comparable the fibre factor χ_f in the energy dissipated during the hardening and softening phase (Figure 2.11a and Figure 2.11b).

The fracture energy G_f is sensitive to the strain rate's amount ε^o, and it increases by increasing ε^o.

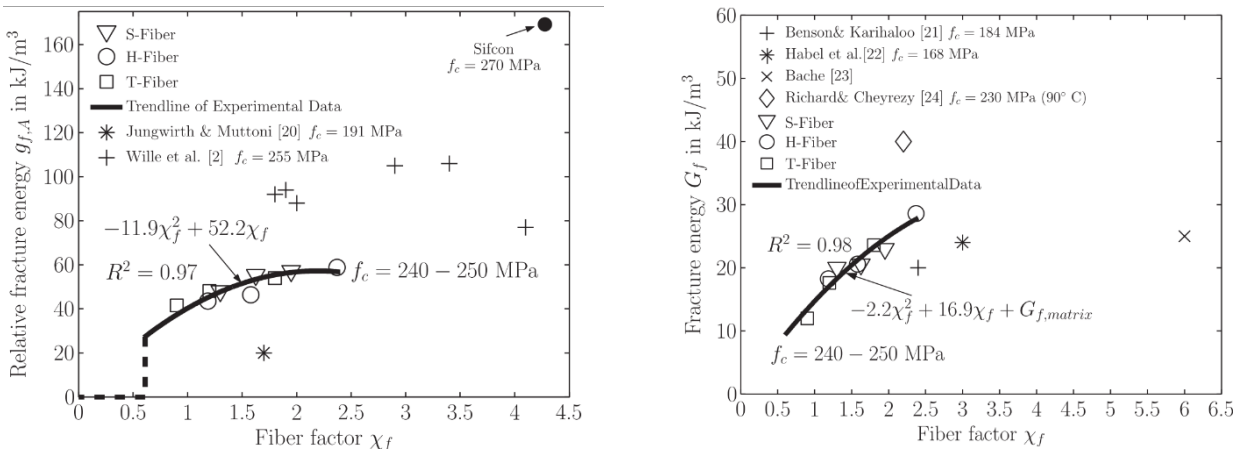

(a) Dissipated energy per unit volume $g_{f,A}$; (b) Fracture energy G_f

Figure 2.11: Energy dissipation (Xu et al., 2015)

2.2.4.5 **Pyo, Wille, El-Tawil and Naaman**

Pyo, Wille, El-Tawil and Naaman (2015) applied the following variable parameters to obtain more detailed knowledge of the tensile behaviour of UHP-FRC under loading with various strain rates:

- Fibre type (twisted and straight)
- Fibre diameter (0.2 - 0.4 mm)
- Fibre length (18 and 25 mm)
- Fibre tensile strength (1850 - 2860 MPa)
- Fibre volume fraction (1%, 2% and 3%)

The result indicated that the first cracking strength σ_{cc}, post-cracking strength σ_{pc} and energy absorption g increase with both reinforcing index $V_f\ (l^2_f/d_f)$ and the strain rate (Figure 2.12).

Moreover, the study showed that σ_{pc} and g versus $V_f (l^2_f/d_f)$ trends are linear. Finally, they observed that increasing the strain rate leads to increasing the σ_{pc}, g

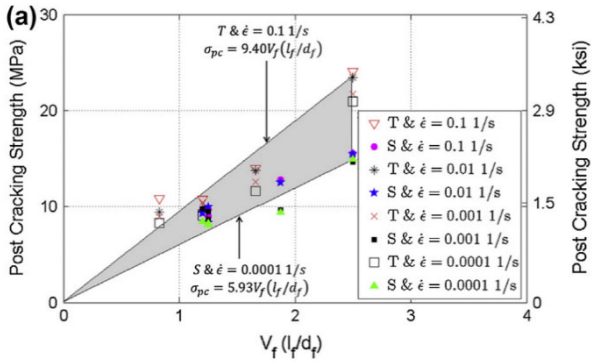

(a) Post cracking

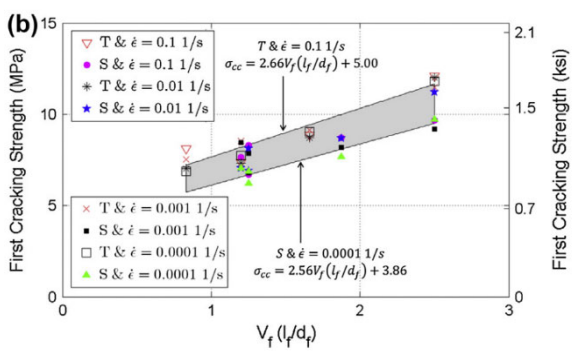

(b) First cracking strength

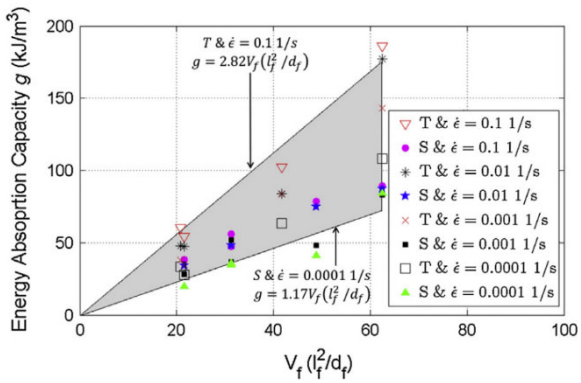

(c) Energy absorption

Figure 2.12 Effects of the fibre reinforcing index on UHPFRC behaviour (Pyo et al., 2015)

2.2.4.6 **Pyo, El-Tawiland and Naaman**

The objective of the study of Pyo, El-Tawiland and Naaman (2016) was to experimentally characterize the direct tensile response of UHPFRC under high strain rates. The research indicated that the fibre aspect ratio and twisting played a significant role in UHPFRC tensile behaviour at a high strain rate. Namely, The specimens with twisted fibre had a more considerable amount in σ_{pc} and g compared to those with smooth fibres (Figure 2.13).

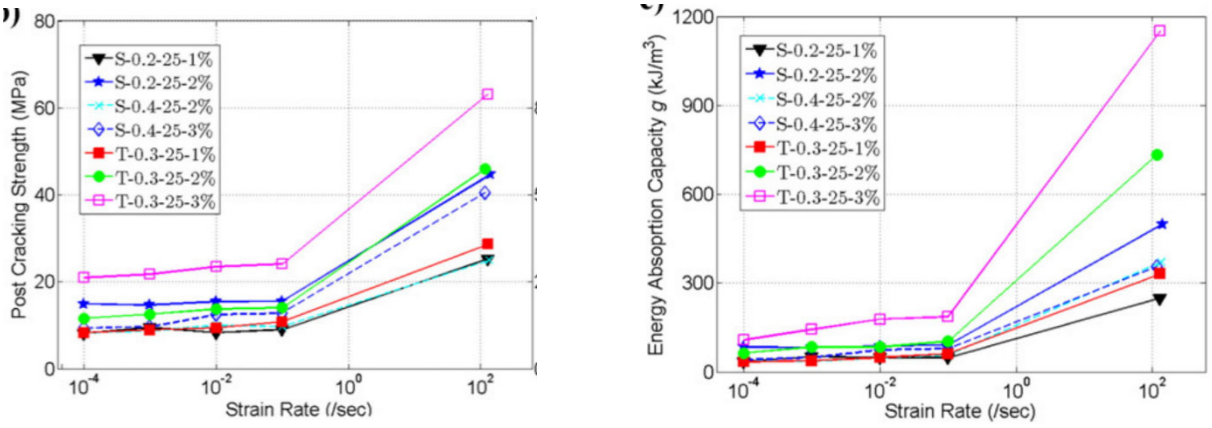

a) post cracking strength b) energy absorption capacity

Figure 2.13 Rate effect of UHP-FRC using different fibres (Pyo et al., 2015)

2.2.4.7 **Abrishambaf, Pimentel and Nunes**

Abrishambaf, Pimentel and Nunes (2017) investigated the effect of fibre orientation on the tensile behaviour of UHPFRC. The study selected the different fibre volume fractions of 1.5% and 3% to examine the influence of fibre orientation.

The results showed that fibre content and fibre orientation affect the tensile stress-strain curve. Moreover, it was observed that the fibre orientation has a significant impact on the tensile behaviour of UHPFRC, especially on the hardening phase (Figure 2.14 and Figure 2.15).

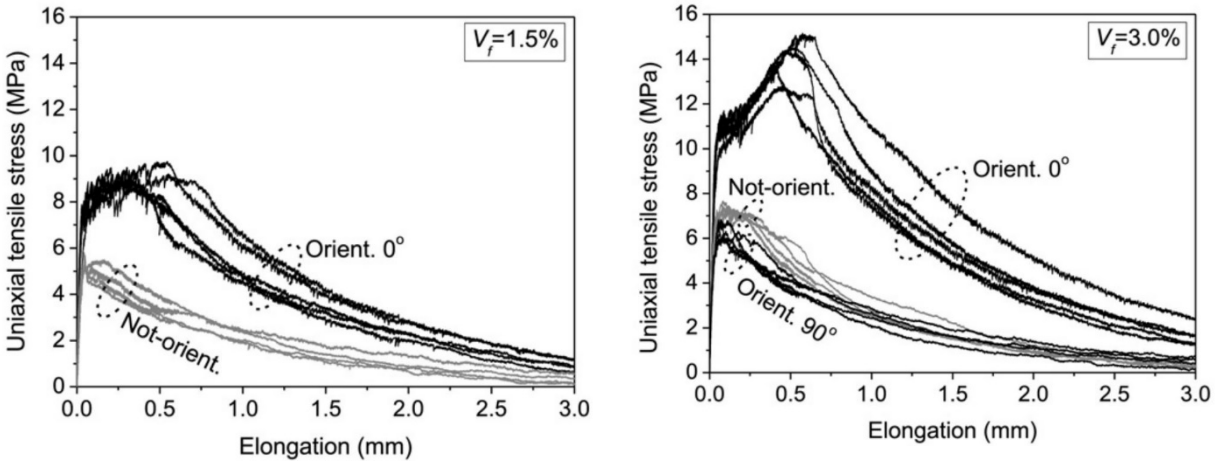

(a) V_f= 1.5% (b) V_f=3.0%

Figure 2.14 Uniaxial tensile stress – elongation relationships for all valid specimens (Abrishambaf et al., 2017)

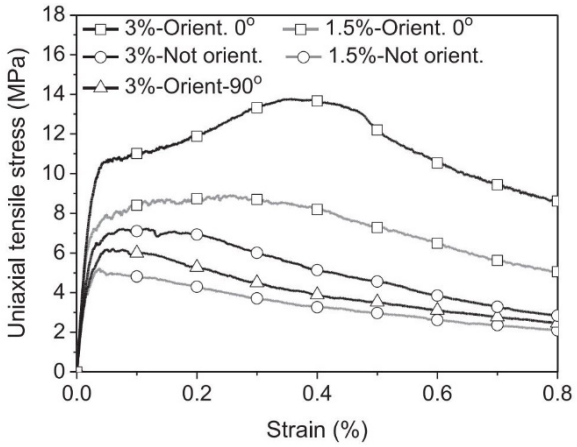

Figure 2.15 The average uniaxial stress-strain relationships (strain valid up to peak stress) (Abrishambaf et al., 2017)

2.2.4.8 **Yu, Ding, Liuand and Bai**

The study of Yu, Ding, Liuand and Bai (2020) investigated the influence of fibre reinforcement index $V_f L_f/d_f$ and water/binder *w/b* ratio on energy dissipation. The research showed the following observation:

- σ_{cc}, σ_{pc}, ε_{pc} and G_f increased by increasing the $V_f L_f/d_f$ (Figure 2.16).
- The strain energy density improved with increasing the $V_f L_f/d_f$ and depended on *w/b*.
- G_f increased with decreasing of *w/b*.
- $G_{f,A}$ increased with both $V_f L_f/d_f$ value and the compressive strength in general.

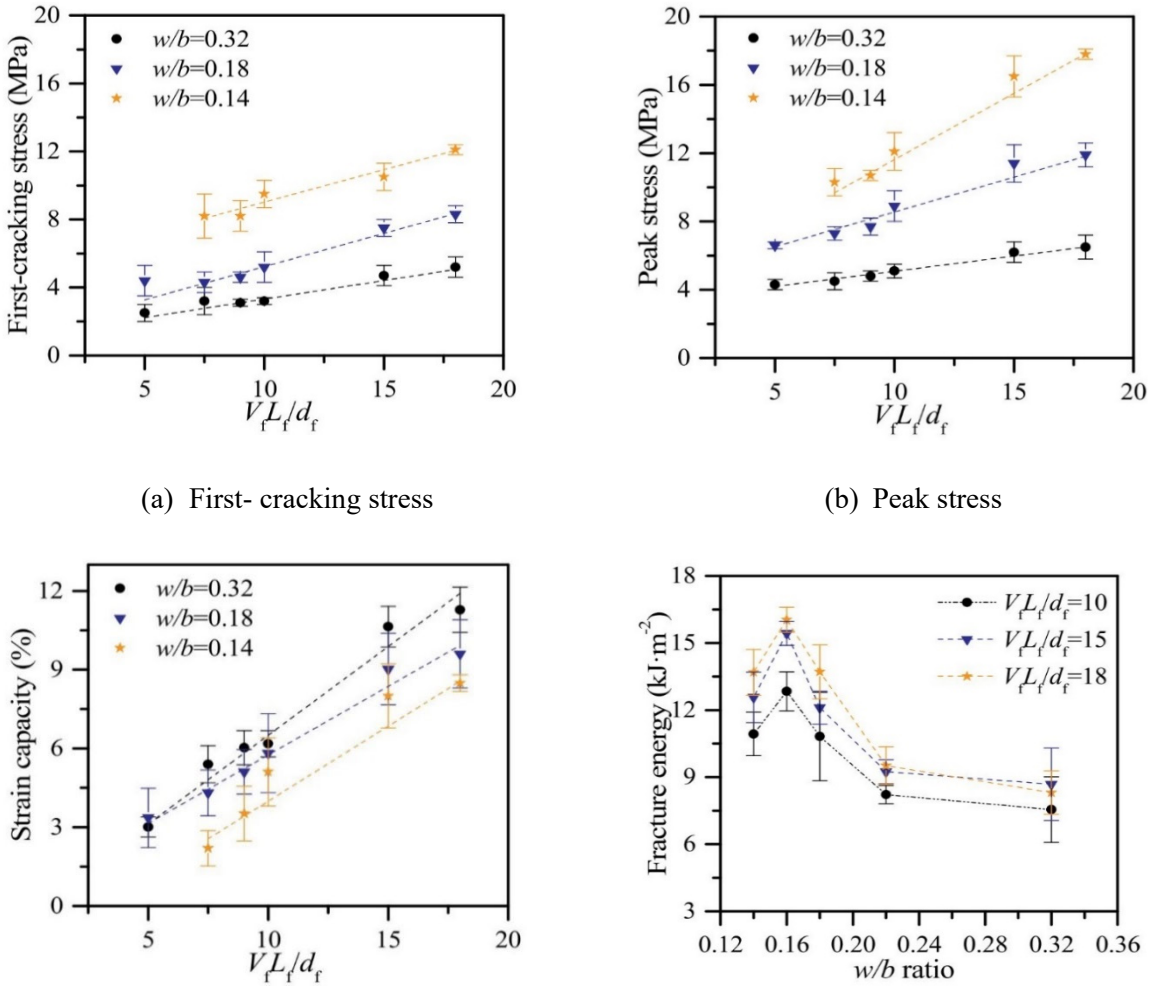

(a) First- cracking stress

(b) Peak stress

(c) Strain capacity

(d) fracture energy

Figure 2.16 Relationships of PE-ECC's critical tensile parameters with V_fL_f/d and w/b ratio (Yu et al., 2020).

2.2.4.9 **Nguyen, Ryu, Koh and Kim**

Nguyen et al. (2014)investigated the effects of size and geometry on the direct tensile strength of UHPFRC, the gauge length, section area, volume and thickness were considered, and the strength, strain capacity and energy absorption capacity were obtained eventually (Figure 2.17).

The increasing of the gauge length, section area and volume of specimens resulted in a little reduction of tensile strength while significantly decreased the strain capacity and energy absorption

capacity and clearly increased the crack spacing of specimens greatly. The crack spacing, or the number of multiple micro-cracks within unit length, was found to be the most sensitive tensile parameter, while the gauge length was the most influencing on the tensile ductility of UHPFRC.

Moreover, when increasing the thickness of the specimen, it was observed that the tensile strength slightly increased. Meanwhile, the strain capacity and energy absorption capacity distinctly increased. The authors conclude that the different thickness to width ratios for tensile test specimen produced an opposite trend in the size effect.

It should be mentioned that in this research, a specific UHPFRC containing 1% macro twisted and 1% micro smooth steel fibers by volume was used, which could affect the proportion of the trend noticed if mono short fibres were used instead.

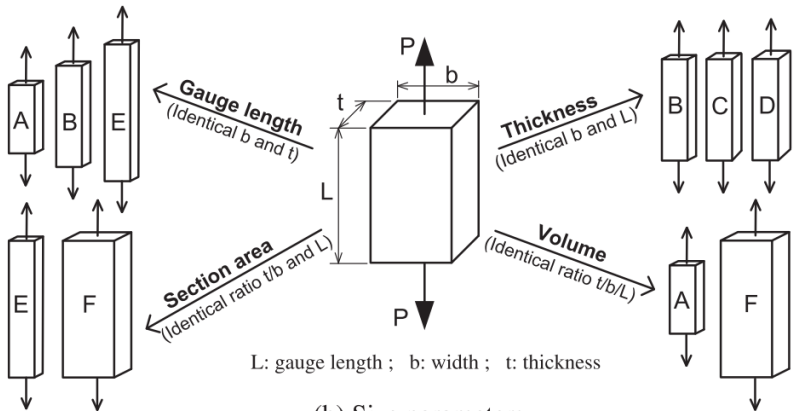

Figure 2.17 Tensile behaviour of UHPFRC and investigated size parameters (Nguyen et al., 2014)

2.3 Effect of tensile properties of UHPFRC on the bond behaviour

2.3.1 Bond behaviour of rebar embedded

Ultra-High-Performance Concrete (UHPC) can be used in many applications of reinforced concretes, especially in critical beam-column connections and high shear zones. The reason is UHPC has several advantages, including high compressive and tensile strength, excellent post-

cracking ductility, and enhanced durability properties compared with conventional and high-performance concrete (B. A. Graybeal et al., 2003; Piérard et al., 2012).

Hence, with the increase of this application, the development of studies on bond behaviour of rebar embedded in UHPC is essential to improve its performance and measure the increasing length of rebar and estimate the overall structural response under an applied load.

Tensile stresses are shifted by rebar across cracks through the combination of chemical adhesion, frictional resistance, and bearing of the ribs on the concrete (Figure 2.18a and Figure 2.18b) (Lutz et al., 1967). Among the mentioned parameters, friction and adhesion have a small role compared with the ribs' bearing. The bar slips lightly, and force is created by diagonal bearing the ribs against the concrete after breaking free of adhesion. The created force is divided into the two components of parallel and perpendicular to the rebar axis. Radial stresses are generated by the perpendicular component of the bearing forces and developed along the rebar perimeter. The mentioned stresses cause radial cracks. These cracks are called splitting cracks or longitudinal cracks (Figure 2.18c). The bond mechanism described above is explained in detail elsewhere. (Azizinamini et al., 1995; Den Uijl et al., 1996; Lutz et al., 1967; Tepfers, 1973). For Fibre Reinforced Concrete (FRC), fibres induce tensile ring redistribution around the whole matrix (Chao et al., 2009). Simultaneous more slippage, following the fibres pullout, longitudinal cracks progress along the bar axis. This state is precisely corresponding when the maximum bond strength estimates. Depending on the function of the fibre, two situations occur. If fibres can bridge the splitting cracks without excessive opening, the failure mode is ductile, and it is called the pullout failure (Figure 2.18d). Otherwise, the sudden splitting failure occurs, and the longitudinal cracks will open (Chao et al., 2009).

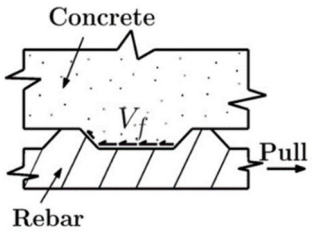

(a) Friction after (408, 2012)

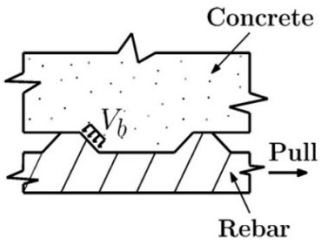

(b) Bearing of the rib after (408, 2012)

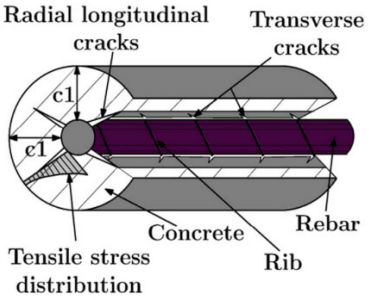

(c) Radial longitudinal cracks in CC after(K. Holschemacher et al., 2004; Tepfers, 1973)

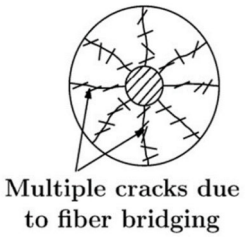

(d) Crack bridging in Fibre Reinforced Concrete (FRC) after (Chao et al., 2009)

Figure 2.18 Idealized bond mechanisms

2.3.2 Influence of the tensile properties of UHPFRC on bond behaviour

2.3.2.1 Chao, Naaman and Parra-Montesinos

In the study of Chao, Naaman and Parra-Montesinos (2009), two fibre volume fractions of 1% and 2% with the different fibre types were selected to investigate the rebar's bond behaviour embedded in the various FRC types. Figure 2.19 indicates the results under the monotonic load. The results show that most of the type of fibre changing the fibre volume fraction from 1% to 2% led to an increase in the amount of bond stress (approximately 60%); moreover, the residual slip is higher at the same stress level (five times).

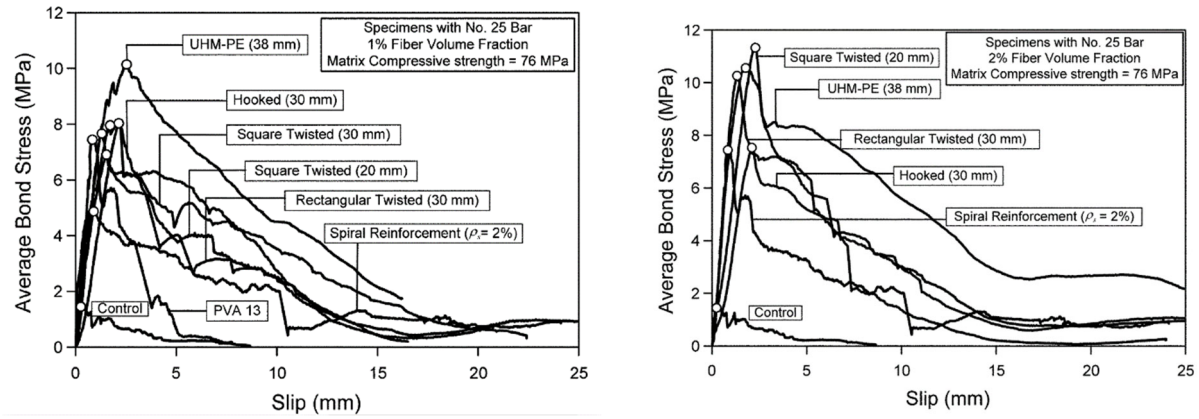

(a) The bond stress-slip behavior of specimens with 1% fibre volume fraction

(b) The bond stress-slip behavior of specimens with 2% fibre volume fraction

Figure 2.19 Comparison of the bond behaviour of the specimens with different fibre volume fraction (Chao et al., 2009)

2.3.2.2 **Lagier, Massicotte and Charron**

Lagier, Massicotte and Charron (2015) experimentally examined the influence of fibre volume fraction (0, 1%, 2% and 4%) on the bond strength in UHPFRC. Figure 2.20 indicates the best direct tensile properties of their specimens. The research for a splice length of 10*db* indicates a considerable increase in the ultimate bond stress. Indeed, by increasing the fibre content from 1% to 2% and 4%, the ultimate bond stress rises 29% and 53% (Figure 2.21).

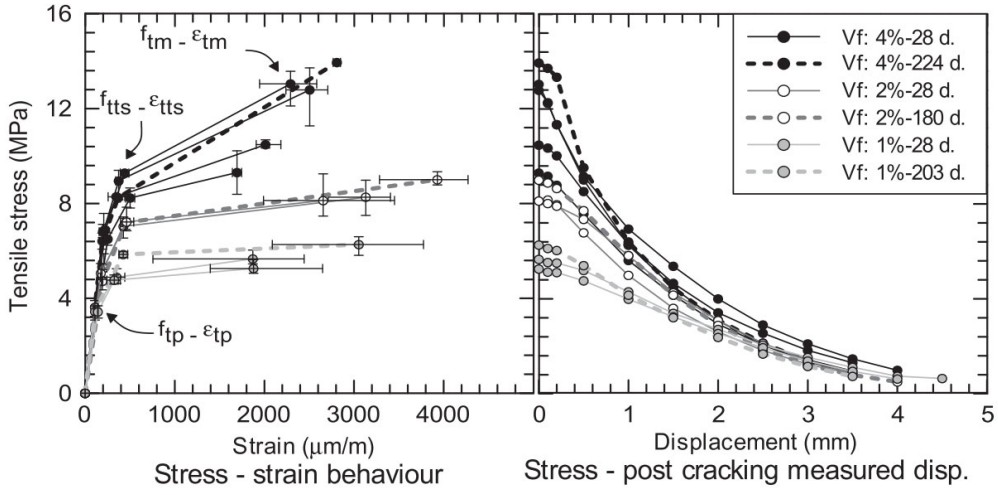

(a) Strain hardening behaviour (b) Post-cracking tensile strength

Figure 2.20 Idealized tensile properties of different UHPFRC batch at the testing day of lap splice specimen (F Lagier et al., 2015a)

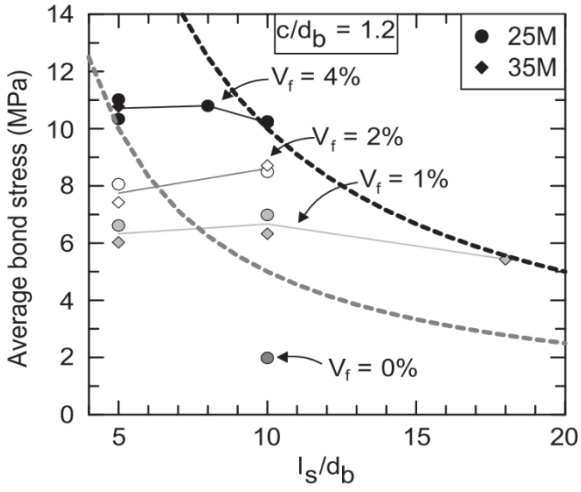

Figure 2.21 Ultimate average bond stress vs splice length to bar diameter ratio (F Lagier et al., 2015a)

2.3.2.3 **Roy, Hollmann and Wille**

Roy, Hollmann and Wille (2017) tried with several fibre volume fractions to achieve the impact of fibre volume fraction and orientation on the bond behaviour (i.e. 0, 1%,2% and 3%). Their research demonstrated the following results:

- As the fibre volume fraction increases, the average bond stress increases (Figure 2.22).
- Considering the constant embedded length and fibre volume fraction, the specimens which have the perpendicular fibre orientation to the load direction demonstrated the highest pullout load. In contrast, those with the parallel fibre orientation to the load direction noted the lowest pullout load. Moreover, specimens with random fibres orientation demonstrated pullout load values between the perpendicular and parallel results (Figure 2.23).
- The maximum load and related slip enhance with the improvement in fibre content.
- Similar results to what was seen above regarding the relationship between pull-out force and fibre orientation, we observed between the slip and fibre orientation for particular fibre volume fraction and embedded length. Namely, slips are maximum for the perpendicular fibre orientation cases and have the lowest for parallel orientation value cases. Regarding random orientation, the value is between the perpendicular and parallel.

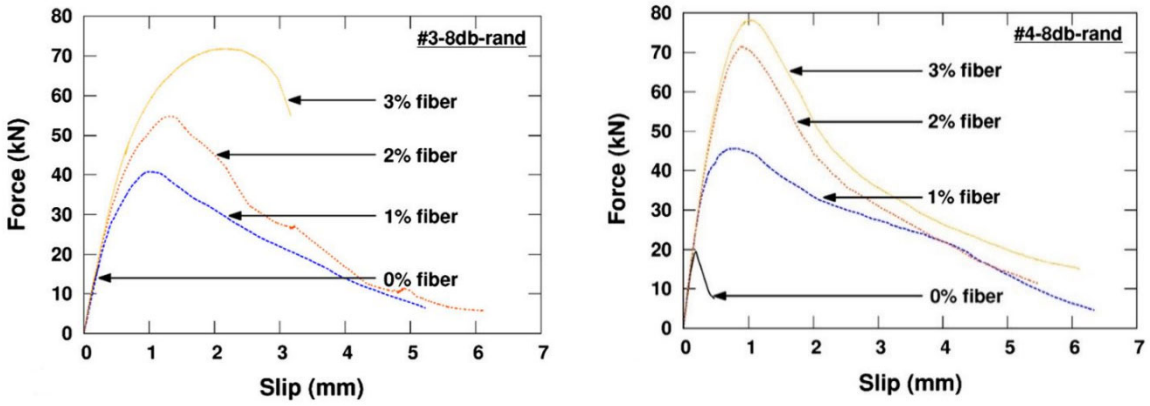

(a) #3 rebar with le =8db (b) #4 rebar with le =8db

Figure 2.22 Effect of V_f on the load-slip response (Roy et al., 2017).

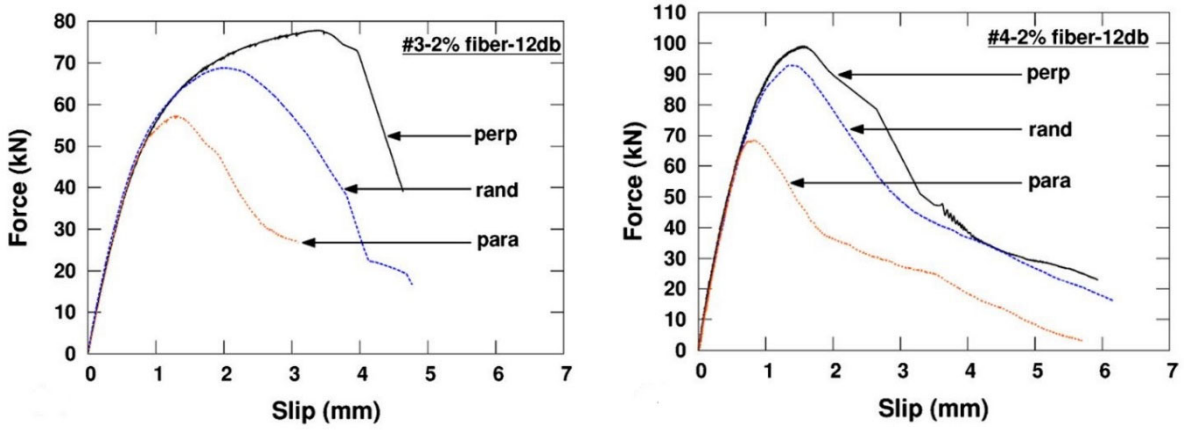

(a) #3 rebar with le = 12 d_b and V_f = 2%

(b) #4 rebar with le = 12 d_b and V_f = 2%

Figure 2.23 Effect of fibre orientation on the load-slip response (Roy et al., 2017).

2.3.2.4 **Deng, Pan and Sun**

Deng, Pan and Sun (2018) evaluated steel bar bond behaviour embedded in Engineered Cementitious Composites (ECC) by direct pullout tests. They used different fibre volume fractions of 0%, 1% and 2% and used three bar diameters of 12, 16 and 20 with two separate mechanical properties of HRB400 and HPB300.

Their observations are as follows:

- The bond strength increases around 71% from concrete to ECC
- The bond-stress curve decreased, accompanied by a slight increase at the decline stage for the specimens with a two percent fibre volume fraction with a bar diameter of 20 (Figure 2.24a).
- As fibre volume fraction increases, bond strength increases (Figure 2.24b)
- The ECC specimens kept distinct integrity following failure and showed notable damage tolerance.

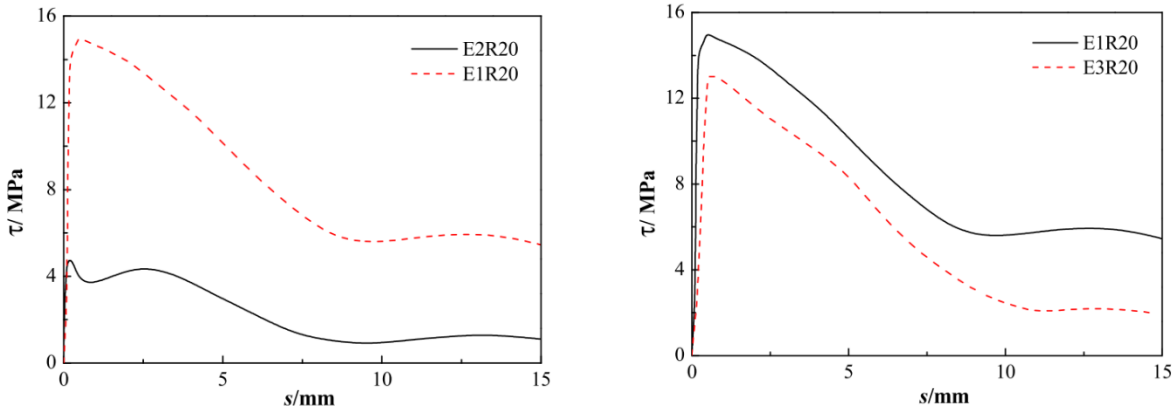

(a) Different ECC strengths bond stress-slip curves

(b) The bond stress-slip curves for varying PVA fibre contents

Figure 2.24 The bond stress-slip curves (Deng et al., 2018)

CHAPTER 3 MODELLING STRATEGY IN BOND BEHAVIOUR

3.1 Introduction

This chapter presents the methodology for creating the 3D numerical model in ABAQUS (2016) to represent the actual behaviour of bond properties in UHPFRC lap splice joints. Numerical methods help better understand the various mechanisms that occur during experimental tests and thereby contribute to improving experimental procedures. Hence, it is essential to create realistic numerical models that will be validated on experimental results. For this purpose, Lagier et al. (2016) developed a strategy to make the numerical models that were validated. Thus, this chapter describes the lap splice modelling challenges, the bond modelling background, and Lagier's (2016) approach.

3.1.1 Lap splice modelling challenges

The numerical simulation of the bond mechanism is a powerful tool to study the various mechanisms that occur internally and provide an insight that cannot be observed from surface measurements experimental testing. The load transfer mechanism between the bars and the concrete in the lap splice regions happens mainly through ribs bearing. The radial components of the inclined force caused at each rib face produce tensile circumferential or hoop stresses around the anchorage bar, which lead to the cracking and then splitting of the concrete cover accompanied with the slip of the anchorage bar relative to concrete. Furthermore, the numerical model must be related to the actual UHPFRC tensile material law for both hardening and softening phases (Figure 3.1).

The numerical model of bond behaviour needs to consider the influence of the governing parameters, including the concrete tensile properties, concrete cover, confinement, boundary conditions, and reinforcing bar state of stress. Therefore, the traditional bar bond-slip modelling does not have the features to explicitly predict the local mechanism of force transfer at the intersection of the bar and concrete and the parameters involved in this phenomenon. Unlike traditional bar bond-slip modelling, the rib scale modelling approach considers the bond mechanism by explicitly modelling the ribs on the bar and associated inclined contact stress

produced on the surrounding concrete. This modelling also considers the concrete and steel interaction characteristics, like adhesion, friction, and cohesive debonding (F Lagier et al., 2016).

Reinhardt et al. (1984) developed the first axisymmetric rib scale models. These models have made a significant improvement in the ability to reproduce fracture, concrete crushing failure, the robustness of contact laws and algorithms. By the simplified simulation of beam-end anchorage of reinforcement, Tholen and Darwin (1996) indicated that rib scale models present valuable insight to understand bond mechanics and can be efficient tools for establishing rational design criteria. Appl et al. (2002) simulated the anchorage of straight and headed reinforcing bars in the ordinary concrete specimens under tension by a 3D model. They found that crack patterns in the experimental results and finite element analysis agreed well, whereas the simulations were able to predict the bond behaviour. Improvements in computer speed and performances led to increasing bond behaviour modelling for ordinary concrete without fibres (Daoud et al., 2012; Fischer et al., 2012). Lagier et al. (2016) used refined nonlinear models of reinforcement-concrete interaction to investigate the bond behaviour in UHPFRC. They modelled the rebars at the rib scale level using 3D solid elements using Abaqus software. They also applied a penalization method for the interface of concrete and steel bars to consider the normal and tangential friction of the Mohr-Coulomb criterion.

3.1.2 Validating the model and methodology

The following section investigates the modelling strategy developed by Lagier (2016) to study the bond behaviour. This strategy considered the challenges indicated previously. It was also validated by Rosini (2018).

3.2 Modelling methodology in finite element software

The bond mechanism in UHPFRC is a complex phenomenon that depends on several factors, such as the stress in the concrete in the vicinity of the lapped reinforcing bar. Hence, using a constitutive model that considers the tensile behaviour of UHPFRC is essential. Lagier et al. (2016) indicated

that it is essential to use a concrete constitutive model which potentially generates the main features of concrete behaviour adequately under multiaxial stress conditions in 3D to achieve the relevant bond behaviour at the rib scale.

Furthermore, to increase the modelling speed and investigate the various objectives and parameter studies, we used the Python programming language for both pre-and post-processing phases of the finite element software.

3.2.1 Material constitutive model

The constitutive model EPM3D developed by Massicotte and Ben Ftima (2015) was selected for modelling the UHPFRC behaviour and was used as a user's subroutine in ABAQUS/Explicit (Hibbitt et al., 2010). This model is suitable for the nonlinear analysis of plain, reinforced, and fibre reinforced concrete in finite element analysis. This orthotropic 3D model relies on a strain-rotating smeared crack approach with uncoupled components and strain decomposition (Bouzaiene et al., 1997). This model explicitly considers the critical characteristics of the concrete behaviour, including tensile cracking, concrete crushing, tension-compression damage coupling, degradation of the elastic modulus under unloading-reloading, the effect of confinement, and non-proportional loading (M. Ben Ftima et al., 2014a; 2014b; B. Massicotte et al., 2015).

The model applies an isotropic post-cracking behaviour for fibre reinforcement concrete (FRC) in tension. In other words, this model determines the post-cracking behaviour as an intrinsic material property by a softening stress-crack opening (σ-w) response. The model also enables to consider the hardening part of stress-strain properties for UHPFRC.

EPM3D considers the properties of UHPFRC differently for the hardening and softening portions of the tensile behaviour. Namely, the program considers the hardening phase based on the bi-linear curve suggested by Naaman and Reinhardt (2006) and considers the softening phase by multilinear segments (Figure 3.1). The hardening portion is defined in the stress-strain domain, whereas the softening portion is defined in the stress-crack opening domain. In this case, the crack opening is equal to the residual strain multiplied by a characteristic length (l_{elemt} in Figure 3.1). Because only one integration point is considered for 3D solid elements in Abaqus/Explicit, this length is taken equal to the cubic root of the element volume.

Reinforcing bars are modelled using 3D solid elements and assume an elastic-entirely plastic behaviour with the specified yield strength, f_y.

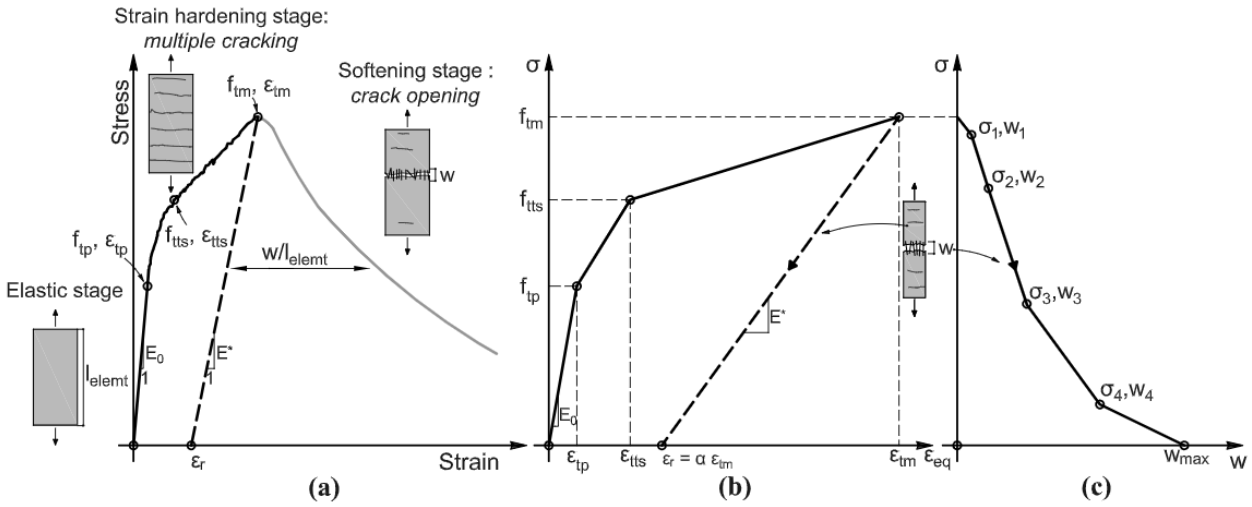

Figure 3.1: Schematic tensile response of a strain hardening UHPFRC: (a) typical global direct tensile test response; (b) simplified stress-strain response with strain hardening; (c) multilinear softening stress crack-opening response (F Lagier et al., 2016)

3.2.2 Bond modelling

Lagier et al. (2016) introduced a strategy to define bond behaviour in FEM analysis. This approach considers that the bond behaviour is produced explicitly by the finite element analysis rather than predefined bond-slip properties. Namely, the approach considers each reinforcing bar rib to simulate the wedging action mechanism between the ribs and concrete. Moreover, applying ABAQUS interface algorithm penalty method considers the normal and tangential contact constraints at the steel-concrete interface. Figure 3.2 shows that the load transfer at the front rib faces to the concrete is applied by hard contact using the penalty method. The penalty stiffness is chosen automatically by ABAQUS when the ribs are in contact with concrete. The concrete-steel interface is free to separate at the rear face of ribs when no contact pressure is transmitted.

A Mohr-Coulomb friction law allowing for normal debonding is adopted along with the interface between two adjacent ribs (Figure 3.2, Figure 3.3a and Figure 3.3d).

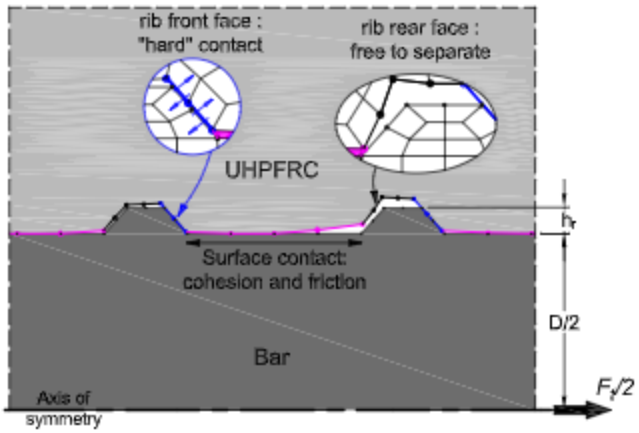

Figure 3.2: Schematic view of different surface interaction properties at the steel-concrete interface (Lagier et al., 2016)

The strategy considers the progressive normal separation at the concrete-steel interface by the cohesive contact in the normal direction (Figure 3.3b). Furthermore, shear stress applies two components at the interface of steel and concrete in the shear direction. These include adhesion and frictional components that are independent and dependent on normal stress, respectively. (Figure 3.3c).

The adhesion influence considers the same concrete-steel interface property described for normal direction, for the two shear directions. Figure 3.3 shows the constitutive model of steel-concrete interface, and Table 3.1 defines the interface parameters involved in the adopted strategy. More details about this approach can be found in Lagier et al. (2016).

Table 3.1 Definition of the interface parameters

Interface parameters			
Traction-separation law	σ_n	(MPa)	Cohesive stiffness
	T_n	(MPa)	Normal adhesion bond strength
	T_s	(MPa)	Shear adhesion bond strength
	K_{nn}	(N/mm^3)	Cohesive normal stiffness
	K_{ss}	(N/mm^3)	Cohesive shear stiffness direction ss
	K_{tt}	(N/mm^3)	Cohesive shear stiffness direction tt
	δ_d	(μm)	Total displacement at failure
Friction model	μ	(-)	Friction coefficient
	$K_{el,f}$	(N/mm)	Elastic slip stiffness

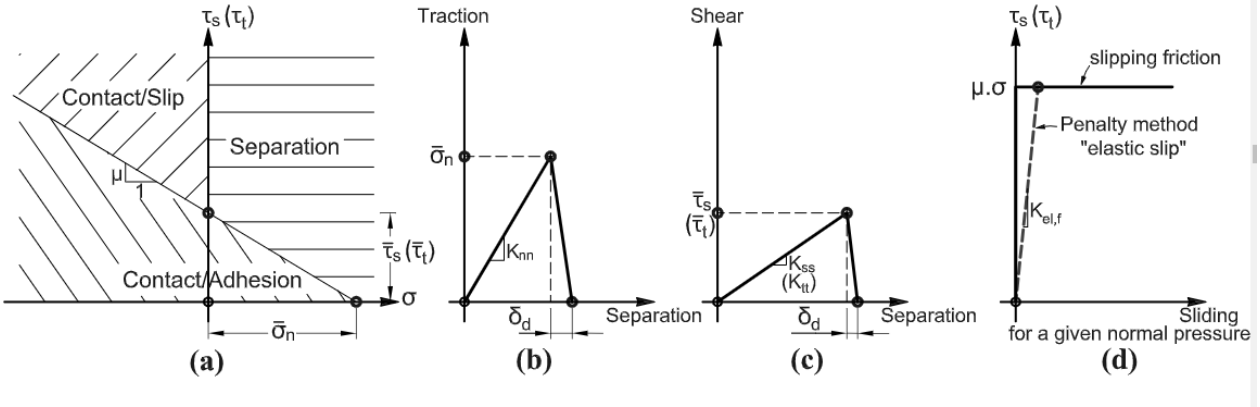

Figure 3.3: Constitutive model of the steel-concrete interface: (a) interface material states on Mohr-Coulomb surface; contact separation law at the interface; (b) normal direction; (c) shear direction; (d) penalty friction method at the interface (Lagier et al., 2016)

3.2.3 Solution strategy

ABAQUS software solves complex models with two different formulations: Implicit and Explicit. The Implicit approach is based on an incremental process by completing successive iterations to check specific convergence patterns (i.e. Newton-Raphson iterative process). The convergence pattern consists of forces, energies and displacements. Selecting these patterns affects the accuracy of the results. In the nonlinear state, such as concrete cracking, computing time may increase

because the implicit formula, based on the inversion of the stiffness matrix, is stable in each unconditional iteration. Explicit formulation solves the equilibrium equations using the explicit central difference method. In other words, the formulation becomes dynamic equations that are solved by a direct integration dynamic procedure. Several research pieces have proved the performance, robustness, and efficiency of explicitly dynamic analysis to simulate quasi-static models with several challenges such as high material nonlinearly, including concrete cracking and complex contact boundary conditions (M. Ben Ftima et al., 2014a; 2014b; Dhanasekar et al., 2008; Kianoush et al., 2008; Prinja et al., 2005; Ziari et al., 2013). Ben Ftima (2013) indicated that the computational time to resolve significant problems reduces. Notwithstanding, this solution often requires more increments over an implicit method.

This research includes the mentioned challenges, including high material nonlinearly, concrete cracking and complex contact boundary conditions. Hence, the present study utilizes the explicit dynamic method to consider the quasi-static simulation. Verifying the quasi-static loading entails considering the following parameters in the explicit dynamic formulation. The internal forces must be insignificant in the system through loading. Additionally, the kinetic energy ratio to internal energy for the whole model must remain as low as possible (i.e. ratio<5%). Therefore, loads must be applied at a slow rate compared with the natural period of the system.

CHAPTER 4 INFLUENCE OF UHPFRC PROPERTIES ON THE BOND PERFORMANCE

4.1 Objectives and assumptions

4.1.1 Objectives

In Chapter 2, we first looked at the parameters influential on the tensile properties of UHPFRC. Then the effects of these parameters were investigated on the bond behaviour. Past studies indicated that changes in tensile curve parameters affect the bond strength significantly. However, research on which of the UHPFRC tensile curve parameters has the most significant impact on bond behaviour has been very limited. Hence, this chapter aims to determine which parameters of the tensile curve of UHPFRC have the most significant effect on the bond behaviour.

This chapter aims at examining the effects of the following parameters on the maximum bond strength:

- the maximum tensile strength.
- the slope of softening.
- the strain at post-cracking.
- the strain-hardening.
- the energy dissipated during the post-peak.
- the tensile stress variation in the first stage of softening.

Isotropic tensile properties are adopted for the analyses presented in this chapter.

4.1.2 Selected parameters

Table 4.1 and Figure 4.1 identify the parameters of the UHPFRC.

Table 4.1 The parameters of UHPFRC tensile properties

Nomenclature	
$f_{t,u}$	Tensile strength at the end of hardening phase (MPa)
$f_{t,ts}$	Tensile strength at the beginning of hardening phase (MPa)
$f_{t,el}$	Tensile strength at the end of the elastic phase (MPa)
$\varepsilon_{t,u}$	Strain at the end of the hardening phase
$\varepsilon_{t,ts}$	Strain at the beginning of hardening phase
$\varepsilon_{t,el}$	Strain at the end of elastic phase
$\varepsilon_{t,r}$	Residual strain
E_{sh}	Hardening modulus (MPa)
E_{PC}	Unloading modulus (MPa)
E_{so}	The slope at initiating of softening phase (MPa/mm)
w_u	Maximum crack opening (mm)
w_{so}	Crack opening at the end of the first stage of softening (mm)
$g_{f,SH}$	Dissipated energy per unit volume (kJ/m^3)
$G_{f,CO}$	Dissipated energy per crack surface area (kJ/m^2)
Δ_{fso}	Tensile stress variations in the first stage of softening (MPa)

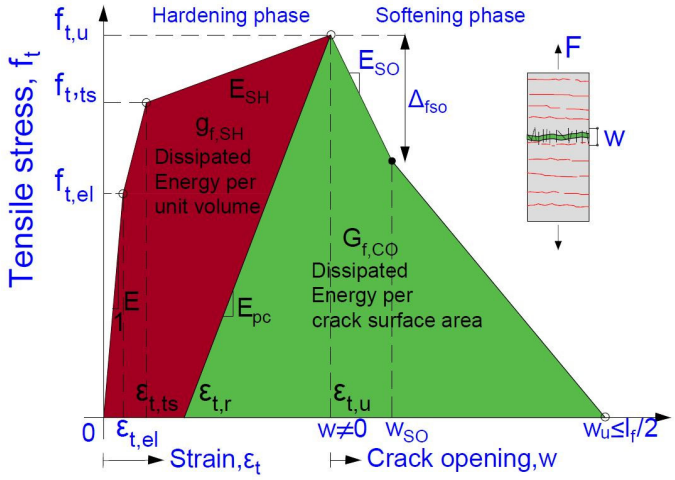

Figure 4.1 Schematic representation of UHPFRC tensile properties

4.2 Finite element modelling

4.2.1 Selection of the reference specimen

A numerical model shown in Figure 4.2 is selected to investigate the parameters. The model is one of the several non-contact bond test specimens tested by Lagier, Maurer and Gatien in 2017. On the several geometries, they considered, the one identified as Direct Tensile Bond (DTB) test specimen was retained by Bastide (2020) as the most efficient configuration for examining the effects of development length for non-contact lap splice performance.

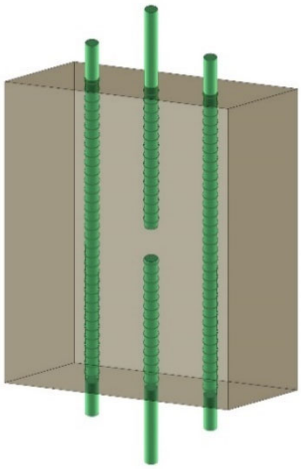

Figure 4.2 DTB numerical model

4.2.2 Geometry, boundary conditions and meshing

This study adopted the same rib scale model as Lagier (2016) and Rosini (2016; 2018) used in their study with 25M bars (Figure 4.3a) and the same mesh size that Rosini utilized. It is worth noting that Lagier selected a bar diameter that is slightly less than 25 mm, as indicated in Figure 4.3. The interaction between steel and concrete interface was considered by the general surface-to-surface contact feature of ABAQUS. Loads were applied as a smooth displacement function at the end of the anchorage bar (AB). The displacement in the longitudinal direction was restrained at the bottom

of the support bar (SB). Displacements in the two directions perpendicular to the bars longitudinal axis were restrained at the intersection of both bars (AB and SB) and concrete (Figure 4.3b).

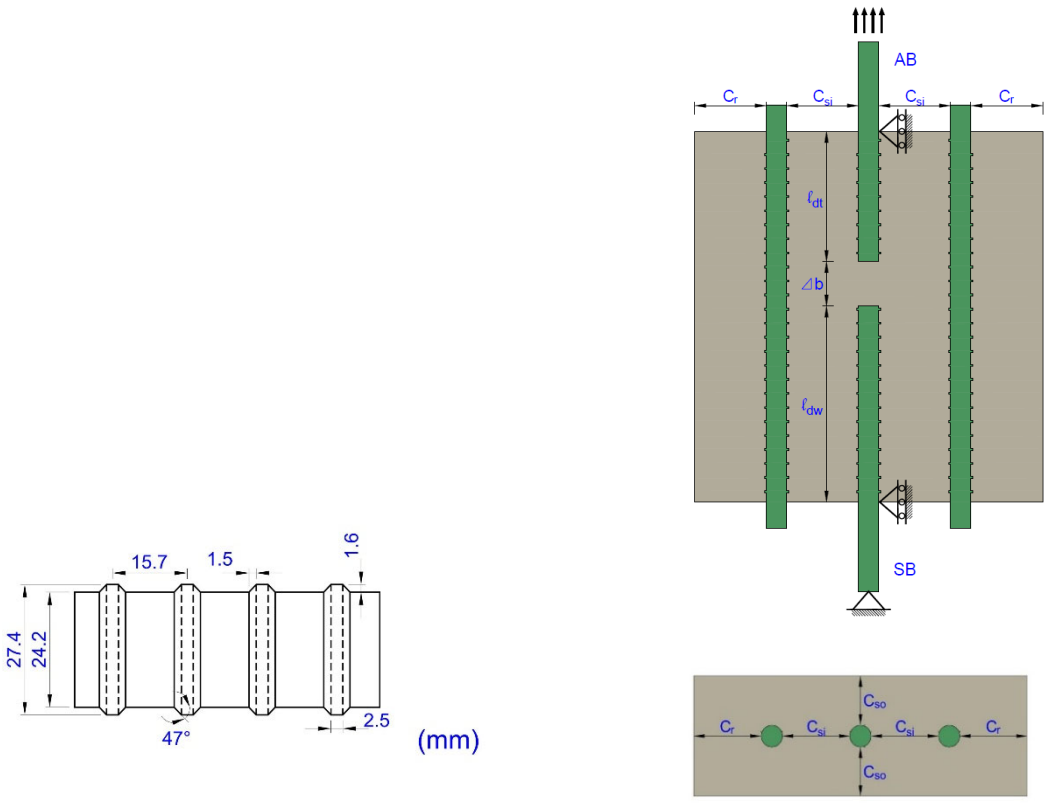

(a) Deformed bar geometry

(b) Boundary conditions and geometry of the model

Figure 4.3 DTB numerical model details

Tridimensional 8-nodes brick elements with reduced integration coupled with the relaxed hourglass stiffness method were selected to mesh the concrete and the bars (Table 4.2). The model meshing of this research is controlled by the mesh size of the ribs. Lagier et al. (2016) indicated a convergence of results based on the mesh size equivalent to the rib dimension. This was selected, and no mesh sensitivity study was performed in this project. Table 4.2 illustrates the mesh dimension and the other geometrical details. Figure 4.4 and Figure 4.5 show the bar and concrete modelling, assembling and meshing in the finite element method.

Table 4.2 Geometrical and modelling properties

Meshing and geometry		
Mesh properties	Size (mm)	3
	Element type	C3D8R
Concrete geometry	Bar cover to the outer face, c_{so}	$1.5d_b$
	Net spacing between the bars, c_{si}	$3.0d_b$
	Cover of side bars to the side face, c_r	$3.5d_b$
	Embedded length of the tested bar, l_{dt}	$8.0d_b$
	Net space between the tested bar and support bar, Δ_b	$1.0d_b$
	Embedded length of the support bar, l_{dw}	$11.0d_b$
Rebar geometry	Nominal diameter, d_b (mm)	24.2
	Average rib depth, h_r (mm)	1.6
	Base rib width, a_r (mm)	1.5
	Top rib width, b_r (mm)	2.5
	Rib spacing, s_r (mm)	15.7
	Rib face angle, θ (°)	47

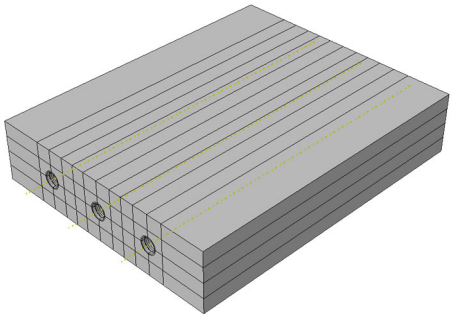

a) Concrete modelling

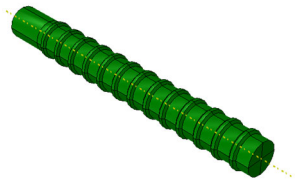

b) Anchorage bar modelling

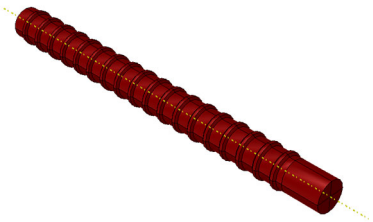

c) Support bar modelling

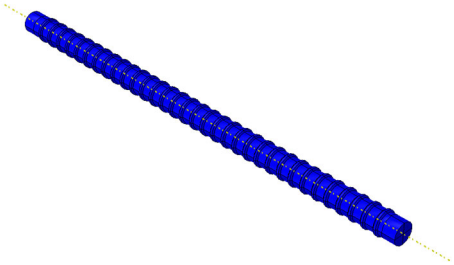

d) Lateral bar modelling

Figure 4.4 Four components of the finite element modelling

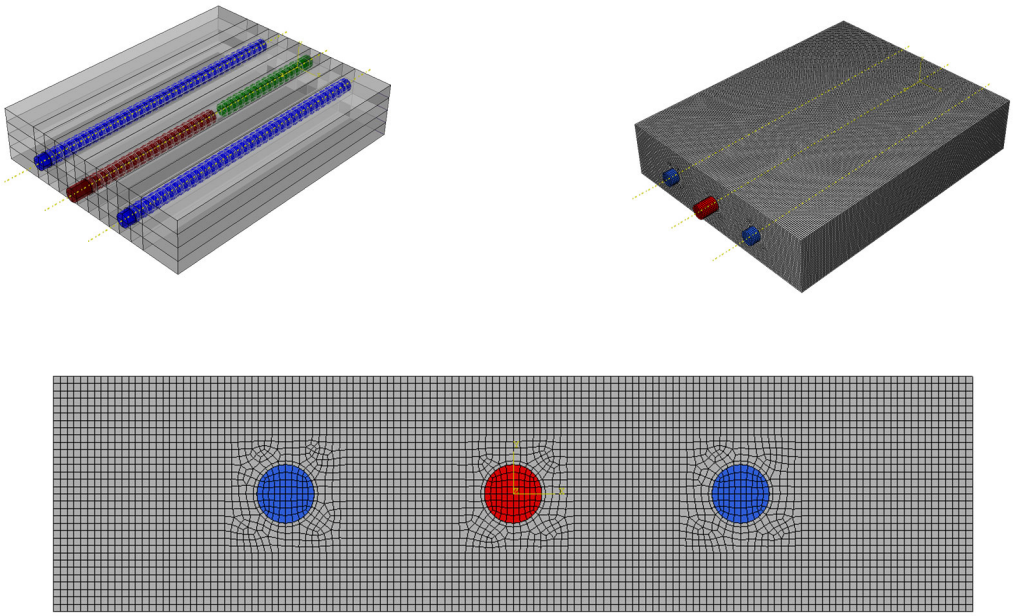

Figure 4.5 Model final assembly and meshing

4.2.3 Material modelling

4.2.3.1 Steel material properties

Linear elastic behaviour is considered for bars to avoid the effect of yielding. Table 4.3 indicates the properties of steel bars used in this study.

Table 4.3 Reinforcement mechanical properties

Steel properties	
Young modulus, E_s (GPa)	200

4.2.3.2 UHPFRC material properties

Table 4.4 summarizes the mechanical properties of UHPFRC in the compression.

Table 4.4 UHPFRC compression mechanical properties

Compression mechanical properties	
Young modulus, E_c (GPa)	45
Poisson's ratio, υ_c	0.2
Uniaxial compressive strength, f'_c (MPa)	100
Uniaxial peak strain corresponding, ε_c	0.0045

UHPFRC tensile properties depend on various parameters (see Chapter 2 for more details) and present a shape that is affected by factors such as the fibre content, fibre orientation, matrix properties, etc. For this study, a simplified UHPFRC tensile properties curve was adopted to examine the main parameter impacts on the bond behaviour individually. The adopted idealized curve follows Wille et al. (2014) proposal for the hardening part and the linear or bilinear curve similar to the curve suggested by Abrishambaf et al. (2019) for the softening part. According to our parametric study objectives, UHPFRC tensile properties were classified into six sets. Each set selected range is approximately based on the UHPFRC properties with a volume fraction of 2% based on the data presented in Chapter 2. Furthermore, the primary assumption in the present chapter is that the UHPFRC has a random fibre orientation with isotropic properties. Namely, the tensile properties in the three main directions of the DTB specimens are the same.

4.2.3.2.1 Set 1: maximum tensile strength – $f_{t,u}$

This section considers maximum tensile strength and the other related parameters as the main variables to investigate their effects on bond behaviour. The other parameters, including residual strain $\varepsilon_{t,r}$ remain constant (Table 4.5). Three E_{so} of 4, 6.7 and 20 are selected for the softening part to examine the slope influence on bond behaviour (Figure 4.6).

Table 4.5 UHPFRC tensile properties in set 1

Parameters type		$\varepsilon_{t,u}$ (%)	$\varepsilon_{t,r}$ (%)									
Constant		0.12	0.045									
	Specimen	E_{sh} (MPa)	E_{PC} (MPa)	$f_{t,el}$ (MPa)	$f_{t,ts}$ (MPa)	$f_{t,u}$ (MPa)	$\varepsilon_{t,el}$ (%)	$\varepsilon_{t,ts}$ (%)	w_u (mm)	E_{SO} (MPa/mm)	$g_{f,SH}$ (kJ/m³)	$G_{f,CO}$ (kJ/m²)
Variables	S1-ftu 4-Eso 20	9	5347	4	4.005	4.01	0.009	0.064	0.2	-20	3.1	0.4
	S1-ftu 6-Eso 20	9	8013	6	6.005	6.01	0.013	0.067	0.3	-20	4.6	0.9
	S1-ftu 8-Eso 20	10	10680	8	8.005	8.01	0.018	0.069	0.4	-20	5.9	1.6
	S1-ftu 10-Eso 20	10	13347	10	10.005	10.01	0.022	0.071	0.5	-20	7.1	2.5
	S1-ftu 4-Eso 6.7	9	5347	4	4.005	4.01	0.009	0.064	0.6	-6.7	3.1	1.2
	S1-ftu 6-Eso 6.7	9	8013	6	6.005	6.01	0.013	0.067	0.9	-6.7	4.6	2.7
	S1-ftu 8-Eso 6.7	10	10680	8	8.005	8.01	0.018	0.069	1.2	-6.7	5.9	4.8
	S1-ftu 10-Eso 6.7	10	13347	10	10.005	10.01	0.022	0.071	1.5	-6.7	7.1	7.5
	S1-ftu 4-Eso 4	9	5347	4	4.005	4.01	0.009	0.064	1	-4.0	3.1	2.0
	S1-ftu 6-Eso 4	9	8013	6	6.005	6.01	0.013	0.067	1.5	-4.0	4.6	4.5
	S1-ftu 8-Eso 4	10	10680	8	8.005	8.01	0.018	0.069	2	-4.0	5.9	8.0
	S1-ftu 10-Eso 4	10	13347	10	10.005	10.01	0.022	0.071	2.5	-4.0	7.1	12.5

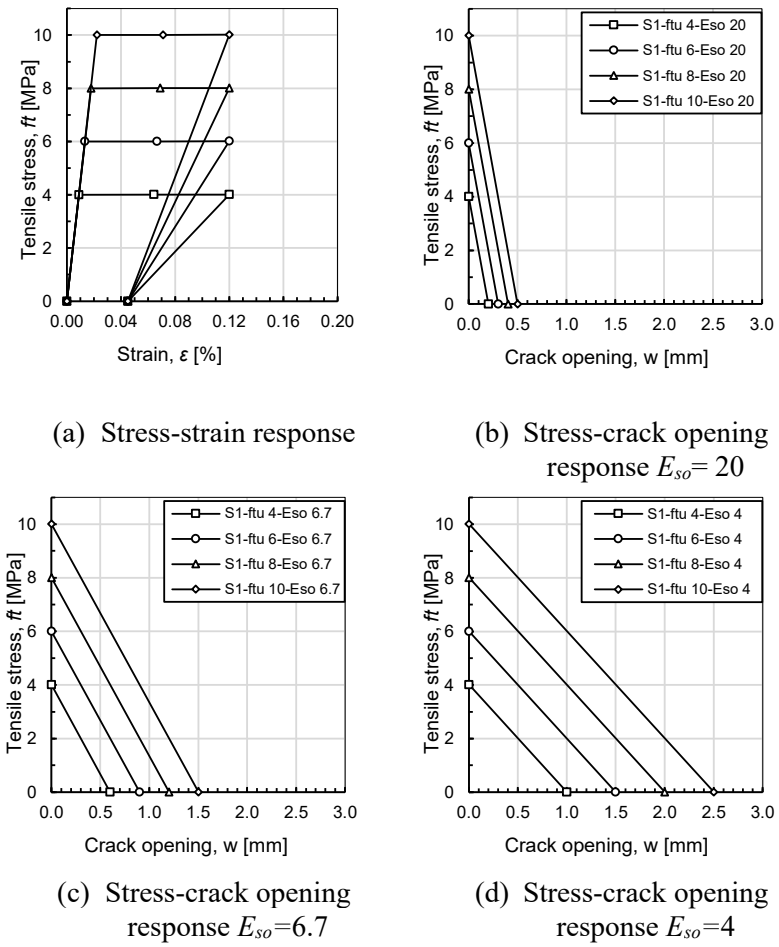

(a) Stress-strain response

(b) Stress-crack opening response E_{so}= 20

(c) Stress-crack opening response E_{so}=6.7

(d) Stress-crack opening response E_{so}=4

Figure 4.6 UHPFRC tensile properties in set 1

4.2.3.2.2 Set 2: Softening slope – E_{so}

This section considers softening slope and the other related parameters as the main variables to investigate their effects on bond behaviour (Table 4.6). The other parameters remain constant (Figure 4.7).

Table 4.6 UHPFRC tensile properties in set 2

Parameters type		E_{sh} (MPa)	E_{PC} (MPa)	$f_{t,el}$ (MPa)	$f_{t,ts}$ (MPa)	$f_{t,u}$ (MPa)	$\varepsilon_{t,el}$ (%)	$\varepsilon_{t,ts}$ (%)	$\varepsilon_{t,u}$ (%)	$\varepsilon_{t,r}$ (%)	$g_{f,SH}$ (kJ/m^3)
Constant		9	8013	6	6.005	6.01	0.013	0.067	0.12	0.045	4.6
	Specimen	w_u (mm)	E_{SO} (MPa/mm)	$G_{f,CO}$ (kJ/m^2)							
Variables	S2-Eso 0.9	6.5	-0.92	19.5							
	S2-Eso 1.8	3.25	-1.85	9.8							
	S2-Eso 3.7	1.625	-3.69	4.9							
	S2-Eso 7.4	0.8125	-7.38	2.4							
	S2-Eso 92.3	0.065	-92.31	0.2							

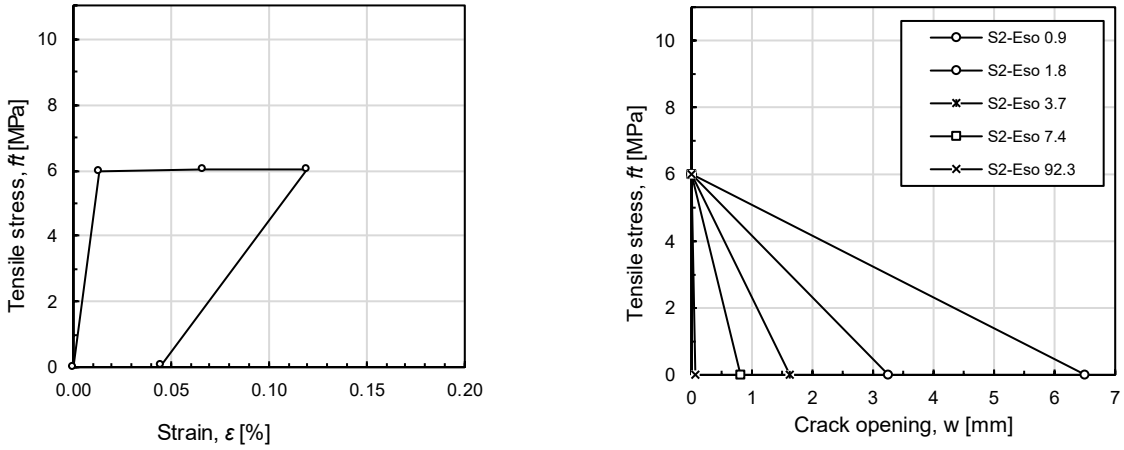

a) Stress-strain response b) Stress-crack opening response

Figure 4.7 UHPFRC tensile properties in set 2

4.2.3.2.3 Set 3: Peak strain – $\varepsilon_{t,u}$

This section considers the ultimate strain and the other related parameters as the main variables to investigate their effects on bond behaviour (Table 4.7). One specimen from the third set (S3-εtu 0.014) is modelled with two different residual strains $\varepsilon_{t,ts}$. Figure 4.8 shows the tensile property curves of UHPFRC in the third set.

Table 4.7 UHPFRC tensile properties in the set 3

Parameters type		$f_{t,el}$ (MPa)	$f_{t,ts}$ (MPa)	$f_{t,u}$ (MPa)	$\varepsilon_{t,el}$ (%)	w_u (mm)	E_{SO} (MPa/mm)	
Constant		6	6.005	6.01	0.013	1	-6.00	
	Specimen	E_{sh} (MPa)	E_{PC} (MPa)	$\varepsilon_{t,ts}$ (%)	$\varepsilon_{t,u}$ (%)	$\varepsilon_{t,r}$ (%)	$g_{f,SH}$ (kJ/m3)	$G_{f,CO}$ (kJ/m²)
Variables	S3-εtu 0.014	5000	71054	0.013	0.014	0.005	0.16	3.01
	S3-εtu 0.014-εtr0	5000	44409	0.013	0.014	0.000	0.01	3.01
	S3-εtu 0.03	60	32053	0.022	0.03	0.011	0.84	3.01
	S3-εtu 0.12	21	16027	0.067	0.12	0.045	2.08	3.01
	S3-εtu 0.24	9	8013	0.127	0.24	0.090	4.55	3.02
	S3-εtu 1.2	4	4007	0.607	1.2	0.450	9.50	3.07
	S3-εtu 7.2	1	801	3.607	7.2	2.700	49.12	3.41

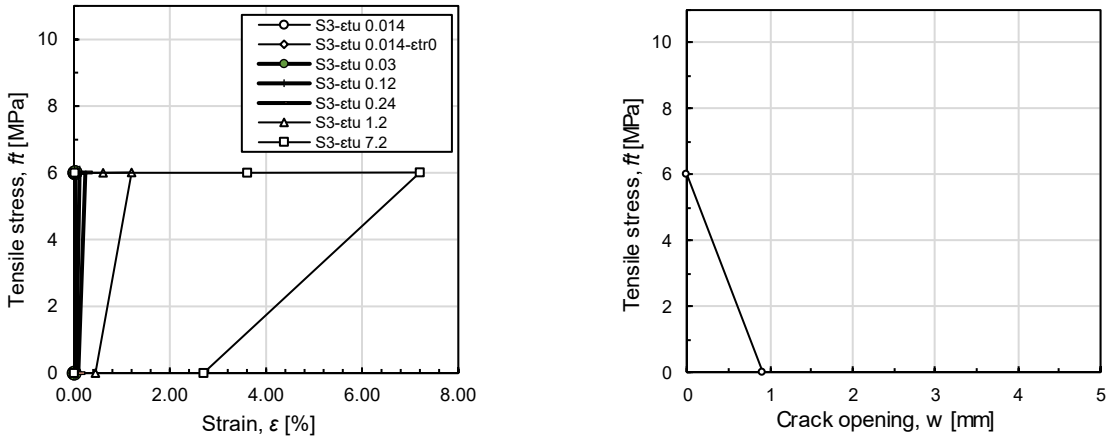

(a) Stress-strain response (b) Stress-crack opening response

Figure 4.8: UHPFRC tensile properties in set 3

4.2.3.2.4 Set 4: Strain-hardening effect-E_{sh}

This section considers the strain-hardening slope and the other related parameters as the main variables to investigate their effects on bond behaviour (Table 4.8). The tensile strength for this set was selected close to the first set parameters (i.e. 4.2.3.2.1) to better observed the hardening effects. Moreover, after the peak, the slope value is selected similarly to the value of the set 1 (i.e. E_{so}=6.7). Additionally, to examine the impact of $g_{f,SH}$ and E_{sh} on the bond behaviour, a specific model (S4-

ft,u10-E_{sh}3-ε_{tu}0.14) was selected. It is worth mentioning that this model and the model of S1-ftu 10-Eso 6.7 described in section 4.2.3.2.1 have the same $g_{f,SH}$ value (i.e. $g_{f,SH=}$7.1 kJ/m^3). However, the $f_{t,u}$ value used the same value presented in S4-ft,u 10- Esh 3.7. The effect of this model is examined in section 4.3.8. Figure 4.9 illustrates the tensile properties curve of UHPFRC in the fourth set.

Table 4.8 UHPFRC tensile properties in set 4

Parameters type		$f_{t,el}$ (MPa)	$\varepsilon_{t,el}$ (%)	E_{SO} (MPa/mm)							
Constant		6	0.013	-6.67							
	Specimen	E_{sh} (MPa)	E_{PC} (MPa)	$f_{t,ts}$ (MPa)	$f_{t,u}$ (MPa)	$\varepsilon_{t,ts}$ (%)	$\varepsilon_{t,u}$ (%)	w_u (mm)	$\varepsilon_{t,r}$ (%)	$g_{f,SH}$ (kJ/m3)	$G_{f,CO}$ (kJ/m²)
Variables	S4-ftu 6-Esh 0	9	8013	6.0	6.01	0.07	0.12	0.9	0.045	4.6	2.7
	S4-ftu 6.6-Esh 0.5	563	8800	6.3	6.6	0.07	0.12	1.0	0.045	4.6	3.3
	S4-ftu 7.2-Esh 1.1	1125	9600	6.6	7.2	0.07	0.12	1.1	0.045	4.7	3.9
	S4-ftu 8.4-Esh 2.2	2250	11200	7.2	8.4	0.07	0.12	1.3	0.045	4.9	5.3
	S4-ftu 9.6-Esh 3.3	3375	12800	7.8	9.6	0.07	0.12	1.4	0.045	5.1	6.9
	S4-ftu 10-Esh 3.7	3759	13347	8.0	10.0	0.07	0.12	1.5	0.045	5.2	7.5
	S4-ftu10-Esh3-εtu 0.14	3060	13347	8.0	10.0	0.08	0.14	1.5	0.0694	7.1	7.5
	S4-ftu 10.8-Esh 4.5	4500	14400	8.4	10.8	0.07	0.12	1.6	0.045	5.3	8.8
	S4-ftu 12-Esh 5.6	5625	16000	9.0	12.0	0.07	0.12	1.8	0.045	5.5	10.8

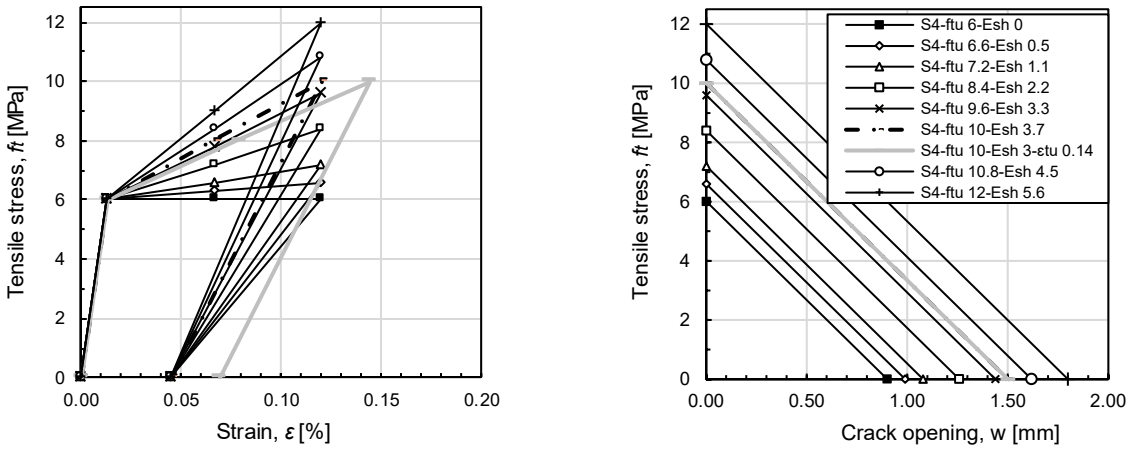

(a) Stress-strain response (b) Stress-crack opening response

Figure 4.9: UHPFRC tensile properties in the set 4

4.2.3.2.5 Set 5: Energy dissipated during the post-peak- $G_{f,co}$

This section considers the softening energy and the other related parameters as the main variables to investigate their effects on bond behaviour. In chapter 2, Xu et al. et al. (2015) indicated that the energy dissipated per crack surface during the softening phase (i.e. $G_{f,co}$) is an essential parameter for categorizing the fibre reinforcement. The present section defines bilinear curves to determine this parameter performance on the bond behaviour during the softening phase. The first part of the curves for all models in this set is kept constant, whereas the second portion of the curve is varied (Figure 4.10). Hence, the second part related parameters are considered the variable parameters (Table 4.9).

Table 4.9 UHPFRC tensile properties in set 5

Parameters type		E_{sh} (MPa)	E_{PC} (MPa)	$f_{t,el}$ (MPa)	$f_{t,ts}$ (MPa)	$f_{t,u}$ (MPa)	$\varepsilon_{t,el}$ (%)	$\varepsilon_{t,ts}$ (%)	$\varepsilon_{t,u}$ (%)	$\varepsilon_{t,r}$ (%)	E_{SO} (MPa/mm)	w_{so} (mm)	$g_{f,SH}$ (kJ/m3)
Constant		9	8013	6	6.005	6.01	0.01	0.07	0.12	0.045	-6.7	0.55	*4.6*
	Specimen	w_u (mm)	$G_{f,CO}$ (kJ/m²)										
Variables	S5-wu 0.9	0.9	2.71										
	S5-wu 1.8	1.8	3.77										
	S5-wu 2.7	2.7	4.82										
	S5-wu 3.6	3.6	5.88										
	S5-wu 4.5	4.5	6.93										

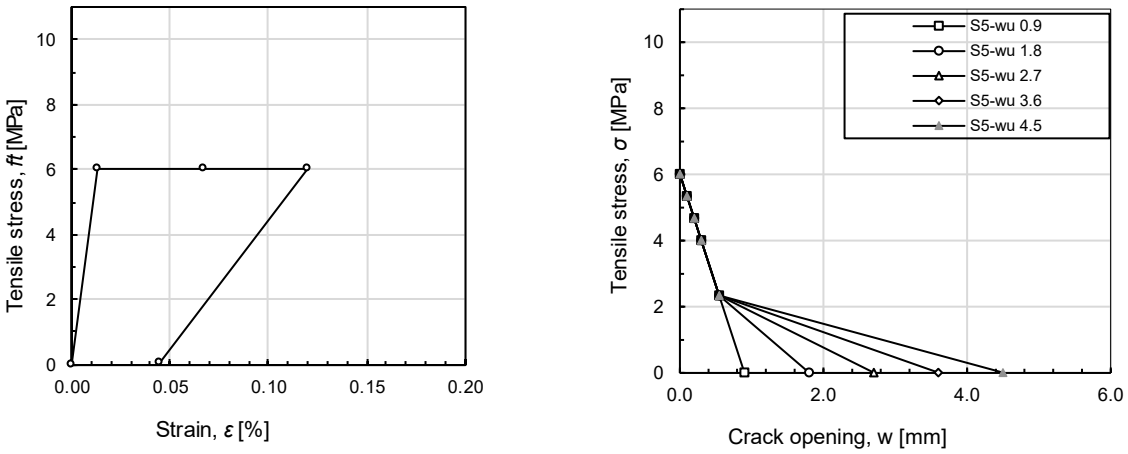

(a) Stress-strain response (b) Stress-crack opening response

Figure 4.10 Tensile properties curve of UHPFRC in the set 5

4.2.3.2.6 Set 6: Tensile stress variations in the first stage of softening- Δ_{fso}

This section considers Δ_{fso} and the other related parameters as the main variables to investigate their effects on bond behaviour. A constant E_{so} of 6.7 MPa/mm is selected for all the set models (Table 4.10 and Figure 4.11).

Table 4.10 UHPFRC tensile properties in set 6.

Parameters type		E_{sh} (MPa)	E_{PC} (MPa)	$f_{t,el}$ (MPa)	$f_{t,ts}$ (MPa)	$f_{t,u}$ (MPa)	$\varepsilon_{t,el}$ (%)	$\varepsilon_{t,ts}$ (%)	$\varepsilon_{t,u}$ (%)	$\varepsilon_{t,r}$ (%)	w_u (mm)	E_{SO} (MPa/mm)	$g_{f,SH}$ (kJ/m3)
Constant		9	8013	6	6.005	6.01	0.01	0.07	0.12	0.045	6.5	-6.7	4.6
	Specimen	Δ_{fso} (MPa)	w_{so} (mm)	$G_{f,CO}$ (kJ/m²)									
Variables	S6-Δfso 0.6	0.6	0.1	17.86									
	S6-Δfso 1.8	1.8	0.3	14.49									
	S6-Δfso 3	3	0.5	11.13									
	S6-Δfso 4.2	4.2	0.6	7.76									
	S6-Δfso 5.4	5.4	0.8	4.40									

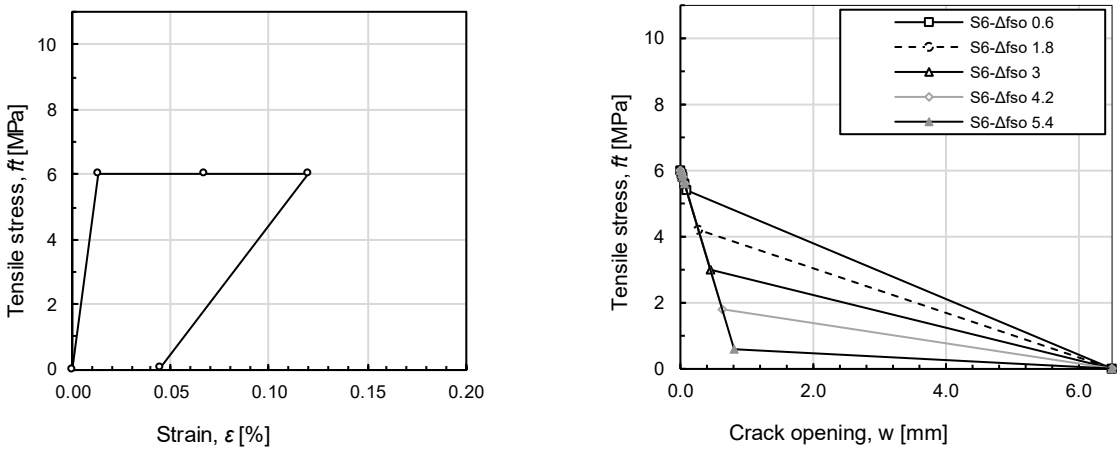

(a) Stress-strain response (b) Stress-crack opening response

Figure 4.11 UHPFRC tensile properties in set 6

4.2.4 Interface parameters

As discussed in section 3.2.2, the strategy of Lagier et al. (2016) is adopted, and the interface parameters are obtained from that research (Table 4.11). These values were also confirmed by Rosini (2018) to model the rib scale interface. They both applied the inverse analysis by comparing numerical and experimental results to obtain the values for normal and tangential strength parameters.

Table 4.11 Steel-UHPFRC interface parameters

Traction-Separation law								
σ_n (MPa)	T_n (MPa)	T_s (MPa)	K_{nn} (N/mm^3)	K_{ss} (N/mm^3)	K_{tt} (N/mm^3)	δ_d (μm)	μ (-)	$K_{el,f}$ (N/mm)
2	1.2	1.2	100	20	20	5	0.6	80

4.2.5 Solution parameters

The load is applied as a smooth displacement function at the end of the anchorage bar (AB) using the Dynamic Explicit method. To avoid the impact of the loading rate (i.e. displacement/time), we considered a constant loading rate for all models (Table 4.12). Moreover, shrinkage and creep effects were not considered. The reasons are to reduce the computing time and focus on investigating the effect of the selected parameters.

Table 4.12 Loading parameters

Loading parameters	
Type	Dynamic, Explicit
Displacement (mm)	4
Smooth step(sec)	0.012

4.3 Results and discussion

As shown schematically in Figure 4.12, this section identifies the possible cracks based on their directions and the plane in which they occur.

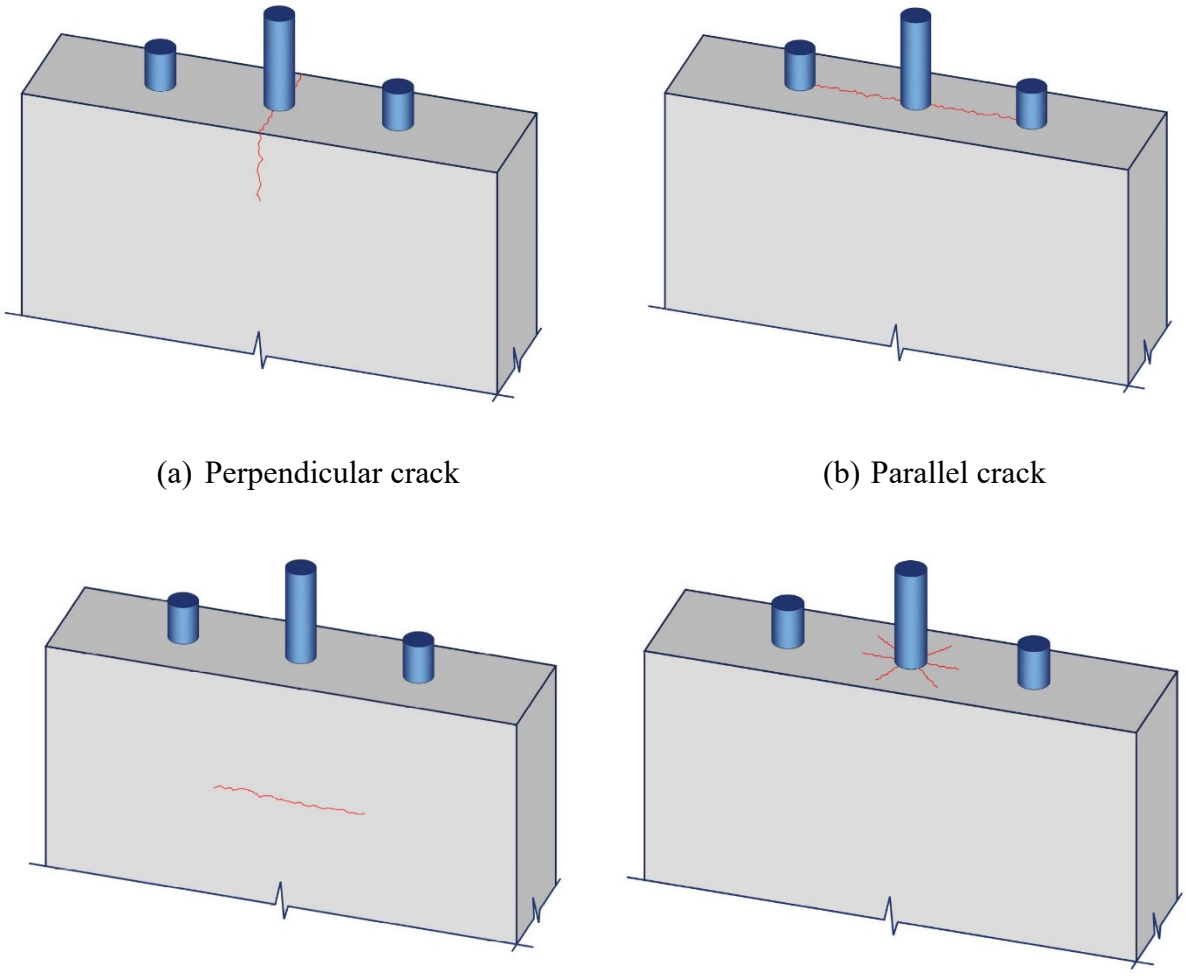

(a) Perpendicular crack (b) Parallel crack

(c) Horizontal crack (d) Radial cracks

Figure 4.12 Crack identification

4.3.1 Failure mode

All models exhibited the same failure mode, namely a perpendicular splitting crack (Figure 4.13, Figure 4.14, Figure 4.15 and Figure 4.16). It can be observed that changing UHPFRC tensile properties did not affect the type of failure mode. Regarding the quasi-static criteria described in the previous chapter (i.e. 3.2.3), the ratio of the total kinetic energy to the entire internal energy (E_k / E_i) remained below 5% at the onset of the main macro-crack and during the failure mode. Between the failure mode and 85% of the maximum force applied after that, the ratio still stayed below 5%.

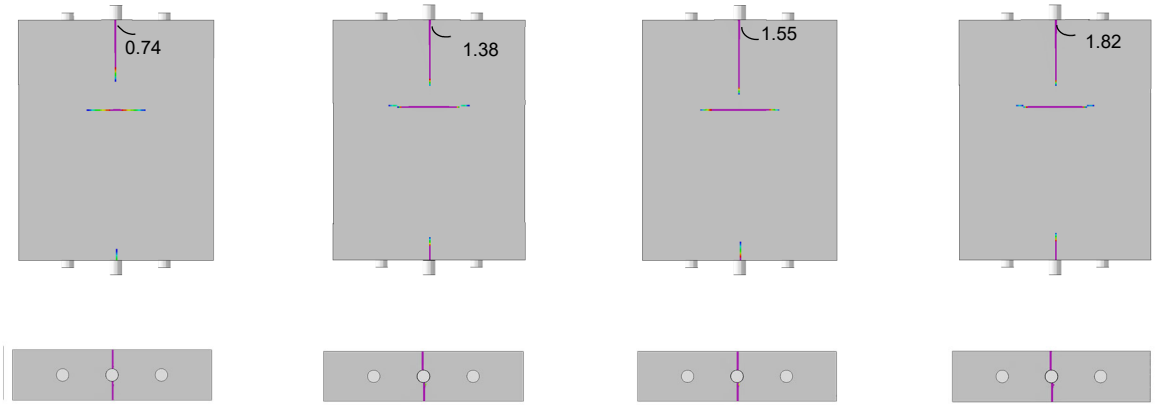

(a) S1-ft,u4-Eso6.7 (b) S1-ft,u10-Eso 6.7 (c) S1-ft,u4-Eso 4 (d) S1-ft,u10-Eso 4

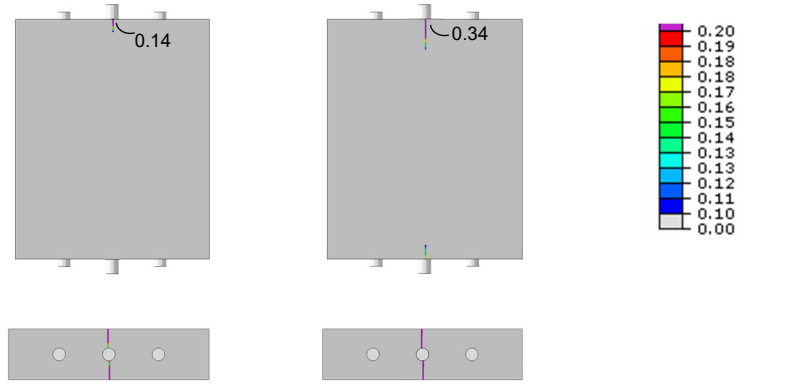

(e) S1-ft,u4-Eso 20 (f) S1-ft,u10-Eso 20 (g) Legend

Figure 4.13 Failure modes in set 1

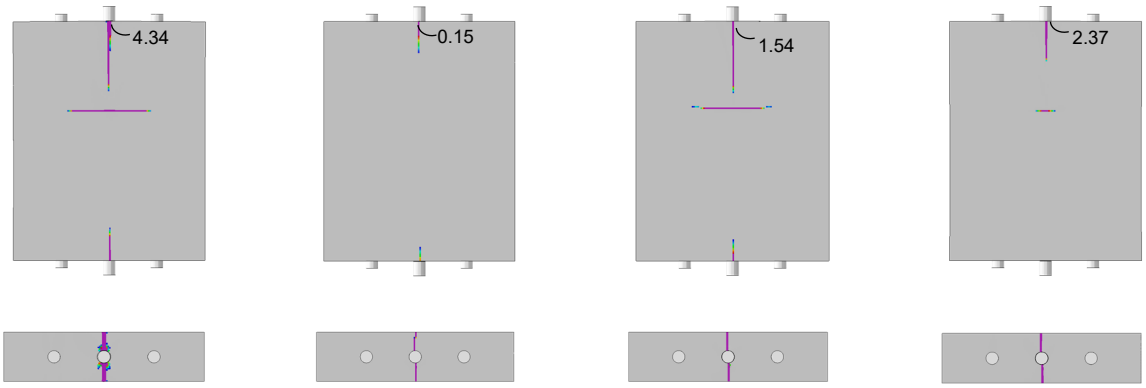

(a) S2- Eso 0.9 (b) S2- Eso 92.3 (c) S3-εt,u0.014 (d) S3-εt,u7.2

Figure 4.14 Failure modes in set 2 and set 3

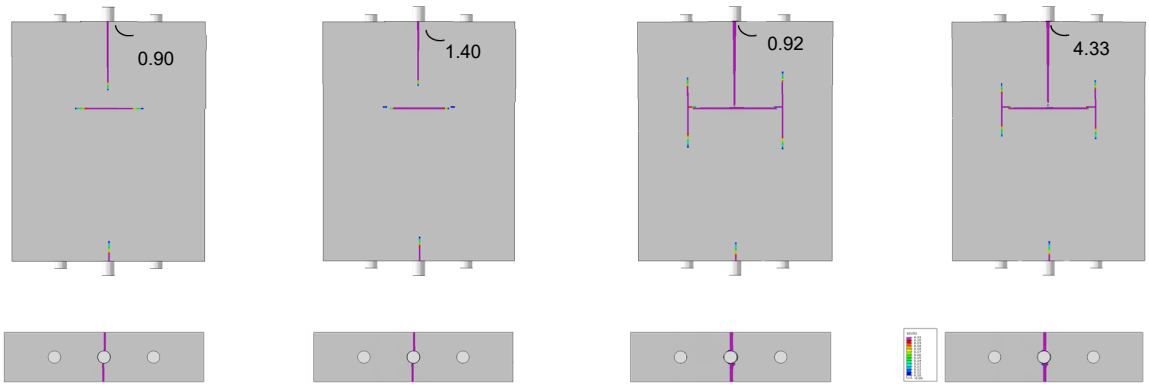

(a) S4-ft,u6.0-Esh 0 (b) S4-ft,u12-Esh5.6 (c) S5-wu 0.9 (d) S5-wu 4.5

Figure 4.15 Failure modes in set 4 and set 5

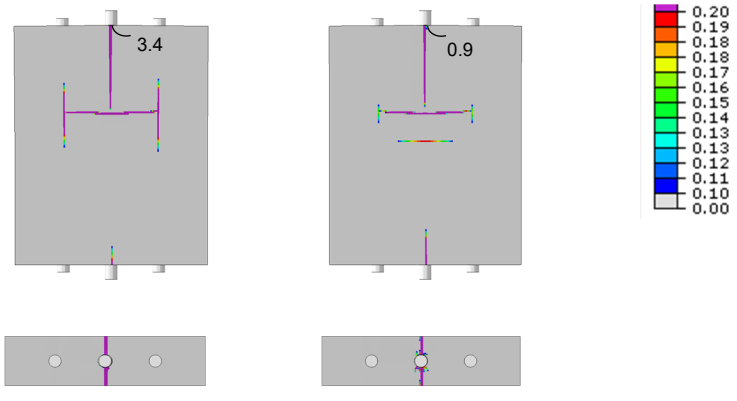

(a) S6- Δ_{fso} 0.6 (b) S6- Δ_{fso} 5.4 (c) Legend

Figure 4.16 Failure modes in set 6

4.3.2 First crack mode

Chapter 2 discussed the different types of cracking processes associated with the bond failure mechanism. In this chapter, the onset of perpendicular cracks is considered as the first crack mode. To separate the micro-cracks and the main cracks, the experimental value of 50 microns was retained as the boundary between micro-cracks and the main crack. In other words, when the crack width reaches the specified value, it is known as the main crack.

Although micro-cracks progress from the bar to edges, the first crack mode characterized by localization occurred for all the sets at the free edges of the specimens at the intersection of the top and the two side faces of the test specimen (Figure 4.17, Figure 4.18, Figure 4.19 and Figure 4.20).

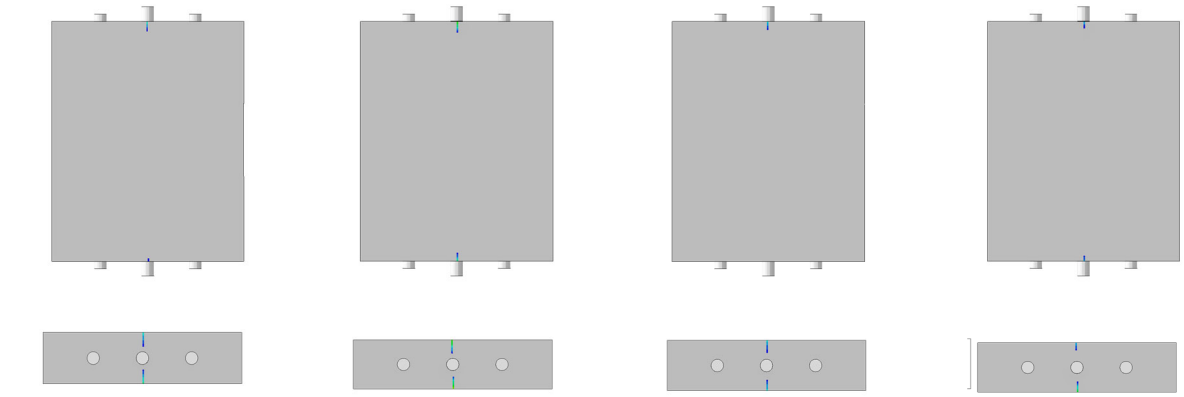

a) S1-ft,u4- Eso 6.7 b) S1-ft,u10- Eso 6.7 c) S1-ft,u 4- Eso 4 d) S1-ft,u10- Eso 4

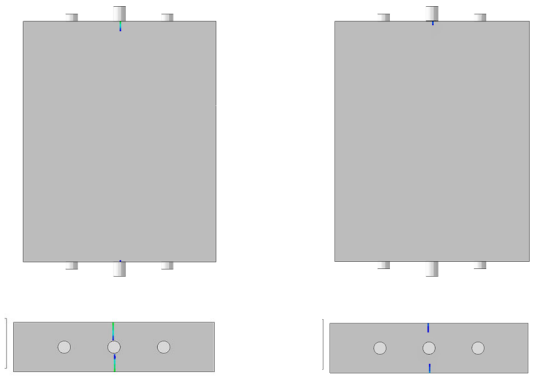

e) S1-ft,u4- Eso 20 f) S1-ft,u10- Eso 20

Figure 4.17 First crack modes in set 1

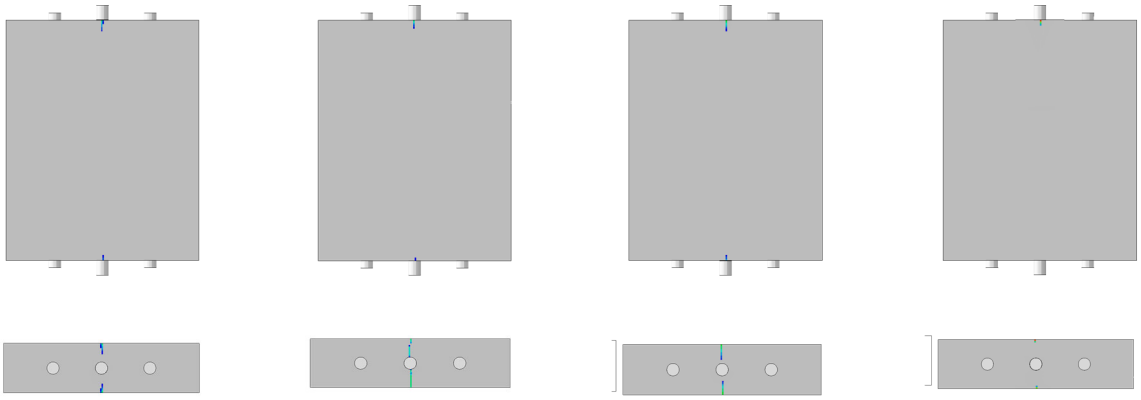

a) S2-Eso0.9 b) S2- Eso 92.3 c) S3-εt,u0.014 d) S3-εt,u7.2

Figure 4.18 First crack modes in set 2 and set 3

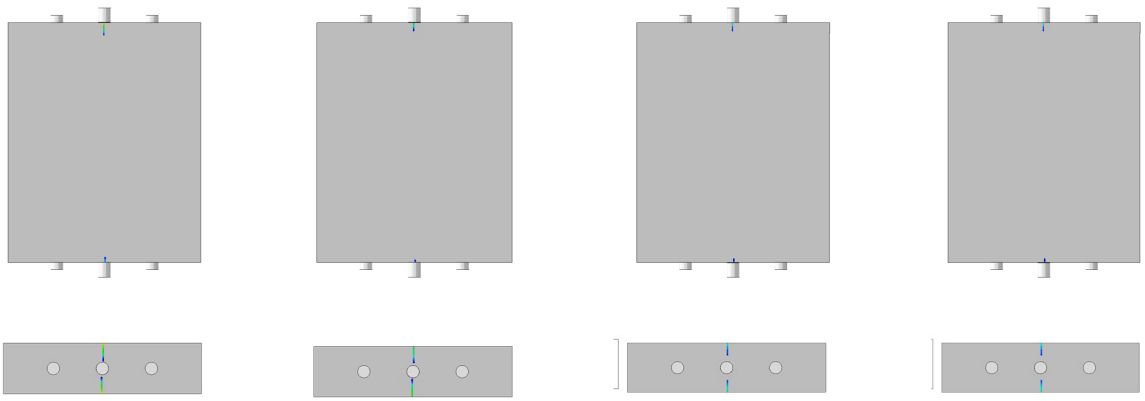

a) S4-ft,u6 -Esh 0 b) S4-ft,u12-Esh 5.6 c) S5-wu 0.9 d) S5-wu 4.5

Figure 4.19 First crack modes in set 4 and set 5

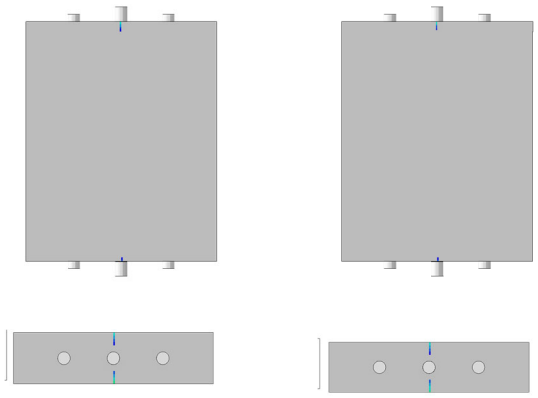

a) S6- Δ_{fso} 0.6 b) S6- Δ_{fso} 5.4

Figure 4.20 First crack modes in the set 6

4.3.3 Results interpretation

Table 4.13 and Figure 4.21 present the definition and location of each impact response. Table 4.15 presents results obtained from all sets. The table includes parameters that show some specimen impact responses we have selected to evaluate the parameters affecting bond behaviour.

For $f_{s,cr}$ and $f_{s,max}$, this study considers the surface elements at the end of the tested rebar (Figure 4.21a). To define the slip, four reference points are considered at the border of the intersection of two faces on the concrete and the central node on the tested bar at the beginning of the concrete and bar intersection (Figure 4.21b).

Four elements were tested on the surface perpendicular to the longitudinal axis and adjacent to the anchorage bar as the inner crack width (Figure 4.21c). Concerning the outer crack width, four elements were examined adjacent to the border of the top face and side faces (Figure 4.21d).

Table 4.13 Definition of the model impact responses

Name of the impact response	Set type	Output type	Output value
Bar stress at first crack ($f_{s,cr}$)	Surface elements	Stress (S33)	Average
Bar stress at maximum force ($f_{s,max}$)	Surface elements	Stress (S33)	Average
Inner crack width at maximum force ($wi_{\_fs,max}$)	Element	Crack width (SDV52)	Exact
Outer crack width at f maximum force ($wo_{\_fs,max}$)	Element	Crack width (SDV52)	Exact
Slip at first crack ($s_{LE\_fs,cr}$)	Node	Displacement (U33)	Exact
Slip at maximum force ($s_{LE\_fs,max}$)	Node	Displacement (U33)	Exact

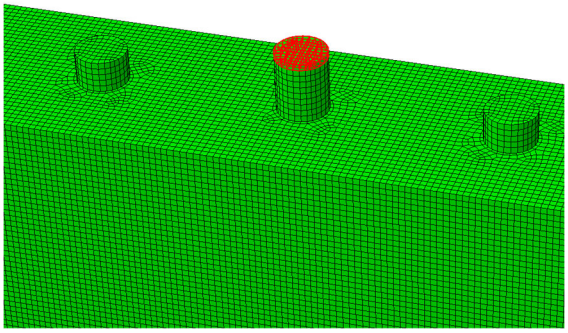

(a) Impact response of the bar stress

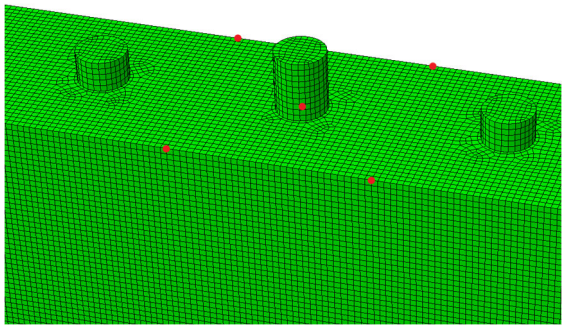

(b) Impact response of the slip

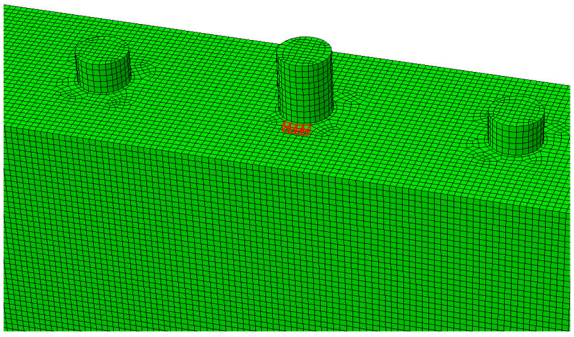

(c) Impact response of the inner crack

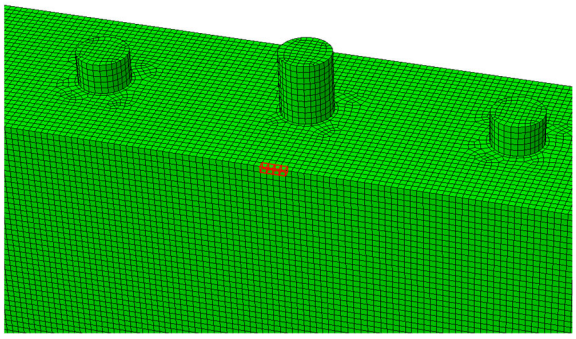

(d) Impact response of the outer crack

Figure 4.21 Location of the model impact responses

To increase the accuracy of the results, we recorded the mentioned responses for every five increments in ABAQUS history output. Then, we eliminated all the response peaks and made them flat by using the Butterworth filter.

This chapter uses the two following ways for interpreting the results:

- the changing rate of each response
- the type of relationship.

The ratio of the maximum value of each impact response to its minimum in each set is considered as the impact response charging rate. In fact, this ratio categorizes each response intensity into four levels of "without, low, moderate and high" effect (Table 4.14). The mentioned levels are defined hypothetically to facilitate the discussion. For instance, considering Table 4.15, this ratio for $f_{s,\,max}$ in set 1 with the E_{so} of 6.7, is equal to 2.3. Hence, it is considered as the high effect intensity, based on Table 4.14.

The intensity mentioned in Table 4.14 is simplified only for the reader to understand the changes. This ratio is valid only for the same set, and it cannot be generalized to other sets to compare them. This is because the ratio of inputs in each set is different.

Table 4.14 Definition of the changing rate intensity

Intensity	Amplitude
Without effect	1.0 to <1.2
Low effect	1.2 to <1.5
Moderate effect	1.5 to <2
High effect	>2

The type of relationship indicates the influence of UHPFRC tensile property parameters on the responses mentioned in Table 4.13. In other words, by using the XY graph, the type of relationships is identified, for example, as linear or nonlinear (Figure 4.22).

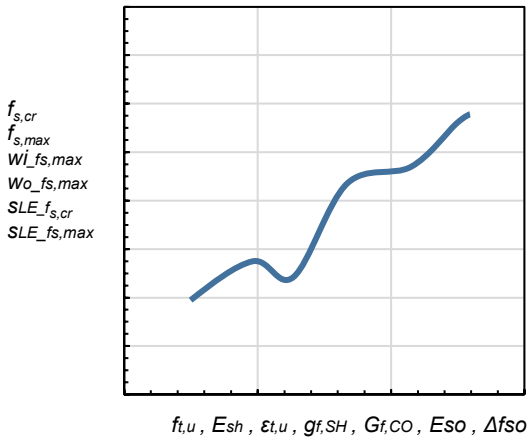

Figure 4.22 Schematic curve of an impact response- tensile properties parameters

Table 4.15 Results for all sets

Specimen	$f_{s,cr}$ (MPa)	$f_{s,max}$ (MPa)	$wi_{fs,max}$ (mm)	$wo_{fs,max}$ (mm)	$SLE_{fs,cr}$ (mm)	$SLE_{fs,max}$ (mm)
S1-ftu 4-Eso 20	182	206	0.12	0.15	0.09	0.13
S1-ftu 6-Eso 20	245	302	0.20	0.25	0.11	0.20
S1-ftu 8-Eso 20	302	397	0.25	0.32	0.14	0.26
S1-ftu 10-Eso 20	357	492	0.29	0.37	0.16	0.31
S1-ftu 4-Eso 6.7	191	265	0.44	0.63	0.10	0.28
S1-ftu 6-Eso 6.7	256	394	0.66	0.95	0.12	0.42
S1-ftu 8-Eso 6.7	317	511	0.88	1.15	0.15	0.55
S1-ftu 10-Eso 6.7	374	622	1.17	1.42	0.17	0.66
S1-ftu 4-Eso 4	191	307	0.79	1.33	0.10	0.42
S1-ftu 6-Eso 4	272	449	1.22	2.22	0.13	0.64
S1-ftu 8-Eso 4	327	575	1.31	1.65	0.15	0.72
S1-ftu 10-Eso 4	398	676	1.14	1.79	0.18	0.76
S2-Eso 0.9	285	547	1.80	3.30	0.14	1.06
S2-Eso 1.8	268	516	1.70	2.81	0.13	0.78
S2-Eso 3.7	280	461	1.24	1.73	0.14	0.66
S2-Eso 7.4	255	385	0.60	0.88	0.12	0.39
S2-Eso 92.3	214	230	0.10	0.11	0.10	0.12
S3-εtu 0.014	250	404	0.74	1.05	0.12	0.45
S3-εtu 0.014	251	404	0.71	0.98	0.12	0.44
S3-εtu 0.03	251	404	0.73	1.02	0.12	0.45
S3-εtu 0.12	259	405	0.70	0.96	0.12	0.44
S3-εtu 0.24	262	398	0.66	0.86	0.13	0.43

Table 4.15 Results for all sets (Continued)

S3-εtu 1.2	305	414	0.63	0.85	0.17	0.44
S3-εtu 7.2	414	489	0.77	2.04	0.34	0.65
S4-ftu 6-Esh 0	256	394	0.66	0.95	0.12	0.42
S4-ftu 6.6-Esh 0.5	277	431	0.70	1.10	0.13	0.45
S4-ftu 7.2-Esh 1.1	297	464	0.75	0.99	0.15	0.49
S4-ftu 8.4-Esh 2.2	322	533	0.85	1.06	0.16	0.55
S4-ftu 9.6-Esh 3.3	349	596	0.96	1.20	0.17	0.63
S4-ftu 10-Esh 3.7	366	619	1.00	1.19	0.18	0.65
S4-ftu 10-Esh 3-εtu 0.14	366	617	1.08	1.14	0.18	0.61
S4-ftu 10.8-Esh 4.5	383	655	0.85	1.11	0.19	0.63
S4-ftu 12-Esh 5.6	410	717	1.05	1.23	0.20	0.70
S5-wu 0.9	256	395	0.65	0.92	0.12	0.42
S5-wu 1.8	257	410	1.28	1.49	0.12	0.60
S5-wu 2.7	256	427	2.05	2.36	0.12	0.85
S5-wu 3.6	256	451	2.78	3.19	0.12	1.13
S5-wu 4.5	257	457	2.81	3.20	0.12	1.15
S6-Δfso 0.6	258	548	2.12	3.38	0.12	1.09
S6-Δfso 1.8	257	511	3.60	3.70	0.12	1.19
S6-Δfso 3	258	472	2.69	3.79	0.12	0.96
S6-Δfso 4.2	256	422	1.86	2.17	0.12	0.79
S6-Δfso 5.4	256	394	0.68	0.87	0.12	0.42

$f_{s,cr}$: Bar stress at first crack mode | $wi_{fs,max}$: Crack width at the inner face | $s_{LE\_fs,cr}$: Slip at first crack mode

$f_{s,max}$: Bar stress at failure mode | $wo_{fs,max}$: Crack width at the outer face | $s_{LE\_fs,max}$: Slip at failure mode

4.3.4 Influence of UHPFRC properties on the maximum bar stress ($f_{s,max}$)

By interpreting the results of Table 4.15 based on the changing rate (Figure 4.23), the following observation can be made.

- Increasing $f_{t,u}$, $g_{f,SH}$ and $G_{f,CO}$ has a high effect (i.e. ratio>2) on $f_{s,max}$ (Set 1). This result agreed with the results of (Chao et al., 2009; Deng et al., 2018; Roy et al., 2017);
- Decreasing E_{so} and which correspond to increasing $G_{f,CO}$ has a high impact (i.e. ratio>2) on the bond strength (Set 2).
- Varying of $\varepsilon_{t,u}$ and $g_{f,SH}$ have a low effect (i.e. ratio<1.4) on the bond strength (Set 3), whereas increasing $g_{f,SH}$ (Table 4.7) does not significantly affect $f_{s,max}$.

- Increasing E_{sh}, $f_{t,u}$, $g_{f,\,SH}$ and $G_{f,CO}$ has a high effect on $f_{s,max}$ (Set 4), which agrees with the results reported in Chapter 2 (Chao et al., 2009; Deng et al., 2018; Roy et al., 2017).
- Increasing $G_{f,CO}$ has a low impact (i.e. ratio=1.2) on $f_{s,max}$ (Set 5).
- Changes in Δ_{fso} value have a low effect (i.e. ratio=1.4) on $f_{s,max,}$ while keeping the E_{SO} constant (Set 6).

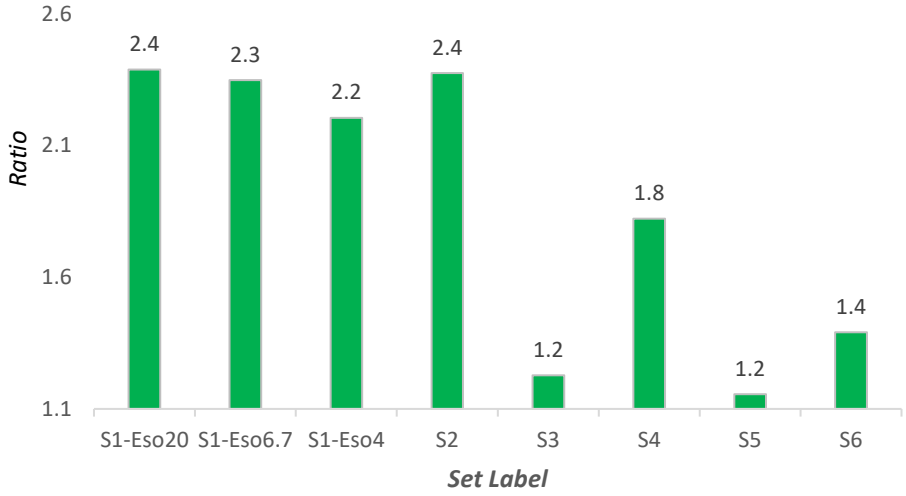

Figure 4.23 The change rate curve for the bar stress at failure mode $f_{s,max}$

By interpreting the results of Table 4.15 based on the observed tendency (Figure 4.24), the following observations can be made:

- Considering the constant *Eso*, we observed the relationship of $f_{s,max}$ versus $f_{t,u}$ is linear, and as $f_{t,u}$ increases, $f_{s,max}$ increases (Figure 4.24a).
- The three *Eso* selected in the first set indicate that if E_{so} reduces $f_{s,max}$ increases (Figure 4.24a).
- The relationship of $f_{s,max}$ and *Eso,* is nonlinear. Moreover, increasing E_{so} causes decreasing $f_{s,max}$ (Figure 4.24b).

The relationship between E_{sh} and $f_{s,max}$ is linear (Figure 4.24d). Also, $G_{f,CO}$ and Δ_{fso} versus bar stress at failure mode have an almost linear relationship (Figure 4.24e and Figure 4.24f).

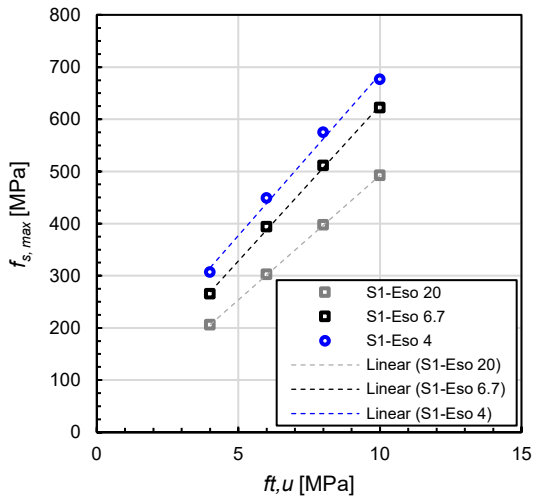

(a) Bar stress-ultimate tensile strength - set 1

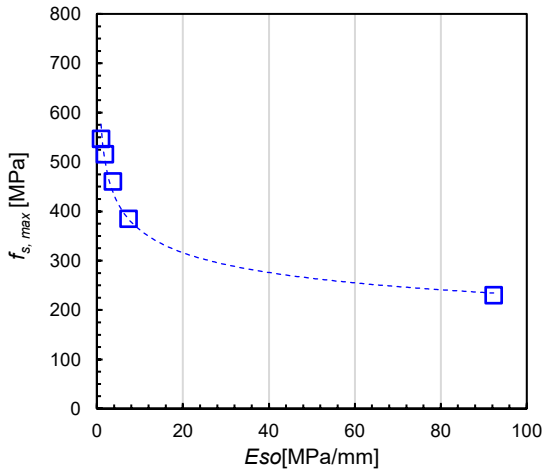

(b) Bar stress-Softening slope - set 2

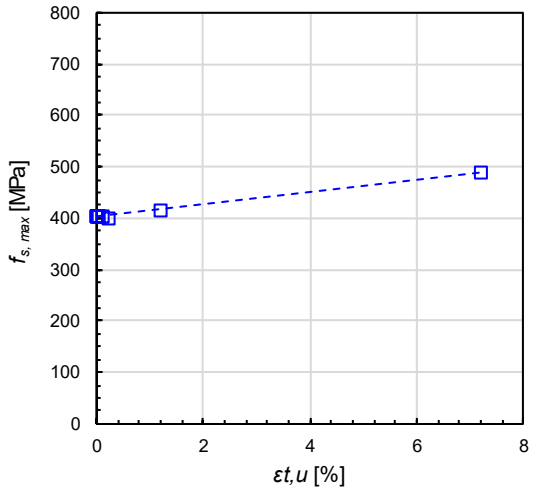

(c) Bar stress-ultimate tensile strain - set 3

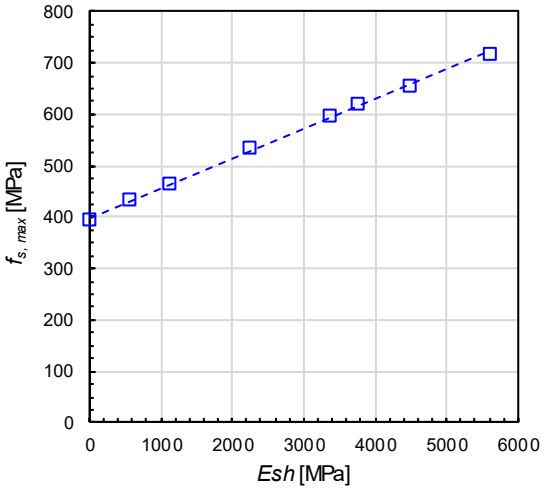

(d) Bar stress- hardening modulus - set 4

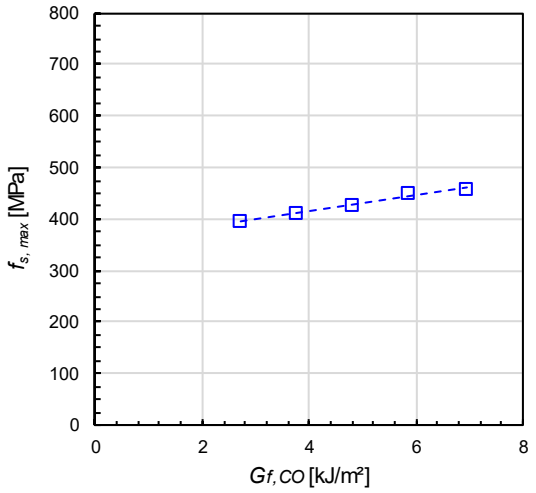

(e) Bar stress- dissipated energy - set 5

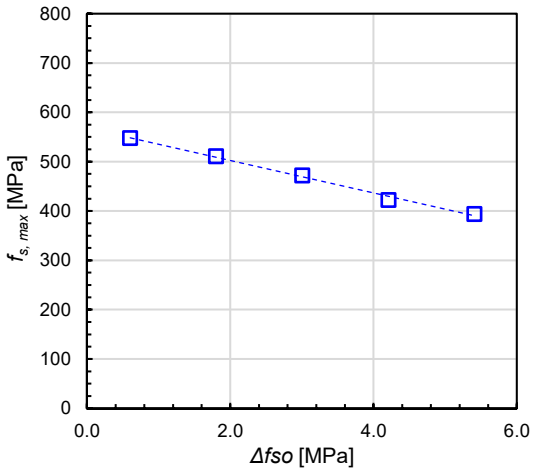

(f) Bar stress- Stress variations of softening - set 6

Figure 4.24 Effects of the parameters on the bar stress at failure

4.3.5 Influence of UHPFRC properties on the bar stress at first crack ($f_{s,cr}$)

By interpreting the results of Table 4.15 based on the changing rate (Figure 4.25), the following observations can be made.

- In Set 1 and Set 4, as $f_{t,u}$, $g_{f,SH}$ and $G_{f,CO}$ increase, $f_{s,cr}$ increases by high intensity (ratio>2), while by increasing $G_{f,CO}$ in the second set, the amount of $f_{s,cr}$ increases by low power (ratio=1.3). From the results, it can be concluded that the changes of $f_{t,u}$, $g_{f,SH}$ have the most significant effect on $f_{s,cr}$.
- The changes of the $\varepsilon_{t,u}$ have a moderate effect (ratio=1.7) on $f_{s,cr}$ (Set 3).
- As expected, the changes of $G_{f,CO}$, and Δ_{fso} have no impact on $f_{s,cr}$ (Sets 5 and 6).

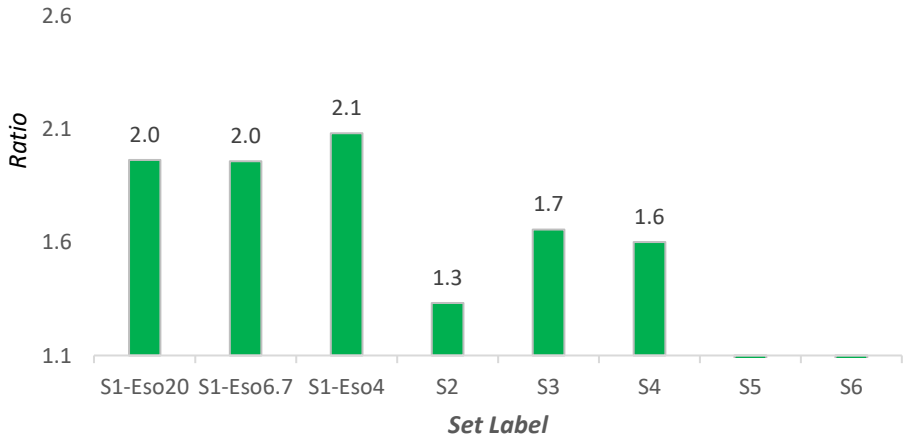

Figure 4.25 The change rate curve for the bar stress at the first $f_{s,cr}$

The graph in Figure 4.26a indicates that as $f_{t,u}$ increases, $f_{s,cr}$ increases linearly. Moreover, the same type of behaviour is observed for E_{sh} and $\varepsilon_{t,u}$ versus $f_{s,cr}$ (Figure 4.26c and Figure 4.26d). Figure 4.26b indicates that the relationship of $f_{s,cr}$ and E_{so} is nonlinear.

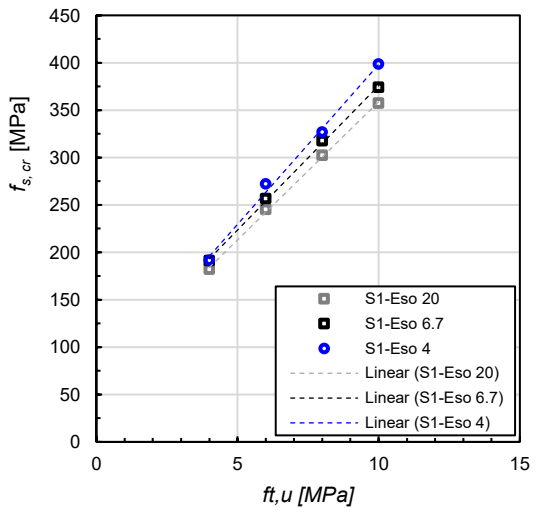

a) Bar stress-ultimate tensile strength - set 1

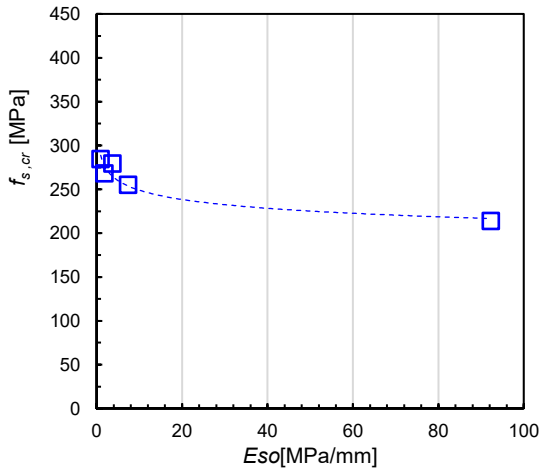

b) Bar stress - Softening slope - set 2

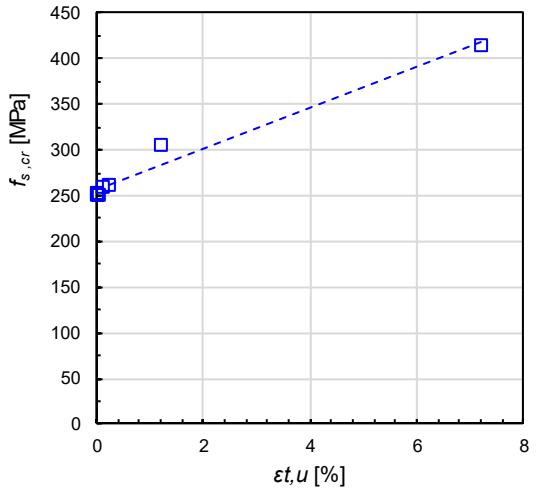

c) Bar stress-ultimate tensile strain - set 3

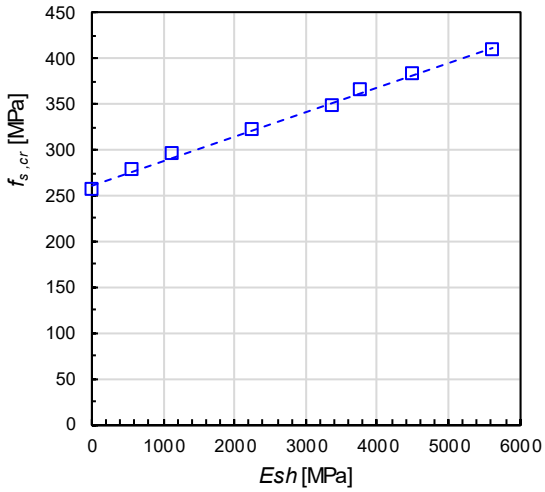

d) Bar stress- hardening modulus - set 4

Figure 4.26 Effect of UHPFRC properties on the bar stress at the first cracking

4.3.6 Influence of UHPFRC properties on the slip at failure (S_{LE_fsmax})

Figure 4.27 indicates the following observations.

- Increasing $f_{t,u}$, $g_{f,\,SH}$ and $G_{f,\,CO}$ has a high effect (i.e. ratio>2) on S_{LE_fsmax} for E_{so} of 20 and 6.7 (Set 1).

- Although increasing $f_{t,u}$ causes S_{LE_fsmax} to increase, results indicate that the amount of changing rate ratio shifts from high to moderate by decreasing E_{so} (Set 1)
- Increasing $\varepsilon_{t,u}$ and $g_{f,\,SH}$ in Set 3 has a moderate effect (i.e. 2>ratio >1.5) on S_{LE_fsmax}.
- Increasing $f_{t,u}$ and E_{sh} in Set 4 has a high effect (i.e. 2>ratio >1.5) on S_{LE_fsmax} (Set 4).
- The changes of $G_{f,\,CO}$, Δ_{fso} affect S_{LE_fsmax} by high intensity (Sets 5 and 6).

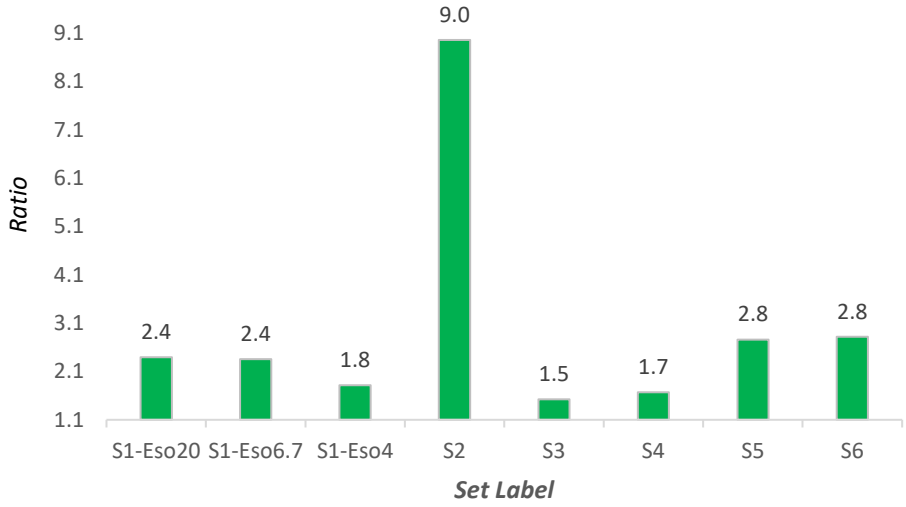

Figure 4.27 The change rate curve for the slip at failure mode S_{LE_fsmax}

Figure 4.28 leads to the following observations.

- The relationship behaviour between $f_{t,u}$ and $S_{LE\_fs,max}$ *more* shifted from linear to nonlinear behaviour if E_{so}*'s* value of 6.7 and 20 changes to 4 (Set one). In other words, the amount of $S_{LE\_fs,max}$ developed nonlinearly by raising the flexibility of UHPFRC.
- We observed the nonlinear trend between E_{so} and $S_{LE\_fs,max}$ similar to section 4.3.4 (Set 2).
- $S_{LE\_fs,max}$ versus E_{sh} and $G_{f,\,CO}$ showed almost linear behaviour (Set 4 and 5).

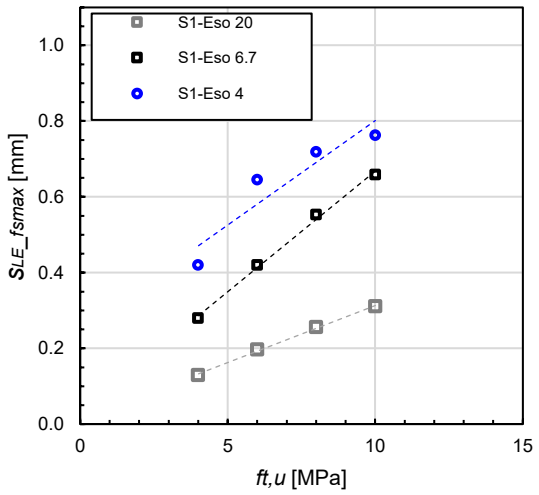

(a) Slip-ultimate tensile strength -set1

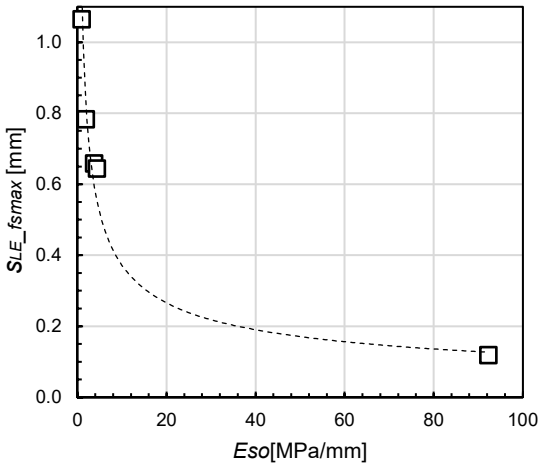

(b) Slip - Softening slope -set2

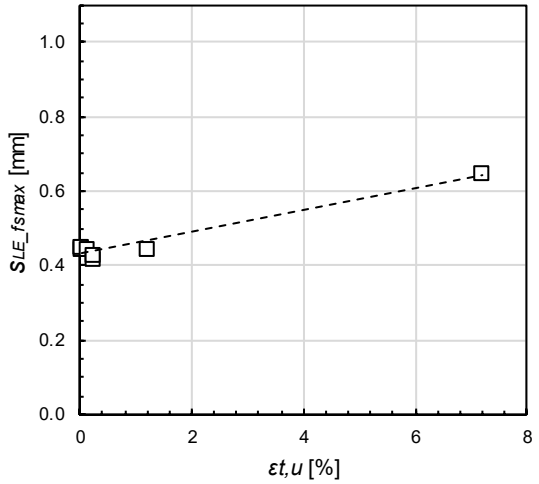

(c) Slip -ultimate tensile strain -set3

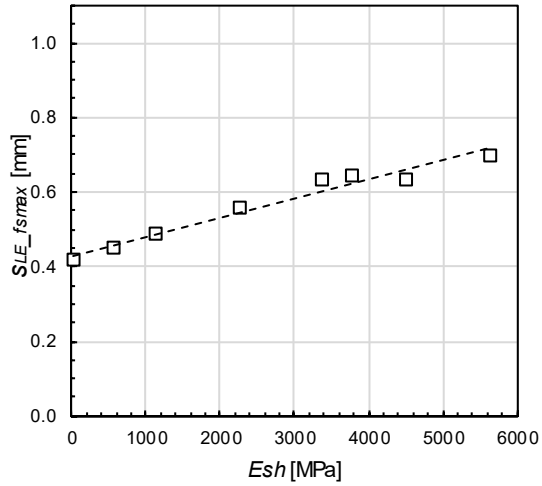

(d) Slip stress- hardening modulus -set4

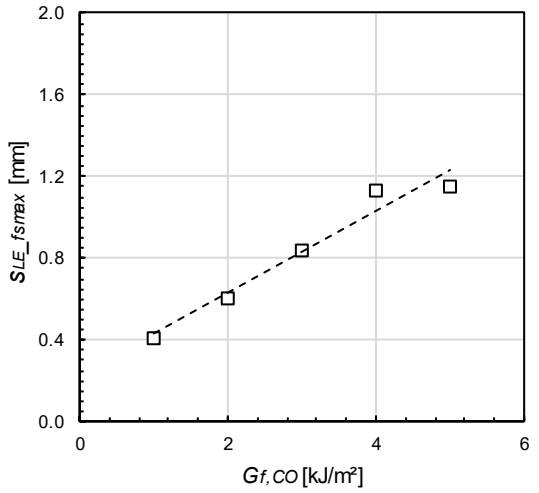

(e) Slip - dissipated energy - set 5

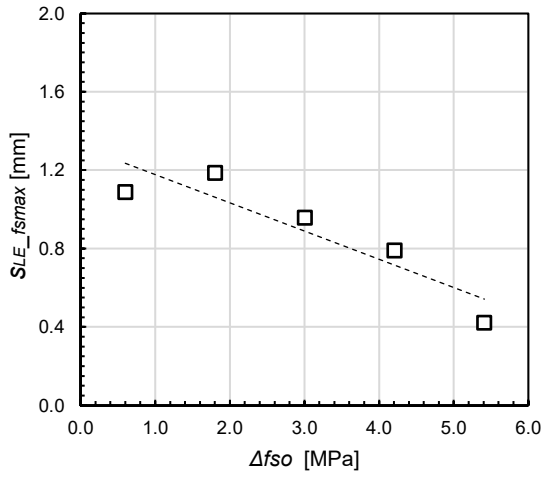

(f) Slip - Stress variations of softening - set 6

Figure 4.28 Effect of UHPFRC properties on the slip at failure

4.3.7 Influence of UHPFRC properties on the crack width at failure (w_i and w_o)

It can be seen that the changes in all material properties, except for $\varepsilon_{t,u}$ in Set 3 and E_{sh} in Set 4, have high and moderate impacts on $wi\_{fs,max}$ and $wo\_{fs,max}$ (Figure 4.29 and Figure 4.30). It is worth noting that changing $\varepsilon_{t,u}$ just affects $wo\_{fs,max}$, and E_{sh} affects $wi\_{fs,max}$.

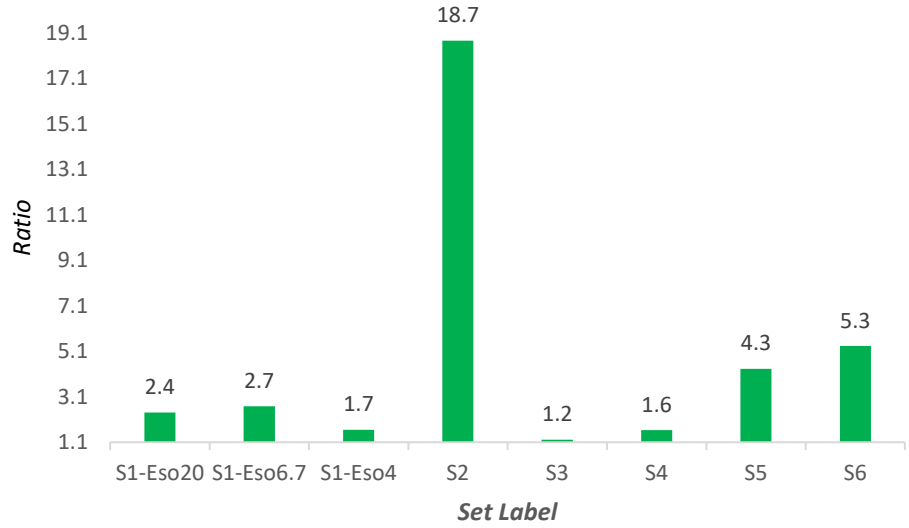

Figure 4.29 The change rate curve for the crack width at the inner face wi_{fsmax}

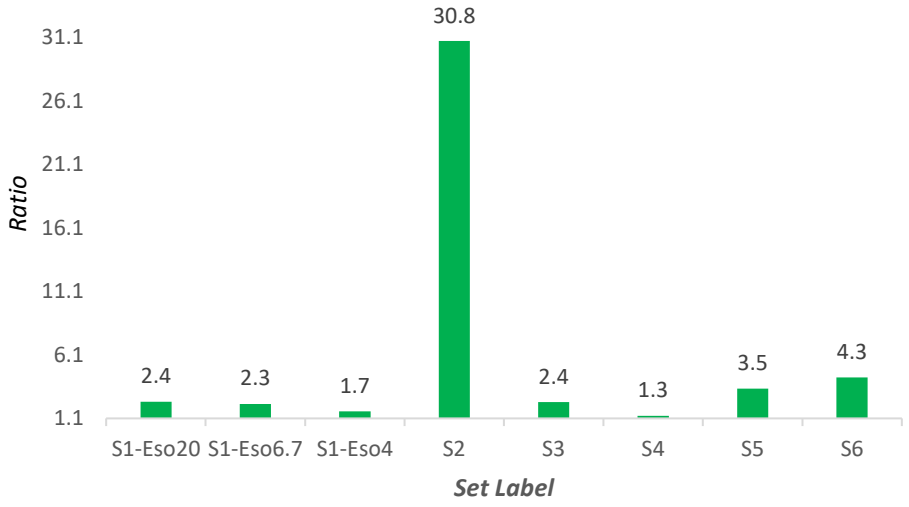

Figure 4.30 The change rate curve for the crack width at the outer face ($wo\_{fs,max}$)

The same relationship was seen in section 4.3.6 regarding $f_{t,u}$ versus $S_{LE\_fs,max}$. A linear trend is also observed between $f_{t,u}$ and both $wi_{\_fs,max}$ and $wo_{\_fs,max}$ (i.e. E_{so} =6.7 and E_{so}=20). Indeed, it switched from linear to nonlinear behaviour for the E_{so} of 4 (Figure 4.31a and Figure 4.31b). The amount of UHPFRC crack width developed nonlinearly by raising flexibility.

The increase in E_{so} causes the values of $wi_{\_fs,max}$ and $wo_{\_fs,max}$ to reduce nonlinearly (Figure 4.31c). It is observed that E_{sh} and $G_{f,CO}$ have an almost linear relationship with both $wi_{\_fs,max}$ and $wo_{\_fsmax}$ (Figure 4.31e and Figure 4.31f). Figure 4.31d and Figure 4.31g show that the relationships of crack width with parameters of $\varepsilon_{t,u}$ and Δ_{fso} are not linear.

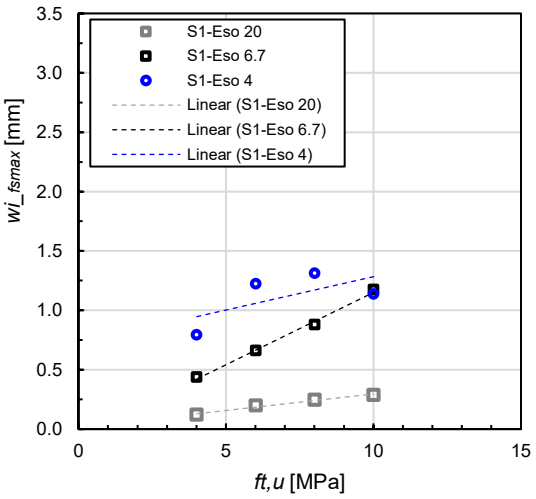

(a) Inner crack width-ultimate tensile strength - set1

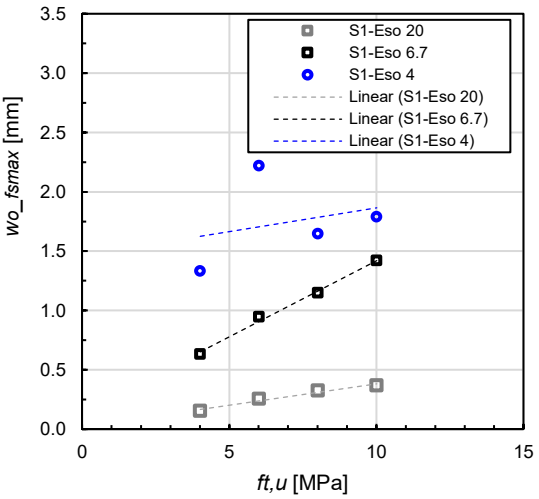

(b) Outer crack width-ultimate tensile strength -set1

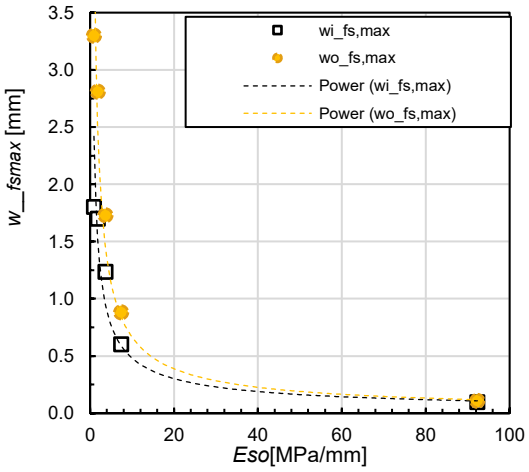

(c) Crack width-softening slope - set 2

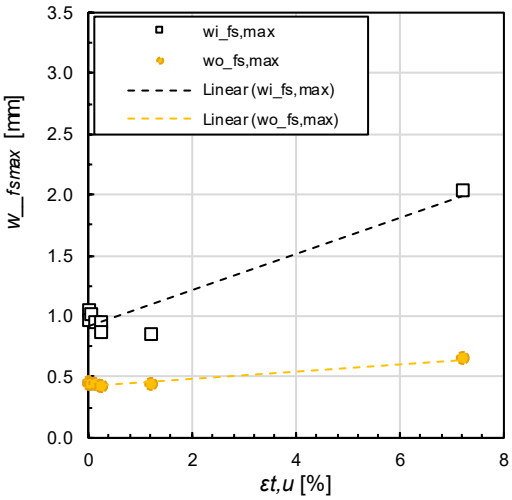

(d) Crack width- ultimate tensile strain - set 3

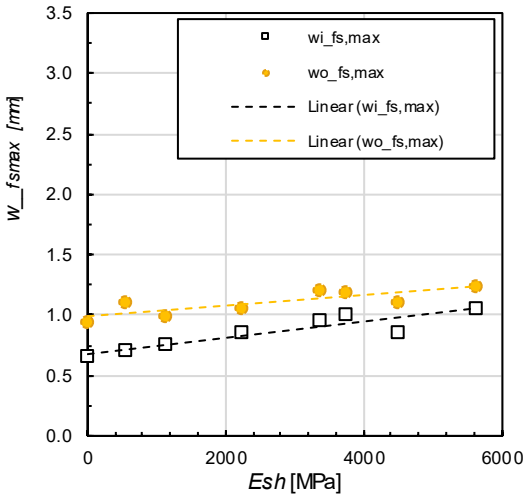

(e) Crack width- hardening modulus - set 4

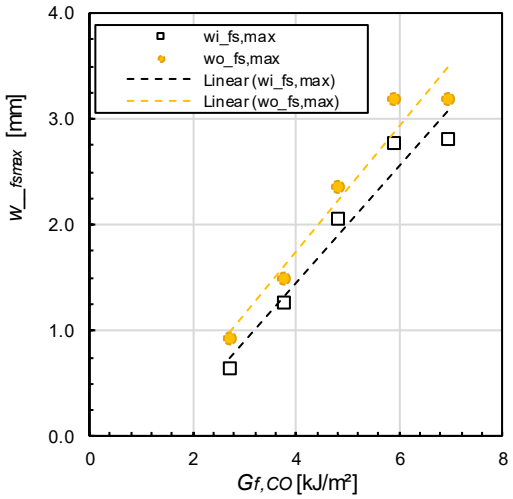

(f) Crack width- dissipated energy per crack surface area - set 5

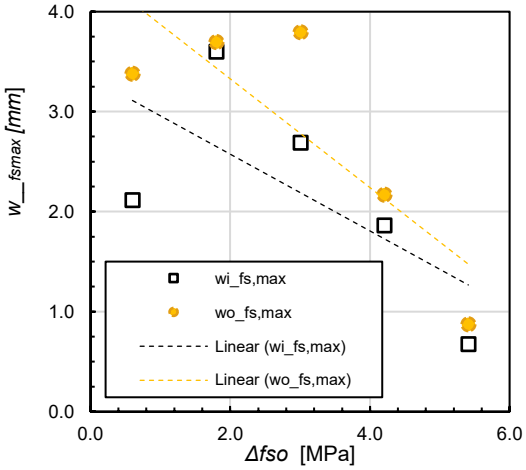

(g) Crack width- Stress variations of softening - set 6

Figure 4.31 Effect of UHPFRC properties on the crack width at failure

4.3.8 Influence of E_{sh} and $g_{f,\,SH}$ on the bar stress at failure ($f_{s,\,max}$)

Section 4.3.4 pointed out that with increasing the values of $f_{t,u}$, $g_{f,\,SH}$ (i.e. set 1) and $f_{t,u}$, $g_{f,\,SH}$, E_{sh} (i.e. set 4), the bar stress $f_{s,max}$ increases. However, it was not clear which of these parameters played a more critical role. Therefore, this section examined S1-ft,u10-Eso6.7 model from the first set and S4-ft,u10-E_{hc}3.7 model and S4-ft,u10-Ehc3.0 model from the fourth set (Figure 4.32). Table 4.16 shows all the models with the same $f_{t,u}$, $G_{f,CO}$ and E_{so}, while E_{sh} and $g_{f,\,SH}$ are different.

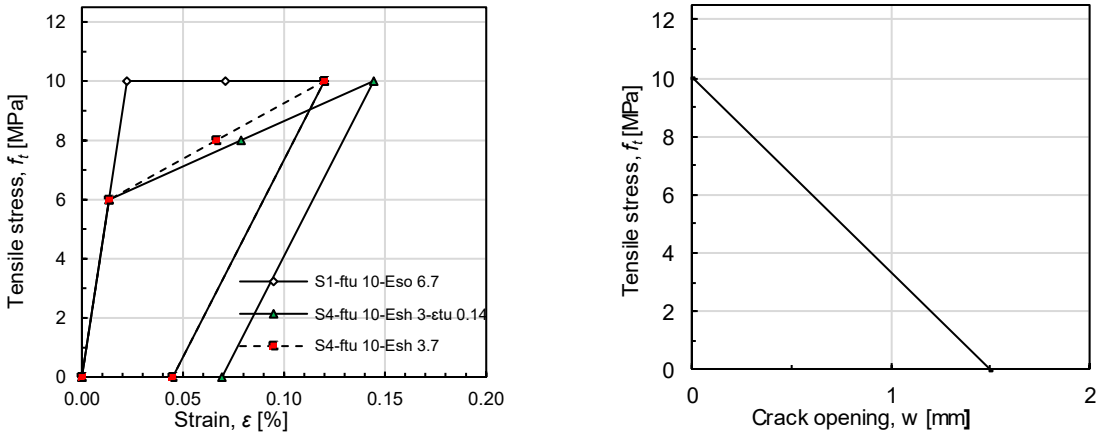

a) Strain hardening response up to peak load b) Crack-opening response

Figure 4.32 UHPFRC tensile properties in the selected models

Table 4.16 UHPFRC tensile properties in the selected models

Specimen	$f_{t,u}$ [MPa]	E_{sh} (MPa)	$\varepsilon_{t,ts}$ (%)	E_{SO} (MPa/mm)	$g_{f,SH}$ (kJ/m3)	$G_{f,CO}$ (kJ/m²)
S1-ftu 10-Eso 6.7	10.0	10	0.12	-6.7	7.1	7.5
S4-ftu 10-Esh 3-εtu 0.14	10.0	3,060	0.14	-6.7	7.1	7.5
S4-ftu 10-Esh 3.7	10.0	3,759	0.12	-6.7	5.2	7.5

Figure 4.33a shows that changing E_{sh} has no significant impact on $f_{s,max}$ while Figure 4.33b indicates that variations of $g_{f,SH}$ do not affect $f_{s,max}$ for models S1-ft,u 10-Eso6.7 and S4-ft,u10-Esh. This result (i.e. $g_{f,SH}$ versus $f_{s,max}$) agreed with the result obtained from section 4.3.4. It means the changes of $g_{f,SH}$ does not affect $f_{s,max}$ if the other parameters (i.e. $f_{t,u}$, E_{so} and $G_{f,CO}$) remain constant.

Therefore, we considered E_{sh} and $g_{f,SH}$ as dependent variables whose changes correlated to $f_{t,u}$ changes.

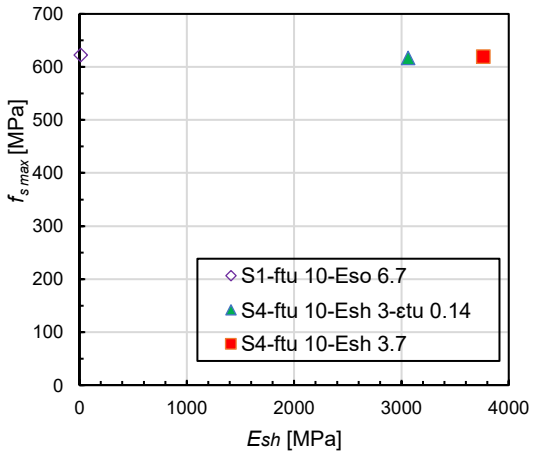

a) Bar stress at failure - hardening modulus

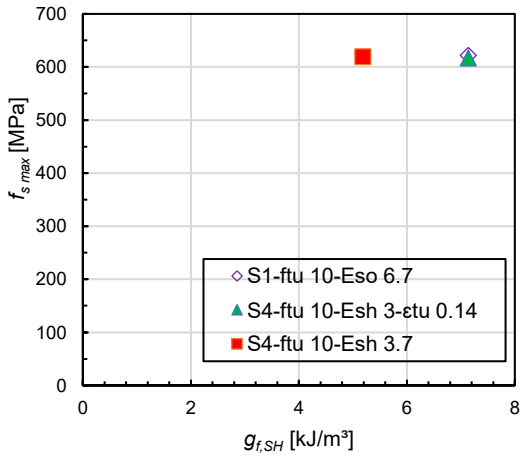

b) Bar stress at failure - dissipated energy per unit volume

Figure 4.33 The relationship behaviour

4.4 Summary and conclusions

Table 4.17 summarizes the results of this parametric study which combined the two strategies mentioned in section 4.3.3.

Table 4.17 Results summary

Set		$f_{s,cr}$	$f_{s,max}$	$wi_{\_fsmax}$	$wo_{\_fsmax}$	s_{LE_fsmax}
S1-Eso20	$f_{t,u}$	L-H	L-H	L-H	L-H	L-H
S1-Eso6.7	$f_{t,u}$	L-H	L-H	L-H	L-H	L-H
S1-Eso4	$f_{t,u}$	L-H	L-H	NL-M	NL-M	NL-M
S2	E_{so}	NL-Lo	NL-H	NL-H	NL-H	NL-H
S3	$\varepsilon_{t,u}$	NL-M	L-Lo	NL-Lo	L-H	NL-M
S4	$f_{t,u}$	L-M	L-H	L-M	L-Lo	L-M
S4	E_{sh}	L-M-D	L-H-D	L-M	L-Lo	L-M- D
S5	$G_{f,\,CO}$	W	L-Lo	L-H	L-H	L-H
S6	Δ_{fso}	W	L-Lo	NL-H	NL-H	NL-H
L: Linear behaviour		Lo: Low effect		H: High effect		D: Dependent parameter
NL: Nonlinear behaviour		M: Moderate effect		W: Without effect		

The parameters defining UHPFRC tensile properties are categorized into the main and the associated parameters based on their effects on the bond behaviour. The main parameters directly affect the bond behaviour, and the associated parameters are either ineffective or, if effective, their impact depends on the main parameters. Table 4.18 presents the main parameters which play a notable role in each impact response. As shown in Table 4.18, $f_{t,u,}$ and E_{so} perform a significant function for all the impact responses. Generally, the softening phase parameters play a more notable role in the impact responses than the hardening phase parameters.

Table 4.18 Main efficient parameters in each impact response

Bond performance parameter	**Main UHPFRC parameters**
Bar stress at failure ($f_{s,max}$)	$f_{t,u}$, E_{so}
Bar stress at first crack ($f_{s,cr}$)	$f_{t,u}$, $\varepsilon_{t,u}$
Slip at failure ($s_{LE\_fs,max}$)	$f_{t,u}$, E_{so} , $\varepsilon_{t,u}$, $G_{f,\,CO}$, Δ_{fso}
Inner crack at failure ($wi_{\_fs,max}$)	$f_{t,u}$, E_{so}, $G_{f,\,CO}$, Δ_{fso}
Outer crack at failure ($wo_{\_fs,max}$)	$f_{t,u}$, E_{so}, $\varepsilon_{t,u}$, $G_{f,\,CO}$, Δ_{fso}

The details of this section are as follows:

- $f_{t,u}$ plays a vital role in the bar stress at failure (i.e. $f_{s,max}$), and the other parameters are associated parameters in the hardening phase, including $\varepsilon_{t,u}$, E_{sh} and $g_{f,SH}$.
- the softening phase parameters E_{so} and $G_{f,\,CO,}$ play a vital role in the magnitude of $f_{s,max}$.
- the relationship of $f_{t,u}$ with the response parameters of $f_{s,max}$ and $f_{s,cr}$ is linear by considering the constant E_{so} (i.e. E_{so}).
- $f_{t,u}$, E_{so}, $G_{f,\,CO}$, Δ_{fso} and $\varepsilon_{t,u}$ values play a role in determining $S_{LE\_fs,\,max}$. It should be noted that the $\varepsilon_{t,u}$ for $S_{LE\_fs,max}$ has a moderate effect compared to other parameters.
- there is a linear relationship between $f_{t,u}$ and $S_{LE\_fs,max}$ for the sharp slopes regarding the constant softening slope (i.e. E_{so}=6.7, 20). It was not observed such a linear relationship in UHPFRC, which highlights the high ductility (i.e. E_{so}=4).

- regarding the constant E_{so}, the relationship between $f_{t,u}$ and the impact response of $wi_{\_fs,max}$ and $wo_{\_fs,max}$ for the sharp slopes (i.e. E_{so}=6.7, 20) is linear. It was not seen such a linear relationship for the low slope (i.e. E_{so}=4).
- E_{so} and $f_{t,u}$ played a role in determining the inner crack's width at failure mode (i.e. wi_f_{smax}), while the sensitivity of $wi_{\_fs,max}$ to E_{so} is more than of $f_{t,u}$.
- $f_{t,u}$, E_{so} , $G_{f,CO}$, $\varepsilon_{t,u}$ and Δ_{fso} played a role in determining the outer crack width at failure mode (i.e. $wo_{\_fs,max}$), while the sensitivity of $wo_{\_fs,max}$ to E_{so} is more than others.

CHAPTER 5 REVIEWING THE MECHANISMS OF STRESS TRANSFER

5.1 Introduction and objectives

Chapter 2 highlighted the importance of the tensile stress mechanism around the rebar, also called the confinement stress, and its role the bond development. As discussed in the bond mechanism in section 2.3.1, the development of tensile stresses around the bar creates radial longitudinal cracks in normal concrete (Figure 5.1). It was also noticed that the bridging effect of fibres contributes to maintaining the confining tensile stresses and thereby increasing the bond strength. Therefore, the investigation of the tensile stress distribution (also called the confinement stress) around the rebar embedded length help to better understand the bond mechanism in the UHFRC

Additionally, as shown in section 4.4, results indicated that $f_{t,u}$ and $E_{so,}$ are the two parameters playing a crucial role in the bar stress at failure. Therefore, this chapter aims to examine the results of chapter 4 based on the confinement stress distribution and the development of the tensile force in the bar.

This chapter contains four sections: first, the strategy of modelling the confinement force and confinement stress. Second, interpreting the result according to confinement stress, third, assessing the mechanism of confinement stress distribution and, finally, the conclusion.

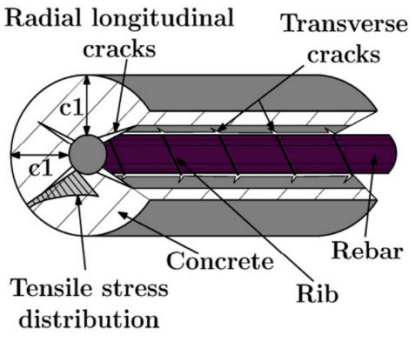

Figure 5.1 Bond mechanism (Chao et al., 2009)

5.2 Strategy for modelling the confinement forces and stresses

This section intends to investigate the magnitude of the confinement stresses in the region around the anchorage bar of length $4d_b$ (Figure 5.2). Two planes were selected, perpendicular and parallel to the plane of the bars, with confinement stress for each plane. The confinement stresses are S_{11} in direction X and are S_{22} in direction Y. In direction Z, the anchorage stress S_{33} is shown in Figure 5.3a and Figure 5.3c.

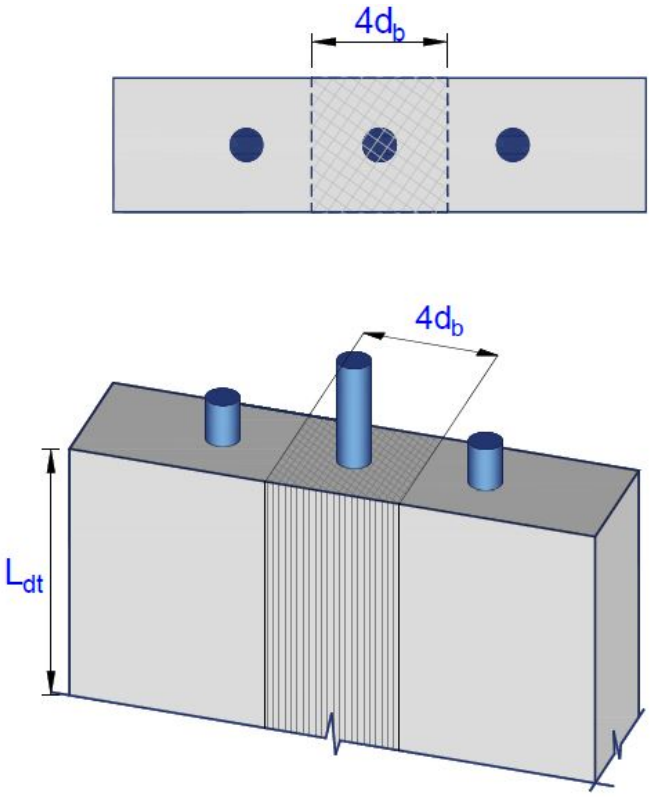

Figure 5.2 Zone of interest

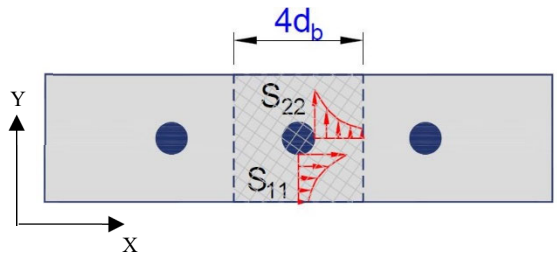

(a) Confinement stresses S_{11} and S_{22}

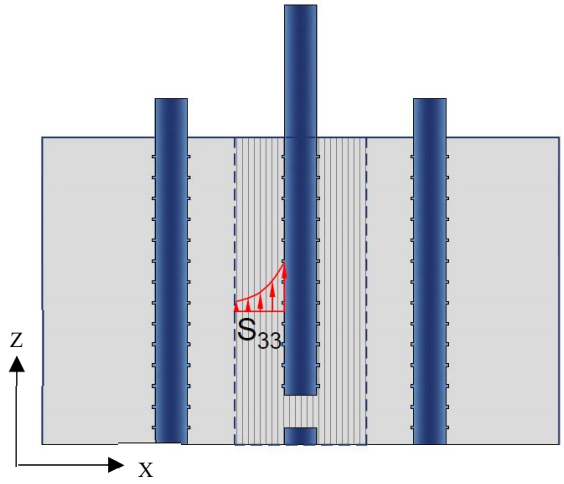

(b) Anchorage stress S_{33} in the plane parallel to the bars

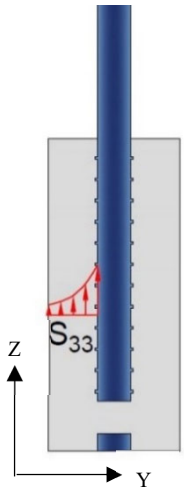

(c) Anchorage stress S_{33} in the plane perpendicular to the bar plane

Figure 5.3 Stress in the bar plane and transverse failure plane

PYTHON programming language was used to compute the confinement stresses in ABAQUS. The strategy consists of selecting the row of the elements in front of each rib in the two planes of failure (Figure 5.4). The length of each row is equal to 1.5 d_b. The average tensile stress between the elements of each row was calculated in the principal directions (i.e. X, Y and Z). In other words, each row in front of the rib indicates the confinement stress at that specific location. A graph for each stress component along the embedded length will be presented as indicated in Figure 5.6a. The blue points in Figure 5.6a indicate the confinement stress at each location along the embedded length. It is noted that the principal directions for the confinement stress are indicated by 1, 2 and 3 in ABAQUS. Given that, the directions X, Y and Z correspond to the indexes 1,2 and 3 (Table 5.1).

Table 5.1 Definition of confinement stresses in the principal directions

Nomenclature	
S_{11}	Confinement stress in direction X for the transverse failure plane [MPa]
S_{22}	Confinement stress in direction Y for the bar plane [MPa]
S_{33}	Anchorage stress in direction Z for both of failure plane and rebars plane [MPa]

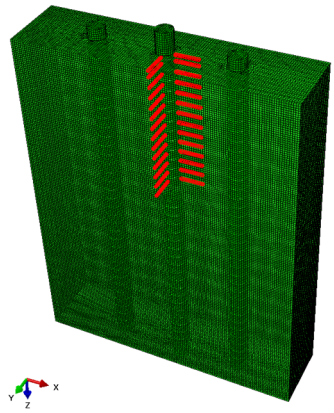

(a) S_{11}, S_{22} and S_{33} for both planes

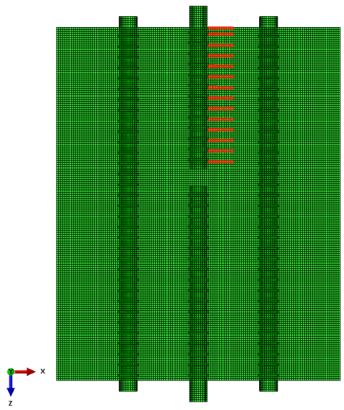

(b) S_{22} and S_{33} in the rebar plane

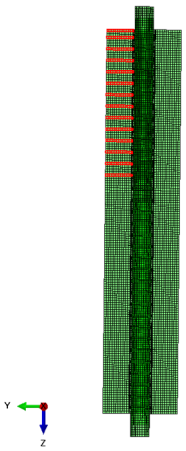

(c) S_{11} and S_{33} in the failure plane

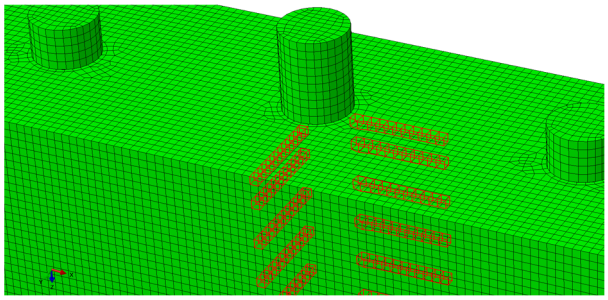

(d) The rows in front of the ribs

Figure 5.4 Post-processing the confinement stresses in the finite element software

In this section, the bar stress along the embedded length is investigated to understand better the bond zone tensile stress distribution mechanism. To do so, we selected the rows behind each rib elements in the tested rebar in ABAQUS (Figure 5.5). The average bar stress (i.e. f_s) has been computed for each row. Each blue point on the curve indicates the moderate stress for each row of elements behind each rib (Figure 5.6b). The reason for collecting the elements behind each rib is to minimize the bearing action effects on the results.

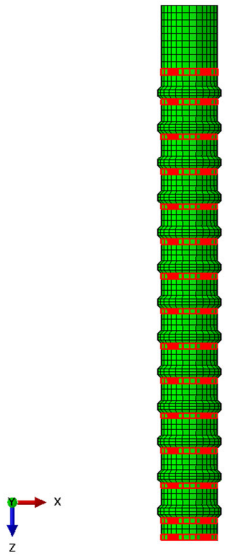

Figure 5.5 Modelling the bar stress along the embedded length

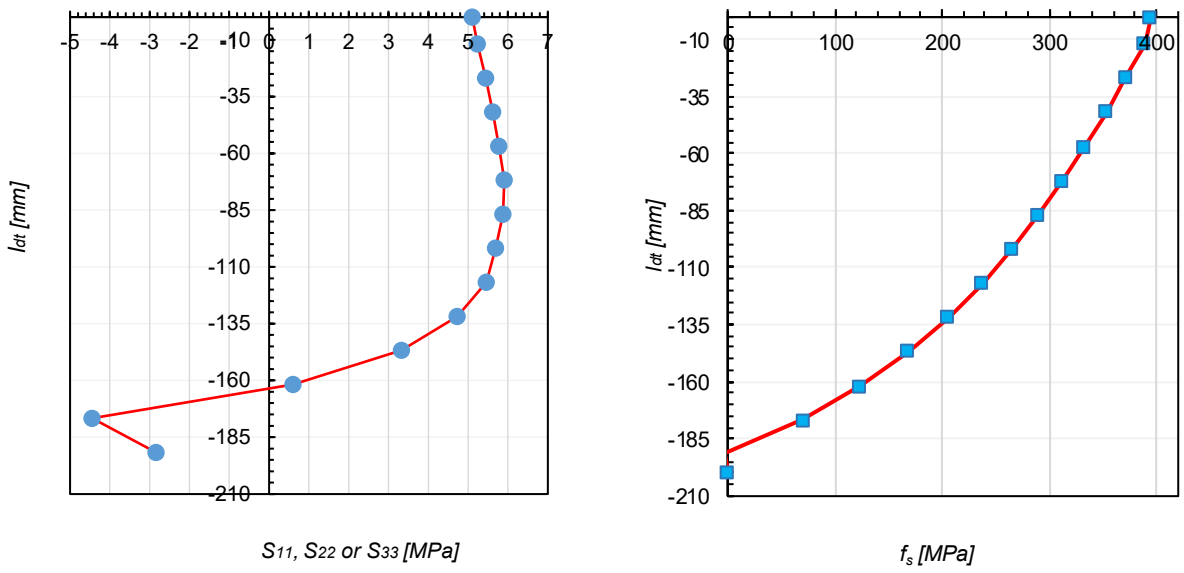

(a) Stresses in the three principal directions (b) Bar stress

Figure 5.6 Schematic curves of confinement stress and bar stress along the embedded length

Another parameter defined in this section is $F_{11,}$ which is called the confinement force. This force corresponds to the confinement stress of S_{11}, and it is then given by:

$$F_{11} = 2\left(1.5 d_b h_r \sum_{0}^{n-1} (S_{11,i} + S_{11,i+1}) 0.5\right) \tag{5-1}$$

where, d_b is the bar diameter, h_r is the distance between the ribs, n is the numbers of the ribs and $S_{11,i}$ is the confinement stress in direction 1 at each embedded length location. It is worth mentioning that by replacing the confinement stress of S_{22} on the above equation, F_{22} can be calculated with the same equation.

5.3 Interpreting the results of chapter four according to the confinement stress

As concluded in chapter four, $f_{t,\,u,}$ and E_{so} are the parameters that play a significant role in bar stress at failure (i.e. $f_{s,\,max}$). Also, we observed that $f_{t,\,u}$ relationship with $f_{s,\,max}$ is linear for the specimens

which have constant E_{so}. Hence, this section examines these results with respect to the variation of the confinement stress S_{11} in the longitudinal direction.

5.3.1 Research models

Two models of Chapter 4 were selected from set 1 (i.e. S1-ft,u6- Eso 6.7 and S1-ft,u10-Eso6.7) and two models from set 2 (i.e. S2-Eso7.4 and S2-Eso0.9) as highlighted in Figure 5.7 and Figure 5.8 (see the section4.2). The main reason for selecting these sets was that $f_{t,u}$ changes while E_{so} is constant in the first set, and in the second set, E_{so} changes while $f_{t,u}$ is kept constant. Figure 5.9 presents the curves of bar stress-slip for both sets.

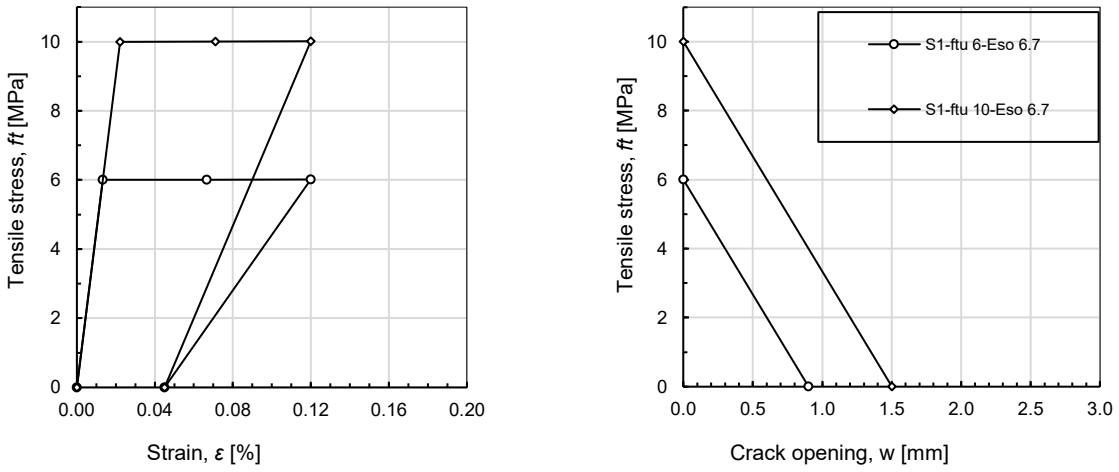

(a) Stress-strain response (b) Stress-crack-opening response

Figure 5.7 Tensile properties curve of UHPFRC for two research models of set 1

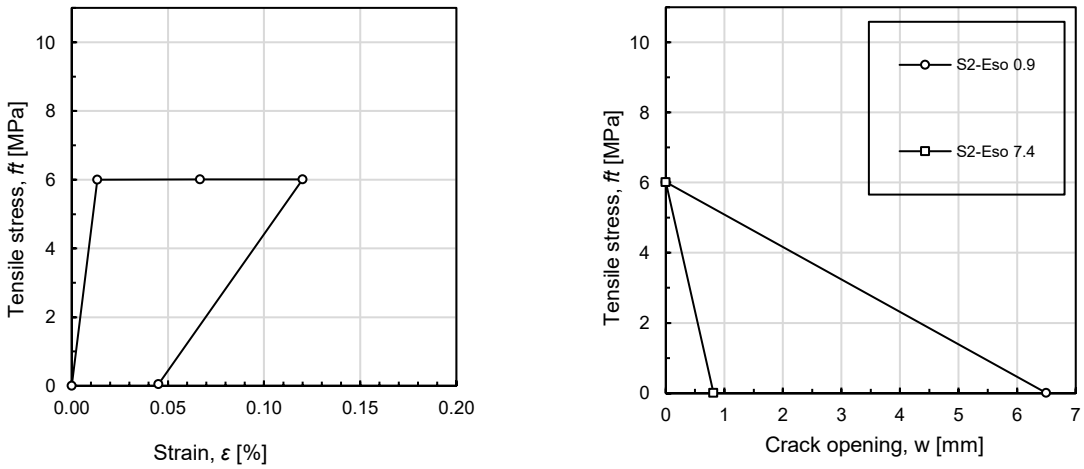

a) Stress-strain response b) Stress-crack-opening response

Figure 5.8 Tensile properties curve of UHPFRC for the two models of set 2

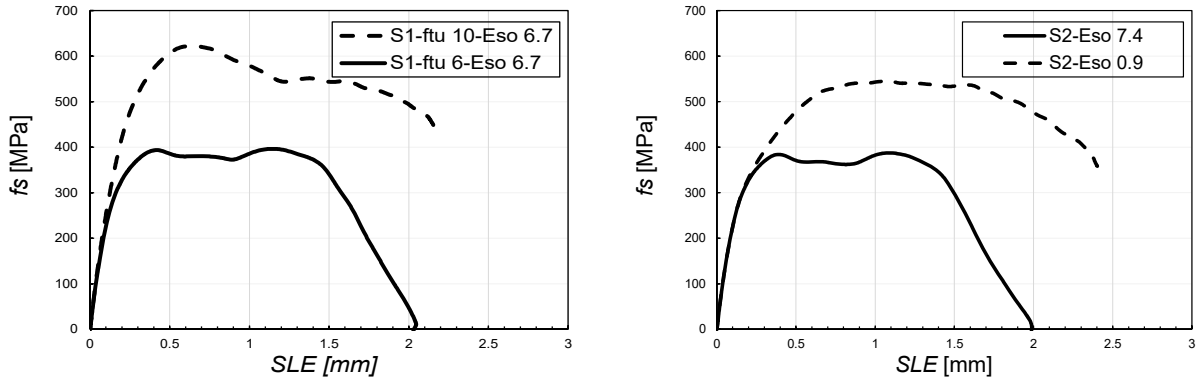

(a) Set 1 (b) Set 2

Figure 5.9 Bar stress-slip curves for the research models

5.3.2 Distribution of bar stress along the rebar embedded length

Figure 5.10 and Figure 5.11 show the amounts of bar stress along the embedded length for several stress levels before the bar stress at failure mode. The following parameter *RA* defines the stress level:

$$RA = \frac{f_s}{f_{s,max}} \tag{5-2}$$

where, f_s is the bar stress for certain stress levels before failure, and $f_{s,\,max}$ is the bar stress at failure. The investigation of stress distribution for various ratio *RA* helps assess the state of changes before the failure mode. The green colour on the curves shows the stress condition at the initiation of the main macro-crack (i.e. $f_{s,\,cr}$), and the red colour shows the stress distribution at failure (i.e. $f_{s,\,max}$).

Nearly all the models show the linear behaviour along the embedded length at *RA* of 0.9 (Figure 5.10a, Figure 5.10b and Figure 5.11a).

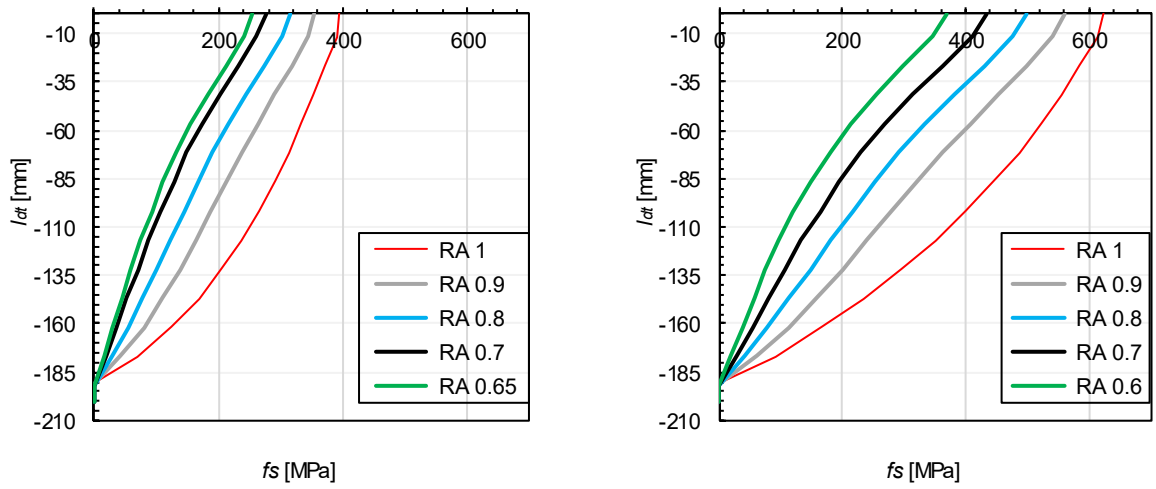

(a) S1-ft,u6-Eso6.7 (b) S1-ft,u10-Eso6.7

Figure 5.10 Bar stress along the embedded length for the two research models of set 1

Nearly all the models show the linear behaviour along the embedded length at *RA* of 0.9. Thus, at this stress level, the linear stress indicated an almost uniform bond distribution (i.e. τ). This can be expressed by:

$$\tau_b = \frac{(f_{s,max}\pi d_b^2)}{\pi d_b l_{dt}} = \frac{f_{s,max} d_b}{4 l_{dt}} \tag{5-3}$$

where, $f_{s,\,max}$ is the bar stress at failure, d_b is bar diameter, and l_{dt} is the embedded length.

Holschemacher et al. (2004; 2006) assumed that in the above equation, the bond stress distributes almost uniformly along the embedded length. So, The assumption of uniform bond stress applies up to a stress corresponding to 90% of $f_{s,max}$. Above that, other mechanisms take place.

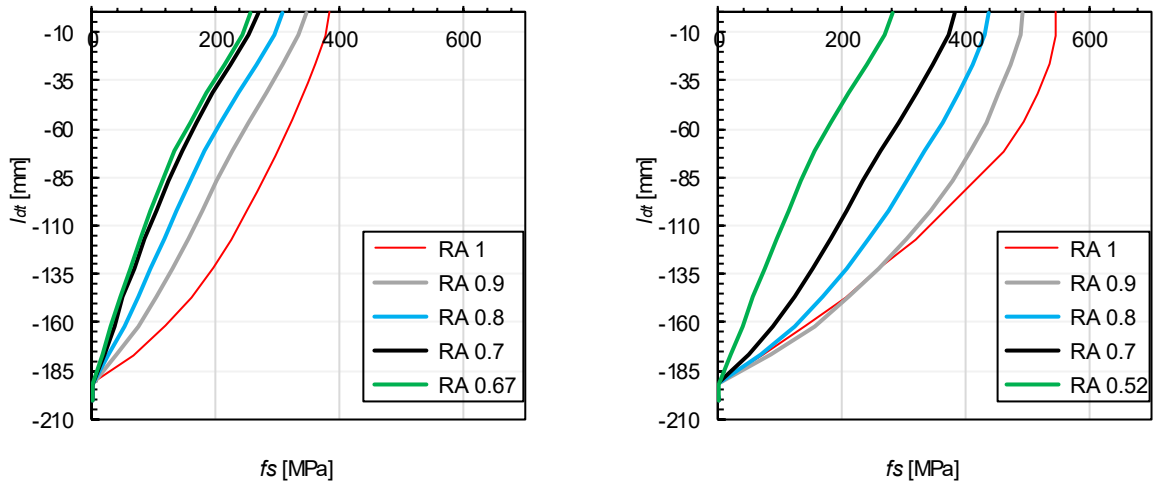

(a) S2-Eso7.4 (b) S2-Eso0.9

Figure 5.11 Bar stress along the embedded length for the two research models of set 2

5.3.3 Distribution of confinement stress along the rebar embedded length

The present section investigates the confinement stress in the failure plane (i.e. S_{11}). Figure 5.12 and Figure 5.15 show S_{11} at several loading stages (i.e., *RA*).

S_{11} distribution for both models in set 1 moves step-by-step from the top to the bottom (i.e. the green curve to the red curve) as shown in Figure 5.12. Figure 5.13 presents the simplified distributions of S_{11} for the loading stage that is equivalent to $f_{s,\,cr}$ (i.e. green curve) and $f_{s,\,max}$ (i.e. red curve) for both models of set 1. This figure indicates that both models at the failure mode present an almost constant stress variation, and their distribution shapes are triangular.

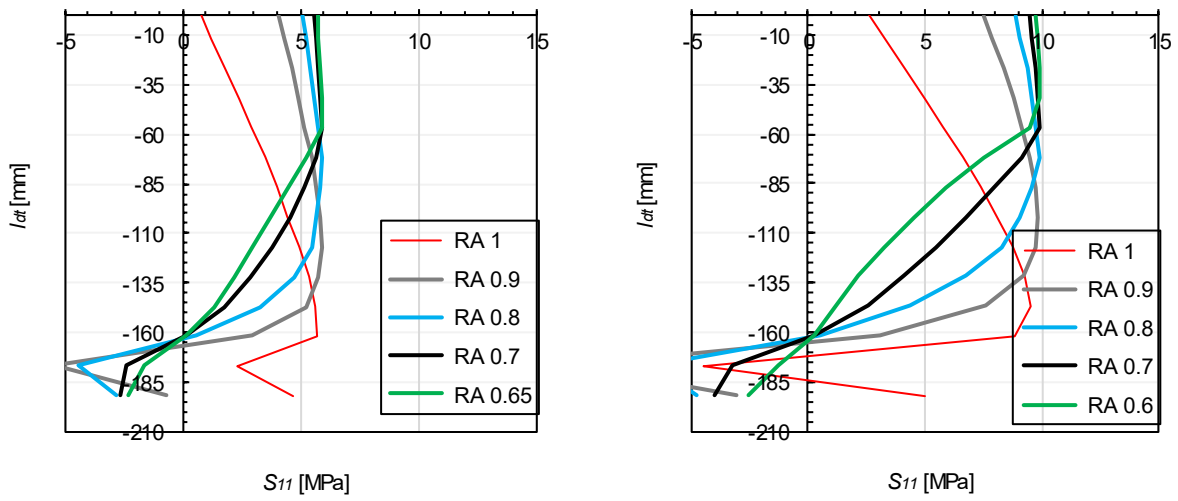

(a) S1-ft,u6-Eso6.7 (b) S1-ft,u10-Eso6.7

Figure 5.12 S_{11} distribution along the embedded length for the two models of set 1

(a) Main macro crack initiation (b) Failure

Figure 5.13 S_{11} simplified distribution along the embedded length for the two models of set 1

Regarding the constant E_{so} in set 1, it seems that for the models that have the same E_{so}, the trend of confinement stress distribution has no changes (Figure 5.14).

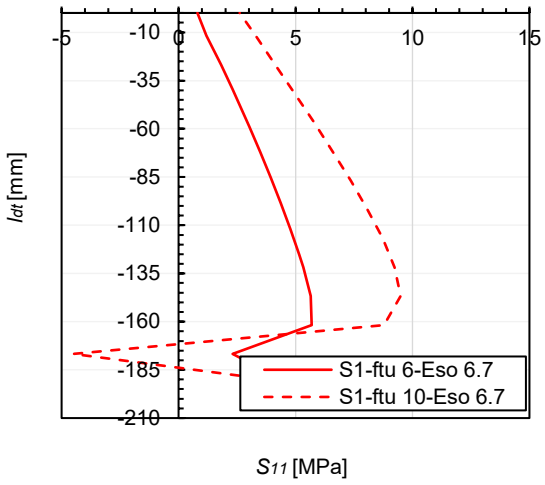

Figure 5.14 Comparison of S_{11} distribution along the embedded length at failure for the two models of set 1

Regarding the confinement force at the failure plane (i.e. F_{11}), one can observe that the forces are maximum at *RA* of 0.9 for both models of set1 (Table 5.2 and Table 5.3).

Table 5.2 Confinement force (S1-ft,u 6-Eso 6.7)

RA	F_{11} (kN)
1	53
0.9	58
0.8	55
0.7	45
0.65	48

Table 5.3 Confinement force (S1-ft,u 10- Eso 6.7)

RA	F_{11} (kN)
1	84
0.9	94
0.8	90
0.7	73
0.6	72

In set 2, S_{11} distribution for the model of S2- Eso 7.4 moves along the bar step-by-step from the top to the bottom, from the green curve to the red curve (Figure 5.15a), while the mentioned distribution is almost uniform for the model S2- Eso 0.9 (Figure 5.15b). Figure 5.16 presents the simplified distribution of S_{11} schematically for the load steps that are equivalent to $f_{s,\,cr}$ (i.e. green curve), $f_{s,\,max}$ (i.e. red curve) for both models of set 2.

It can be observed that S_{11} distribution changes from a triangular shape in model S2- Eso 7.4 to an almost rectangular uniformed shape in model S2- Eso 0.9 at failure (Figure 5.17). Therefore, Chapter 4 results can be interpreted as follows: the post-cracking slope (i.e. E_{so}) changes affect the confinement stress distribution. Indeed by changing E_{so} in the model, the trend of confinement stress distribution has changed

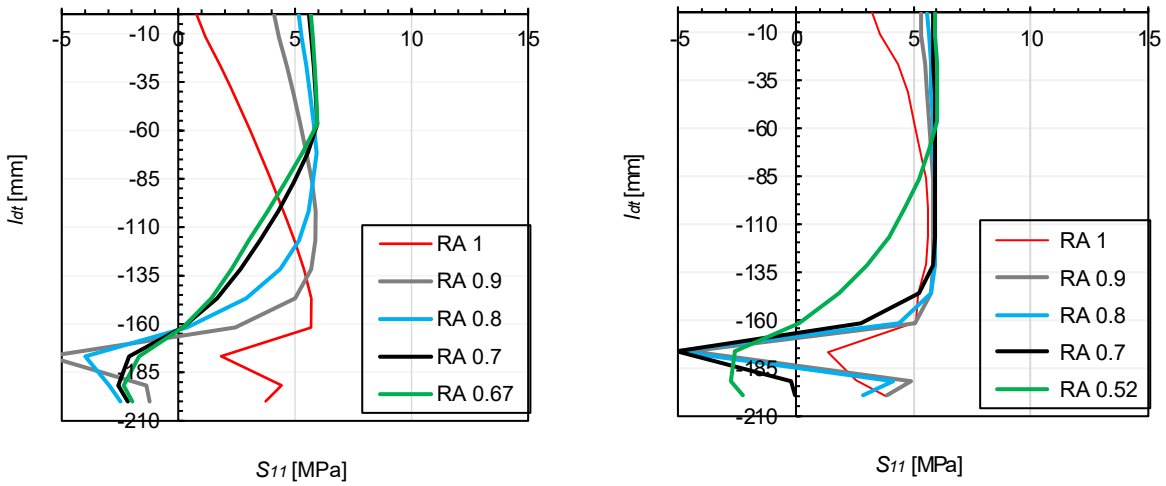

(a) S2- Eso 7.4 (b) S2- Eso 0.9

Figure 5.15 S_{11} distribution along the embedded length for the two models of set 2

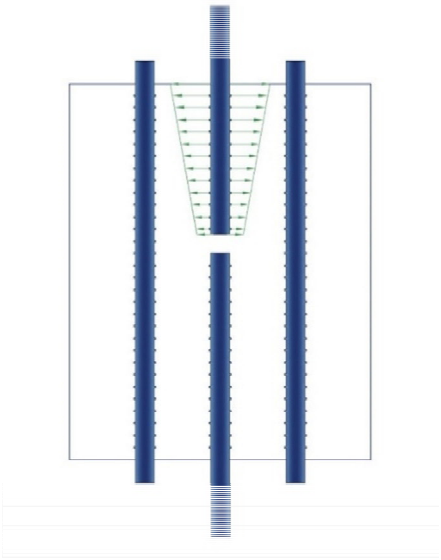

(a) Main macro crack initiation (S2- Eso 7.4)

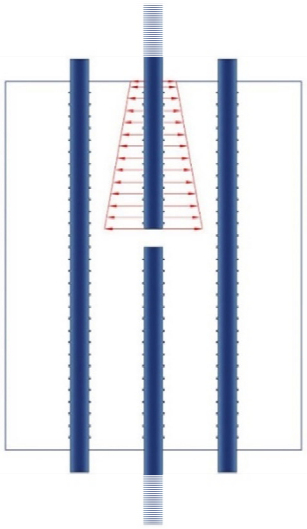

(b) Failure mode (S2- Eso 7.4)

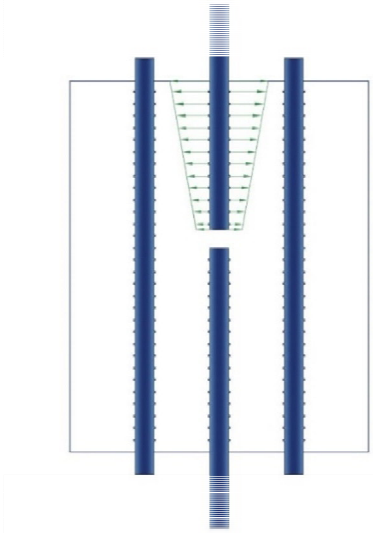

(c) Main macro crack initiation (S2- Eso 0.9)

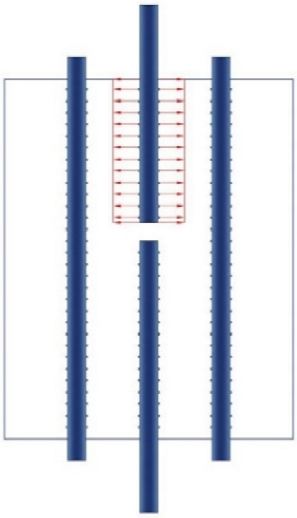

(d) Failure mode (S2- Eso 0.9)

Figure 5.16 S_{11} simplified distribution along the embedded length for the two models of set 2

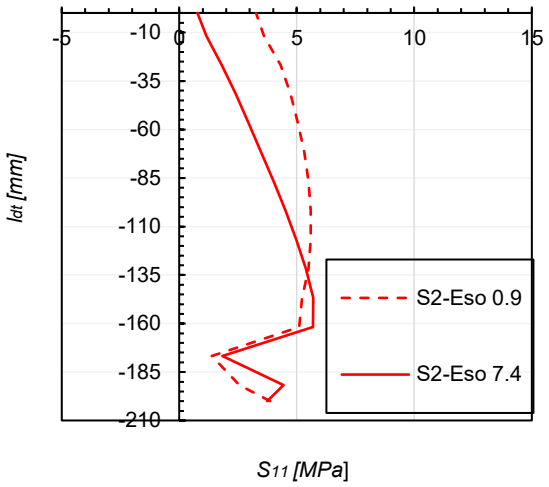

Figure 5.17 Comparison of S_{11} distribution along the embedded length at failure mode for the two models of set 2

Regarding the confinement force at the failure in the direction parallel to the bar plane (i.e. F_{11}), one can observe the same results in set 2 that those obtained in set 1. Given that, the force amplitude is maximum for both models of set 2 at *RA* of 0.9 (Table 5.4 and Table 5.5).

Table 5.4 Confinement force (S2- Eso 7.4)

RA	F_{11} (kN)
1	52
0.9	56
0.8	54
0.7	44
0.67	48

Table 5.5 Confinement force (S2- Eso 0.9)

RA	F_{11} (kN)
1	67
0.9	69
0.8	69
0.7	58
0.52	52

5.3.4 Transverse strain ε_{xx} distribution

Based on estimated observations on strain behaviour on another model similar to the research model of S2-Eso7.4 with the $10d_b$ embedded length, it has been found that transverse strain (i.e. ε_{xx}) distribution from outer surface at 25 mm from the loaded end is very localized. As shown schematically in Figure 5.18, this localization was observed on the width in which the transverse

strain is in tension in the vicinity of the bar for both cases of bar stress at the first crack (i.e. $f_{s,cr}$) and bar stress at the maximum force (i.e. $f_{s,max}$). So, it is highly recommended to consider this localization for obtaining the ε_{tu} from the dog-bone test. The reason is that the strain gauge length on the DTB test is much less than the gauge length of the direct tension test (dog-bone)

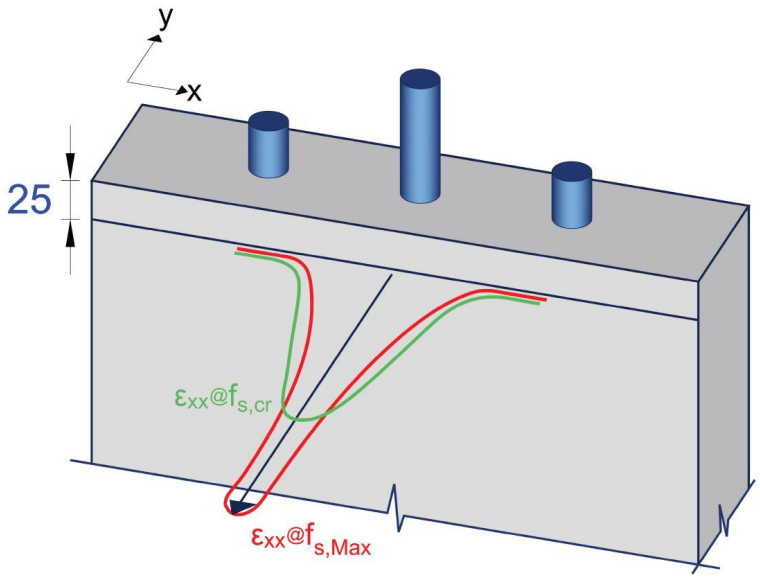

Figure 5.18 Schematic strain ε_{xx} distribution

5.4 Studying the mechanism of confinement stress distribution

This section evaluates the resisting mechanism associated with the confinement stresses. This investigation aims to understand better our model limits and allows us to make a better decision about developing the DTB numerical model.

5.4.1 Research model

The model S2- Eso 7.4 from Chapter 4 was selected in this section to investigate the confinement stresses. Figure 5.19 presents UHPFRC tensile properties of the model. This investigation includes the confinement stresses in both planes of failure (i.e. S_{11}, S_{22}) as well as the anchorage stress (S_{33}).

The stress slip-curve (Figure 5.20) of model S2-Eso 7.4 is characterized by two peaks, the phenomenon also observed in most analytical behaviour. This selection addresses the question related to the second peak and examines the confinement stress mechanism. The stress slip-curve is divided into the five segments (Figure 5.20) as follows:

- Phase I: prior to initiating the main macro-crack (i.e. $f_{s,cr}$).
- Phase II: after initiating the first macro-crack (i.e. $f_{s,cr}$) and before failure (i.e. $f_{s,\,max}$).
- Phase III: after the failure and before the point at minimum stress before the second peak.
- Phase IV: after the minimum stress point and before the second peak.
- Phase V: after the second peak.

This section examines the confinement stresses in various stress ratio *RA* and also at several selected locations on the bar stress-slip curve after the first peak (i.e. $f_{s,\,max}$). The locations are identified as A, B, C, and D (Table 5.6).

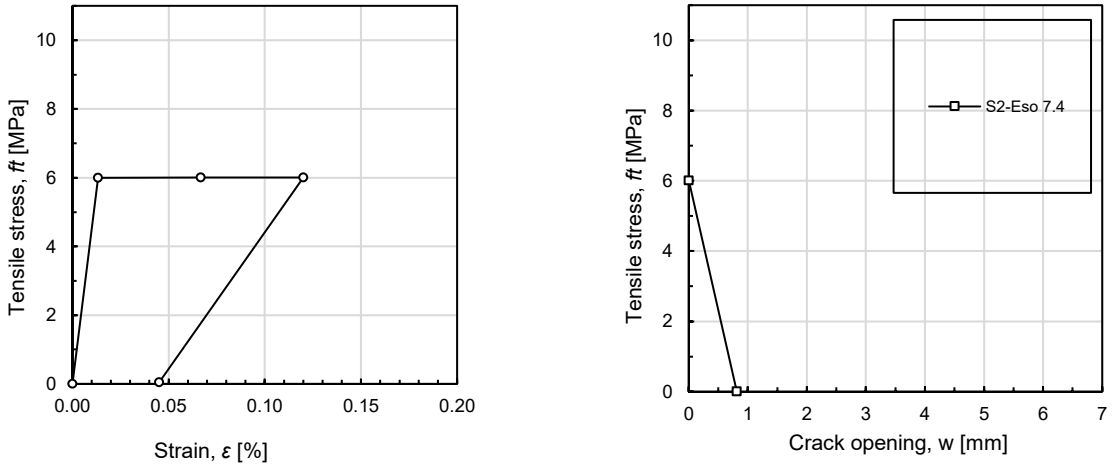

a) Stress-strain response b) Stress-crack-opening response

Figure 5.19 Tensile properties curve of UHPFRC for the model selection

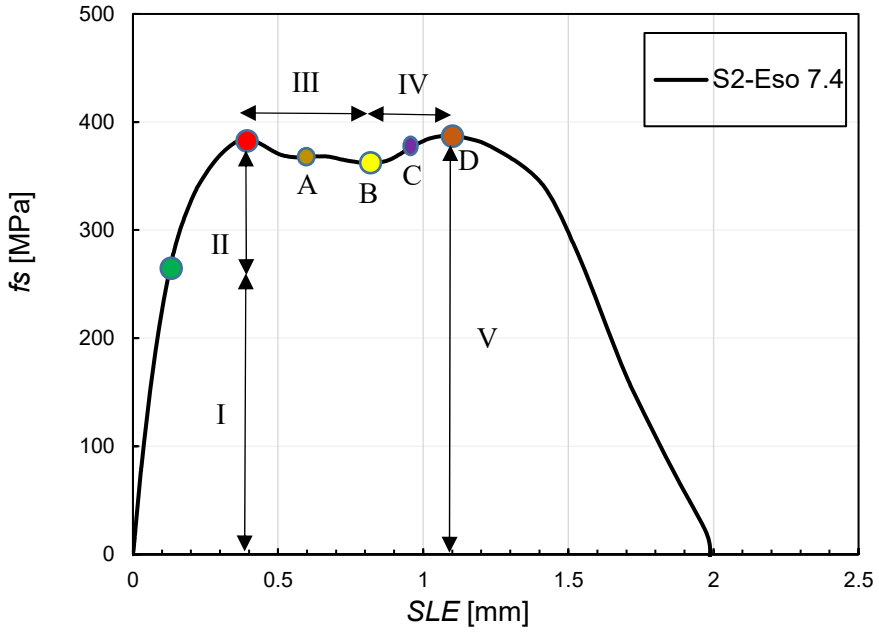

Figure 5.20 Dividing the bar stress-slips curve based on the defined phases (S2- Eso 7.4)

Table 5.6 Nomenclature of the locations after the first peak

Name	Location
A	An approximate location after the first peak and before the minimum stress between two peaks
B	Minimum stress between two peaks
C	An approximate location after minimum stress between two peaks and before the second peak
D	Second peak

5.4.2 Confinement stress distribution at failure plane

The failure plane investigation shows that both S_{11} and S_{33} have increased in phase I (Figure 5.21). In phase II, S_{11} distribution changes and increases while S_{33} decreases (Figure 5.22). In phase III,

we observe that S_{11} decreases while S_{33} goes to the pressure mode (Figure 5.23). In phase IV, S_{11} is almost equal to zero, and S_{33} is in pressure mode (Figure 5.24).

We also observe that the distribution process of S_{11} changes from phase I to phase II. In phase I, the trend distribution is almost constant and triangular. The values begin to increase (Figure 5.21a), while in phase II, S_{11} increases at each loading step from the top to the bottom along the embedded length (i.e. from RA= 0.67 to RA= 1) (Figure 5.22a). In contrast, the distribution trends for S_{33} do not change from phase I to phase II, and the values first increase and then decrease (Figure 5.21b and Figure 5.22b).

While investigating the phases in certain locations of the embedded length, we observe that S_{33} and S_{11} almost approached $f_{t,u}$. equal to 6.01MPa for the present model (i.e. S2- Eso 7.4),

Phase I

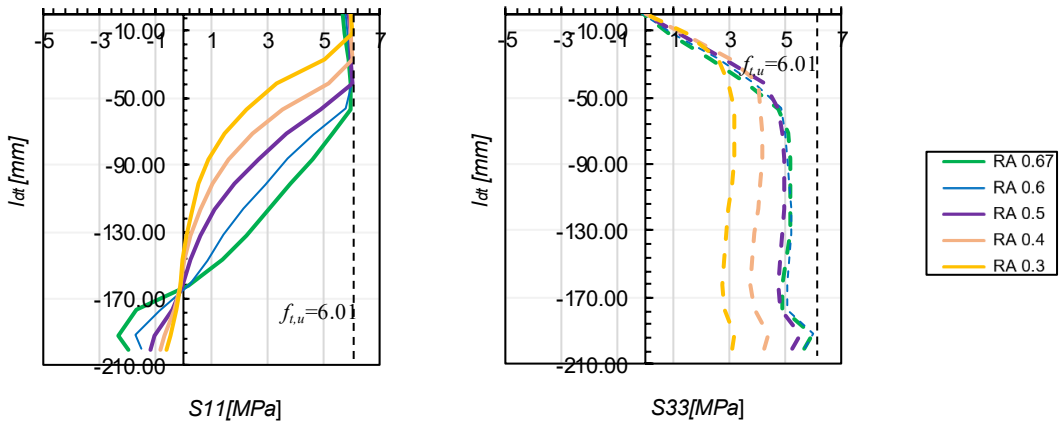

(a) S_{11} distribution (b) S_{33} distribution

Figure 5.21 S_{11} and S_{33} distribution along the embedded length (Phase I)

Phase II

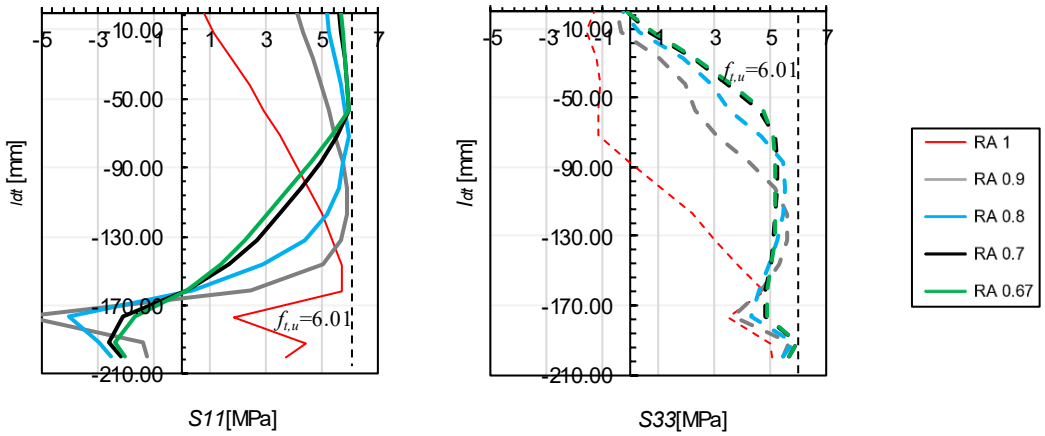

(a) S_{11} distribution (b) S_{33} distribution

Figure 5.22 S_{11} and S_{33} distribution along the embedded length (Phase II)

Phase III

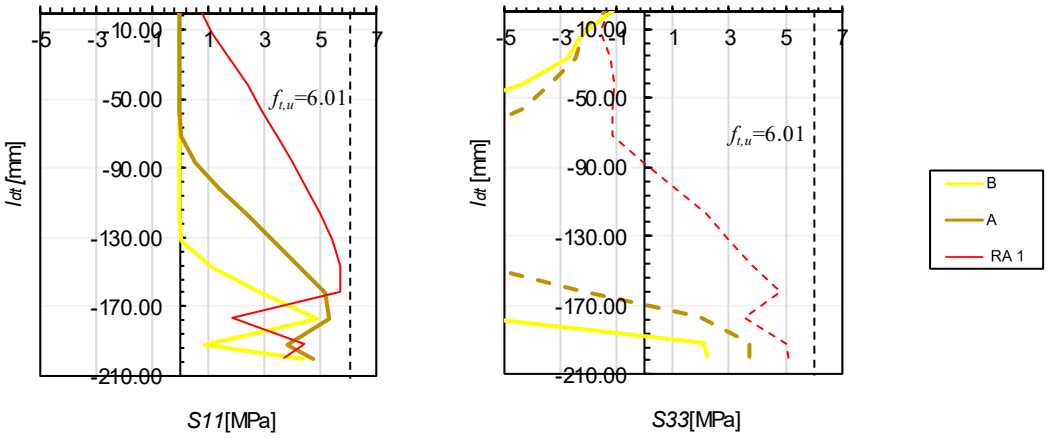

(a) S_{11} distribution (b) S_{33} distribution

Figure 5.23 S_{11} and S_{33} distribution along the embedded length (Phase III)

Phase IV

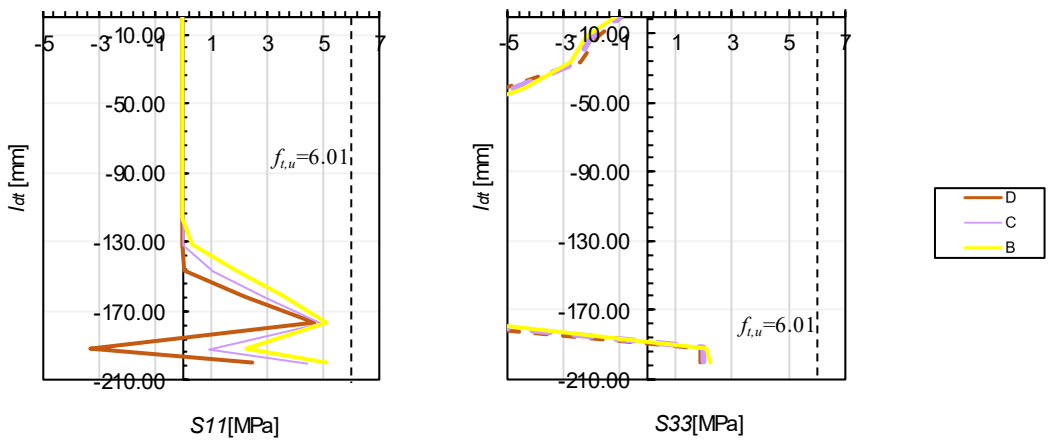

(a) S_{11} distribution (b) S_{33} distribution

Figure 5.24 S_{11} and S_{33} distribution along the embedded length (Phase IV)

5.4.3 Confinement stress distribution at the rebars plane

We have also observed that S_{22} and S_{33} increase in phase I (Figure 5.25). Considering the loading stage $f_{s,cr}$ (i.e. RA=0.67), S_{22} reaches the maximum strength at the top of the embedded length (Figure 5.25a) while S_{33} reaches the maximum strength at the end of the embedded length (Figure 5.25b).

In phase II, the trends of S_{22} increase slowly., except for RA that equals one. In this phase, the trends of S_{33} decrease (Figure 5.26). Figure 5.27 shows that in phase III, S_{22} increases while S_{33} is in the pressure state. Finally, in phase IV, S_{22} increases and reaches the maximum strength in the middle of the embedded length (Figure 5.28a). Moreover, S_{33} is still in the pressure state (Figure 5.28b).

It can be observed that the second peak occurs due to S_{22}. To be specific, after the failure, the model can still develop tensile stress distribution in direction 2 (Figure 5.27a and Figure 5.28a).

Similar to the investigation has done in the failure plane in all phases, we observed that S_{33} and S_{22} almost reached $f_{t,u}$ (i.e. 6.01MPa) in certain locations of the embedded length.

Phase I

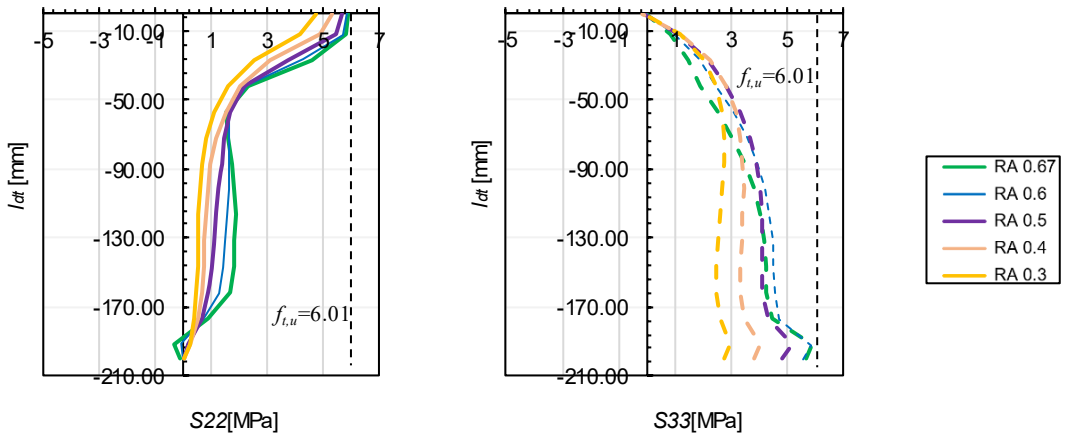

(a) S_{22} distribution (b) S_{33} distribution

Figure 5.25 S_{22} and S_{33} distribution along the embedded length (Phase I)

Phase II

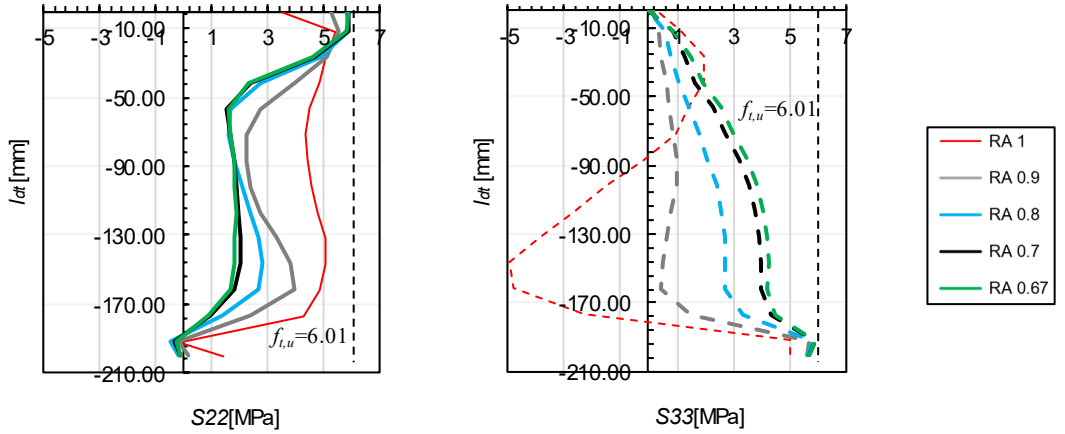

(a) S_{22} distribution (b) S_{33} distribution

Figure 5.26 S_{22} and S_{33} distribution along the embedded length (Phase II)

Phase III

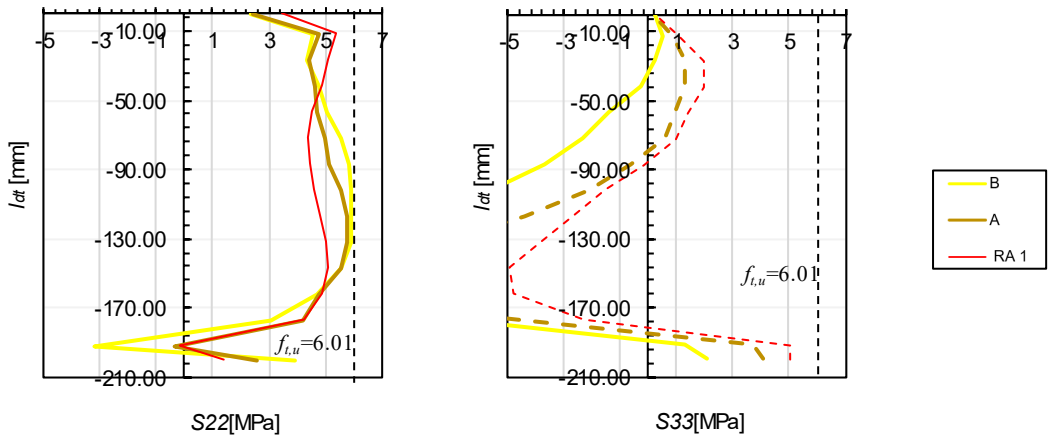

(a) S_{22} distribution (b) S_{33} distribution

Figure 5.27 S_{22} and S_{33} distribution along the embedded length (Phase III)

Phase IV

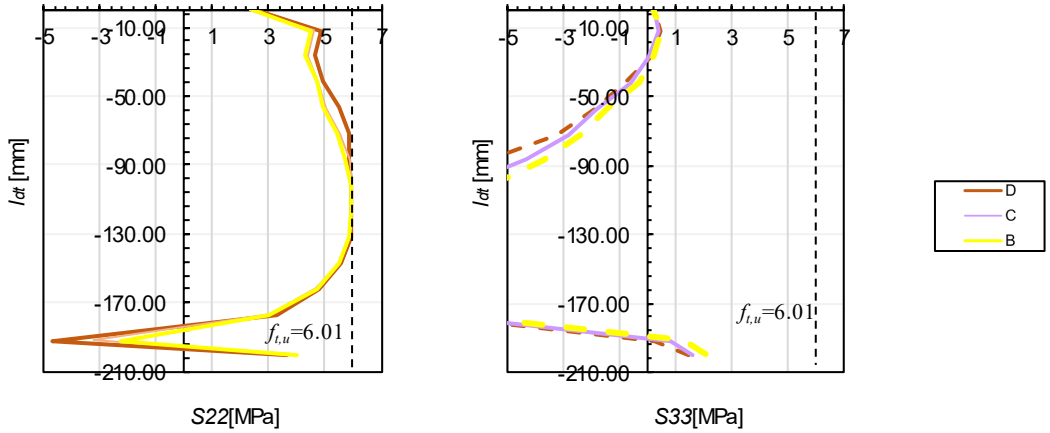

(a) S_{22} distribution (b) S_{33} distribution

Figure 5.28 S_{22} and S_{33} distribution along the embedded length (Phase IV)

5.5 Conclusion

According to the confinement stress distribution, the present chapter intends to review the results obtained in Chapter 4. This study also aims to find the confinement stress distribution mechanism for the investigated DTB test. The following conclusions can be drawn:

- $f_{t,u}$ affects the magnitude of the confinement stress.
- The slope (i.e. E_{so}) changes affect the confinement stress distribution.
- Since the S_{11}, S_{22}, and S_{33} reached the maximum tensile strength (i.e. $f_{t,u}$ = 6.01MPa) in certain locations of the embedded length of the bar, it can be verified that EPM3D performance was adopted for isotropic fibre properties.

Table 5.7 shows the summary of the mechanism of confinement stress distribution of the model S2- Eso 7.4, illustrated in Figure 5.29. All the mentioned confinement stresses in Table 5.7 are started from the origin, and their values equal zero at the origin.

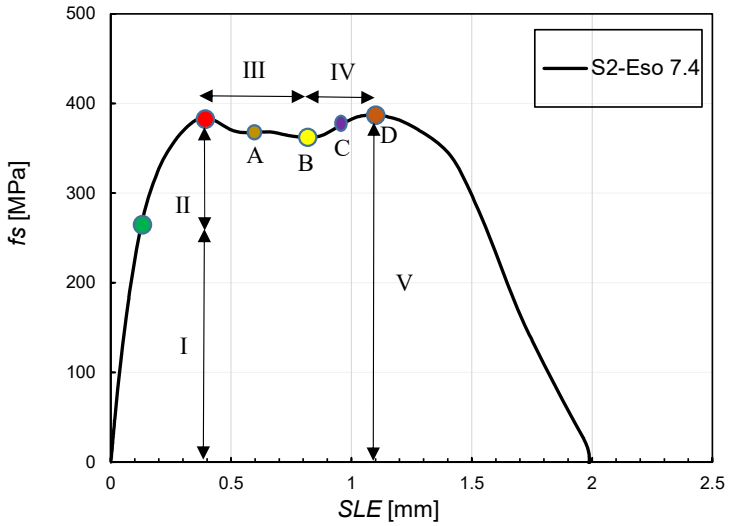

Figure 5.29 Dividing the bar stress-slips curve based on the defined phases (S2- Eso 7.4)

Table 5.7 Summary of the confinement stresses distribution mechanism

	Perpendicular plane		Parallel plane	
Phase	S_{11}	S_{33}	S_{22}	S_{33}
I	+[(1)]	+	+	+
II	+	-[(2)]	+	-
III	-	P[(3)]	+	P
IV	0	P	+	P
V	0	P	-	P

[(1)]+: Increasing the area under the curve (i.e. Confinement stress or Anchorage stress)
[(2)]-: Decreasing the area under the curve (i.e. Confinement stress or Anchorage stress)
[(3)]P: The area under the curve (i.e. Confinement stress or Anchorage stress) is in the pressure state

CHAPTER 6 DEVELOPING THE MODEL BASED ON FIBRES ORIENTATION

6.1 Introduction

6.1.1 Challenges and objectives

As discussed in sections 2.2.4 and 2.3.2, fibre orientation has a significant role in the tensile properties of UHPFRC (Abrishambaf et al., 2017; Delsol et al., 2013; Roy et al., 2017) and therefore on the bond behaviour. The role of splitting cracks in bond failure emphasizes the importance of the tensile properties of concrete cover. Thus, with a rib-scale strategy to simulate the real bond performance, it is essential to consider the fibre orientation effect of UHPFRC cover surrounding the anchored bar in the numerical model.

In the models presented in Chapters 4 and 5, isotropic fibre properties were adopted. Such assumption represents the condition of random fibre distribution, which can be found in actual situations. However, this does not represent the situation of the DTB test carried out by Bastide (2020), in which the fibres were deliberately oriented in the direction perpendicular to the bar axis, as shown in Figure 6.1.

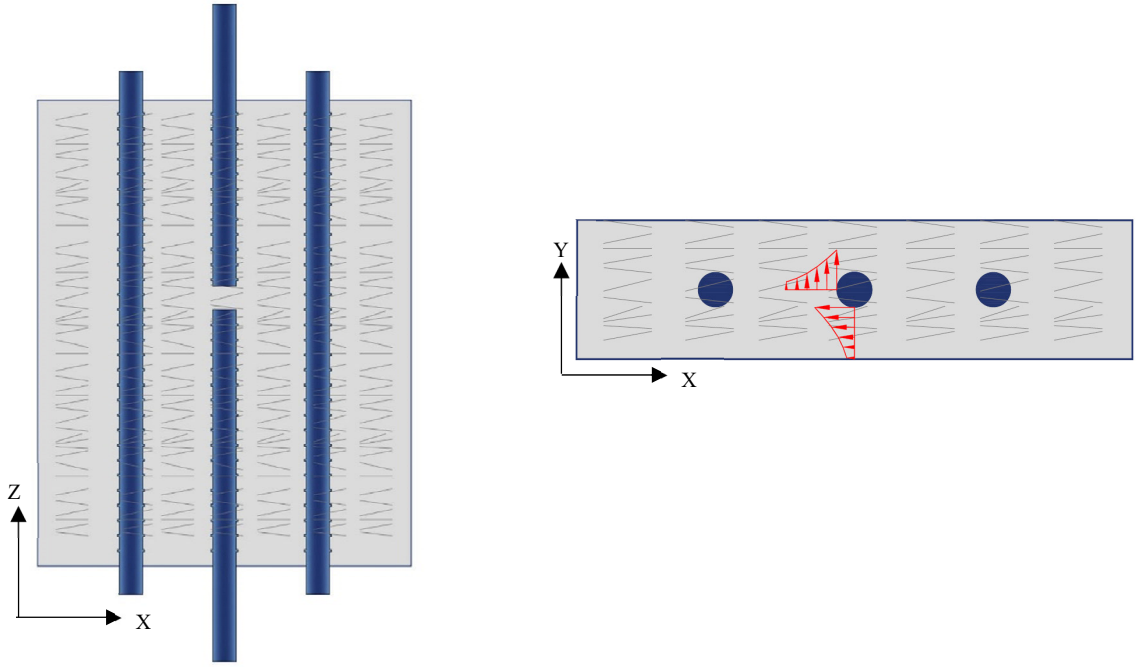

(a) Side view (b) Tensile stresses around the rebar

Figure 6.1 Schematical Orientation of the fibres perpendicular to the bar axis

Consequently, UHPFRC in DTB specimens presents orthotropic tensile properties: in the X direction, the properties are likely to be close to dog-bone test results, while in the Y and Z directions, reduced tensile properties are expected.

The calibration process is an essential step in nonlinear finite element modelling of concrete structures (Ben Ftima and Massicotte 2014). Several assumptions are adopted in UHPFRC, whereas even the determination of the tensile properties is still a scientific debate. The nonlinear analysis must be calibrated to experimental results with well-defined properties. The DTB test specimens with preferential fibre orientation are proper models to fulfill the objective of the calibration. For modelling Bastide's DTB test specimens, two options are possible: 1) introducing orthotropic properties in EPM3D that represent the actual values in the specimens or 2) adopting two sets of properties according to the actual UHPFRC tensile strength where cracking is known to occur. The first option is the preferred solution, but unfortunately, orthotropic tensile properties

for fibre reinforced concrete is not yet implemented in EPM3D. The alternative consists of introducing bands with specific tensile properties.

Nonlinear finite element results obtained by Bastide(2020) for DTB specimens of various shapes identified three regions where cracking occurs. Modified properties would be applied to these regions to calibrate DTB test specimens.

- The perpendicular crack (Figure 6.2a) is in the direction parallel to the fibres. The properties in this direction would likely be similar to the dog bone results. More importantly, the tensile properties in this direction could be adjusted. This direction is associated with S_{11} discussed in the previous chapter. A contribution of this stress component similar to the observation of Chapter 5 is expected in this direction.
- Cracks parallel to the bar plane in Figure 6.2b would form in the plane of the bars. Due to the fibre orientation in DTB specimens, it is expected that a zone with reduced strength and ductility should better represent the actual behaviour along that plane. This direction is associated with S_{22} discussed in the previous chapter. A reduced contribution of this stress component is therefore expected when compared to the conclusions of Chapter 5.
- The horizontal crack at the end of the anchored bar (Figure 6.2a.) develops due to the force transfer from the bar to the concrete. Due to the fibre orientation in DTB specimens, it is expected that a zone with reduced strength and ductility should better represent the actual behaviour. This direction is associated with S_{33} discussed in the previous chapter. A reduced contribution of this stress component is therefore expected when compared to the conclusions of Chapter 5.

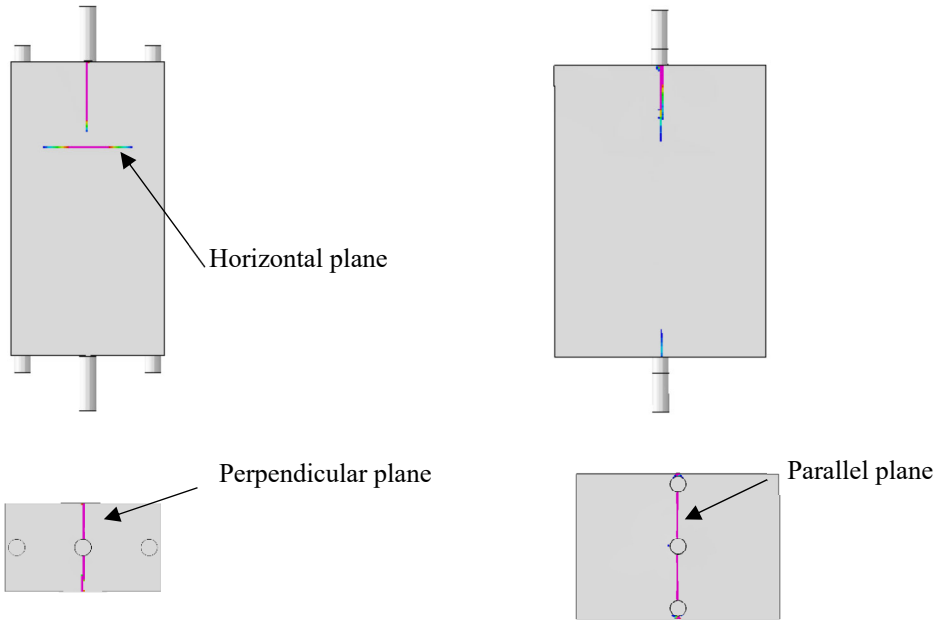

a) Crack in the perpendicular and horizontal planes

b) Crack in the parallel plane

Figure 6.2 Crack planes (Bastide, 2020)

In Chapter 5, a behaviour with two peaks was observed in the analytical results for the bar stress-slip response. Such behaviour was not obtained in Bastide's (2020) test series. Beyond introducing regions with reduced tensile properties, the origin of this discrepancy needs to be identified. Hence, the present chapter intends to investigate the following subjects:

- to develop the existing DTB numerical model with consideration of fibre orientation by introducing weak bands using the current version of EPM3D.
- to confirm the main results of Chapters 4 and 5 with the developed model.
- to validate the experimental program of Bastide's research by the developed model.

6.1.2 Numerical model

In this section, the model S2- Eso 7.4 from Set 2 in chapter 4 was selected to be developed (see section 4.2). The reason for selecting the model is that the mechanism of the model confinement stress was studied in Chapter 5 represents the approximate tensile properties with random fibre orientation, which will allow comparing the impact of fibre orientation. Figure 6.3 and Figure 6.4 present the tensile properties and the bar stress-slip curve, respectively, for the model. All the parameters and the solution strategy selected in Chapter 4 are valid here as well.

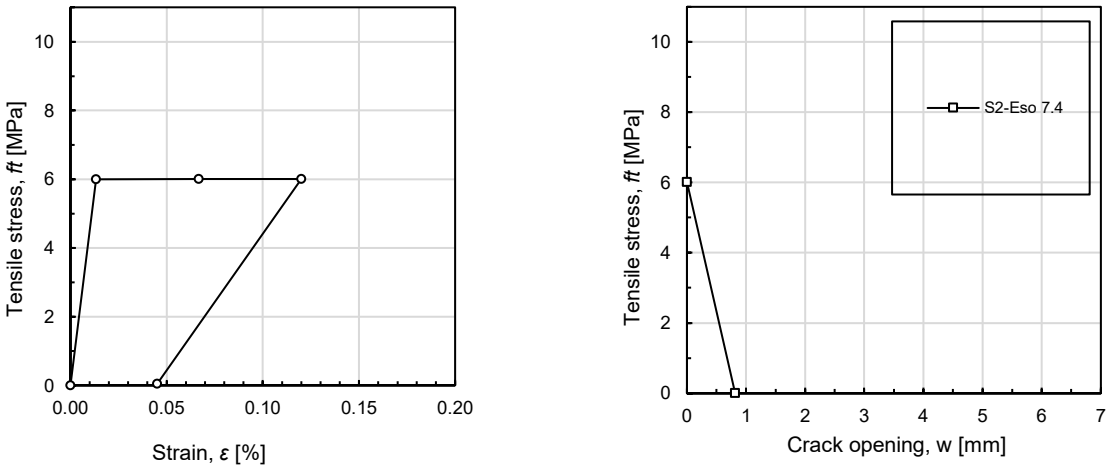

a) Stress-strain response b) Stress-crack-opening response

Figure 6.3 Tensile properties curve of UHPFRC for the numerical model

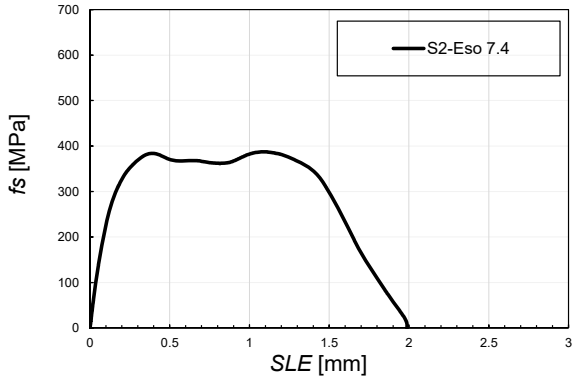

Figure 6.4 Bar stress-slip curve for the model

6.1.3 Reference test

Bastide (2020) tested 12 specimens to investigate the effects of three parameters: the bar embedded length, the cover and the presence of stirrups. The configuration of specimens is similar to the model proposed in the previous sections and is detailed in Figure 6.5. Bastide used #10 high-strength bars (diameter of 32 mm), whereas this model has used adopted 25 mm bars. Although different bar size is selected, all dimensions are defined proportionally with the bar diameter. It is assumed, as observed in the literature, that trends should remain the same.

Bastide specimen #4 was selected as a reference. Its geometry is similar to the models of this thesis. Table 6.1 explains the similarity between the numerical models and the laboratory specimens. Table 6.2 displays the result of tensile properties of UHPFRC from the dog-bone specimen with a 300 mm gauge length and a cross-section of 100 x 50 mm.

Based on Section 5.3.4, this chapter considered 6000 um/m for ε_{tu}. The reason is that the strain gauge length on the DTB test is much lower than the gauge length of the direct tension test (dog-bone).

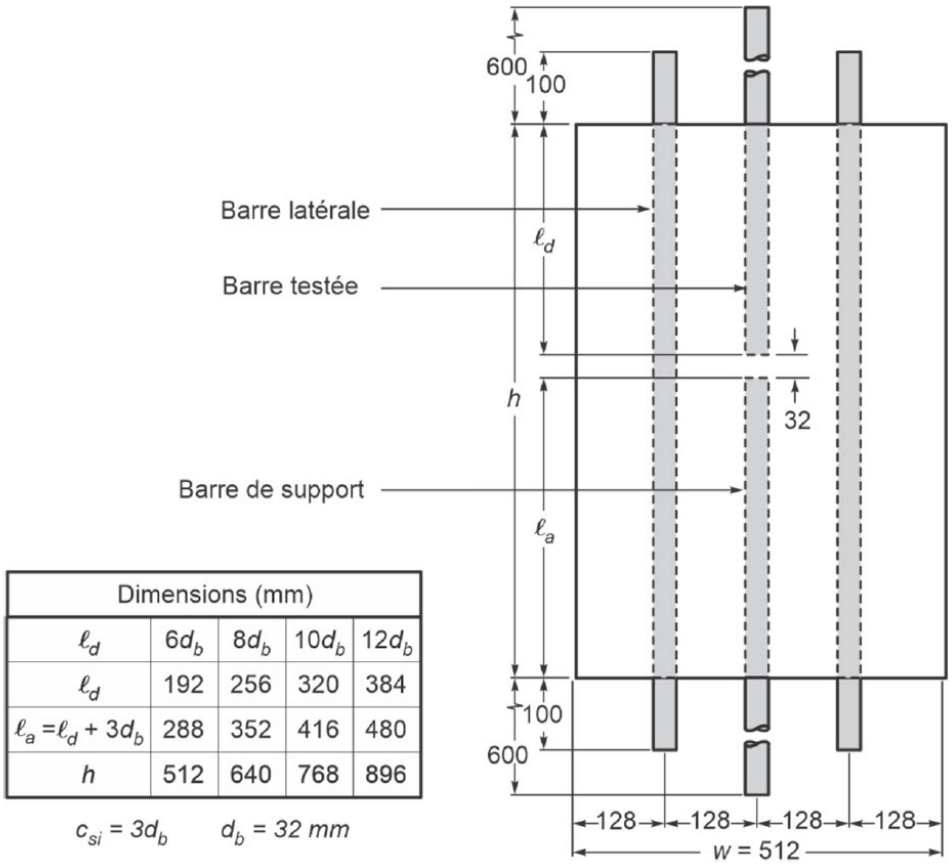

Dimensions (mm)				
ℓ_d	$6d_b$	$8d_b$	$10d_b$	$12d_b$
ℓ_d	192	256	320	384
$\ell_a = \ell_d + 3d_b$	288	352	416	480
h	512	640	768	896

$c_{si} = 3d_b$ $d_b = 32\ mm$

(a) Side view

Dimensions (mm)		
t	128	160
$a = c_{so}$	48	64
$b = c_{so}$	48	64

$c_{si} = 3d_b$ $d_b = 32\ mm$

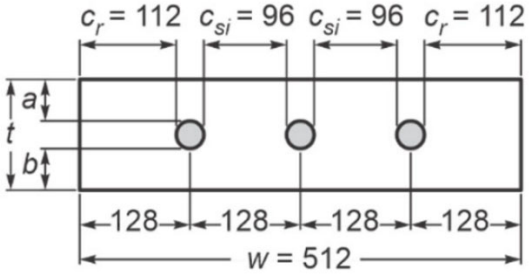

(b) Cross-section

Figure 6.5 DTB specimen geometry (Bastide, 2020)

Table 6.1 Comparison of specimen geometry and steel grades of Bastide (2020) and numerical model

Identification	Anchored and support bars	Lateral bar	d_b (mm)	ℓ_d (d_b)	c_{so} (d_b)	c_{si} (d_b)	c_r (d_b)	h (d_b)	b (d_b)	e (d_b)
Specimen #04	A1035	400W	32	8	1.5	3	3.5	20	16	4
Numerical model	Elastic		25	8	1.5	3	3.5	20	16	4

Table 6.2 UHPFRC tensile properties from dog-bone specimen (Bastide, 2020)

Stress-strain parameters				Stress-crack opening parameters			
$f_{t,el}$ (MPa)	8	$\varepsilon_{t,el}$ (%)	0.025	$f_{w,1}$ (MPa)	11.5	w_1 (mm)	0.2
$f_{t,ts}$ (MPa)	10.6	$\varepsilon_{t,ts}$ (%)	0.055	$f_{w,2}$ (MPa)	8	w_2 (mm)	0.8
$f_{t,u}$ (MPa)	12.325	$\varepsilon_{t,u}$ (%)	0.600	$f_{w,3}$ (MPa)	4	w_3 (mm)	2.0
$E_{t,c}$ (MPa)	21000			f_u (MPa)	0	w_u (mm)	5.5
E_{pc} (MPa)	8767			$G_{f,CO}$ (kJ/ m²)	21.7		
$g_{f,SH}$ (kJ/ m³)	43.7						

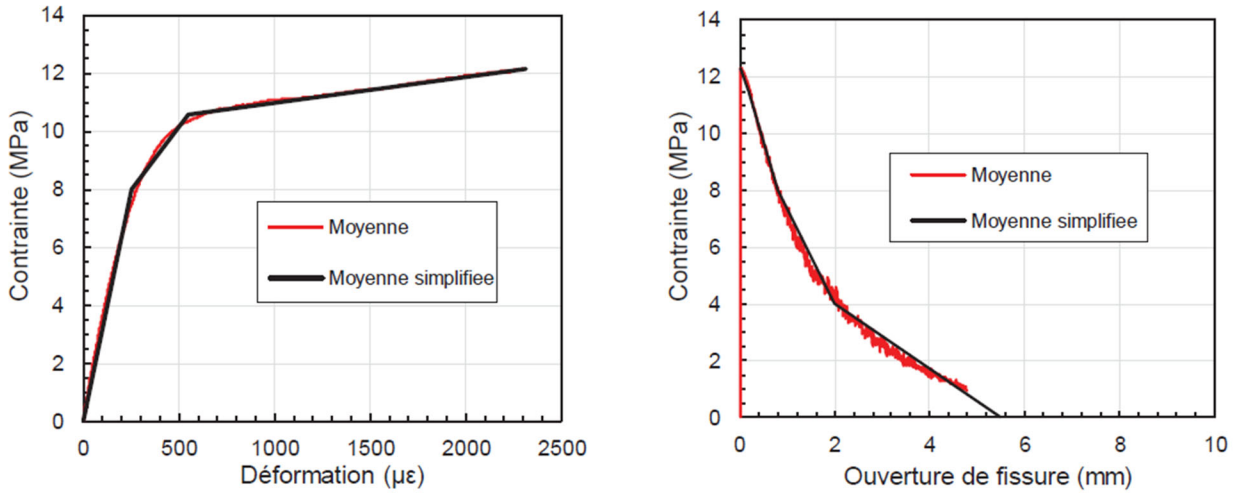

Figure 6.6 Measured direct tensile properties (Bastide, 2020)

The test results are illustrated in Figure 6.7 and Figure 6.8. Figure 6.7 shows that only one peak was observed experimentally, contrary to the model for which two peaks are obtained (Figure 6.4). Figure 6.8 presents the strain and displacements measurement on the specimen vertical faces. In Figure 6.8a, the letter G refers to the strain gauge measurements, whereas the letter P is related to the results of the potentiometer. Additional information on the measurements is presented in section 6.2.2.

It is worth noting that linear elastic behaviour was assumed for the steel, similar to Chapters 4 and 5. The reason is that the tested bar steel of the reference specimen has a yield strength of around 770MPa, which is more than the maximum bar stress (i.e. 480 MPa) presented in Figure 6.7.

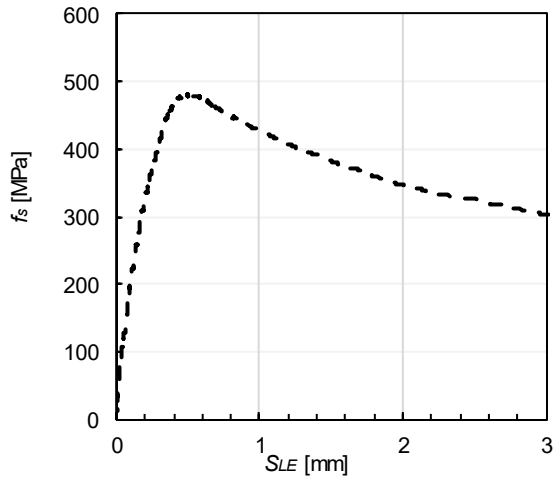

Figure 6.7 Experimental results for the bar stress-slip response (Bastide, 2020)

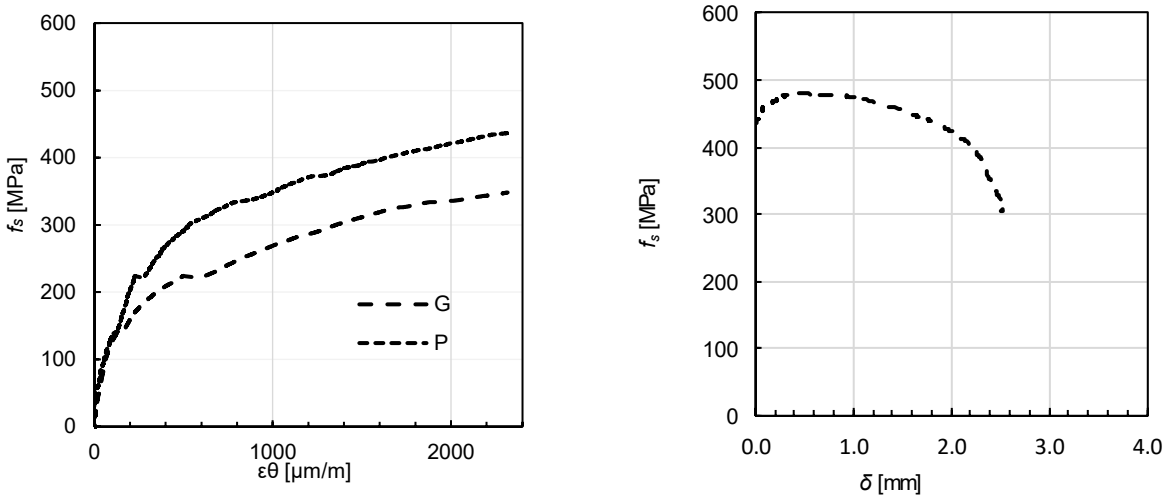

(a) Ortho-radial strain (b) Post cracking measured displacement

Figure 6.8 Reference model behaviour (Bastide, 2020)

6.2 Model development procedure

The present section first explains what conditions must be applied to the numerical model to consider fibre orientation. Second, it describes the additional impact responses that need to be considered in the model, and lastly, it describes the analysis procedure.

6.2.1 Adding weak bands

Two sets of properties were defined based on fibre orientation as an approximate method: 1) the first set corresponds to regions where the fibre orientation are mainly parallel to the governing stress and the regions not directly involved in the bond resisting mechanism, and 2) a second set, called weak band, for regions where fibres are orientated perpendicular to the main tensile stress as described previously. The later regions have been identified in two following locations:

- A plane that has been placed between the anchored bar and the support bar with a thickness equals to one rebar diameter.

- A plane that has been placed at the end of the anchored bar equal to the total cross-section of the specimen with a thickness equals to the sum of the one bar diameter plus two times the mesh size (i.e. 30mm).

These weak bands are highlighted by green in Figure 6.9 and Figure 6.10.

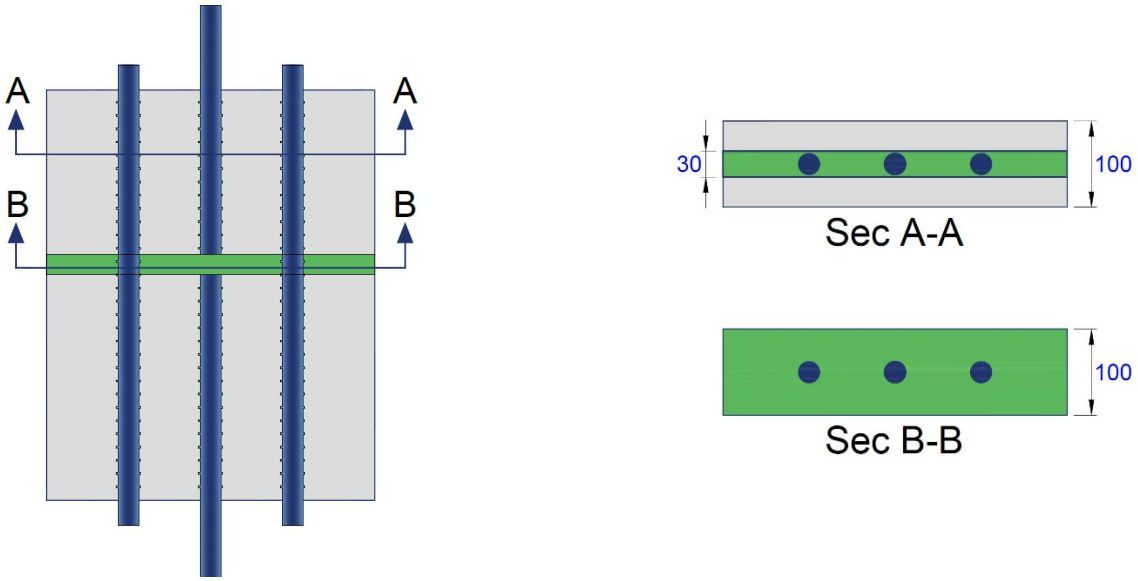

Figure 6.9 Weak bands locations

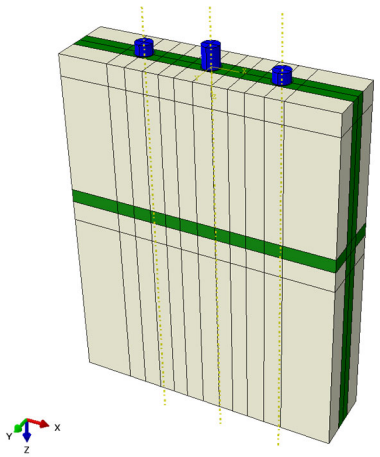

Figure 6.10 Weak bands modelling in the finite element model

It is worth noting that the quality and the size of the mesh around the rebar influenced selecting a width of 30 mm. Indeed, it should have been better to choose a width less than 30 mm, but this was not possible due to the limitations indicated above.

The UHPFRC tensile properties were based on Delsol et al.'s (2013) results for the weak bands. The material properties for the conditions with preferential alignment (0 degrees) reported by Delsol are very similar to those of Bastide (2020), as observed when comparing Figure 6.11. This similarity supports adopting the properties of Delsol at 90 degrees for the weak bands. The maximum tensile strength for unfavourable orientation is chosen around 6 MPa, which is half of the maximum strength with well-orientated fibres. For the softening phase, a value for E_{so} equals 7.4 was selected. Table 6.3 indicates the weak band tensile properties, whereas Figure 6.11 illustrates the alignment of the weak band tensile properties with Delsol et al.'s (2013) results.

Table 6.3 Weak bands tensile properties

Strain-hardening phase							Softening phase	
$f_{t,el}$ (MPa)	$f_{t,ts}$ (MPa)	$f_{t,u}$ (MPa)	E_{pc} (MPa)	$\varepsilon_{t,el}$ (%)	$\varepsilon_{t,ts}$ (%)	$\varepsilon_{t,u}$ (%)	w_u (mm)	E_{so} (MPa/mm)
6	6.005	6.01	45000	0.013	0.014	0.02	0.8	-7.38

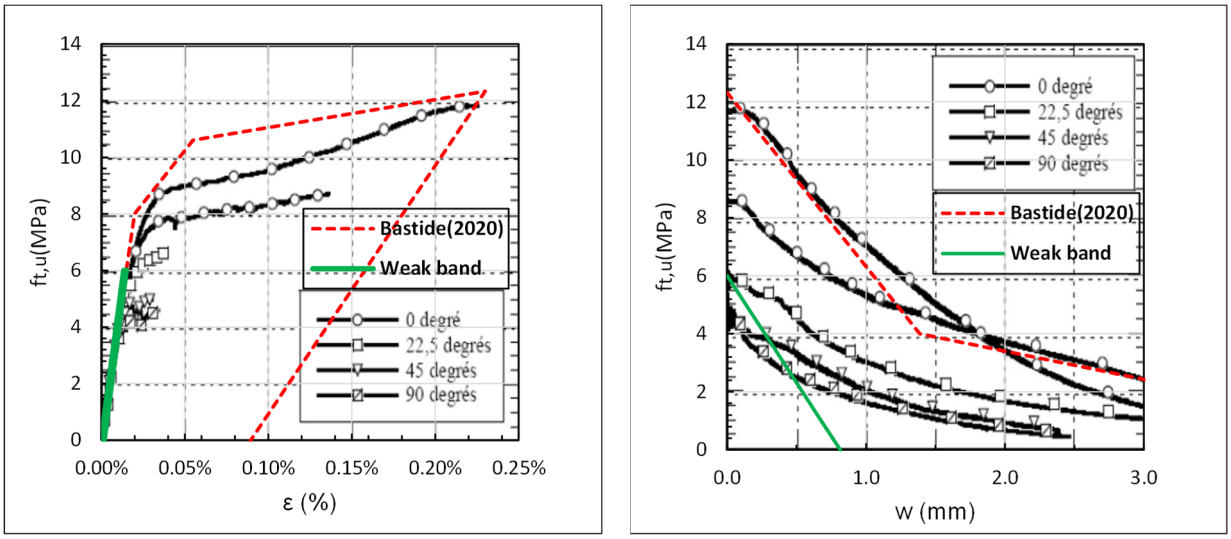

Figure 6.11 Comparison of the dog-bone specimen (Bastide, 2020) and weak bands tensile properties with Delsol (2013) results

6.2.2 Parameters for comparisons between simulations and experiments

We applied the same method described in section 4.3.3 to consider $f_{s,max}$ and $s_{LE\_fs,max}$. As shown in Figure 6.12 for $f_{s,max}$, this section considers the surface elements at the end of the tested rebar. Furthermore, for $s_{LE\_fs,max}$, we modelled four reference points at the border of the intersection of two faces on the concrete and the central node on the tested bar at the beginning of the concrete and bar intersection (Figure 6.12). The details are presented in Table 6.4

In this section, to compare the results of the analytical model with the specimen, two different responses measured by Bastide (2020) are considered: a strain gauge measurement and the relative displacement between the two points. Their locations are in the model are similar to the locations that have been used in Bastide's study (Figure 6.12).

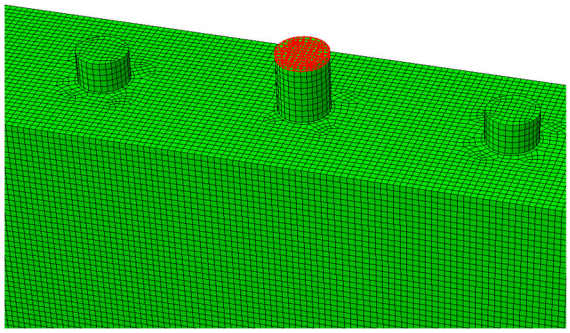

(a) Impact response of the bar stress

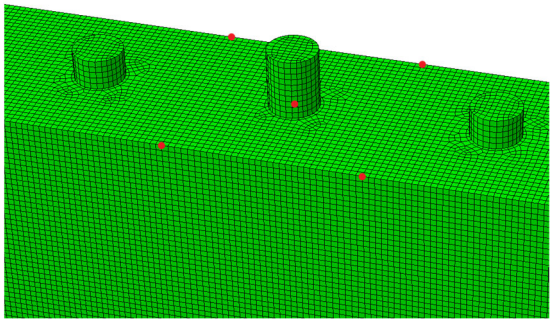

(b) Impact response of the slip

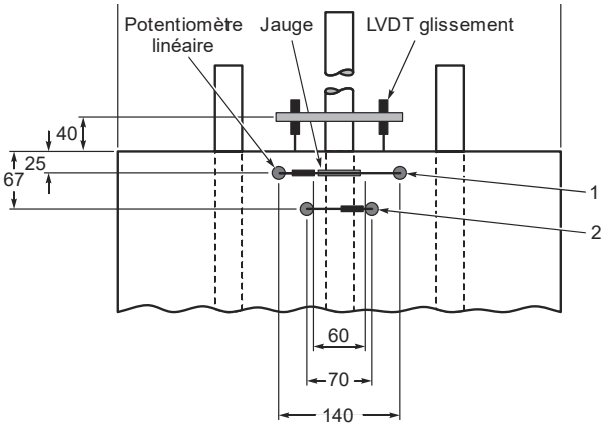

(c) Specimen (Bastide, 2020)

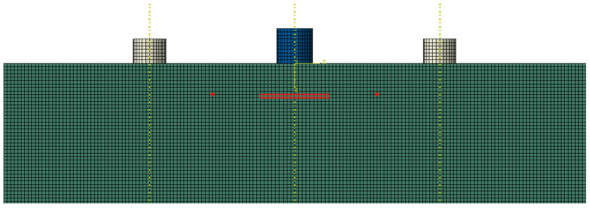

(d) Impact response of the strain and the displacement between two points

Figure 6.12 Response locations

A row of elements with a length of 60 mm, equal to the actual gauge, represents the strain gauge response. The average strain in direction X or direction 11 is determined for these elements (Table 6.4).

Two nodes were selected, precisely at the location indicated in Bastide's study for modelling the potentiometer gauge used in the test. The computed displacement between these nodes is compared to the measured values (Table 6.4).

Table 6.4 The impact responses details

Name of the impact response	Set type	Output type	Output value
Bar stress at maximum force ($f_{s,max}$)	Surface elements	Stress (S33)	Average
Slip at maximum force ($s_{LE\_fs,max}$)	Node	Displacement (U33)	Exact
Strain (εɵ)	A row of elements	Strain (LE11)	Average
Displacement between two points(δ)	Node	Displacement(U1)	Exact

6.2.3 Analysis steps

The adopted analysis approach used a combined strategy of the inverse analysis and trial and error process to develop the numerical model. Several models with different parameters were evaluated to comply with the observed experimental behaviour. The selected parameters are the concrete shrinkage, the concrete-steel friction along the bar, and all UHPFRC tensile properties. For each model, the bar stress-slip behaviour was compared to the specimen response, and then the decisions were made to apply the new parameters for the new models. The models can be divided into six groups based on the following steps:

- Step 1: Influence of shrinkage
- Step 2: Influence of the concrete bar friction
- Step 3: Influence of pre-peak properties of UHPFRC
- Step 4: Influence of the hardening tensile properties
- Step 5: Influence of the softening tensile properties
- Step 6: Influence of the unloading modulus

Before going into each step details, it worth mentioning that this section considers three types of models based on adding the weak bands (Figure 6.13). Indeed, the weak bands have been introduced step-by-step to follow their impacts on global behaviour. Type A model considers the model before introducing the weak bands. For the type B model, weak bands were placed between the anchored bar and the support bar. In the type C model, all the weak bands were introduced.

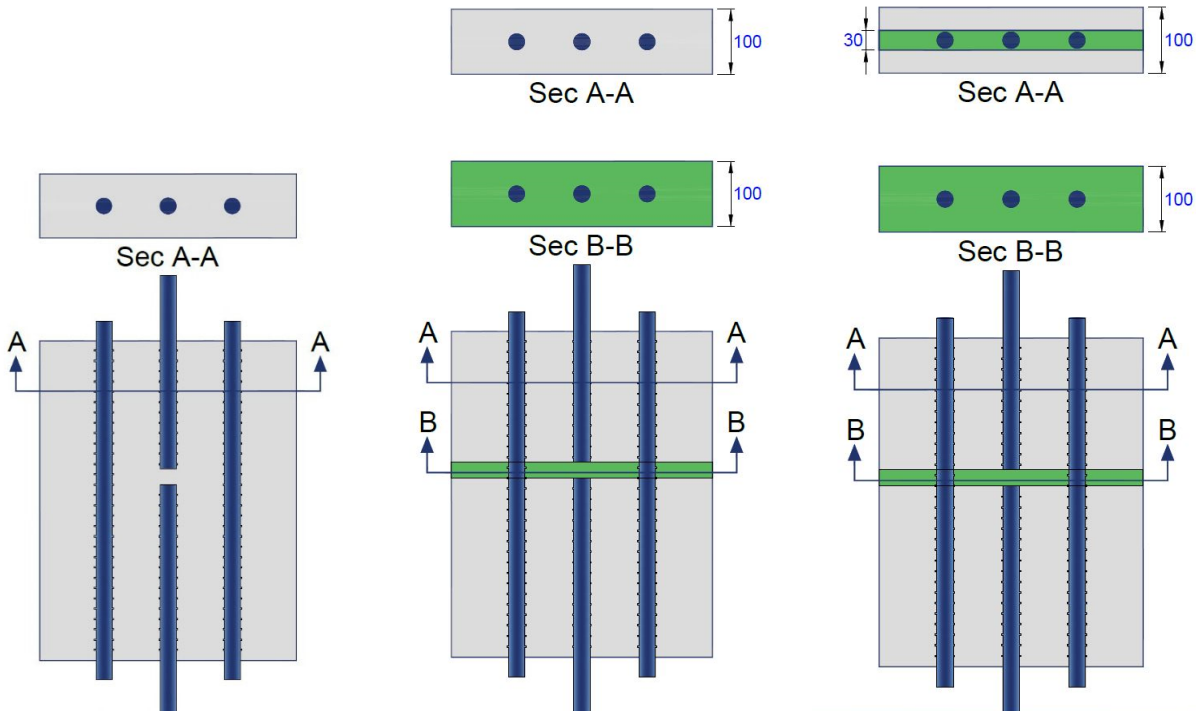

(a) Type A (b) Type B (c) Type C

Figure 6.13 Model types based on adding weak bands

6.2.3.1 **Step 1: Influence of shrinkage**

UHPFRC presents high autogenous shrinkage. The restraining effects of bars or a rigid interface generates internal tensile stresses in the concrete and compressive stresses into the bars that could affect the bond performance. So, unlike the models of Chapter 4 and 5, an additional step was introduced to simulate the shrinkage. The shrinkage target value is -480 micro-strains based on the tests carried out by Lagier (2015). The shrinkage is modelled in ABAQUS by applying a uniform temperature reduction to the concrete volume only. A temperature of −40 ˚C, and a thermal expansion coefficient of 12.10^{-6}, are applied through a Smooth Step, similar to the imposed displacement. Test #11 represents this step in Table 6.5 and Table 6.6. In these tables, the research model is displayed with number #1. As indicated in Table 6.6, model Type A was used as the first try (Figure 6.13a).

6.2.3.2 **Step 2: Influence of the concrete bar friction**

Although concrete-bar friction plays a small role in bond strength compared to the rib bearing, this step investigates the impact of the parameter on the bar stress-slip curve behaviour. This parameter was selected to investigate the effect of the compression stress that forms at the end of the anchored bar (see Figure 5.15) with the splitting crack propagation and may contribute to increasing the bar anchorage force. Two tests were done: one with friction (i.e. Test #77) and another for which friction is ignored (i.e. Test #7) (Table 6.5). Model Type B was used in this step (Figure 6.13b). The friction parameter was not considered for the next steps. The reason for ignoring the friction parameter is discussed in the results section.

UHPFRC tensile properties that have been used in these two steps are presented in Figure 6.14 and Table 6.6.

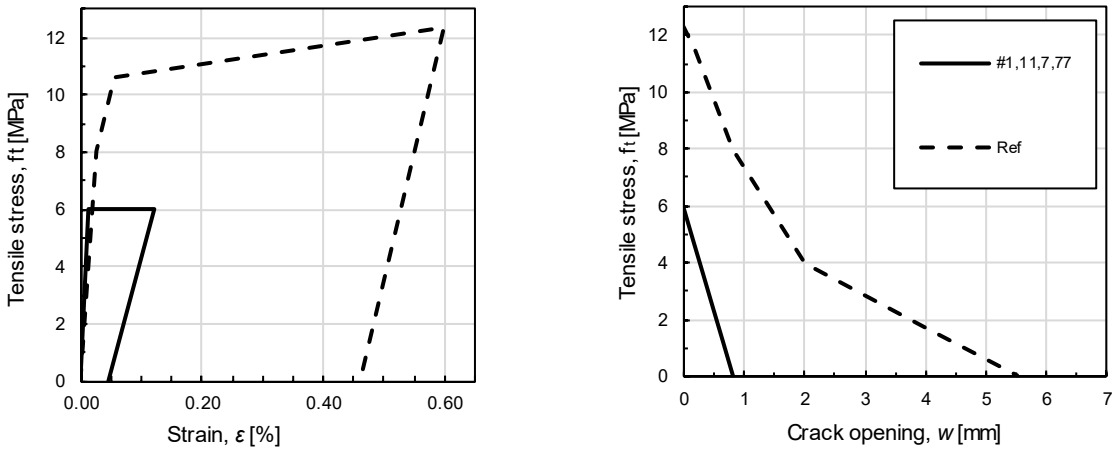

(a) Strain hardening response (b) Crack-opening response

Figure 6.14 UHPFRC tensile properties for the reference model, step 1 and step 2

6.2.3.3 **Step3: Influence of pre-peak properties of UHPFRC**

This step aims to monitor the bar stress-slip curve behaviour for different $f_{t,u}$ values. Three tests were done (i.e. test #8, #9 and #10). From this step forward, we applied all the weak bands and

used Model Type C (Figure 6.13c). The tensile properties are presented in Figure 6.15 and Table 6.6. We considered E_{so} constant during the step regarding the importance of the post-peak slope.

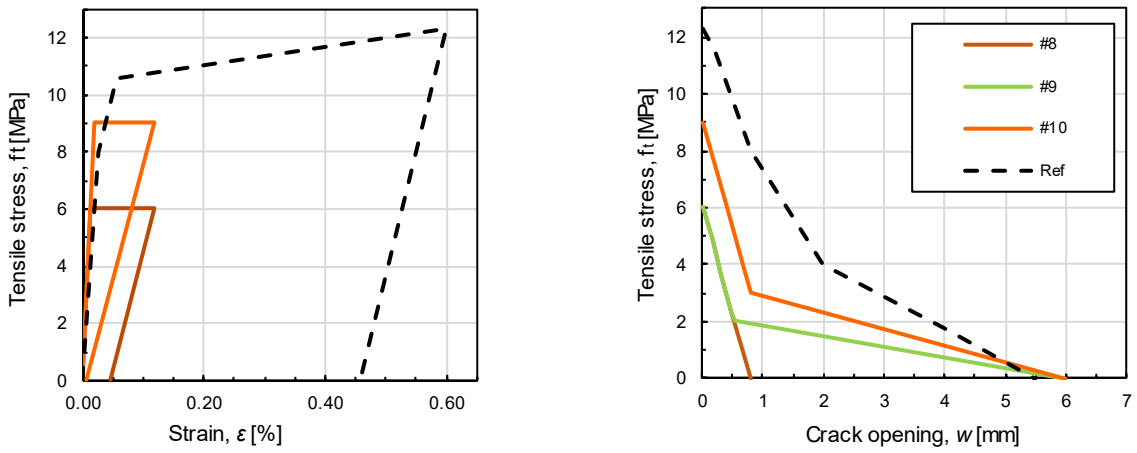

(a) Strain hardening response (b) Crack-opening response

Figure 6.15 Comparison of UHPFRC tensile properties for the reference test and third step tests

6.2.3.4 **Step 4: Influence of the hardening tensile properties**

Tests #12, #13 and #14 have been examined to monitor the hardening phase (Figure 6.16). The $f_{t,u}$ and the softening phase are considered constant in this step (Table 6.5 and Table 6.6).

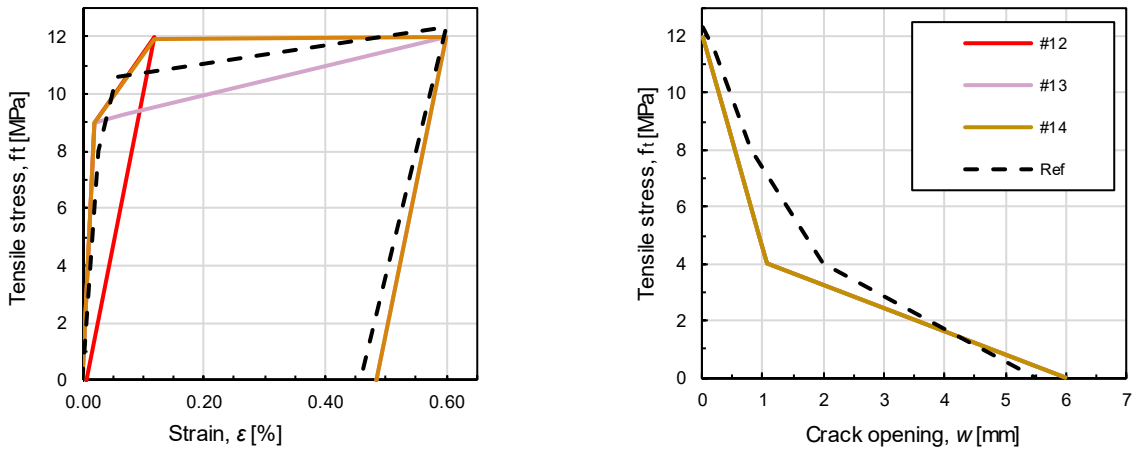

(a) Stress-strain hardening response (b) Stress-crack-opening response

Figure 6.16 Comparison of UHPFRC tensile properties for the reference model and fourth step tests

6.2.3.5 **Step 5: Influence of the softening tensile properties**

Test #15 was performed to evaluate E_{so}. Although a bilinear curve was selected in the softening phase, the curve was chosen as close to the reference test. The hardening part was selected according to the previous test (i.e. #14). Figure 6.17, Table 6.5 and Table 6.6 indicate the present stage.

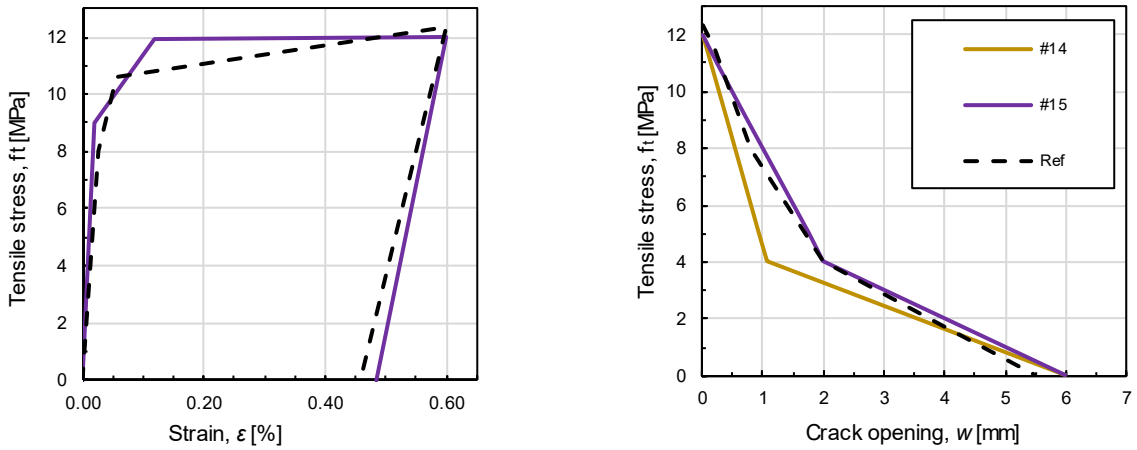

(a) Stress-strain hardening response (b) Stress-crack-opening response

Figure 6.17 Comparison of UHPFRC tensile properties for the fifth step tests

6.2.3.6 **Step6: Influence of the unloading modulus**

Test #16 was done to investigate the impact of E_p on the global behaviour. This test has the same softening phase as test #15, and in the hardening phase, only E_{pc} was changed (Table 6.5, Table 6.6 and Figure 6.18).

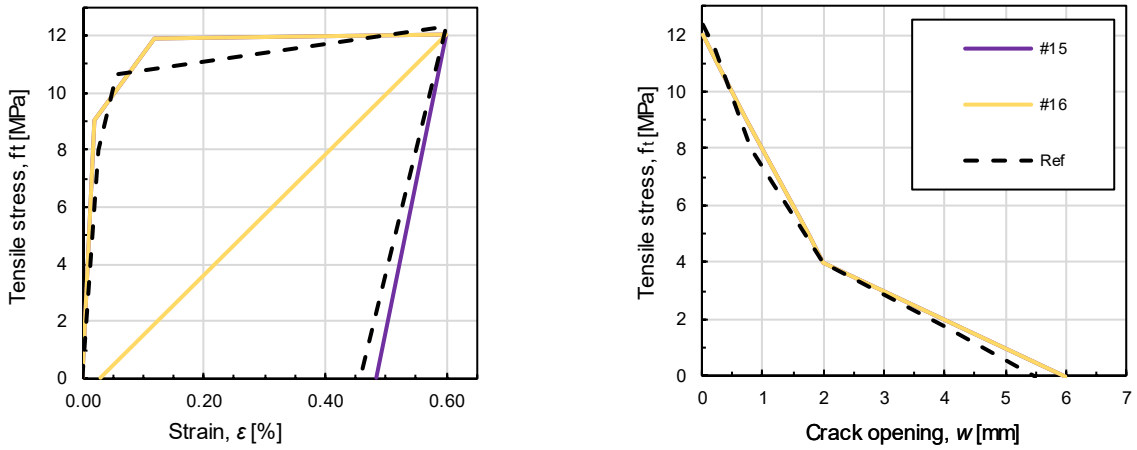

(a) Stress-strain hardening response (b) Stress-crack-opening response

Figure 6.18 Comparison of UHPFRC tensile properties for the sixth step

The summary of all the steps is presented in Table 6.5 and Table 6.6. These are the steps that were considered during the trial-and-error strategy. Test #1 represents the numerical reference model.

6.5 Summary of the steps' details based on the impact of shrinkage and friction

Step	Test	Shrinkage impact	Friction impact
1	#1	NC	C
	#11	C	C
2	#7	C	NC
	#77	C	C
3	#8	C	NC
	#9	C	NC
	#10	C	NC
4	#12	C	NC
	#13	C	NC
	#14	C	NC
5	#15	C	NC
6	#16	C	NC

C: Considered

NC: Not considered

Table 6.6 Summary of the step details based on the model type and tensile properties

Step	Test	Model type	Hardening phase							Softening phase			
			$f_{t,el}$ (MPa)	$f_{t,ts}$ (MPa)	$f_{t,u}$ (MPa)	E_{pc} (MPa)	$\varepsilon_{t,el}$ (%)	$\varepsilon_{t,ts}$ (%)	$\varepsilon_{t,u}$ (%)	$f_{w,1}$[4] (MPa)	w_1[5] (mm)	w_u (mm)	E_{so}[6]
1	#1	A[1]	6	6.005	6.01	8013	0.013	0.067	0.12	-	-	0.8	7.38
	#11	A	6	6.005	6.01	8013	0.013	0.067	0.12	-	-	0.8	7.38
2	#7	B[2]	6	6.005	6.01	8013	0.013	0.067	0.12	-	-	0.8	7.38
	#77	B	6	6.005	6.01	8013	0.013	0.067	0.12	-	-	0.8	7.38
3	#8	C[3]	6	6.005	6.01	8013	0.013	0.067	0.12	-	-	0.8	7.38
	#9	C	6	6.005	6.01	8013	0.013	0.067	0.12	2	0.5	6.0	7.38
	#10	C	9	9.005	9.01	8013	0.020	0.067	0.12	3	0.8	6.0	7.38
4	#12	C	9	10.4	12	10500	0.020	0.067	0.12	4	1.1	6.0	7.38
	#13	C	9	9.24	12	10500	0.020	0.067	0.60	4	1.1	6.0	7.38
	#14	C	9	11.9	12	10500	0.020	0.120	0.60	4	1.1	6.0	7.38
5	#15	C	9	11.9	12	10500	0.020	0.120	0.60	4	2.0	6.0	4
6	#16	C	9	11.9	12	2100	0.020	0.120	0.60	4	2.0	6.0	4

[1] Model Type A: No weak band
[2] Model Type B: Weak band at loaded end
[3] Model Type C: All required weak band included
[4] $f_{w,1}$: Tensile stress at the junction of two lines for bilinear curves
[5] w_1: Crack opening at the junction of two lines for bilinear curves
[6] *pp:* The beginning slop of softening phase for bilinear curves

6.3 Results and validation

This section presents the results from three measurements: the global behaviour characterized by bar stress-slip curve, the bar stress-strain curve, and the bar stress- displacement curve between two points. The last two ones are discussed after step 3.

6.3.1 Summary table and failure mode

Table 6.7 presents a summary of all tests. Regarding the quasi-static criteria in section 3.2.3, the total Kinetic Energy ratio to the Entire Internal (i.e. E_k / E_i) remained below 5% at the onset of the main macro-crack and during the failure mode. Between the failure mode and post-peak stress equal to 0.85 $f_{s,max}$, the ratio still stayed below 5%. It means that the quasi-static analysis assumption

is acceptable. Moreover, for all tests, the failure mode was a by splitting in the direction perpendicular to the bar plane, similar to the reference test.

Table 6.7 Summary of the step results

Step	Test	Failure mode	$f_{s,\,max}$ (MPa)	s_{LE_fsmax} (mm)	$\delta_{\_fsmax}$ (mm)
	Ref[1]	PS[2]	480	0.51	0.53
1	#1	PS	385	0.39	-
	#11	PS	324	0.35	-
2	#7	PS	306	0.35	-
	#77	PS	330	0.37	-
3	#8	PS	295	0.34	-
	#9	PS	350	1.19	-
	#10	PS	397	0.45	-
4	#12	PS	481	0.57	0.63
	#13	PS	504	0.61	0.69
	#14	PS	488	0.59	0.66
5	#15	PS	534	0.76	1.00
6	#16	PS	526	0.77	1.07

[1]Ref: Reference test #4
[2]PS: Perpendicular splitting

6.3.2 Bar stress-slip curve behaviour

All the bar stress-slip curves of the tests are presented in Figure 6.19.

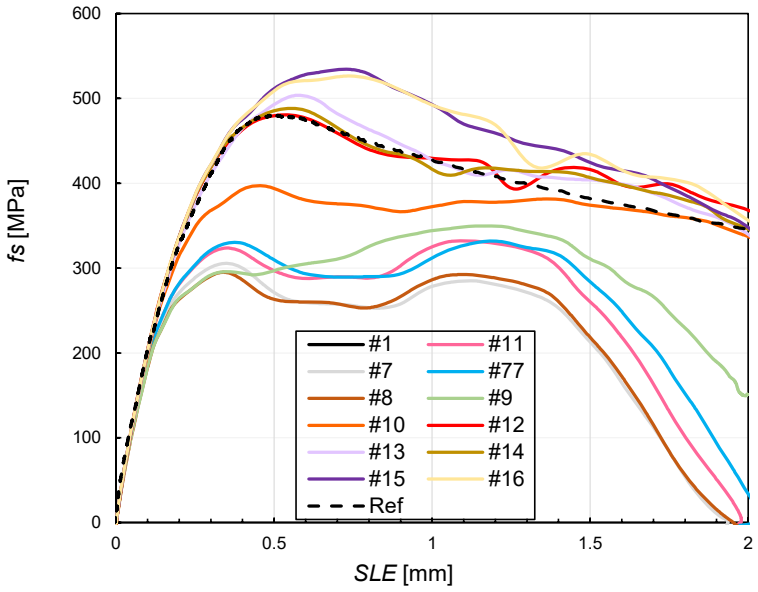

Figure 6.19 Bar stress-slip curves of all tests

In the first step, by comparing the curves of test #1 (no shrinkage) and test #11 (with shrinkage), the shrinkage has the effect of shifting the curve of test #1 downward (Figure 6.20a). This offset corresponds to 15% of $f_{s,max}$ for model (i.e. #1) (Table 6.7).

Friction affects the behaviour after the first peak when comparing test curves of # 7 (without friction) and # 77 (with friction) (Figure 6.20b). Indeed, eliminating the friction caused a decrease in the second peak compared to the first one. A review of the bar stress slip curves published in the literature indicates no second peak. Therefore, it seems that the friction parameter increases the second peak. Therefore, no friction has been included in the following steps.

Figure 6.20c presents the analysis that was done in step 3, in which the model behaviour varies according to the value of $f_{t,u}$. It is observed that changing the softening properties in tests #8 and #9 has a strong impact on the bond-slip behaviour. This phenomenon can be interpreted through the result of Chapter 5. This implies that the changes in the softening process cause a change in the distribution of confinement stresses.

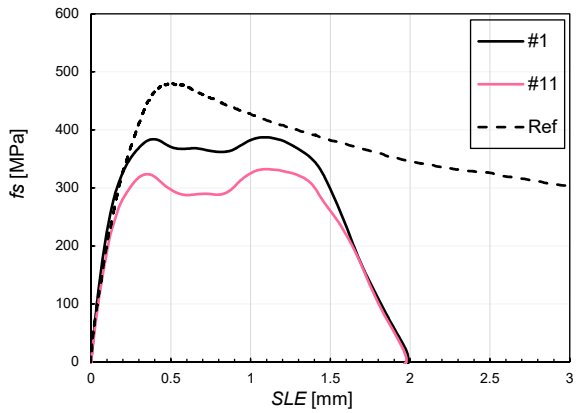

(a) Steps 1

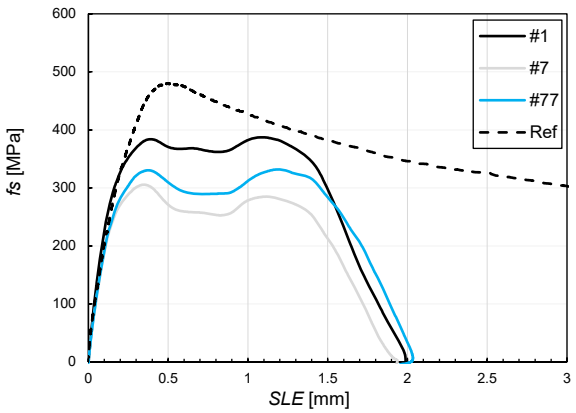

(b) Step 2

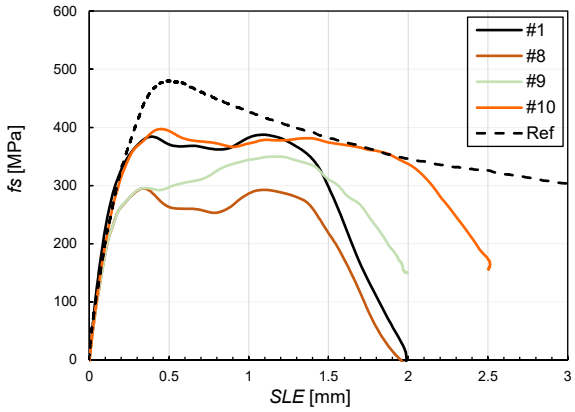

(c) Step 3

Figure 6.20 Bar stress-slip curves

When the tensile properties are selected close to the direct tensile properties with preferential fiber orientation, the bar stress-slip curves start to provide a good agreement with the reference test.

Regarding the curves in Step 4 (Figure 6.21a), the parameters $g_{f,SH}$, E_{sh} have a minor effect on $f_{s,max.}$ This result is in agreement with the results from Chapter 4.

Step 5 results shown in Figure 6.21b indicate that changes in the softening phase, including E_{so} and $G_{f,\,CO}$, influence $f_{s,\,max}$ and $S_{LE\_fs,max}$. This result is also in agreement with Chapter 4 results about the role of E_{so} and $G_{f,\,CO}$ on the bar stress and the slip at the failure.

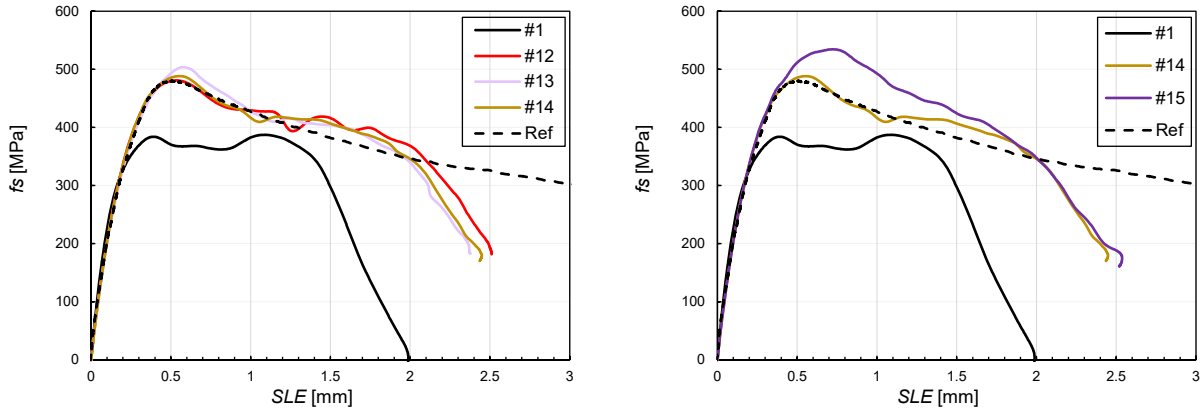

(a) Step 4 (b) Step 5

Figure 6.21 Bar stress-slip curves

Considering test curves #15 and #16 in Figure 6.22 for Step 6, one observe that the unloading modulus (E_p) does not play a vital function in the bar stress-slip response as well as the magnitude of $f_{s,\ max}$ and $S_{LE\_fs,max}$ (Figure 6.22 and Table 6.7). The impact of E_p is more highlighted as a wave on the behaviour of the curve after the peak (Figure 6.22).

Considering the test #9, #10 and #12, which have constant E_{so}, validates Chapter 4 results. In other words, in models with constant E_{so} value, the relationship between $f_{t,u}$ and $f_{s,max}$ is linear, whereas increasing $f_{t,u}$, leads to values of $f_{s,max}$ increasing linearly(Figure 6.23).

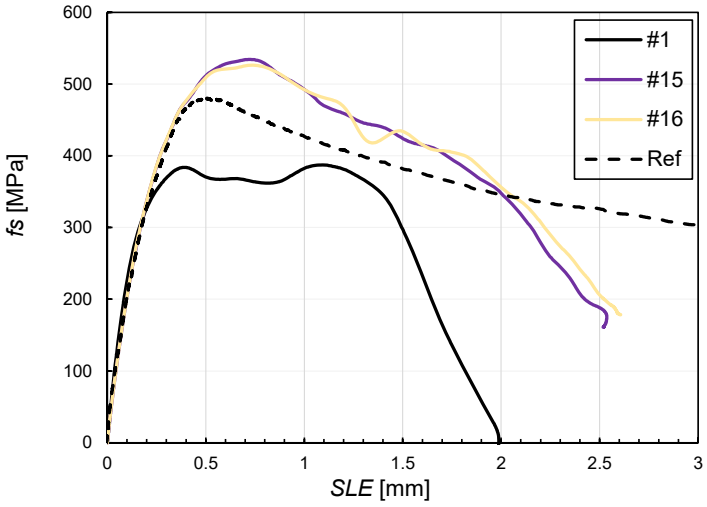

Figure 6.22 Bar stress-slip curve of step 6

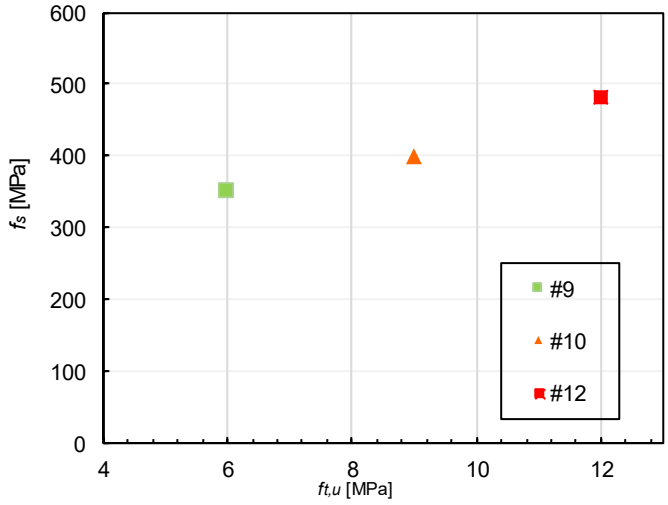

Figure 6.23 The relationship of the bar stress- peak tensile strength at failure (Test #9, #10, #12)

Since models #14 and #15, among the performed tests, have similarities with the tensile properties of the reference specimen, it can be observed that the bar stress-slip curves and reference specimen response curve are very similar and show a good agreement. The maximum bar stress value for model #14 (i.e. 488 MPa) shows almost the same value as the maximum bar stress in the reference

specimen (i.e. 480 MPa), and the maximum bar stress for model #15 (i.e. 534 MPa) is about 10% higher than the reference specimen maximum bar stress (Table 6.7). In fact, these differences highlight the sensitivity of the models to E_{so} or the softening properties.

6.3.3 Investigating the strain and the distance between two points

The impact responses of ε_{θ} and δ defined in section 6.2.2 were applied and compared with their corresponding values on the reference specimen to evaluate better the performed tests after step 3 (Figure 6.24). The range under consideration for the strain is taken from the range presented in the reference specimen. As shown in Figure 6.24a, tests #14 and #15 responses, which have tensile properties similar to the reference specimen, are close to the reference curves, and particularly to the strain gauge curve. This accordance indicates that the developed model has satisfactory accuracy.

Figure 6.24b shows the comparison between potentiometer curve with the numerical prediction curves. It is observed that the curve of test #14 in the maximum bar stress region is in good agreement with the reference specimen curve. Table 6.7 indicates that the values of $\delta_{\_fsmax}$ for test #14 and the reference specimen are very close, while this correlation was not observed in test #15. This difference explains the sensitivity of this parameter to the softening phase, which is significantly higher than other impact responses such as the bar stress and the slip.

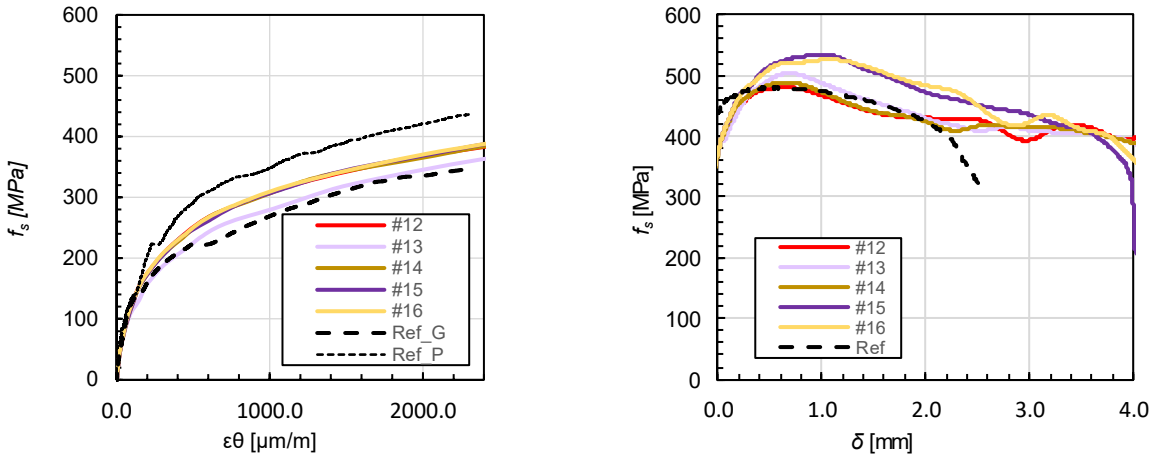

(a) Ortho-radial deformation (b) Distance between two points

Figure 6.24 The tests behaviour for the impact responses of deformation and distance between two points

6.3.4 Conclusion

In this study, an attempt was made to develop the DTB numerical model to consider the effects of fibre orientation in the validation process of the DTB experimental test. Besides, this chapter intended to verify the main results of Chapter 4. Following are the results of the first objective of this study:

- Considering the current version of EPM3D, using the weak bands introduced in this chapter is an acceptable approximate method to reflect the orientation of the fibres on bond simulations.
- The final models (i.e.#14 and #15), which have the tensile properties close to the tensile properties of the reference test, showed acceptable accuracy in the bar stress-slip curve behaviour in general, as well as the magnitude of bar stress and the slip at failure. The difference between the numerical values and the reference specimen was less than 10%.
- From the two models close to the reference specimen (i.e.#14 and #15), model #14 presents good accuracy for the relative displacement between two points. The difference between

the two models was in the softening phase. Hence, it is concluded that the opening of the crack width is a sensitive parameter with respect to UHPFRC softening properties.

Regarding the second objective of this study, we have concluded that Chapter 4 main results are valid. The results of this objective are as follows.

- The hardening phase changes such as $g_{f,sh}$, E_{sh}, and $\varepsilon_{t,u}$ have a reduced effect on the bar stress amplitude and the slip at failure. This result agrees with results from Chapter 4, which indicated that $g_{f,SH}$, E_{sh} and $\varepsilon_{t,u}$ are associated parameters. In other words, they do not play a vital role in the bar stress at failure.
- The softening phase changes, including E_{so} and $G_{f,CO,}$ affect the bar stress and the slip at the failure mode.
- Unloading modulus (i.e. E_{pc}) does not present a crucial effect on the failure responses such as the bar stress and the slip. The impact of E_{pc} is more highlighted as a wave on the behaviour of the bar stress-slip curve after the peak.
- In models with constant E_{so}, the relation between $f_{t,u}$ and $f_{s,max}$ is linear: increasing $f_{t,u}$ generate a proportional increase of $f_{s,max}$.

6.4 Calibration of the model with experimental test results

This section aims to calibrate the developed model presented in section 6.2 with Bastide's (2020) experimental study.

6.4.1 Bastide test series

Table 6.8 and Table 6.9 present details related to Bastide's (2020) specimens. This part also follows explanations presented previously in section 6.1.3.

Table 6.8 Introduction of Bastide's experimental tests (Bastide, 2020)

Specimen identification		d_b (mm)	Anchored and support bar type	Nominal lateral bar diameter (mm)	Lateral bar type	Anchorage length ℓ_d/d_b	Cover c_{so}/d_b	Stirrup area A_{tr} (mm^2)
01	M-10-c1.5-WoS	32	A1035	30	400W	10	1.5	-
02	M-10-c1.5-WoS	32	A1035	30	400W	10	1.5	-
03	M-10-c1.5-WoS	32	A1035	30	400W	10	1.5	-
04	M-8-c1.5-WoS	32	A1035	30	400W	8	1.5	-
05	M-12-c1.5-WoS	32	A1035	32	A1035	12	1.5	-
06	M-6-c2.0-WoS	32	A1035	30	400W	6	2	-
07	M-8-c2.0-WoS	32	A1035	30	400W	8	2	-
08	M-10-c2.0-WoS	32	A1035	32	A1035	10	2	-
11	M-10-c1.5-WS	32	A1035	30	400W	10	1.5	2x200

Table 6.9 Specimen geometry (Bastide, 2020)

Specimen	d_b	ℓ_d		c_{so}		c_{si}		c_r		h	b	e
	(mm)	(d_b)	(mm)	(d_b)	(mm)	(d_b)	(mm)	(d_b)	(mm)	(mm)	(mm)	(mm)
#01-M-10-c1.5-WoS	32	10	320	1.5	48	3	96	3.5	112	768	512	128
#02-M-10-c1.5-WoS	32	10	320	1.5	48	3	96	3.5	112	768	512	128
#03-M-10-c1.5-WoS	32	10	320	1.5	48	3	96	3.5	112	768	512	128
#04-M-8-c1.5-WoS	32	8	256	1.5	48	3	96	3.5	112	640	512	128
#05-M-12-c1.5-WoS	32	12	384	1.5	48	3	96	3.5	112	896	512	128
#06-M-6-c2.0-WoS	32	6	192	2	64	3	96	3.5	112	512	512	160
#07-M-8-c2.0-WoS	32	8	256	2	64	3	96	3.5	112	640	512	160
#08-M-10-c2.0-WoS	32	10	320	2	48	3	96	3.5	112	768	512	160
#11-M-10-c1.5-WS	32	10	320	1.5	48	3	96	3.5	112	768	512	128

6.4.2 Modelling

The entire modelling process follows the procedure mentioned in section 6.2. The models were changed to consider #10 (32 mm) tested bars and 30M lateral bars to satisfy the experimental tests. The details of the ribs were modelled precisely according to the new rebars dimension (Table 6.10). The assumptions and parameters that were considered in section 4.2.2 in terms of mesh details and boundary conditions are also valid for these analyses.

Table 6.10 Rebars geometry

Rebars geometry		
#10 (d_b = 32 mm)	Nominal diameter, d_b (mm)	30.8
	Average rib depth, h_r (mm)	2.2
	Base rib width, a_r (mm)	1.5
	Top rib width, b_r (mm)	2.56
	Rib spacing, s_r (mm)	21.2
30M (d_b = 30 mm)	Nominal diameter, d_b (mm)	28.2
	Average rib depth, h_r (mm)	1.5
	Base rib width, a_r (mm)	1
	Top rib width, b_r (mm)	3.4
	Rib spacing, s_r (mm)	19.2

The diameter of the stirrups is 10 mm. They were modelled using the wire feature of ABAQUS. The location of the stirrups exactly matched those of the test specimens (Figure 6.25).

Moreover, to have an appropriate comparison of the bar stress-slip behaviour, the reference points on the concrete in the numerical model were changed according to the LVDT slip locations in experimental tests (Figure 6.26).

Regarding the modelling of the weak bands, the strategy mentioned in section 6.2.1 was adopted in this study. The thickness of the plane in the bar plane equals the sum of the one rebar diameter and two times of the mesh size (i.e. 38mm).

It is worth noting that the other parameters presented in section 6.2 are applied for this section, such as the amount of shrinkage and the interface parameters without considering friction.

Additionally, the introduced solution parameters in section4.2.5, such as the type of analysis, the amount of the displacement and the step time, are also valid for this part.

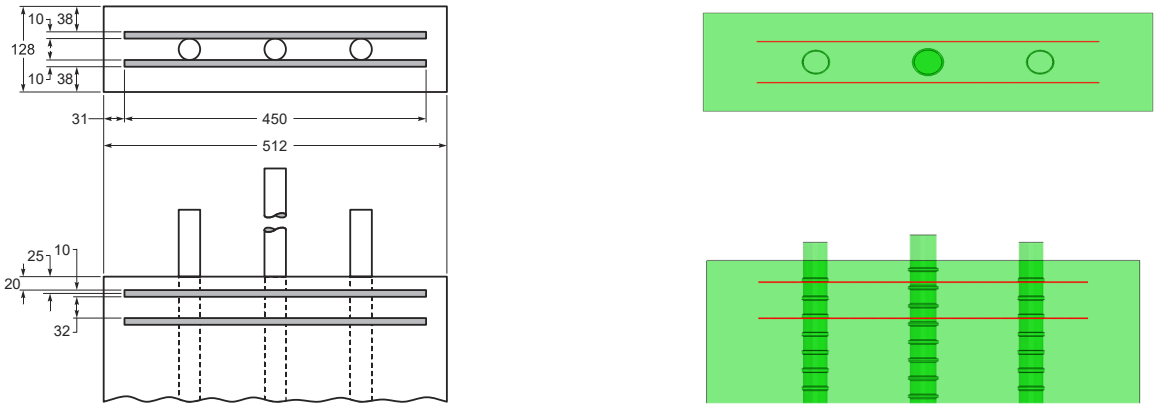

(a) Test specimen (Bastide, 2020) (b) Numerical model

Figure 6.25 Modelling of the stirrups

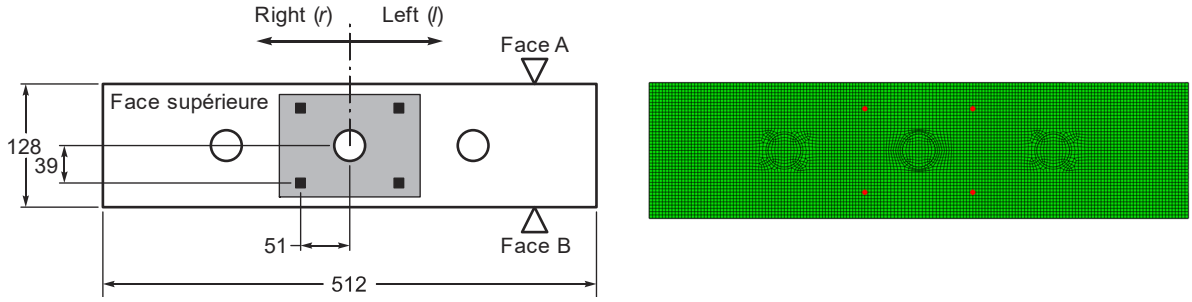

(a) Test specimen (Bastide, 2020) (b) Numerical model

Figure 6.26 Modeling of the slip

6.4.3 Material

Table 6.11 and Figure 6.27 present the UHPFRC tensile properties, which are utilized in the numerical models. The tensile properties of weak bands are displayed in the table and figure.

Table 6.11 UHPFRC tensile properties

Tests	Hardening phase							Softening phase			
	$f_{t,el}$	$f_{t,ts}$	$f_{t,u}$	E_{pc}	$\varepsilon_{t,el}$	$\varepsilon_{t,ts}$	$\varepsilon_{t,u}$	$f_{w,1}$[(1)]	w_1[(2)]	w_u	Eso[(3)]
	(MPa)	*(MPa)*	*(MPa)*	*(MPa)*	*(%)*	*(%)*	*(%)*	*(MPa)*	*(mm)*	*(mm)*	
Numerical	8.0	10.6	12.33	8767	0.025	0.055	0.6	4	1.38	5.5	-6
Weak bands	6.0	6.005	6.01	45000	0.013	0.067	0.12	2.41	1	5.5	-4

(1) $f_{w,1}$: Tensile stress at the junction of two lines for bilinear curves (2) *pp:* The beginning slop of softening phase for bilinear curves

(2) w_1: Crack opening at the junction of two lines for bilinear curves

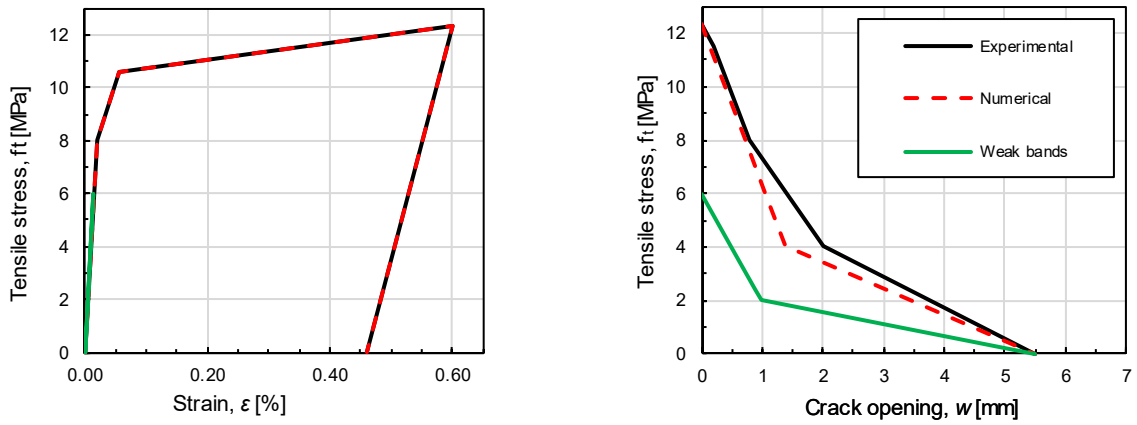

Figure 6.27 Tensile properties curve of UHPFRC in the numerical model

Figure 6.28 presents the nominal stress-strain curves of the bars that were utilized in the experimental study. To consider the plasticity data in ABAQUS, we converted the plastic material data from nominal stress-strain values to true stress-strain values.

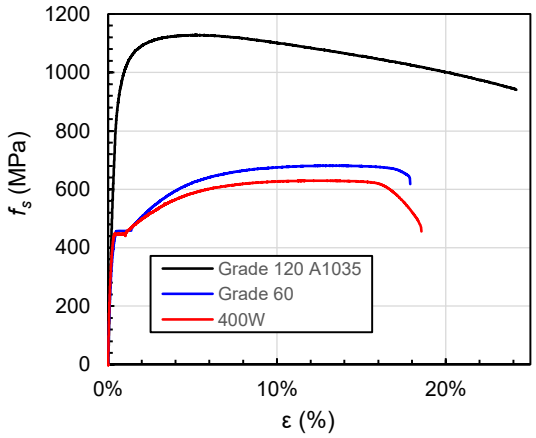

Figure 6.28 Stress-strain curve of steel rebars in the experimental models (Bastide, 2020)

6.4.4 Primary result and calibration process

As indicated in AFGC (2013), dog-bone test tensile results do not reflect the exact value of the UHPFRC mechanical properties used in a lap splice joint. The reason is that several phenomena in the implementation of concrete can lead to significant weaknesses (i.e. flow front, plugs, geometry). Hence, it is necessary to consider these phenomena through the calibration process by applying a reduction factor. The values of this reduction factor in Lagier et al. (2016) and Rossini's (2018) studies were equal to 0.5 and 0.75, respectively. It worth mentioning that in their studies, the random fibre orientation was investigated.

For this study, the specimen of M-10-c1.5-WoS from Table 6.8 was selected as the reference model to do the calibration process. Its geometry was considered for numerical models. The reason for this selection is that there are three results for the mentioned specimen, which help to do the calibration with more reliable accuracy. Figure 6.29 and Table 6.12 indicate the preliminary results of the numerical model and compare them with the experimental results. As observed in these figures, the general numerical behaviour resembles the experimental curves with reasonable precision, which indicates the numerical model accuracy.

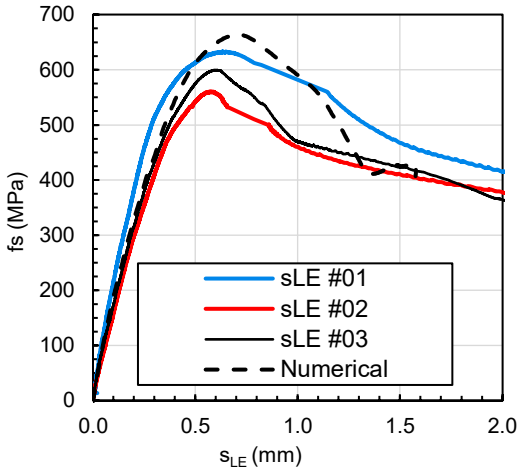

(a) Bar stress-slip

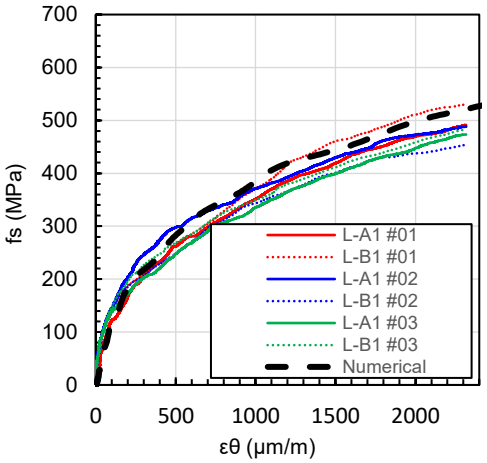

(b) Ortho-radial strains

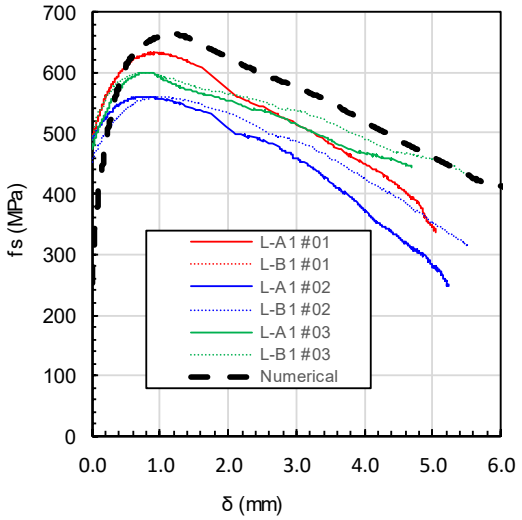

(c) Elongation of the specimen face

Figure 6.29 Comparing the primary numerical curves with the experimental curves

Table 6.12 Primary results of the numerical model

Specimen	$f_{s,\,max}$ (MPa)		$s_{LE\ fsmax}$ (mm)		$\delta_{\ fsmax}$ (mm)	
	EXP	NUM	EXP	NUM	EXP	NUM
#01	633		0.65		0.97	
#02	561	663	0.57	0.71	0.86	1.16
#03	600		0.60		0.80	

EXP: Experimental results
NUM: Numerical results

The bar stress value of test #3 (i.e. 600MPa) was selected as the average of these three experimental tests. Comparison of experimental and numerical results show a difference of approximately 10% (Table 6.12) when using the measured material properties. This indicates that a reduction factor of 0.9 is needed, and it reflects fibre efficiency globally. This reduction factor is much higher than the value of 0.5, and 0.75 suggested in the previous studies by Lagier et al.(2016) and Rosini (2018), respectively. This difference is explained by the preferential orientation of the fibres specifically obtained from the experimental program of Bastide (2020).

As concluded in section 6.4, post-peak slope (i.e. E_{so}) plays a crucial role in the amplitude of bar stress at failure mode, while changing the hardening phase has a reduced impact. Hence, the reduction factor of 0.9 is applied only to the tensile strength of UHPFRC in such a way that the post-peak slope remains constant in the softening part. The ultimate strain was kept constant in the hardening phase through the calibration process (Table 6.13 and Figure 6.30).

Table 6.13 UHPFRC tensile properties before and after the calibration process

Tests	Hardening phase							Softening phase			
	$f_{t,el}$	$f_{t,ts}$	$f_{t,u}$	E_{pc}	$\varepsilon_{t,el}$	$\varepsilon_{t,ts}$	$\varepsilon_{t,u}$	$f_{w,1}$[(1)]	w_1[(2)]	w_u	E_{so} [(3)]
	(MPa)	*(MPa)*	*(MPa)*	*(MPa)*	*(%)*	*(%)*	*(%)*	*(MPa)*	*(mm)*	*(mm)*	
Numerical	8	10.6	12.33	8767	0.025	0.055	0.6	4	1.38	5.5	-6
Numerical_calibration	7.2	9.54	11.1	8767	0.025	0.055	0.6	3.6	1.24	5.5	-6

(1) $f_{w,1}$: Tensile stress at the junction of two lines for bilinear curves

(2) w_1: Crack opening at the junction of two lines for bilinear curves

(3) *pp:* The beginning slop of softening phase for bilinear curves

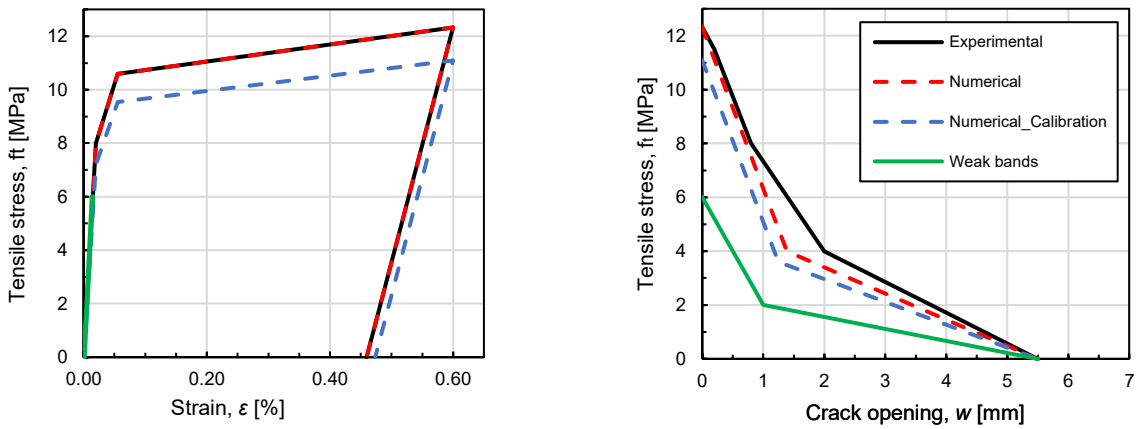

Figure 6.30 Tensile properties curve of UHPFRC in the numerical model after the calibration process

As shown in Table 6.14 and Figure 6.31, the numerical model results after the calibration process are very close to the average test results (i.e. specimen #03) very satisfactory accuracy from two points: the global behaviour and the monitored parameter values at failure. The accuracy indicates that the UHPFRC tensile properties after calibration are acceptable for evaluating the remaining experimental tests.

Table 6.14 Primary results of the numerical model after the calibration process

Specimen	$f_{s,\,max}$ (MPa)			$s_{LE\ fsmax}$ (mm)			$\delta_{\ fsmax}$ (mm)		
	EXP	NUM_CA	ERROR(%)	EXP	NUM_CA	ERROR(%)	EXP	NUM_CA	ERROR(%)
#03	600	602	0%	0.60	0.64	7%	0.80	1.16	34%

EXP: Experimental results

NUM_CA: Numerical results after the calibration process

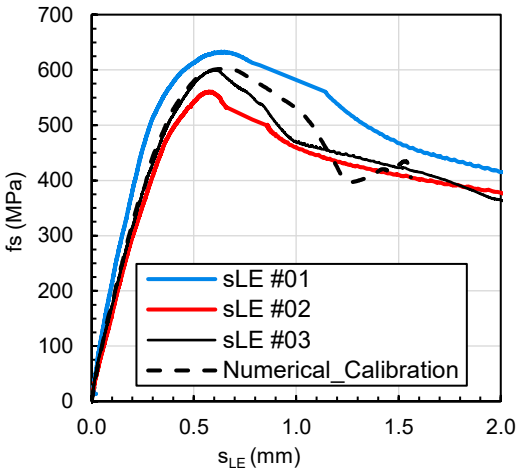

(a) Bar stress-slip

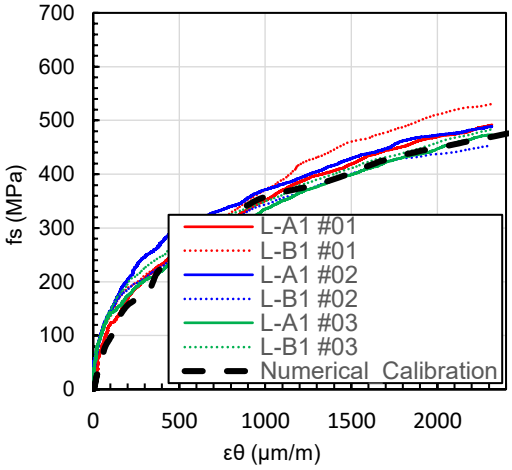

(b) Ortho-radial strains

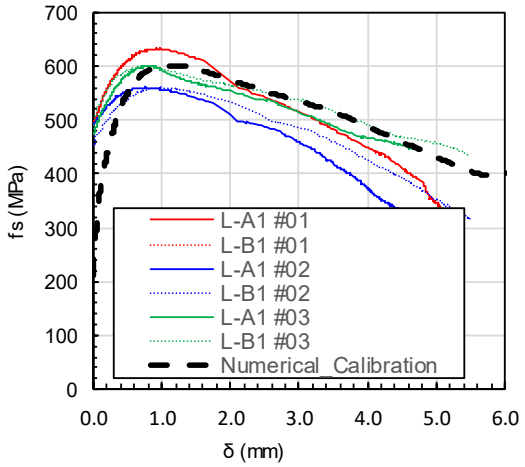

(c) Elongation of the specimen face

Figure 6.31 Comparison of numerical predictions with the experimental results

6.4.5 Validation and comparison

The present section evaluates other experimental specimens according to the calibrated UHPFRC tensile properties obtained in the previous section (i.e. 6.4.4). Regarding the quasi-static criteria in section 3.2.3, the total Kinetic Energy ratio to the Entire Internal (i.e. E_k / E_i) remained below 5% at the onset of the main macro-crack and during the failure mode. Between the failure mode and 85% of the maximum force applied after that, the ratio still stayed below 5%. It means that the

quasi-static analysis assumption is acceptable. Besides, all the numerical failure modes were in good agreement with the experimental failure modes. (Figure 6.32).

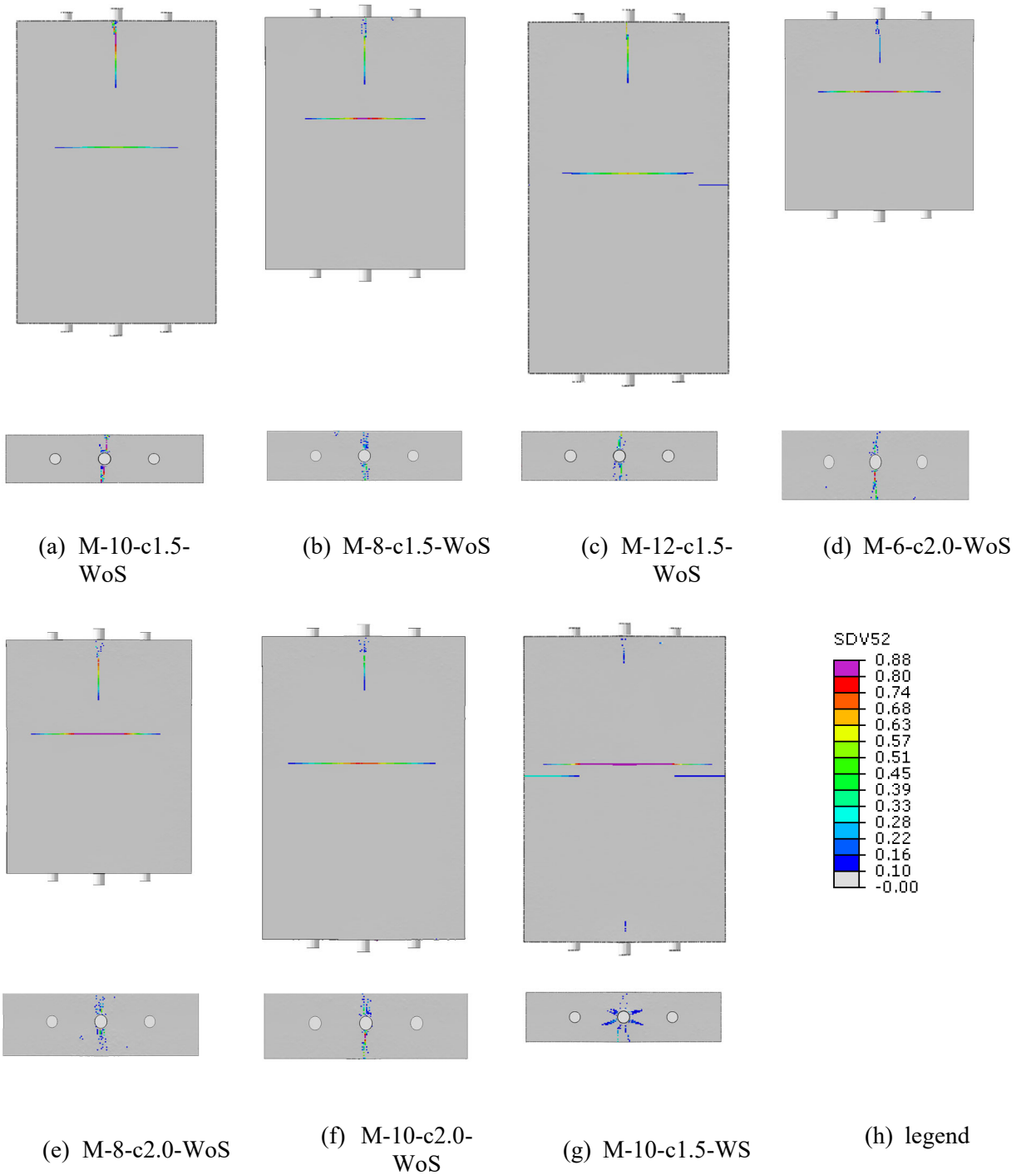

(a) M-10-c1.5-WoS (b) M-8-c1.5-WoS (c) M-12-c1.5-WoS (d) M-6-c2.0-WoS

(e) M-8-c2.0-WoS (f) M-10-c2.0-WoS (g) M-10-c1.5-WS (h) legend

Figure 6.32 Failure modes of all numerical models

The numerical models were examined and compared with the experimental results from two points: the global behaviour and the monitored parameter values at failure. The following observations can be made.

- As shown in Figure 6.33, the bar stress-slip curves for all numerical models are in good agreement with experimental curves, especially for models with c_{so} equals $1.5d_b$.
- Figure 6.34 indicates that the bar stress-deformation curves of the numerical models agreed with experimental curves in perfect accuracy. Based on Bastide's (2020) study, the gauge which measures the distance between two points is designated by the letter "L". Moreover, the letters "A" and "B" displayed the two sides of each specimen.
- Regarding the bar stress-face elongation response, most numerical models present a good agreement with the experimental measures (Figure 6.35a, Figure 6.35b, Figure 6.35d, Figure 6.35e, Figure 6.35f).
- A difference between the numerical models and experimental results is observed by comparing the bar stress at the origin of each curve (Figure 6.35). This difference is related to the assumption of initiating the main macro crack in the experimental program. In other words, Bastide's (2020) research has assumed that the mentioned crack has occurred for $\varepsilon_{t,u}$ equals 0.0024, an assumption that is not valid for the numerical models. Indeed, starting the main macro crack depends on each numerical model geometry, and it is determined precisely by the numerical model.

Moreover, from the latter point of view (i.e. the monitored parameter values at failure), the following observations can be made.

- The bar stress values in the numerical models are in good agreement with experimental data. This observation is more highlighted for the model with c_{so} equals $1.5d_b$. The probable reason is that the value of c_{so} of $1.5d_b$ for the reference model (i.e. #03) was considered for the calibration process.
- The slip values in the numerical models are in perfect agreement with experimental data. This conclusion is more significant for the models with c_{so} equals $1.5d_b$.

- Regarding the side face elongation between the two points, the models with l_d more than $10d_b$ presented a good accuracy with the experimental results, while a reduced accuracy was obtained for other models.

Additionally, the amount of bar stress at the strain of 0.0024 has been compared for the numerical and the experimental specimens. The results show a perfect agreement for all models (Table 6.16).

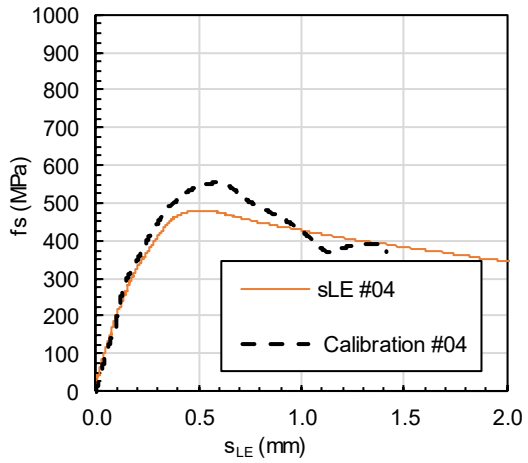

(a) M-8-c1.5-WoS

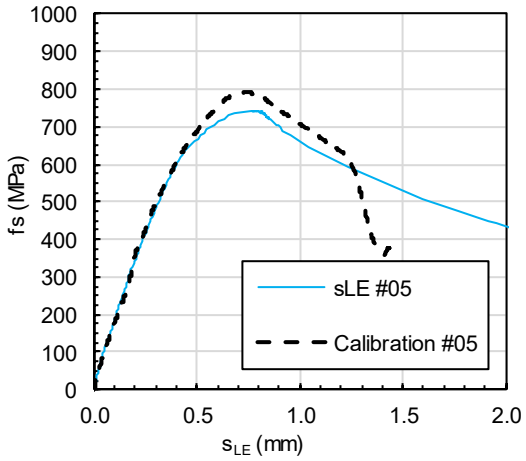

(b) M-12-c1.5-WoS

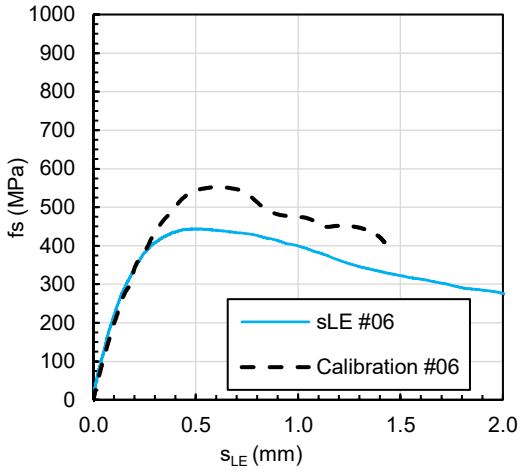

(c) M-6-c2.0-WoS

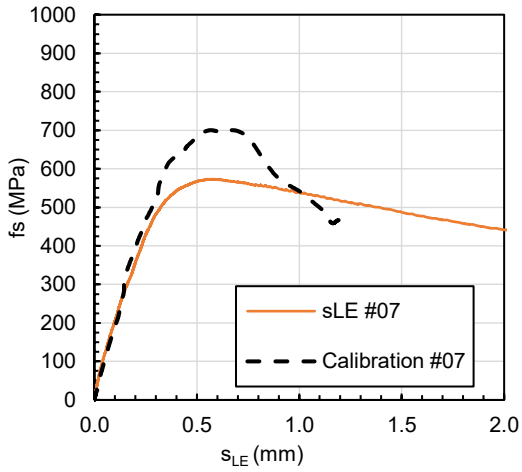

(d) M-8-c2.0-WoS

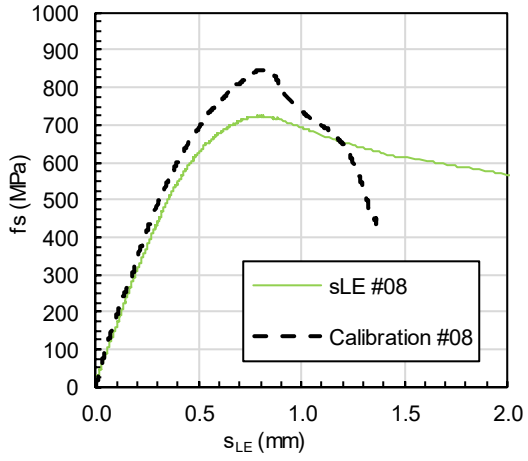

(e) M-10-c2.0-WoS

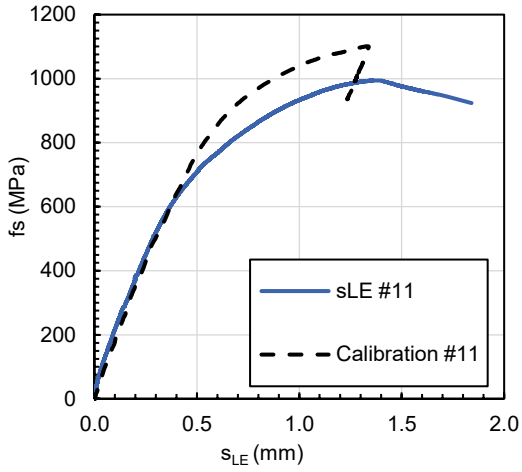

(f) M-10-c1.5-WS

Figure 6.33 Comparison of the experimental and numerical responses for the bar stress-slip

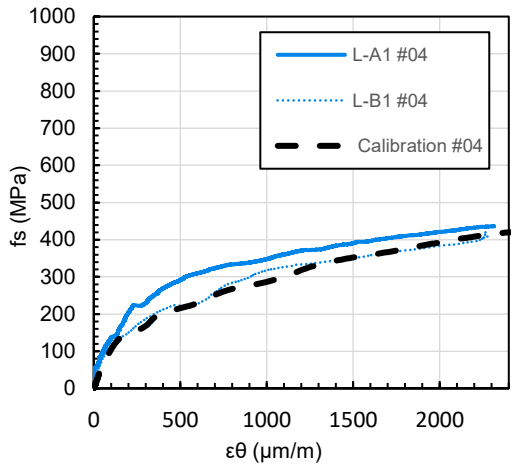

(a) M-8-c1.5-WoS

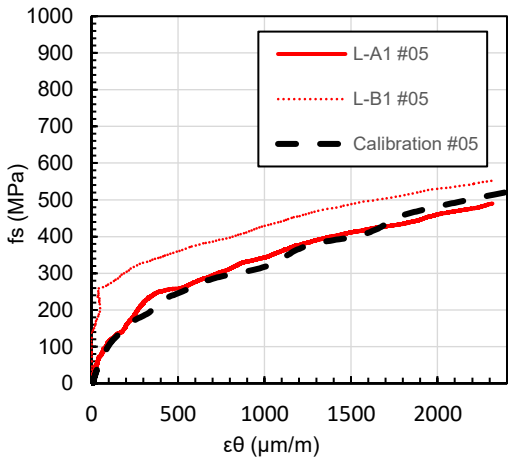

(b) M-12-c1.5-WoS

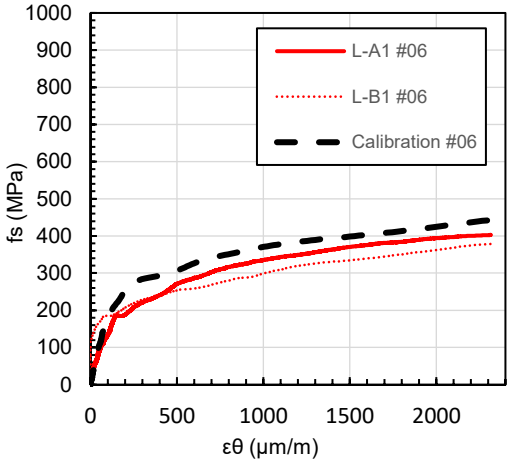

(c) M-6-c2.0-WoS

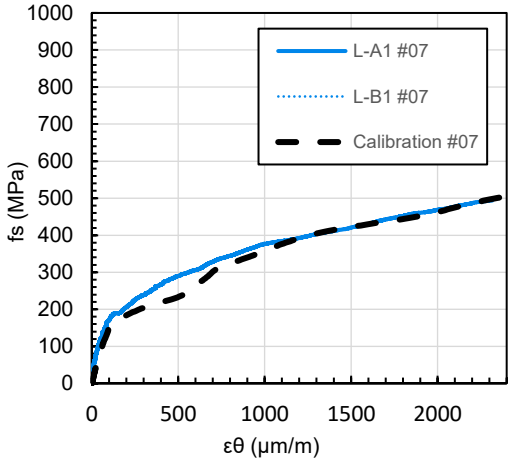

(d) M-8-c2.0-WoS

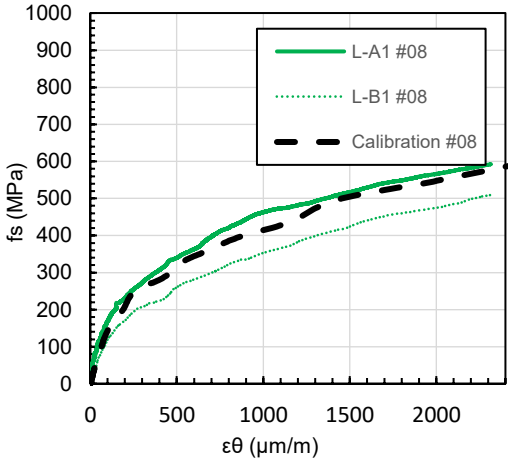

(e) M-10-c2.0-WoS

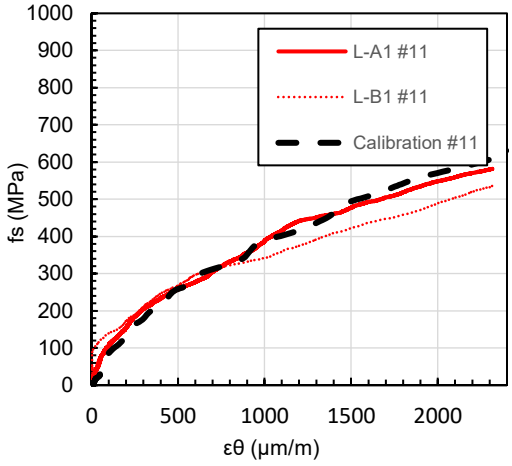

(f) M-10-c1.5-WS

Figure 6.34 Comparison of the experimental and numerical responses for the face elongation

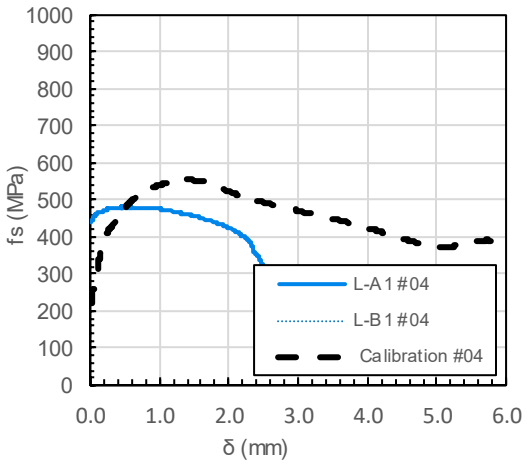

(a) M-8-c1.5-WoS

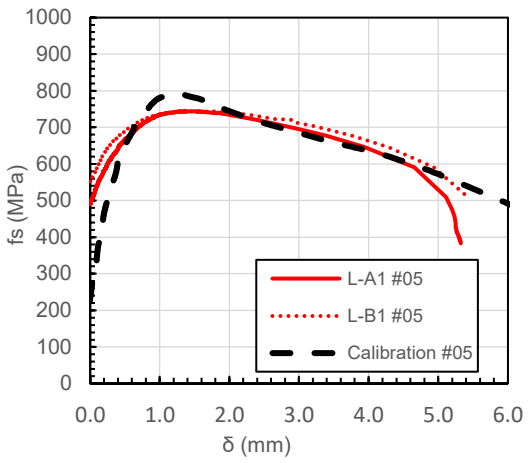

(b) M-12-c1.5-WoS

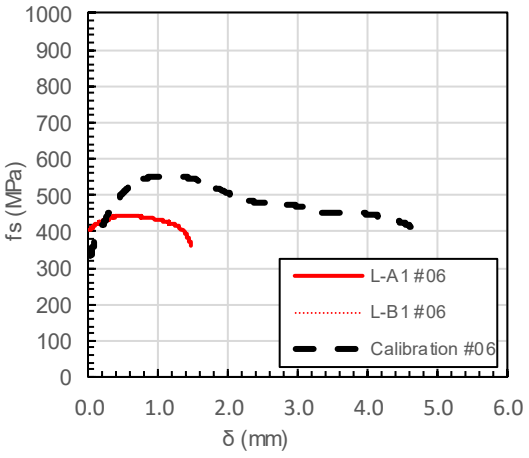

(c) M-6-c2.0-WoS

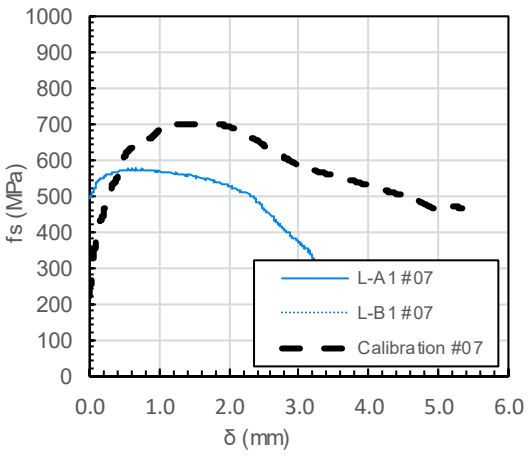

(d) M-8-c2.0-WoS

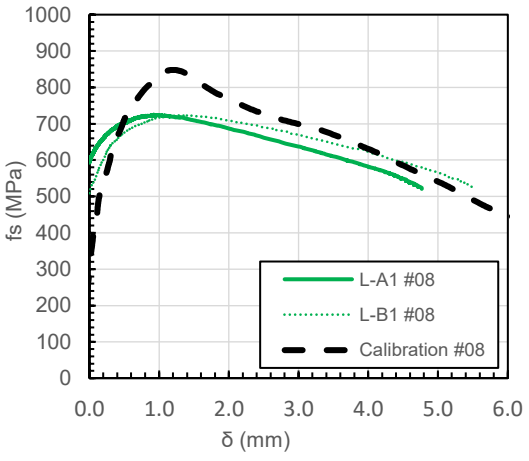

(e) M-10-c2.0-WoS

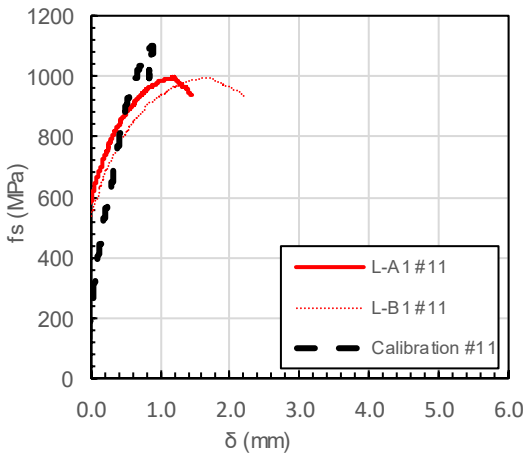

(f) M-10-c1.5-WS

Figure 6.35 Comparison of the experimental and numerical responses for the elongation

Table 6.15 Comparison of the responses at failure

Number	Specimen	$f_{s,\,max}$ (MPa)			$s_{LE\ fsmax}$ (mm)			$\delta_{\ fsmax}$ (mm)		
		EXP[(1)]	NUM_CA[(2)]	EXP/ NUM_CA	EXP	NUM_CA	EXP/ NUM_CA	EXP	NUM_CA	EXP/ NUM_CA
#04	M-8-c1.5-WoS	483	553	0.87	0.51	0.58	0.87	0.53	1.38	0.38
#05	M-12-c1.5-WoS	744	791	0.94	0.76	0.75	1.02	1.52	1.28	1.19
#06	M-6-c2.0-WoS	444	553	0.80	0.48	0.61	0.79	0.50	1.12	0.45
#07	M-8-c2.0-WoS	573	700	0.82	0.57	0.67	0.85	0.84	1.74	0.48
#08	M-10-c2.0-WoS	724	848	0.85	0.79	0.81	0.97	1.12	1.21	0.93
#011	M-10-c1.5-WS	994	1101	0.90	1.27	1.34	0.95	1.46	0.88	1.66

[(1)]EXP: Experimental results

[(2)]NUM_CA: Numerical results after the calibration process

Table 6.16 Comparison of the responses at a strain of 0.0024

Number	Specimen	$f_{s,\,0.24}$[(3)] (MPa)		
		EXP	NUM_CA	EXP/ NUM_CA
#04	M-8-c1.5-WoS	437	415	1.05
#05	M-12-c1.5-WoS	521	512	1.02
#06	M-6-c2.0-WoS	403	442	0.91
#07	M-8-c2.0-WoS	481	496	0.97
#08	M-10-c2.0-WoS	551	577	0.95
#011	M-10-c1.5-WS	595	606	0.98

[(1)]EXP: Experimental results

[(2)]NUM_CA: Numerical results after the calibration process

[(3)]$f_{s,\,0.24}$: Bar stress at the strain of 0.0024

CHAPTER 7 CONCLUSION AND RECOMMENDATIONS

7.1 Review of the objectives

A research project has been conducted in Polytechnique of Montreal to develop UHPFRC lap splice joint design standards for connecting prefabricated bridge elements. These joints must fulfill seismic ductility requirements. As a result, it is required to enhance the lap splice joint efficiency. Loading regimes, system and geometrical parameters, reinforcement properties, and concrete properties are the criteria that these lap splice joints are classified. As a part of this research project, the present thesis focused on the impact of UHPFRC tensile properties on the bond behaviour in non-contact lap splice joints. This thesis objectives are as follows:

1. determining the influence of UHPFRC tensile properties on the bond performance with random fibre orientation.
2. understanding the mechanisms of confinement stress distribution (hoop tensile stress) in the bond zone and interpreting the influences of the first objective according to the confinement stress.
3. developing the numerical models for the certain fibre orientation and calibrating the model with the experimental results of Bastide (2020).

These objectives were investigated separately in Chapter 4, Chapter 5 and Chapter 6. It should be noted that this investigation has been done numerically. We used the finite element software ABAQUS (2016) to model the lap splice behaviour. This research used the constitutive model EPM3D developed by Massicotte et al. (2015) and a rib scale approach to considerer the interaction between reinforcing bar and UHPFRC as defined by Lagier (2015). All the procedures of preprocessing and post-processing in the finite element software have been made by PYTHON.

7.2 Conclusions of the research project

7.2.1 Influence of UHPFRC tensile properties on the bond performance for random fibres orientation

The parameters defining UHPFRC tensile properties are categorized into the main and the associated parameters based on their effects on the bond behaviour. The main parameters directly affect the bond behaviour, and the associated parameters are either ineffective or, if effective, their impact depends on the main parameters. Table 7.1 presents the main parameters which play a notable role in each impact response. As shown in Table 7.1, the parameters $f_{t,u}$ and E_{so} affect all factors related to bond performance. For a given $f_{t,u}$, the parameters associated with the softening phase show more significant influence than the hardening phase parameters on the bond response.

Table 7.1 Main efficient parameters in each impact response

Bond performance parameter	Main UHPFRC parameters
Bar stress at failure ($f_{s,max}$)	$f_{t,u}$, E_{so}
Bar stress at first crack ($f_{s,cr}$)	$f_{t,u}$, $\varepsilon_{t,u}$
Slip at failure ($s_{LE\_fs,max}$)	$f_{t,u}$, E_{so} , $\varepsilon_{t,u}$, $G_{f,CO}$, Δ_{fso}
Inner crack at failure ($wi_{\_fs,max}$)	$f_{t,u}$, E_{so} , $G_{f,CO}$, Δ_{fso}
Outer crack at failure ($wo_{\_fs,max}$)	$f_{t,u}$, E_{so}, $\varepsilon_{t,u}$, $G_{f,CO}$, Δ_{fso}

The details of this section are as follows:

- $f_{t,u}$ plays a key role in the bar stress at failure (i.e. $f_{s,max}$), and the other parameters are associated parameters in the hardening phase, including $\varepsilon_{t,u}$, E_{sh} and $g_{f,SH}$.
- the softening phase parameters E_{so} and $G_{f,CO,}$ play a vital role in the magnitude of $f_{s,max}$.
- the relationship of $f_{t,u}$ with the response parameters of $f_{s,max}$ and $f_{s,cr}$ is linear by considering the constant E_{so}.

- $f_{t,u}$, E_{so}, $G_{f,CO}$, Δ_{fso} and $\varepsilon_{t,u}$ values play a role in determining $S_{LE\_fs,max}$. It should be noted that $\varepsilon_{t,u}$ has a moderate effect on $S_{LE\_fs,max}$ compared to other parameters.
- there is a linear relationship between $f_{t,u}$ and $S_{LE\_fs,max}$ for the sharp slopes regarding the constant softening slope (i.e. E_{so}=6.7, 20). It was not observed such a linear relationship in UHPFRC, which highlights the high ductility (i.e. E_{so}=4).
- regarding the constant E_{so}, the relationship between $f_{t,u}$ and the impact response of $wi\_{fs,max}$ and $wo\_{fs,max}$ for the sharp slopes (i.e. E_{so}=6.7, 20) is linear. It was not seen such a linear relationship for the low slope (i.e. E_{so}=4).
- E_{so} and $f_{t,u}$ played a role in determining the inner crack's width at failure mode (i.e. wi_f_{smax}), while the sensitivity of $wi\_{fs,max}$ to E_{so} is more than of $f_{t,u}$.
- $f_{t,u}$, E_{so} , $G_{f,CO}$, $\varepsilon_{t,u}$ and Δ_{fso} played a role in determining the outer crack width at failure mode (i.e. $wo\_{fs,max}$), while the sensitivity of $wo\_{fs,max}$ to E_{so} is more than others.

7.2.2 Investigation on the mechanisms of stress transfer on the anchorage of rebars in UHPFRC

- According to the confinement stress distribution, the present chapter intends to review the results obtained in Chapter 4. This study also aims to find the confinement stress distribution mechanism for the investigated DTB test. The following conclusions can be drawn: The slope (i.e. E_{so}) changes affect the confinement stress distribution.
- $f_{t,u}$ affects the magnitude of the confinement stress.
- By investigating confinement stress distribution (i.e. S11 and s22) and anchored stress of S33, it can be verified that EPM3D performance was adopted for isotropic fibre properties. The reason is that S_{11}, S_{22}, and S_{33} reached the maximum tensile strength (i.e. $f_{t,u}$) in some locations along of embedded length.

7.2.3 Developing the model based on fibres orientation

In the first step, an attempt was made to develop the DTB numerical model to consider the effects of fibre orientation in the DTB experimental test validation process. Following that in the second step, we confirmed the main results of Chapter 4. In the end, the developed model was validated with the experimental results of Bastide (2020). The results are as follows:

Developing the DTB model

- Considering the current version of EPM3D, using the weak bands introduced in section 6.2.1 is an acceptable approximate method to reflect the orientation of the fibres in certain zones of particular interest.
- The final models (i.e.#14 and #15), which have the tensile properties close to the tensile properties of the reference test, showed acceptable accuracy in the bar stress-slip curve behaviour in general, as well as the amplitude of bar stress and the slip at the failure mode. The difference between the numerical values and the reference specimen was less than 10%.
- From the two models close to the reference model (i.e.#14 and #15), model #14 had good accuracy for capturing the elongation between two points on the specimen face in the anchorage zone. The difference between the two models was in the softening phase. Hence, it is concluded that the splitting crack opening is sensitive to the softening parameters of UHPFRC law used.

Validation of the results of Chapter 4 by the developed model

The softening phase parameters play a more notable role in the bond responses than the hardening phase parameters. The results of this section are as follows:

- The hardening phase changes such as $g_{f,sh}$, E_{sh}, and $\varepsilon_{t,u}$ have a reduced effect on the bar stress amplitude and the slip at failure This result agrees with results from Chapter 4, which indicated that $g_{f,SH}$, E_{sh} and $\varepsilon_{t,u}$ are dependent parameters. In other words, they do not play a key role in the bar stress at failure.
- The softening phase changes, including E_{so} and $G_{f,CO,}$ affect the bar stress and the slip at the failure mode.

- The unloading modulus (i.e. E_{pc}) does not present a crucial effect on the failure responses such as the bar stress and the slip. The impact of E_{pc} is more highlighted as a wave on the behaviour of the bar stress-slip curve after the peak.
- In models with constant E_{so} (i.e. E_{so} =4), the relation between $f_{t,u}$ and $f_{s,max}$ is linear. Increasing $f_{t,u}$ generates a proportional increase of $f_{s,max}$.

Calibration of the developed model with the experimental results

The calibration process led to using a reduction factor equal to 0.9 compared to the UHPFRC tensile law obtained experimentally. This coefficient reflects fibre efficiency globally. This reduction factor is much higher than the value of 0.5, and 0.75 suggested in the previous studies by Lagier et al.(2016) and Rosini (2018), respectively. This difference is explained by the preferential orientation of the fibres specifically obtained from the experimental program of Bastide (2020).

The numerical models were examined and compared with the experimental results from two points: the global behaviour and the monitored parameter values at failure. The following observations can be made.

- the bar stress-slip curves for all numerical models are in good agreement with experimental curves, especially for models with c_{so} equals $1.5d_b$.
- the bar stress-transversal strain curves on the UHPFRC surface close to the loading end are in good agreement with the experimental response.
- Regarding the bar stress-face elongation response, most numerical models present a good agreement with the experimental

Regarding the monitored parameter values at failure, the following observations can be made.

- The bar stress values in the numerical models are in good agreement with experimental data. This observation is more highlighted for the models with c_{so} equals $1.5d_b$.
- The slip values in the numerical models are in perfect agreement with experimental data. This conclusion is more significant for the models with c_{so} is equals to $1.5d_b$.

- Regarding the side face elongation between the two points, the models with l_d more than $10d_b$ presented a good accuracy with the experimental results, while a reduced accuracy was obtained for other models.
- the amounts of bar stress at the strain of 0.0024 have been compared for the numerical and the experimental specimens. The results show a perfect agreement for all models.

7.3 Recommendations

Although the present study has developed a numerical model with acceptable accuracy, this development relies on an approximate method by adding the weak bands. This method faced some limitations in modelling those bands, such as meshing quality and mesh size around the bars. This strategy was adopted due to the current limitations of EPM3D, in which only isotropic UHPFRC tensile properties can be defined. Therefore, for considering the orthotropic properties, the development of EPM3D is highly recommended in a way that it considers the UHPFRC tensile properties in each principal direction separately. Developing this further in the EPM3D can easily investigate the high-performance lap splice joints with any casting directions of fibres. This development requires a validation step from experimental programs in the literature from material scale to structural elements, including fibre orientation effects.

7.4 Future research

After developing the EPM3D, the following studies are suggested:

- Validating the main results obtained in this research include the influence of UHPFRC tensile properties on bond behaviour in both cases of random orientation and orthotropic fibre distribution.
- Validating the numerical models of several continuous lap splice joints with different configurations by the experimental study of Renaud-Laprise (2021) (Figure 7.1).

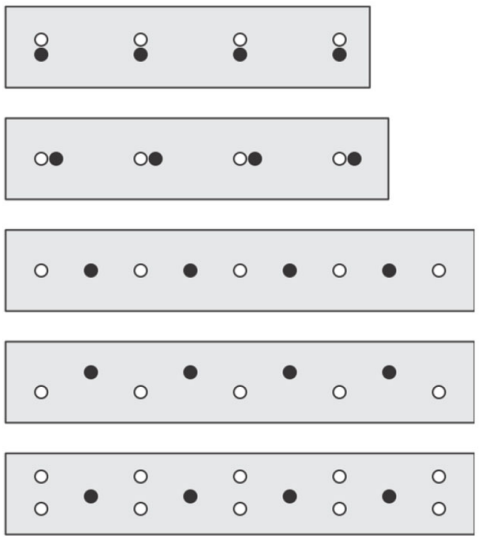

Figure 7.1 Geometry of the joints (Renaud-Laprise, 2021)

- Investigating the UHPFRC tensile properties on contact and non-contact lap splice joints.
- Investigating the impact of the shrinkage on the bond behaviour more precisely.

REFERENCES

408, J. A.-A. C. (2012). 408.2R-12: Report on Bond of Steel Reinforcing Bars Under Cyclic Loads.

Abrishambaf, A., Pimentel, M., & Nunes, S. (2017). Influence of fibre orientation on the tensile behaviour of ultra-high performance fibre reinforced cementitious composites. *Cement and Concrete Research, 97*, 28-40. doi:10.1016/j.cemconres.2017.03.007

Abrishambaf, A., Pimentel, M., & Nunes, S. (2019). A meso-mechanical model to simulate the tensile behaviour of ultra-high performance fibre-reinforced cementitious composites. *Composite Structures, 222*, 110911. doi:10.1016/j.compstruct.2019.110911

AFGC. (2013). Ultra High Performance Fibre-Reinforced Concretes. *Recommendations - Revised edition*.

Appl, J., Eligehausen, R., & Ozbolt, J. (2002). *Numerical analysis of splices with headed deformed reinforcing bars.* Paper presented at the Proceeding of the 3rd Conference on Bond in Concrete - from research to standards Budapest, Hungary.

Azizinamini, A., Chisala, M., & Ghosh, S. K. (1995). Tension development length of reinforcing bars embedded in high-strength concrete. *Engineering Structures, 17*, 512-522. Retrieved from http://dx.doi.org/10.1016/0141-0296(95)00096-P

Bastide, R. (2020). *Comportement de joints de chevauchement en BFUP pour la construction de culées préfabriquées* (Maîtrise ès sciences appliquées). Polytechnique Montréal,

Ben Ftima, M. (2013). *Utilisation de la méthode des éléments finis non-linéaire pour la conception des structures en béton armé : Applications aux structures massives.* (Ph.D). Polytechnique Montréal, Montréal, Canada.

Ben Ftima, M., & Massicotte, B. (2014a). Utilization of Nonlinear Finite Elements for the Design and Assessment of Large Concrete Structures. I: Calibration and Validation. *Journal of Structural Engineering*, 04014217.

Ben Ftima, M., & Massicotte, B. (2014b). Utilization of Nonlinear Finite Elements for the Design and Assessment of Large Concrete Structures. II: Applications. *Journal of Structural Engineering*.

Bouzaiene, A., & Massicotte, B. (1997). Hypoelastic tridimensional model for nonproportional loading of plain concrete. *Journal of Engineering Mechanics ASCE, 123*(11), 1111-1120.

Braike, S. (2006). *Conception d'éléments préfabriqués de ponts avec des bétons fibrés à haute et ultra-haute performance.* (Master's thesis). École Polytechnique Montréal,

Bruno Massicotte. (2019). *Développement et validation du renforcement sismique de piles rectangulaires de ponts par gainage en BFUP*. Retrieved from Département des génies civil, géologique et des mines Polytechnique Montréal:

Canada, G. S. o. (2015). Seismic Hazard Map. Retrieved from https://earthquakescanada.nrcan.gc.ca/hazard-alea/simphaz-en.php

Chao, S.-H., Naaman, A. E., & Parra-Montesinos, G. J. (2009). Bond behavior of reinforcing bars in tensile strain-hardening fiber-reinforced cement composites. *ACI Structural Journal, 106*(6), 897-906. doi:DOI: 10.14359/51663191

Dagenais, M.-A., Massicotte, B., & Boucher-Proulx, G. (2018). Seismic retrofitting of rectangular bridge piers with deficient lap splices using ultrahigh-performance fiber-reinforced concrete. *Journal of Bridge Engineering, 23*(2), 04017129.

Daoud, A., Maurel, O., & Laborderie, C. (2012). *Mesoscopic modelling of the interaction between steel reinforcement and early-age cracking during cement hydration*. Paper presented at the Proceeding of the 4th Conference on Bond in Concrete: Bond, Anchorage, Detailing, Brescia, Italy.

Delsol, S. (2012). *Évaluation du coefficient d'orientation des fibres dans les bétons renforcés de fibres métalliques.* (M.Sc.). Ecole Polytechnique de Montréal, Canada, Qc., Canada.

Delsol, S., & Charron, J.-P. (2013). *Numerical modeling of UHPFRC mechanical behavior based on fibre orientation*. Paper presented at the Proceedings of the RILEM-fib-AFGC International Symposium on Ultra-High Performance Fibre-Reinforced Concrete, Marseille, France.

Den Uijl, J. A., & Bigaj, A. J. (1996). A bond model for ribbed bars based on concrete confinement. *HERON, 41 (3), 1996*.

Deng, M., Pan, J., & Sun, H. (2018). Bond behavior of steel bar embedded in Engineered Cementitious Composites under pullout load. *Construction and Building Materials, 168*, 705-714.

Dhanasekar, M., & Haider, W. (2008). Explicit finite element analysis of lightly reinforced masonry shear walls. *Computers & Structures, 86*(1), 15-26.

Fischer, C., & Ozbolt, J. (2012). *Influence of bar diameter and concrete cover on bond degradation due to corrosion*. Paper presented at the Proceeding of the 4th Conference on Bond in Concrete: Bond, Anchorage, Detailing, Brescia, Italy.

Graybeal, B. (2013). *UHPC for PBES Connections in Seismic Regions*. Paper presented at the Seventh National Seismic Conferenceon Bridges&Highways.

Graybeal, B. (2019). *Design and construction of field-cast ultra-high performance concrete connections*. Retrieved from

Graybeal, B., & Baby, F. (2013). Development of Direct Tension Test Method for Ultra-High-Performance Fiber-Reinforced Concrete. *ACI Materials Journal, 110*(2).

Graybeal, B., Baby, F., Marchand, P., & Toutlemonde, F. (2012). *Direct and flexural tension test methods for determination of the tensile stress–strain response of UHPFRC.* Paper presented at the Kassel international conference, HIPERMAT.

Graybeal, B. A., & Hartmann, J. L. (2003). *Strength and durability of ultra-high performance concrete.* Paper presented at the Concrete Bridge Conference.

Guénet, T. (2016). *Modélisation du comportement des Bétons Fibrés à Ultra-hautes Performances par la micromécanique : effet de l'orientation des fibres à l'échelle de la structure.* (PhD thesis). Université Paris-Est et Université Laval,

Habel, K. (2004). *Structural behaviour of elements combining ultra-high performance fibre reinforced concretes (UHPFRC) and reinforced concrete.* (PhD Thesis). Swiss Federal Institute of Technology in Lausanne.

Hibbitt, Karlsson, & Sorensen. (2010). *ABAQUS/Explicit user's Manual version 6.11-2* (Vol. 1): Hibbitt, Karlsson & Sorensen.

Holschemacher, K., & Weisse, D. (2004). *Bond of reinforcement in fibre reinforced concrete*. Paper presented at the Sixth RILEM Symposium on Fibre Reinforced Concrete (FRC) BEFIB Varenna, Italy.

Holschemacher, K., Weiße, D., & Klotz, S. (2004). *Bond of reinforcement in ultra high strength concrete.* Paper presented at the Proceedings of the International Symposium on Ultra High Performance Concrete.

Holschemacher, K., WieBe, D., & Klotz, S. (2005). *Bond of reinforcement in ultra high- strength concrete*. Paper presented at the Seventh International Symposium on Utilization of High Strength High Performance Concrete

Kianoush, M., Acarcan, M., & Ziari, A. (2008). Behavior of base restrained reinforced concrete walls under volumetric change. *Engineering Structures, 30*(6), 1526-1534.

Lagier, F. (2015). *Étude du comportement de chevauchement d'armatures en traction directe dans du béton fibré ultra performant (Study of the behaviour of lap splices under direct tension in UHPFRC).* (Ph.D thesis). Polytechnique Montreal, Montreal, QC, Canada.

Lagier, F., Massicotte, B., & Charron, J.-P. (2015a). Bond strength of tension lap splice specimens in UHPFRC. *Construction and Building Materials, 93*, 84-94.

Lagier, F., Massicotte, B., & Charron, J.-P. (2016). 3D Nonlinear Finite-Element Modeling of Lap Splices in UHPFRC. *Journal of Materials in Civil Engineering ASCE, in press*. doi:DOI: 10.1061/(ASCE)MT.1943-5533.0001169

Li, V. C., & Maalej, M. (1996). Toughening in cement based composites. Part I: Cement, mortar, and concrete. *Cement and Concrete Composites, 18*(4), 223-237. doi:10.1016/0958-9465(95)00028-3

Lutz, L. A., & Gergely, P. (1967). Mechanics of bond and slip of deformed bars in concrete. *ACI Journal, 64*(11), 711-721.

Massicotte, B., & Ben Ftima, M. (2015). *EPM3D-v3.4 - A user-supplied constitutive model for the nonlinear finite element analysis of reinforced concrete structures*. Retrieved from Report SR15-08, Montreal, Canada:

Massicotte, B., Massicotte, G. R., & Conciatori, D. (2010). *État des connaissances sur la préfabrication des ponts en béton*. Retrieved from

Naaman, A. (2003). Engineered Steel Fibers with Optimal Properties for Reinforcement of Cement Composites. *Journal of Advanced Concrete Technology, 1*(3), 241-252. doi:10.3151/jact.1.241

Naaman, A., & Reinhardt, H. (2006). Proposed classification of HPFRC composites based on their tensile response. *Materials and Structures, 39*(5), 547-555. doi:DOI: 10.1617/s11527-006-9103-2

Naaman, A. E., & Wille, K. (2012). The path to ultra-high performance fiber reinforced concrete (UHP-FRC): five decades of progress. *Proceedings of Hipermat*, 3-15.

Namman, A., & Reinhardt, H. (2003). *Setting the stage, toward performance based classification of FRC composites, High Performance Fiber Reinforced Cement Composties (HPFRCC 4).* Paper presented at the Proc. of the 4th Int. RILEM Workshop.

Nguyen, D. L., Ryu, G. S., Koh, K. T., & Kim, D. J. (2014). Size and geometry dependent tensile behavior of ultra-high-performance fiber-reinforced concrete. *Composites Part B: Engineering, 58*, 279-292. doi:10.1016/j.compositesb.2013.10.072

Piérard, J., Dooms, B., & Cauberg, N. (2012). *Evaluation of durability parameters of UHPC using accelerated lab tests.* Paper presented at the Proceedings of the 3rd International Symposium on UHPC and Nanotechnology for High Performance Construction Materials, Kassel, Germany.

Prinja, N. K., Shepherd, D., & Curley, J. (2005). Simulating structural collapse of a PWR containment. *Nuclear engineering and design, 235*(17), 2033-2043.

Pyo, S., Wille, K., El-Tawil, S., & Naaman, A. E. (2015). Strain rate dependent properties of ultra high performance fiber reinforced concrete (UHP-FRC) under tension. *Cement and Concrete Composites, 56*, 15-24. doi:10.1016/j.cemconcomp.2014.10.002

Reinhardt, H. W., Blaauwendraad, J., & Vos, E. (1984). Prediction of bond between steel and concrete by numerical analysis. *Materials and Structures, 17*(100), 311-320.

Renaud-Laprise, C. (2021). *Conception parasismique de culées préfabriquées.* (Mémoire de maîtrise). Polytechnique Montréal (en rédaction),

Rosini, A. (2018). *Conception des connexions en BFUP à la base de piles préfabriquées répondant aux critères de performance sismique* (Mémoire de maîtrise). Polytechnique Montréal,

Roy, M., Hollmann, C., & Wille, K. (2017). Influence of volume fraction and orientation of fibers on the pullout behavior of reinforcement bar embedded in ultra high performance concrete. *Construction and Building Materials, 146*, 582-593.

Schumacher, P. (2006). Rotation capacity of self-compacting steel fiber reinforced concrete.

Tepfers, R. (1973). *A theory of bond applied to overlapped tensile reinforcement splices for deformed bars.* (Ph.D. Thesis). Chalmers University of Technology, Goteborg, Sweden.

Tholen, M. L., & Darwin, D. (1996). *Effects of deformation properties on the bond of reinforcing bars*. Retrieved from

Wille, K. (2008). *Load Carrying Behaviour of Novel Composite Structures with regard to a Two-dimensional*

Reinforcement. (Doctoral Thesis). University of Leipzig,

Wille, K., El-Tawil, S., & Naaman, A. (2014). Properties of strain hardening ultra high performance fiber reinforced concrete (UHP-FRC) under direct tensile loading. *Cement and Concrete Composites, 48*, 53-66.

Wille, K., El-Tawil, S., & Naaman, A. E. (2014). Properties of strain hardening ultra high performance fiber reinforced concrete (UHP-FRC) under direct tensile loading. *Cement and Concrete Composites, 48*, 53-66.

Wille, K., & Naaman, A. E. (2010). *Fracture energy of UHPFRC under direct tensile loading.* Paper presented at the FraMCoS-7 International Conference.

Xu, M., & Wille, K. (2015). Fracture energy of UHP-FRC under direct tensile loading applied at low strain rates. *Composites Part B: Engineering, 80*, 116-125.

Yu, K., Ding, Y., Liu, J., & Bai, Y. (2020). Energy dissipation characteristics of all-grade polyethylene fiber-reinforced engineered cementitious composites (PE-ECC). *Cement and Concrete Composites, 106*, 103459. doi:10.1016/j.cemconcomp.2019.103459

Ziari, A., & Kianoush, M. R. (2013). Finite-Element Parametric Study of Bond and Splitting Stresses in Reinforced Concrete Tie Members. *Journal of Structural Engineering, 150*(5), 1-10.

APPENDIX A CONFIRMING THE EFFICIENCY OF THE WEAK BANDS

In this part, to completely understand that adding the weak bands displayed in section 6.2.1 is an effective approximate method, we examined the numerical model of M-10-c1.5-WoS presented in section 6.4.4 in two states: without weak bands and with weak bands(Figure A.1). Figure A.2 indicates the results of the mentioned states compared to the experimental model of M-10-c1.5-WoS (i.e. sL#03).

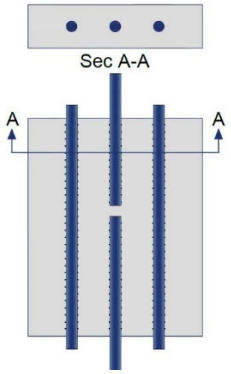

(a) Numerical_WO_Weak bands

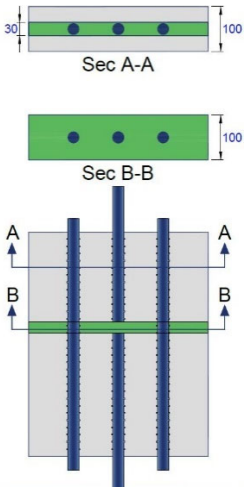

(b) Numerical_W_Weak bands

Figure A.1 Modeling of M-10-c1.5-WoS in two states

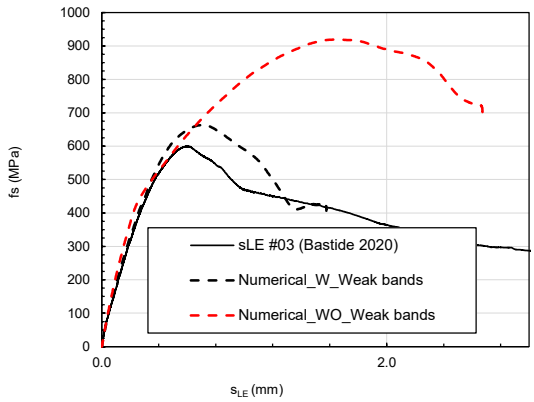

Figure A.2 The results of M-10-c1.5-WoS in two states

APPENDIX B INVESTIGATION OF CONTINUOUS UHPFRC JOINTS

The present Appendix aims to help Camille Renaud-Laprise's (2021) research to assess the various arrangement of the continuous lap-splice UHPFRC joins. Indeed, this section investigates the behaviour of her specimens before the experimental program. Figure B.1, Figure B.2 and Figure B.3 display all the geometries of Renaud-Laprise's (2021) specimens.

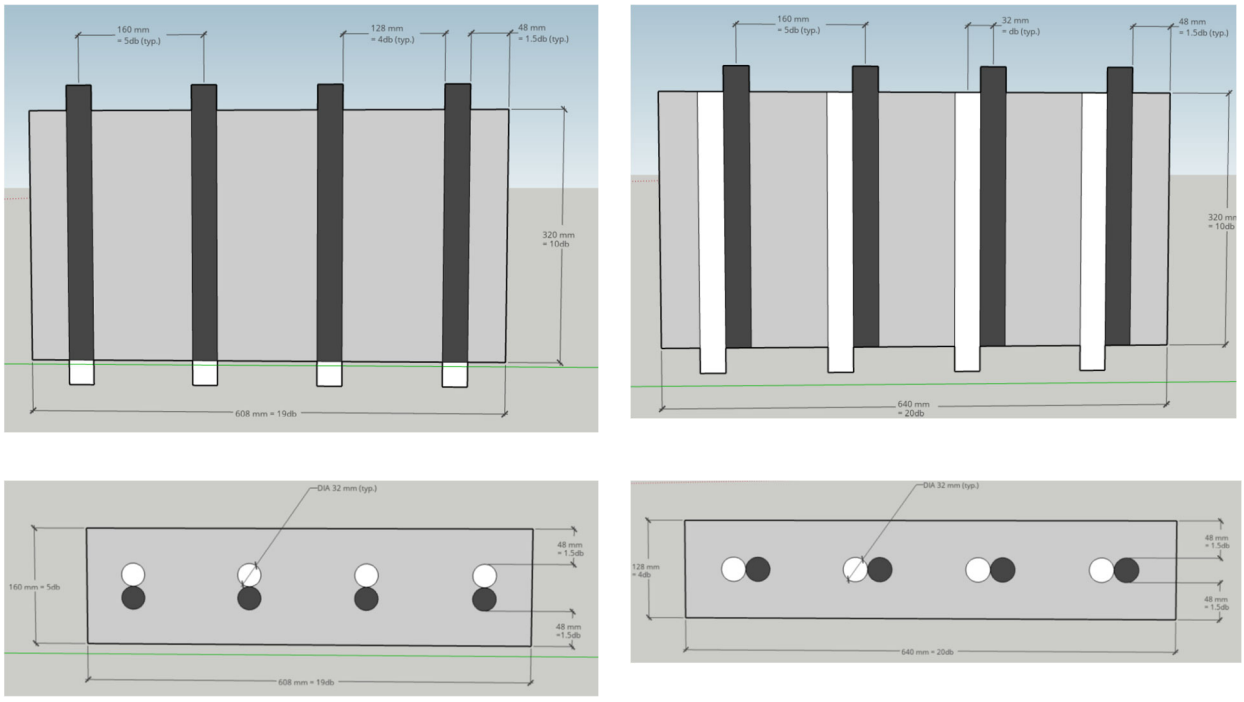

(a) F1 (b) F2

Figure B.1 The geometry of specimens F1 and F2 (Renaud-Laprise, 2021)

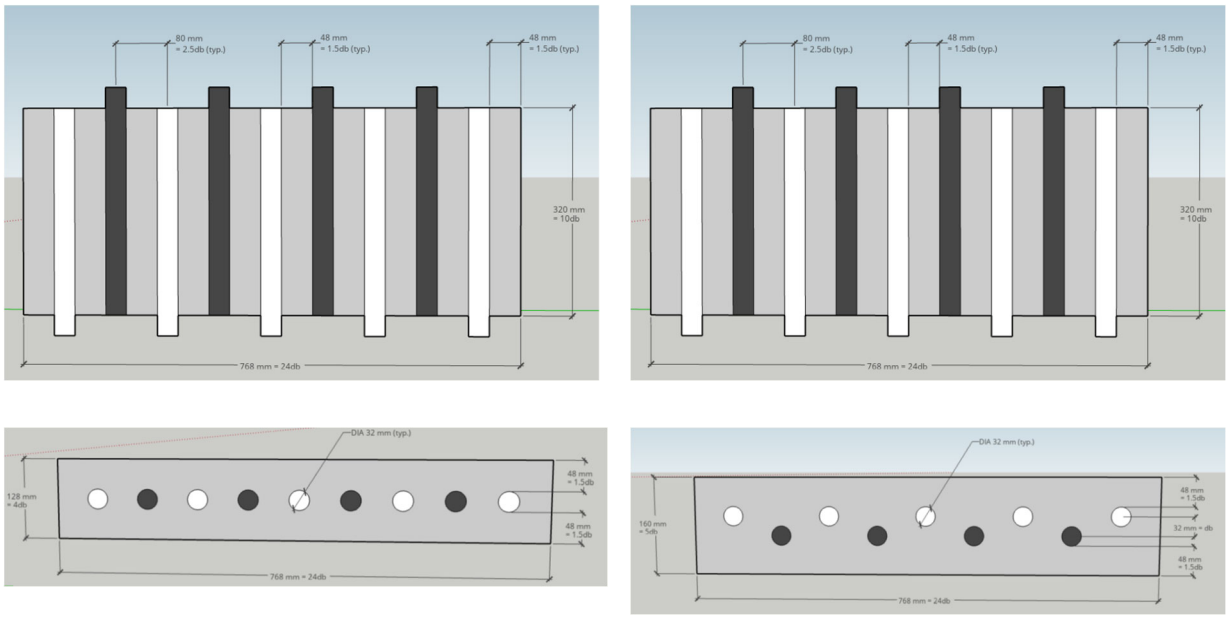

(a) F3 (b) F4

Figure B.2 The geometry of specimens F3 and F4 (Renaud-Laprise, 2021)

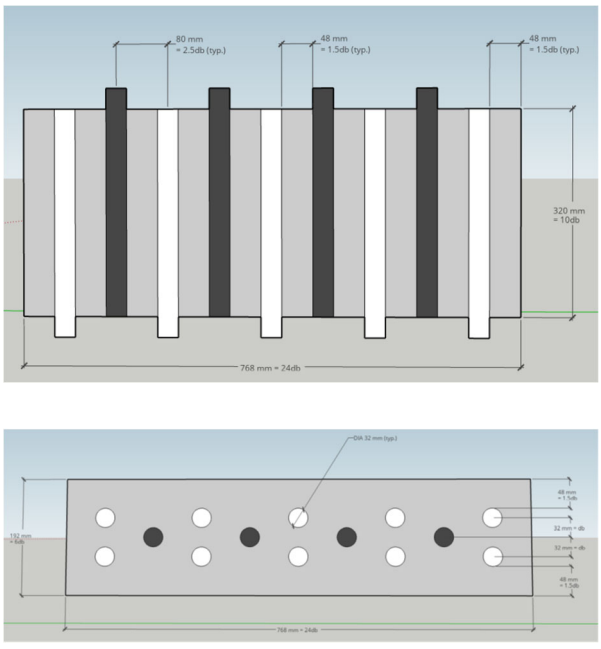

(a) F5

Figure B.3 The geometry of specimens F5 (Renaud-Laprise, 2021)

The load is applied as a displacement function at the end of the tested bars (TR) and the waiting bars (WR) through smooth imposing by using the Dynamic Explicit method. To avoid the impact of the loading speed rate (i.e. Displacement/time), we considered the constant speed load for all of the models (Table B.1). Moreover, Shrinkage and Creep impacts are not considered.

The intersections of both reinforcement bars (TR and WR) and concrete at the central node were restrained in two directions perpendicular to the rebar's axis. Figure B. 4 displays the mentioned boundary conditions for one of the specimens (i.e. F1).

Table B.1 Loading parameters

Loading parameters	
Type	Dynamic, Explicit
Displacement (mm)	2
Smooth step(sec)	0.026

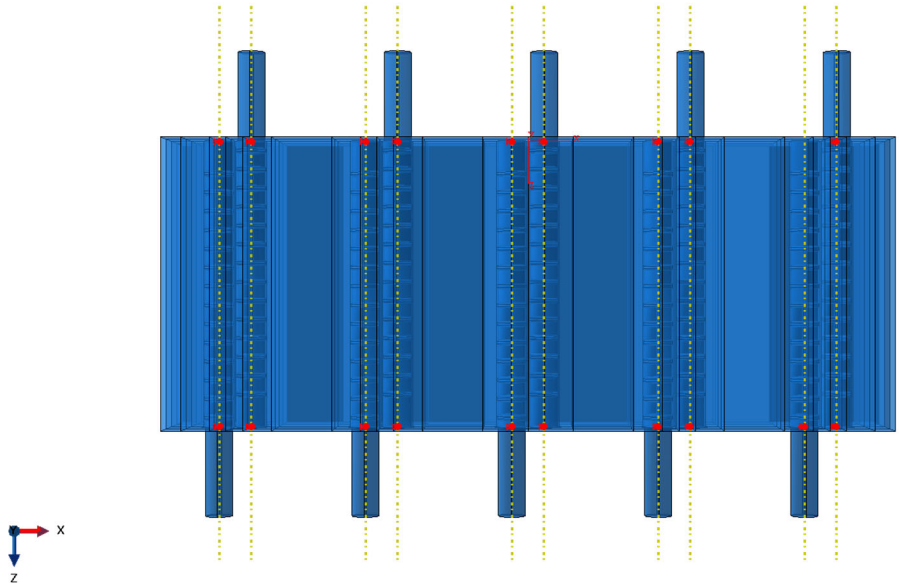

Figure B. 4The boundary conditions of specimen F1

The primary UHPFRC tensile properties are presented in Table B. 2 and Figure B.5. Moreover, at this stage, the linear elastic behaviour is considered for rebars to avoid the effect of steel bar yielding (Table B.3).

Table B. 2 Compression mechanical properties

Compression mechanical properties	
Young modulus, *Ec* (GPa)	45
Poisson's ratio, v_c (MPa)	0.2
uniaxial compressive strength, *f'c*	-100
Uniaxial peak strain corresponding, ε_c	0.0045

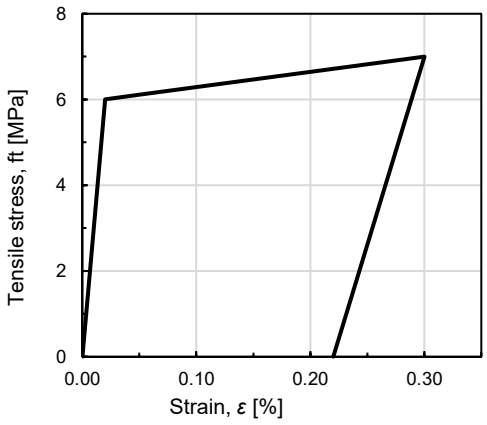

(a) Strain hardening response

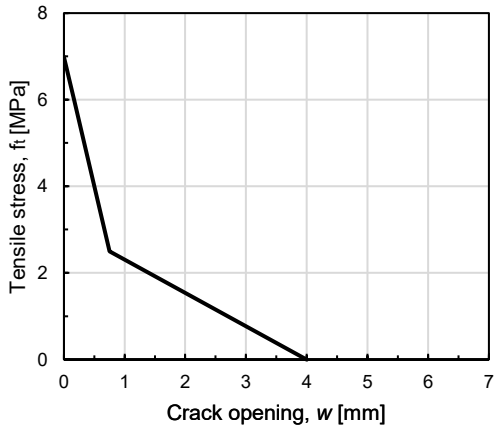

(b) Crack-opening response

Figure B.5 Tensile properties of UHPFRC

Table B.3 Steel material properties

Steel material properties	
Young modulus, Es (GPa)	200
Yield strength, fy (MPa)	460

The results of bar stress for tested rebars are presented in Table B.4. The number of tested rebars indicates in Figure B.6.

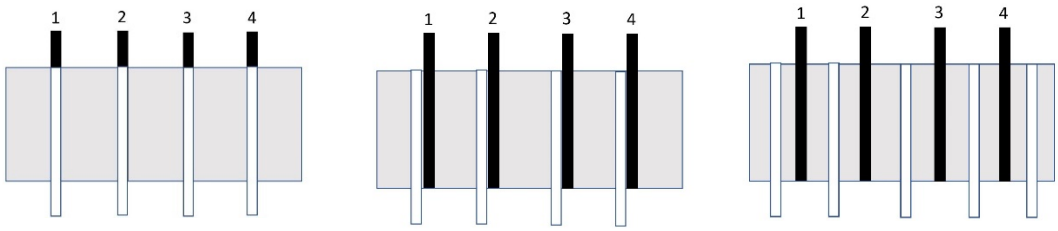

F1 F2 F3, F4 and F5

Figure B.6 Tested rebar numbers

Table B.4 Bar stress at failure mode for tested rebars

Tested rebars number		Average	***1***	*2*	*3*	*4*
Specimen	Failure mode	$f_{s,\,max}$ *(MPa)*	$f_{s,\,max}$ *(MPa)*	$f_{s,\,max}$ *(MPa)*	$f_{s,\,max}$ *(MPa)*	$f_{s,\,max}$ *(MPa)*
S1	P[(1)]		508	665	663	511
S2	RS[(2)]+P		623	663	654	454
S3	RS+P		685	625	624	685
S4	RS+P		663	636	640	660
S5	RS+P		988	959	959	988

[(1)]P: Perpendicular to the rebar axis

[(2)]RS: Radial Splitting

Figure B.7, Figure B.8, Figure B.9, Figure B.10, Figure B.11, and Figure B.12 display the bar stress curves and failure modes of all the specimens.

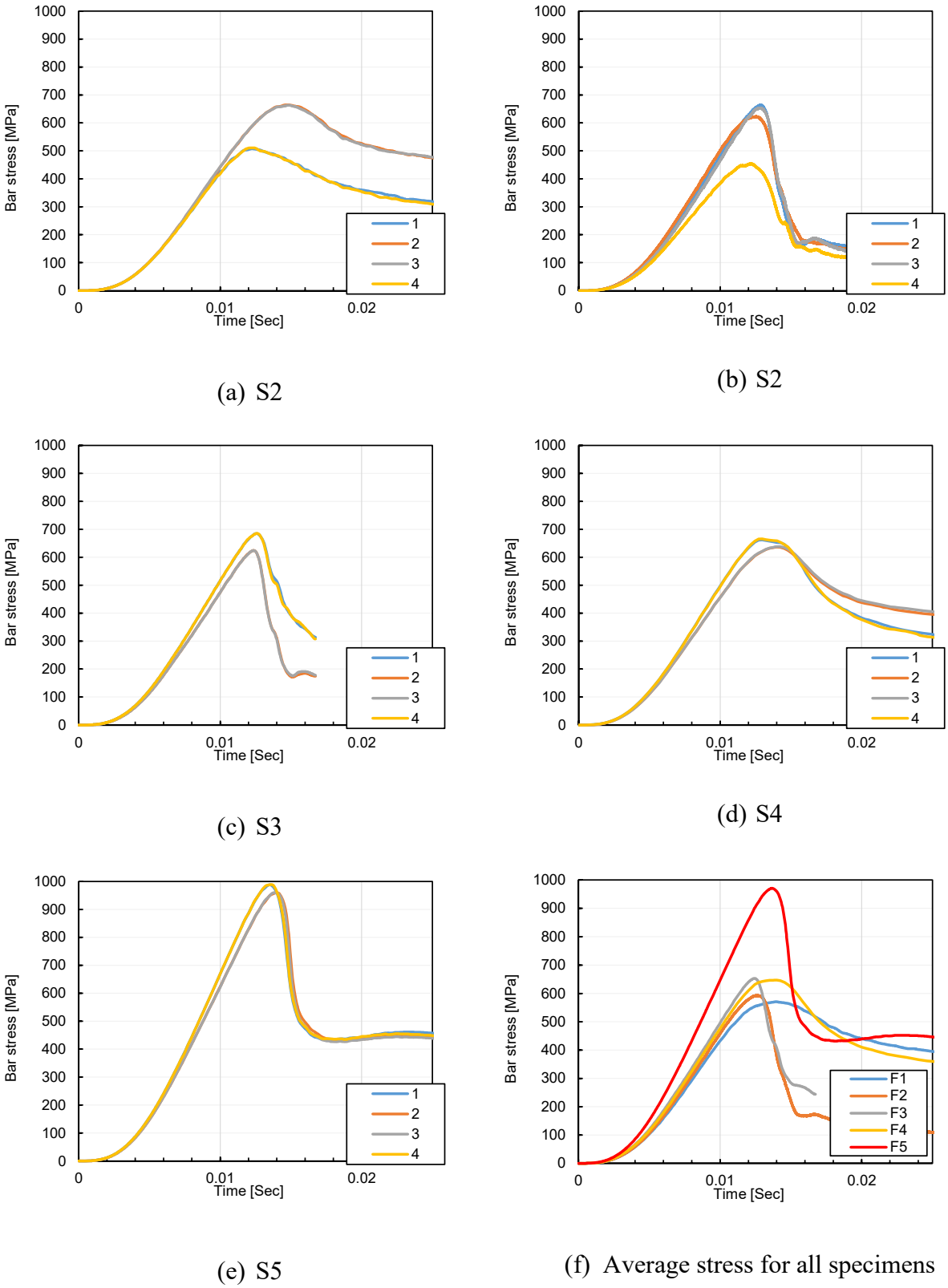

(a) S2

(b) S2

(c) S3

(d) S4

(e) S5

(f) Average stress for all specimens

Figure B.7 Bar stress curves

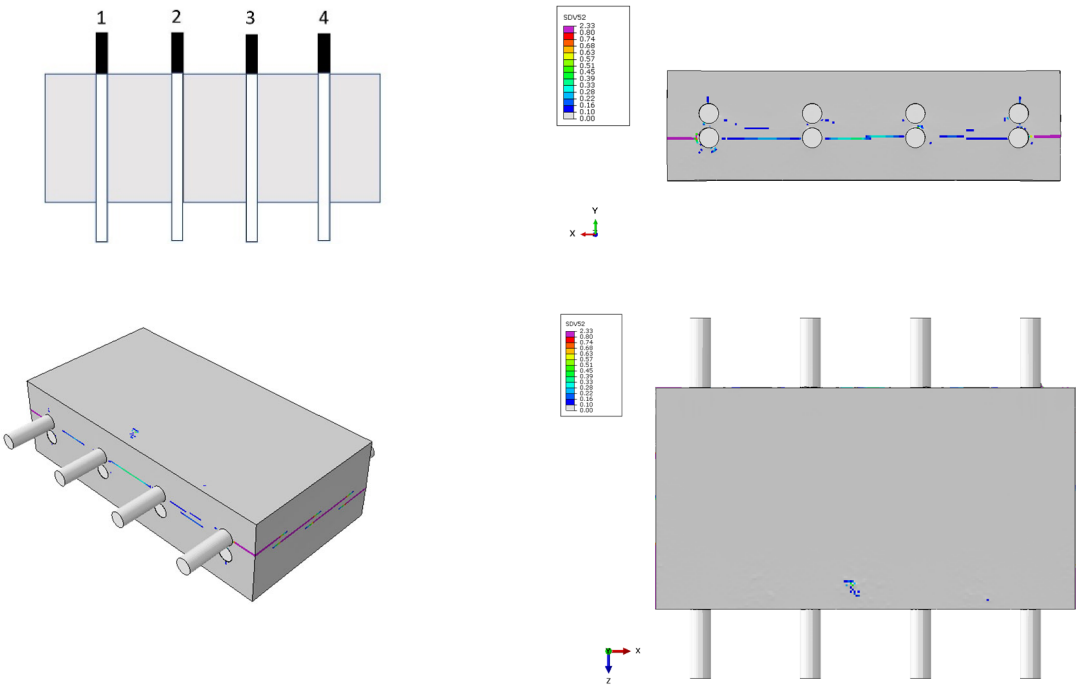

Figure B.8 Failure model of the specimen F1

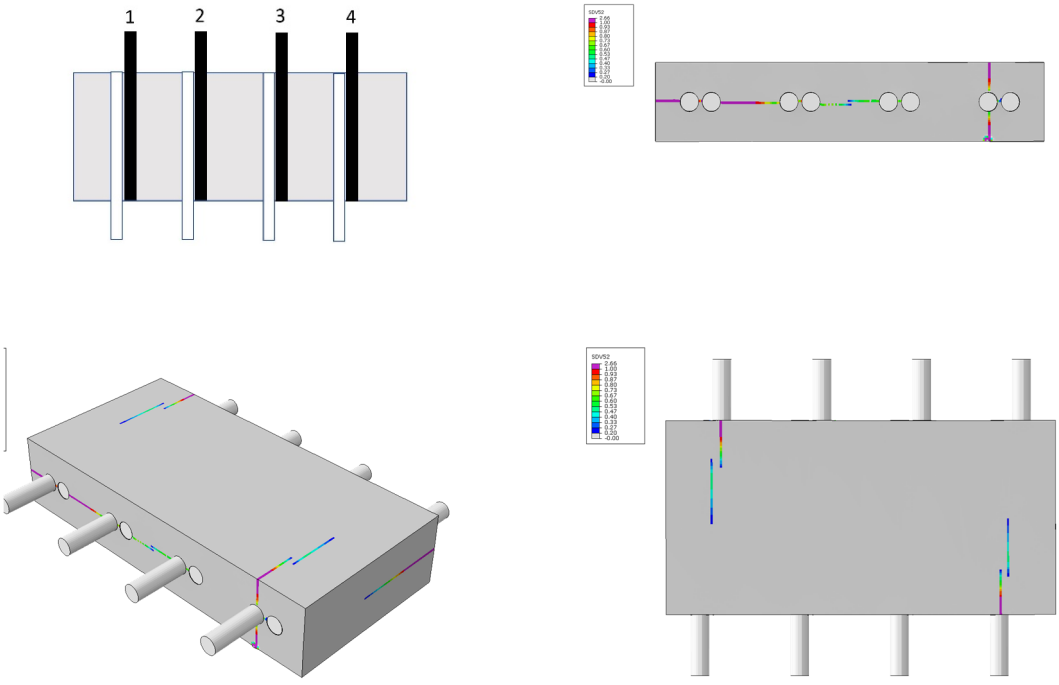

Figure B.9 Failure model of the specimen F2

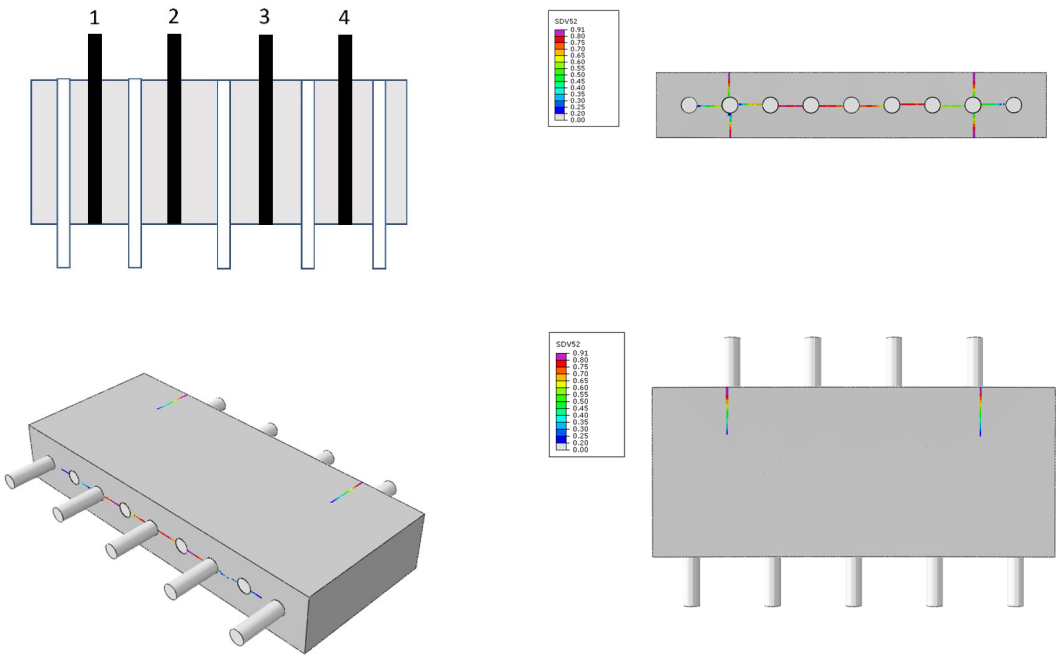

Figure B.10 Failure model of the specimen F3

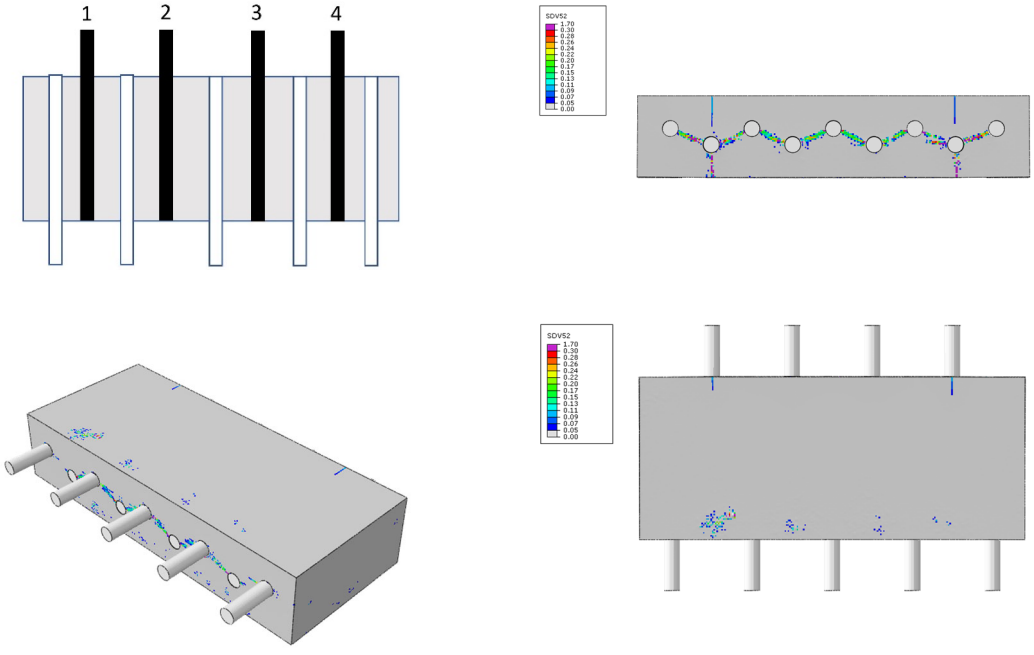

Figure B.11 Failure model of the specimen F4

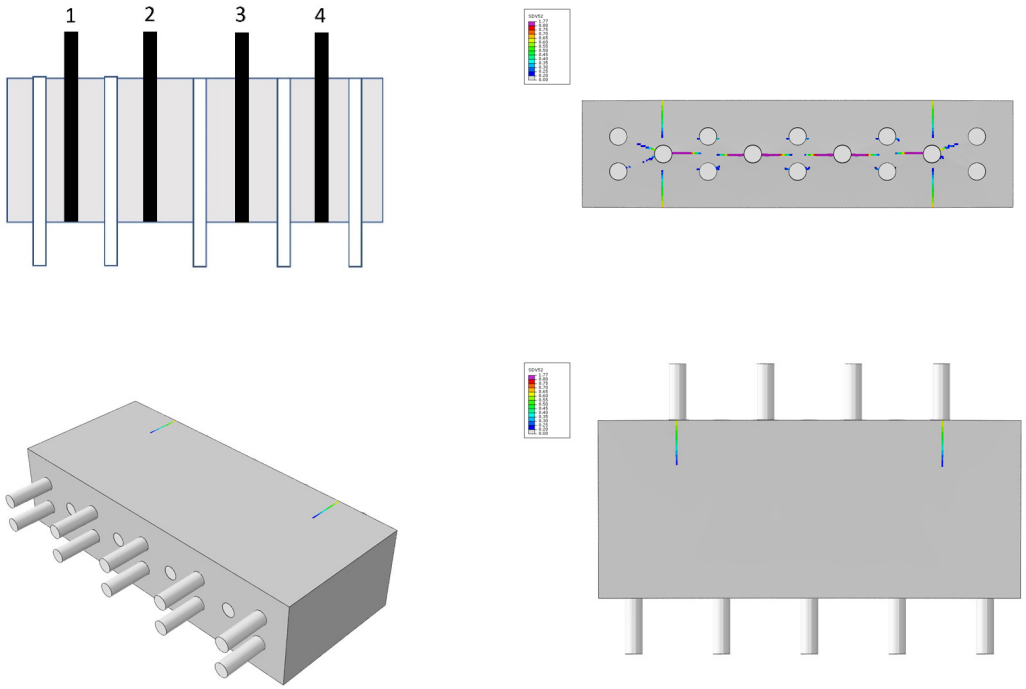

Figure B.12 Failure model of the specimen F5